HYDROGEN PRODUCTION VIA STEAM REFORMING OF GLYCEROL

A THESIS SUBMITTED TO
THE GRADUATE SCHOOL OF NATURAL AND APPLIED SCIENCES
OF
MIDDLE EAST TECHNICAL UNIVERSITY

BY

SEVİL GÖKTÜRK

IN PARTIAL FULFILLMENT OF THE REQUIREMENTS
FOR
THE DEGREE OF MASTER OF SCIENCE
IN
CHEMICAL ENGINEERING

FEBRUARY 2021

ABSTRACT

HYDROGEN PRODUCTION VIA STEAM REFORMING OF GLYCEROL

Göktürk, Sevil
Master of Science, Chemical Engineering
Supervisor: Prof. Dr. Naime Aslı Sezgi
Co-Supervisor: Prof. Dr. Timur Doğu

February 2021, 301 pages

Today, intensive studies are carried out on alternative energy sources that will replace fossil fuels due to its limited sources, soaring of prices and negative effects on people and environment. Hydrogen energy offers a solution to minimize these problems as a clean and renewable energy carrier. One of the most important applications of hydrogen is its use in fuel cell-derived vehicles. However, the implementation of hydrogen in the transport sector is limited by the difficulty of storage and the lack of infrastructure for its distribution. On-board hydrogen generation is a great solution to overcome these limitations, particularly by allowing hydrogen produced from renewable sources to be fed directly into the fuel cell without itself being stored. Bio-glycerol is one of the most attractive biomass-derived oxygenated compounds since its utilization in hydrogen production through steam reforming process is economically viable and environmentally friendly. In addition, theoretically one mole of glycerol produces 7 moles of hydrogen gas. Bio-glycerol is produced as a by-product of 10% by weight of biodiesel synthesis produced by

transesterification of vegetable oils or animal fats, allowing it to be used as a low-cost raw material in a large supply of renewable materials. Generally, metal-loaded mesoporous supports are used to achieve higher hydrogen yield in steam reforming of glycerol.

In this study, silica aerogel was used for the first time as a catalyst support in the steam reforming of glycerol. To activate the silica aerogel, various types and amounts of metal precursors were loaded onto the silica aerogel by wet-impregnation or co-precipitation methods. According to the characterization results, all catalysts are mesoporous and in crystal forms with Lewis dominant acid sites.

The activities of the catalysts were tested in a conventional fixed-bed quartz reactor in the presence of a constant weight of catalyst at constant carrier gas flow rate, atmospheric pressure, and various reaction parameters. According to the experimental results, the increase in water/glycerol molar ratio resulted in an increase in H_2 yield, furthermore, H_2 yield increased first and then decreased slightly at elevated temperatures consistent with the equilibrium line. In addition, the increase in the metal amount increased the H_2 yield, while the catalyst synthesis method and loaded-metal types affected the H_2 yield in various ways. In particular, Ni-Ru containing bimetallic catalysts showed greater activity among the catalysts used in the reaction.

As a result of the experiments, the highest activity was achieved at 550^{o}C, atmospheric pressure, water-glycerol feed flow rate of 0.9 ml/h and 30 ml/min of Ar flow rate with the W/G molar ratio of 9 in the presence of 0.15 g catalyst. Under these conditions, the highest H_2 yield was obtained as 84.5%, with coke deposition as 0.06 $g_c/g_{cat}h^{-1}$ in the presence of 10Ni-2Ru/SA catalyst.

Keywords: Glycerol, Hydrogen, Steam Reforming, Mesoporous Materials, Silica Aerogel

ÖZ

GLİSEROLÜN BUHARLI REFORMLANMASI İLE HİDROJEN ÜRETİMİ

Göktürk, Sevil
Yüksek Lisans, Kimya Mühendisliği
Tez Yöneticisi: Prof. Dr. Naime Aslı Sezgi
Ortak Tez Yöneticisi: Prof. Dr. Timur Doğu

Şubat 2021, 301 sayfa

Günümüzde sınırlı kaynakları, artan fiyatları, insan ve çevre üzerindeki olumsuz etkileri nedeniyle fosil yakıtların yerini alacak alternatif enerji kaynakları konusunda yoğun çalışmalar yapılmaktadır. Hidrojen enerjisi, temiz ve yenilenebilir bir enerji taşıyıcısı olarak bu sorunları en aza indirmek için bir çözüm sunar. Hidrojenin en önemli uygulamalarından biri yakıt hücresinden türetilmiş araçlarda kullanılmasıdır. Ancak, taşımacılık sektöründe hidrojenin uygulanması, depolama güçlüğü ve dağıtımındaki altyapı eksikliği nedeniyle sınırlıdır. Yerleşik hidrojen üretimi, özellikle yenilenebilir kaynaklardan üretilen hidrojenin depolanmadan doğrudan yakıt hücresine beslenmesini sağlayarak bu sınırlamaların üstesinden gelmek için harika bir çözümdür. Biyo-gliserol, buharla dönüştürme işlemi yoluyla hidrojen üretiminde kullanımı ekonomik olarak uygun ve çevre dostu olduğundan dolayı biyokütleden türetilmiş en çekici oksijenli bileşiklerden biridir. Ek olarak, bir mol gliserol teorik olarak 7 mol hidrojen gazı üretir. Biyo-gliserol, bitkisel yağların veya hayvansal yağların transesterifikasyonuyla üretilen biyodizel sentezinin ağırlıkça

%10'u olarak bir yan ürün olarak üretilir, bu da onun büyük bir yenilenebilir malzeme tedariğinde düşük maliyetli hammadde olarak kullanılmasını sağlar. Genellikle, metal yüklü mezogözenekli destekler, gliserolün buharlı reformlanmasında daha yüksek hidrojen verimi elde etmek için kullanılır.

Bu çalışmada, silika aerojel ilk kez gliserolün buharlı reformlanmasında katalizör desteği olarak kullanılmıştır. Silika aerojeli aktif hale getirmek için, silika aerojel üzerine ıslak emdirme veya eş zamanlı çöktürme yöntemleri ile çeşitli tiplerde ve miktarlarda metal öncüleri yüklenmiştir. Karakterizasyon sonuçlarına göre, tüm katalizörler mezogözeneklidir ve Lewis baskın asit bölgeleri ile kristal formlardadır.

Katalizörlerin aktiviteleri, sabit bir katalizör ağırlığının mevcudiyetinde, atmosferik basınçta, sabit taşıyıcı gaz akış hızında ve çeşitli reaksiyon parametrelerinde geleneksel sabit yataklı kuvars reaktörde test edilmiştir. Deney sonuçlarına göre, su/gliserol molar oranındaki artış, H_2 veriminde bir artış sağlamıştır, ayrıca H_2 verimi denge eğrisi ile tutarlı olarak, artan sıcaklıklarda önce artıp sonra hafifçe azalmıştır. Ek olarak, metal miktarındaki artış H_2 verimini artırırken, katalizör sentez yöntemi ve yüklenen metal türleri çeşitli şekillerde H_2 verimini etkilemiştir. Özellikle Ni-Ru içeren ikili metalik katalizörler, reaksiyonda kullanılan katalizörler arasında daha fazla aktivite göstermiştir.

Deneyler sonucunda en yüksek aktivite 550^oC, atmosferik basınç, su-gliserol besleme akış hızı 0,9 ml/saat ve 30 ml/dk Ar akış hızı ile W/G molar oranı 9 iken 0,15 g katalizör varlığında elde edilmiştir. Bu koşullar altında en yüksek H_2 verimi, 10Ni-2Ru/SA katalizörü varlığında 0,06 $g_c/g_{cat}h^{-1}$ kok birikmesi ile %84,5 olarak elde edilmiştir.

Anahtar Kelimeler: Gliserol, Hidrojen, Buhar Reformlama, Mezogözenekli Malzemeler, Silika Aerojel

To my beloved family

ACKNOWLEDGMENTS

I would like to express my deep and sincere gratitude to my supervisor Prof. Dr. Naime Aslı Sezgi and my co-supervisor Prof. Dr. Timur Doğu for giving me the opportunity to do research and providing invaluable guidance during this study. It was a great privilege and honour to work under their dynamism, vision, sincerity and motivation.

I would like to extend my special thanks to my lab-mate Merve Sarıyer for being there to help me with her patience and kindness. Without her support and belief, the study would be much harder. I would like to thank Pınar Değirmencioğlu for her help and patience. I would also thank all of my lab-mates Seda Sivri, Salih Ermiş, Sohrab Nikazar, Abdul Rehman Habib and Çağla Bozcuoğlu for their friendship and support.

I would also like to thank Mihrican Açıkgöz, Doğan Akkuş and all the staff at METU Central Lab and Department of Chemical Engineering for the characterization analysis of the catalysts. I would like to express my special thanks to İsa Çağlar and Cemil Araçlı for helping me whenever I need. I would also like to thank all the instructors and staff at METU Chemical Engineering Department.

I thank all my dear friends, Edanur Uzunmehmetoğlu, Burcu Altunoğlu, Merve Bağrıyanık, Begüm Erbaş, Ece Yurtlu, Ece Şahin, Neslin Güler, Zeynep Öztan, Ezgi Altıntaş, Salih Ermiş, Büşra Karakaya, İsmihan Altıparmak, Özgün Memioğlu, Batıkan Özdamar and Gökhan Gök for their endless friendship and continuous support.

I am deeply grateful to my family for their love, prayers, care and sacrifices to educate me and prepare me for my future. I am very much thankful to my mother

Nejla Altuğ and my brother Emir Göktürk for their endless support, belief, courage and understanding in completing this study.

I would like to extend my special thanks to my friend Eren Dereli for his deep love, care, patience, understanding, belief and support.

Finally, I would like to thank everyone who supported me in completing this study directly or indirectly.

TABLE OF CONTENTS

LIST OF TABLES

TABLES

LIST OF FIGURES

FIGURES

NOMENCLATURE

$\mathbf{A_i}$: Area of component i read from GC

B: Full width at half maximum, radian

c: Crystal shape factor

$\mathbf{C_{gas\ total}}$: Total concentration of the gas mixture at 20°C and 1 atm, mole/ml

$\mathbf{F^o_{C_3H_8O_3}}$: Initial molar flow rate of glycerol, mole/min

$\mathbf{F_{C_3H_8O_3,liquid}}$: The molar flow rate of glycerol in the liquid phase, mole/min

$\mathbf{F_i}$: Molar flow rate of species i, mole/s

$\mathbf{MW_i}$: Molecular weight of species i, g/mole

$\mathbf{N_i}$: Number of moles of species i

P: Pressure, atm

$\mathbf{Q_{Ar}}$: Volumetric flow rate of argon, ml/s

$\mathbf{Q_i}$: Volumetric flow rate of species i, ml/s

$\mathbf{Q_{gas\ products}}$: Total volumetric flow rate of gas products, ml/s

R: Ideal gas constant, J/mole-K

T: Temperature, °C

$\mathbf{T_{calcination}}$: Calcination temperature, °C

$\mathbf{T_{reduction}}$: Reduction temperature, °C

$\mathbf{T_{room}}$: Room temperature, °C

$\mathbf{T_{rxn}}$: Reaction temperature, °C

$\mathbf{t_{crystallite}}$: Crystallite size, nm

$\mathbf{X_{C_3H_8O_3}}$: Conversion of glycerol

$\mathbf{x_i}$: Mole fraction of species i in the liquid

$\mathbf{y_i}$: Mole fraction of species i in the gas mixture

$\mathbf{Y_{H_2}}$: Hydrogen yield, mole hydrogen produced/mole glycerol supplied

$\mathbf{Y_{H_2}}(\%)$: Hydrogen yield, percent

Greek Letters

β_i : Beta factor of component i

ρ_i : Density of species i at 20°C, g/ml

λ : Wavelength of radiation, nm

θ : Bragg angle, °

Abbreviations

B: Bronsted Acid Site

BDDT: Brunauer-Deming-Deming-Teller

BET: Brunauer-Emmett-Teller

BJH: Barrett-Joyner-Halenda

DRIFTS: Diffuse Reflectance Infrared Fourier Transform Spectroscopy

FFR: Feed (Water & Glycerol) Flow Rate

GC: Gas Chromatograph

GSR: Glycerol Steam Reforming

L: Lewis Acid Site

L+B: Lewis+Bronsted Acid Sites

L/(L+B): Lewis-to-(Lewis+Bronsted)

W/G: Water-to-Glycerol

WGMR: Water-to-Glycerol Molar Ratio

WGSR: Water Gas Shift Reaction

S/C: Steam-to-Carbon

SA: Silica Aerogel

SBA-15: Santa Barbara Amorphous-15

SEM: Scanning Electron Microscopy

TCD: Thermal Conductivity Detector

TEOS: Tetraethylorthosilicate

TGA: Thermogravimetric Analysis

TMCS: Trimethylchlorosilane

TPD: Temperature Programmed Desorption

XRD: X-Ray Diffraction

CHAPTER 1

INTRODUCTION

Today, approximately 80% of energy demand is met by non-renewable energy sources that exist in the form of fossil fuels such as coal, petroleum and natural gas (Kothari et al., 2008). Even though they are cheap and easy to use, they are available on the earth in limited quantity and are foreseen to vanish fifty-sixty years from now. Therefore, their prices are soaring day by day. In addition, they are not environmentally friendly since the fossil fuels are put through a process called combustion to produce energy and can have serious effect on health. Combustion releases pollutants containing carbon dioxide, nitrous oxide and sulphur dioxide that can cause global warming and acid rain (Hosseini and Wahid, 2016).

The ever-increasing global demand for energy and the rapid depletion of fossil fuel resources in the world bring along the need to find alternative forms of energy from renewable energy sources. Renewable energy sources include solar energy, wind, geothermal energy, biomass and hydropower. They are available in the abundant quantity and free to use. They have low carbon emissions; therefore, they are considered as green and environmentally friendly. However, the start-up cost for a plant is very high and they are not appropriate for continuous use (Hosseini and Wahid, 2016). The use of renewable energy depends on the weather, if atmospheric conditions are not optimal, there will be a lack of energy generation. For instance, there must be enough rainfall to fill the dams to use hydropower, while, solar power requires clear skies and sunlight which means that solar energy cannot be ensured on cloudy days and/or nights, for wind energy the wind speed must be sufficient to move the wind turbine blades and geothermal energy power plants are established in very

rare places containing hot rocks where volcanoes are concentrated and earthquakes are frequent (Mohtasham 2015).

At this point, hydrogen appears as a great solution to diminish fossil fuel dependence and to mitigate environmental concerns as a clean, renewable and sustainable energy carrier (Dincer and Acar, 2014). Among the alternative energy sources hydrogen has received much attention due to its excellent energy storage capacity and zero carbon emission during its usage. Hydrogen is also a clean fuel, and it is not toxic and carcinogenic. Hydrogen is considered as secondary energy source because it is converted to energy by combustion or electrochemical reactions (Colella et al., 2005).

The use of hydrogen as a fuel in fuel cells produces only water by combining hydrogen and oxygen to generate heat and electricity. Fuel cells are a promising technology used as a source of heat and electricity for buildings and as a source of electrical power for electric motors in vehicles. One of the most important applications of hydrogen is its use in fuel cell-derived vehicles. However, the implementation of hydrogen in the transport sector is limited due to its storage difficulty and the lack of infrastructure for its distribution. At this point, on-board hydrogen production plays a fundamental role to circumvent these limitations by feeding directly into the fuel cell without itself being stored, in particular when generating hydrogen from renewable sources (Staffell et al., 2018).

The use of biofuels for hydrogen production provides significant environmental benefits since the produced CO_2 is consumed for biomass growth and thus contributes to a low carbon dioxide emitting energy supply. Glycerol is produced as a by-product of 10% by weight of biodiesel synthesis produced by transesterification of animal fats or vegetable oils with methanol in the presence of homogeneous catalysts, allowing it to be used as a low-cost raw material in a large supply of renewable materials. The produced crude glycerol contains 12–16% alkalis, 15–18% methyl esters, 8–12% methanol, and 2–3% water and various elements such as

calcium, magnesium, phosphorus, and/or sulphur and other components as well as more than half of glycerol (Seadira et al., 2017; Bagnato et al., 2017; Kent, 2013).

The use of glycerol produced as a by-product of the biodiesel production process to produce hydrogen offers an economically viable, sustainable and environmentally friendly process, particularly through steam reforming process where 7 moles of hydrogen gas are theoretically produced from one mole of glycerol (Cheng, 2011; Seadira et al., 2017).

1.1 Hydrogen

Hydrogen is a chemical element with symbol H and atomic number 1. It is the lightest element on the periodic table with a standard atomic weight of 1.008. Hydrogen, the simplest element in the universe consisting of only one proton and one electron, makes up the major part of the composition of the universe. It is also the most plentiful element in the universe. On the earth's surface, hydrogen exists as a compound with other elements such as oxygen, carbon, and nitrogen; most hydrogen is found as a compound with oxygen, in the form of water. Normally, pure hydrogen exists in the form of a hydrogen molecule with two atoms, H_2 (Honig 2003).

Physically, hydrogen is a colourless, odourless, tasteless, flammable gas and the lightest chemical. It is a useful and clean fuel, not toxic and carcinogenic, slightly more soluble in organic solvents than water. Hydrogen also produces clean power and/or heat for transport and stationary applications (Yusuf et al., 2015; Honig et al., 2003). At room temperature hydrogen is not a very reactive compound unless it has been activated in some way; however, it is highly reactive at high temperatures.

Moreover, hydrogen has a high energy density that makes it suitable for long-term storage. Hydrogen gas is mixed with natural gas and can be transported over long

distances through pipes that allows the energy distribution between the countries. (Dincer and Acar, 2014)

The gaseous storage of hydrogen creates some issues since it can diffuse through materials such as paper, fabric, rubber, and some metals such as platinum, iron, and steel. Therefore, hydrogen can be stored in liquid form or in a chemical compound, as well as in gaseous form (Eftekhari et al., 2017).

In addition, hydrogen can be produced without a carbon footprint by water electrolysis or steam reforming process. Unlike other fossil fuels, the combustion products contain water, oxygen and nitrogen when hydrogen is completely burned with air. Nitrogen oxide emissions are very low in engines that use hydrogen as fuel compared to petrol-burning engines (Mazloomi et al., 2012).

1.2 Hydrogen Applications

Hydrogen energy applications are basically divided into three: as a fuel, in fuel cells, and in refinery and petrochemical complexes.

1.2.1 Use of Hydrogen as a Fuel

Recent developments in the field of hydrogen energy have pointed that hydrogen is an ideal replacement for fossil fuels in furnaces, heating boilers, internal combustion engines, turbines, jet engines and hybrids. The fact that hydrogen is a clean and endless energy enables hydrogen to be used as an environmentally friendly fuel. When hydrogen is used as fuel, the production of both other pollutants and greenhouse gases is negligible compared to fossil energy sources (Dincer and Acar, 2014). For instance, hydrogen-powered vehicles do not produce significant amounts of carbon monoxide (CO), hydrocarbons (HCs), sulphur oxides (SO_x), sulfuric acid residues, ozone and other oxidants, benzene and other carcinogenic aromatic

compounds, formaldehyde and other aldehydes, other toxic metals, and other greenhouse gases either directly or indirectly. The only pollutant produced may be nitrogen oxides (NO_x). But NO_x emission is at least 200 times lower than that of the normal vehicles currently used (Güler Şentürk et al., 2010).

However, hydrogen burns with oxygen only under certain conditions. Due to its low density, hydrogen has to be compressed to liquid state and stored the same way at lower temperatures to ensure its effectiveness and efficiency as an energy source. It also explains why hydrogen should always be stored and transported under high pressure; therefore, transportation, storage and distribution are far from feasible. In addition, hydrogen is an extremely flammable and explosive gas, which makes it very dangerous (Mazloomi et al., 2012).

1.2.2 Use of Hydrogen in Fuel Cells

Fuel cells are electrochemical cells that convert chemical energy into electricity through electrochemical reactions of hydrogen with oxygen to generate electricity cleanly and efficiently. The use of hydrogen in fuel cells generates heat and electricity, and only water is released as a product (Eberle et al., 2012). There are numerous fuel cells in practice. Fuel cells operate on the same general principle, consisting of three parts, anode, electrolyte and cathode. Two chemical reactions occur at the interfaces of three different segments. The net result of the two reactions is the consumption of fuel, the production of water, and the generation of an electric current that can be used to power electrical devices (Kirubakaran et al., 2009).

Fuel cells are envisioned as an ideal replacement for conventional power generators, such as combustion engines or large batteries in cars, buses, forklift trucks, submarines, and backup and power plants (Colella et al., 2005). Fuel cells are environmentally friendly and reliable systems with their modular structure, high energy production efficiency and short assembly time. In addition, their operating

features provide practical convenience. Therefore, their development potential is quite high in the future (Mohamed et al., 2009).

1.2.3 Use of Hydrogen in Refinery and Petrochemical Complexes

Hydrogen is widely used in the production of bulk chemicals, intermediates and special chemicals. Mixture of hydrogen (H_2) and carbon monoxide (CO), known as syngas, is used for large-scale production of various products such as higher alcohols and aldehydes (Ramachandran and Menon 1998). It is also used to convert crude oil to refined fuels such as gasoline and diesel and to remove contaminants such as sulphur from these fuels. Approximately 75% of hydrogen currently consumed by refineries is supplied by large hydrogen plants that produce hydrogen from natural gas or other hydrocarbon fuels (Davis et al., 2004).

1.3 Hydrogen Production

Hydrogen can be produced using a number of different processes such as thermochemical processes, biological processes, direct solar water splitting processes and electrolytic processes. Each method has advantages in terms of cost, H_2 production efficiency, applicability and availability (Kothari et al., 2008).

Thermochemical processes use heat and chemical reactions to produce hydrogen from organic materials such as fossil fuels and biomass through natural gas reforming, coal gasification, biomass gasification and biomass-derived liquid reforming. Thermochemical processes are clean and sustainable methods, especially when using renewable feedstocks that offer feedstock availability. However, due to the high operating temperature, more heat resistant reactors are required and thereby higher capital cost is involved.

Water (H_2O) can be split into hydrogen (H_2) and oxygen (O_2) using electrolysis or solar energy. Direct solar water splitting or photolytic processes utilize light energy to split water into hydrogen and oxygen. These processes are currently in the early stages of research but offer long-term potential for sustainable hydrogen production with low environmental impact. In addition, in the electrolytic process, electrolysers use electricity to split water into hydrogen and oxygen. This technology is well developed and commercially available that offers no pollutant gas production. However, water electrolysis process has a low efficiency (about 55-75%) in terms of producing pure H_2 using the alkaline electrolysis systems (AES). Even though, the pure H_2 production efficiency is increased by using proton exchange membrane (PEM) electrolysers instead (about 80%) (Bernholz 2018), the process is uneconomical since the electrodes used are usually coated with costly platinum.

In biological process, microbes such as bacteria and microalgae can produce hydrogen through microbial biomass conversion and photobiological processes, using sunlight or organic matter. These technology pathways are at an early stage of research, but in the long-term have the potential for sustainable, low-carbon hydrogen production. This process provides clean and sustainable energy generation at low operating temperature. However, the energy production rate is very slow, operating cost is high and the efficiency is low (Hosseini et al., 2016).

According to the above-stated hydrogen production processes, various colours of hydrogen can be produced. Briefly, hydrogen production through coal gasification, where the emissions are released to the atmosphere, refers to brown hydrogen, while hydrogen production by preventing greenhouse gas emission from water electrolytically, photo-electrolytically, or thermo-electrolytically refers to green hydrogen. Hydrogen can also be produced through steam reforming processes. The process that releases CO_2 to the atmosphere is called grey whereas the CO_2 produced is captured is called blue. Besides these, in processes that do not produce CO_2 (e.g.,

methane pyrolysis), the colour of hydrogen is represented as turquoise (Newborough and Graham, 2020).

1.3.1 Hydrogen Production from Hydrocarbons

Hydrogen is mostly produced from hydrocarbons via steam reforming, partial oxidation and autothermal reforming. These methods have considerable superiorities in terms of feasibility, high hydrogen efficiency and applicability in fuel cells (Docekal et al., 1986; Ahmed et al., 2001).

1.3.1.1 Steam Reforming

Steam reforming (SR) is currently one of the most widespread processes for hydrogen production (Docekal et al., 1986). Its advantages arise from the high efficiency of its operation and the low operating costs. The most frequently used raw materials are natural gas and lighter hydrocarbons, methanol, and other oxygenated hydrocarbons (Ahmed et al., 2001). Steam reforming is generally endothermic reactions in which oxygenated hydrocarbon reacts with water and produces CO_2 and H_2. The steam reforming catalytic process requires a raw material free of sulphur-containing compounds to prevent deactivation of the catalyst used, and requires modest temperatures (Farrauto et al., 2003; Song et al., 2002). The used catalysts can be divided into two types: nonprecious metal (typically nickel) and precious metals from Group VIII elements (typically platinum or rhodium) (Adris et al., 1996).

1.3.1.2 Partial Oxidation

Partial oxidation (POX) and catalytic partial oxidation (CPOX) of hydrocarbons have been proposed in hydrogen production for automobile fuel cells and some other

commercial applications (Adris et al., 1996; Hohn et al., 2001). The raw materials may be methane, biogas, and heavy oil fractions (e.g., vacuum remnants, heating oil) whose further treatment and utilization are difficult (Krummenacher et al., 2003).

Compared to steam reforming, more CO is produced in POX. Therefore, the process is complemented by the conversion of CO with steam into H_2 and CO_2. The partial oxidation reaction can be generally defined as the formation of carbon dioxide and hydrogen exothermically as a result of the reaction of oxygenated hydrocarbons with oxygen. Since the process does not require the use of a catalyst, it is not necessary to remove sulphurous elements from natural gas, which reduce the efficiency of the catalyst.

Besides this method, catalysts can be used in the partial oxidation system (CPOX) to lower the operating temperature. However, the control of temperature becomes difficult due to the coke formation and the exothermic nature of the reactions (Hohn et al., 2001). For natural gas conversion, catalysts are typically based on Ni or Rh; however, nickel has a strong tendency towards coke, and the cost of Rh is high (Yu et al., 2009). In addition, high operating temperatures and safety concerns can make their use difficult for practical and compact portable devices due to thermal management (Farrauto et al., 2003).

1.3.1.3 Autothermal Reforming

Autothermal reforming (ATR) is a combination of both steam reforming (endothermic) and partial oxidation (exothermic) reactions (Mondal and Dalai 2017). In other words, oxygenated hydrocarbon reacts with both water and oxygen and produces carbon dioxide and hydrogen. The overall reaction is generally exothermic.

ATR has significant advantages over SR. There is no need of external heat in ATR process, leading to the process being simpler and cheaper. ATR has lower capital

cost and the potential for economies of scale (Wilhem et al., 2001). In addition, ATR process can be shut down and started very rapidly (Mondal and Dalai, 2017). For hydrocarbon reforming, the thermal efficiency is higher than POX and slightly less than SR. Gasoline and other higher hydrocarbons can be converted into hydrogen in automobiles using appropriate catalysts in autothermal processes (Ayabe et al., 2003).

1.4 Hydrogen Separation

Hydrogen can be purified through some techniques such as pressure swing adsorption (PSA), cryogenic distillation, or membrane separation.

Pressure swing adsorption process is the most extensively used industrial process to separate H_2 from a mixture of gases. This system has mostly been used in the chemical and petrochemical industries. It has an advantage of ability to bring undesirable impurities down to a low level and to produce high-purity, up to 99.99%, hydrogen (Adhikari et al., 2006).

Cryogenic distillation process is a low temperature separation process that uses the difference in boiling temperatures of feed components. Cryogenic distillation process is widely used to separate fluid mixtures but, it consumes a considerable amount of energy, which makes the process is highly expensive (Pinacci et al., 2013).

Pressure swing adsorption (PSA) and cryogenic distillation processes are commercially available separation techniques. However, they are energy intensive.

Besides these, membrane related processes are considered as one of the most promising technologies for high purity hydrogen production (Fernandez et al., 2017). It is a good alternative process for both PSA and cryogenic distillation by providing high H_2 purity, easy scale of production and consuming less energy with continuous operation. In addition, catalytic reforming can be embedded into the membrane to

shift the reversible reforming reaction to the product side, resulting in enhancement of hydrogen conversion (Adhikari et al., 2006).

1.5 Hydrogen Storage

Gaseous hydrogen can pass through the materials by diffusion. This property of hydrogen creates some issues related to storage. Hydrogen can be stored in liquid form, or in a chemical compound, as well as in gaseous form. In either compressed gas or liquid form, hydrogen has significant explosion hazards. Therefore, storage by adsorption in a metal hydride can be regarded as safer and more convenient due to the fact that this method allows the storage of large amounts of hydrogen in small volumes at low pressure and room temperature. However, the use of hydrides to store hydrogen has some drawbacks, such as loss of hydrogen capacity after repeated use due to the limited alloy operating life, and difficulty in extraction of all stored hydrogen (Eftekhari et al., 2017).

1.6 Hydrogen Safety

Hydrogen is a flammable compound that ignites very quickly with oxygen and/or ignition source. The flammability range of hydrogen is 4% to 74% concentration in air and 4% to 94% in oxygen. In addition, hydrogen is ignited with only 0.02 millijoules of energy, less than 7% of the energy required to ignite natural gas (Rhodes, 2011). Since hydrogen burns in the ultraviolet colour range, it is difficult to detect the burning with naked eyes (Pasman et al., 2011).

Any cryogenic liquid (hydrogen becomes a liquid below −252.88°C) can cause severe frostbite if the liquid comes into contact with the skin. Therefore, liquid hydrogen containers should be used with double-walled, vacuum jacketed, super-insulated containers designed to safely discharge hydrogen in a gaseous state when

a breach is detected in the outer or inner wall. Hydrogen hazards can be kept to a minimum if proper safety precautions are taken (Mirza et al., 2011).

The use of hydrogen as a fuel source does not create fumes, pollute the atmosphere, or cause global warming (Dincer and Acar, 2014). The major drawback may be the release of water vapour (Eberle et al., 2012) to the atmosphere during the combustion of hydrogen with oxygen, which causes an increase in atmospheric humidity and a greenhouse effect as a greenhouse gas. However, since water vapour is released to the atmosphere by human activities such as irrigation, powerplant cooling, aviation and domestic water use as well as evaporation from the oceans, it does not seem possible to prevent water vapour release (Sherwood et al., 2018).

CHAPTER 2

GLYCEROL AS A RAW MATERIAL FOR H_2 PRODUCTION

With the recent development of economic and modern society, issues such as global warming and energy shortages increase the importance of renewable energy studies. Due to the technological advances in fuel cell devices that use hydrogen as fuel in the development of zero emission power systems, great emphasis has been placed on the improvement of catalytic processes for converting bio-renewable raw materials to hydrogen.

The use of biofuels for hydrogen production emits low carbon dioxide as the CO_2 produced is consumed for biomass growth, which provides significant environmental benefits. Bio-glycerol is produced as a by-product of biodiesel synthesis produced by transesterification of vegetable oils or animal fats, allowing it to be used as a low-cost raw material in a large supply of renewable materials. Bio-glycerol is produced as a by-product of 10% by weight of biodiesel whose production reached 400,000 barrels/day in the world as of 2011 (Silva et al., 2015). In addition to being produced as a by-product of biodiesel production, glycerol is produced through propylene synthesis (Shukla et al., 2017) and hydrolysis.

In the production of biodiesel and thereby glycerol, the reaction between vegetable oils and methanol takes place in the presence of a homogeneous catalysts, generally sodium hydroxide or sodium methylate. After the reaction, the final mixture contains not only glycerol and fatty esters (or biodiesel), but also water, dissolved salts and unreacted methanol (Bagnato et al., 2017). The glycerol phase and biodiesel phase are separated using a settler unit based on the densities of the two phases. Glycerol is then purified by vacuum distillation process from other components containing almost half of the glycerol phase, such as water, dissolved salts, unreacted methanol,

and unused catalyst (Kent, 2013). However, the use of purified glycerol in industrial applications is limited due to the uneconomic purification process. Therefore, it is anticipated that using crude glycerol as a raw material may make the process industrially feasible and competitive (Fasolini et al., 2019; Adeniyi et al., 2019; Checa et al., 2020). In propylene chlorination, allyl chloride reacts to produce glycerol dichlorohydrine. Afterwards, glycerol dichlorohydrine is hydrolysed to glycerol with caustic soda or directly, then the epichlorohydrine formed is separated and hydrated to glycerine with caustic soda. This process enables a final glycerol yield of about 90%. Furthermore, in hydrolysis process, soap and glycerol are produced by the reaction between triglyceride and alkaline hydroxide (caustic soda) (Marchetti et al., 2007; Bagnato et al., 2017)

Physically, glycerol is a clear, colourless, odourless, non-flammable, biodegradable and viscous liquid. It is completely soluble in water and alcohols. Moreover, glycerol offers other advantages as well as its natural availability such as low toxicity, safe storage and handling (Silva et al.,2015; Reddy et al., 2011); these expand the use of glycerol in the lots of industries such as in cosmetics, food, alkyl resine, tobacco, pharmaceutical, polyurethane etc. In addition, glycerol can be converted into other compounds, such as butanol, 1,3-propanediol, 2,3-butanediol, citric acid, lipid, poly (hydroxyalkanoates), dihydroxyacetone, glyceric acid, glyceraldehyde, hydroxypyruvic acid, glycolic acid, acrolein, monoglycerides, etc., via oxidation, reduction, esterification, dehydrogenation, halogenation, pyrolysis etc., by conventional or fermentation process (Bagnato et al., 2017).

Glycerol is one of the most attractive biomass-derived oxygenated compounds, as its utilization in hydrogen production through steam reforming process is economically viable and environmentally friendly and allows easy scaling of the process in industrial applications. In steam reforming of glycerol process, glycerol reacts with water in the presence of an appropriate catalyst, and theoretically one mole of glycerol produces 7 moles of hydrogen gas (Cheng, 2011).

In the view of various aspects, glycerol is a promising candidate as a raw material for the steam reforming process to reduce concerns of the impending global energy crisis by providing good hydrogen yield for energy sustainability (Adeniyi et al., 2019).

2.1 Hydrogen Production Processes from Glycerol

Hydrogen can be produced from glycerol through several processes, such as steam reforming, partial oxidation and autothermal reforming.

2.1.1 Steam Reforming

Steam reforming is the most widely used method for hydrogen production because this process is economically viable, environmentally friendly, and allows easy scaling of the process in industrial applications. In this process, glycerol reacts with water vapour in the presence of a catalyst, produces mainly hydrogen, carbon dioxide and carbon monoxide. Even though the presence of water increases the hydrogen yield, a large amount of water is necessary to prevent coke deposition on the catalyst. In addition, glycerol steam reforming is an endothermic reaction; therefore, it requires high operating temperature that increases energy consumption and inherently operating cost. In addition, due to the high operating temperature, more heat resistant reactors are required and thereby higher capital cost is involved. In particular, at lower temperatures, in addition to the main products, CH_4 is formed that decreases the selectivity of H_2.

In glycerol steam reforming reaction 7 moles of hydrogen is produced by one mole of glycerol. In essence, it may be viewed as the combination of glycerol decomposition and water-gas shift reactions.

Glycerol Steam Reforming:

$C_3H_8O_3 + 3H_2O \leftrightarrow 3CO_2 + 7H_2$ $\Delta H_R = 128$ kJ/mole

Glycerol Decomposition:

$C_3H_8O_3 \rightarrow 3CO + 4H_2$ $\Delta H_R = 250$ kJ/mole

Water Gas Shift Reaction:

$CO + H_2O \leftrightarrow CO_2 + H_2$ $\Delta H_R = -41$ kJ/mole

However, these reactions may also be accompanied by methanation, methane dry reforming, methane steam reforming and a series of carbon formation reactions (Adhikari et al., 2007; Schwengber et al., 2011; Cheng, 2011; Fasolini et al., 2019).

Methanation:

$CO_2 + 4H_2 \leftrightarrow CH_4 + 2H_2O$ $\Delta H_R = -165$ kJ/mole

Methane Dry Reforming:

$CH_4 + CO_2 \leftrightarrow 2CO + 2H_2$ $\Delta H_R = 259$ kJ/mole

Methane Steam Reforming:

$CH_4 + H_2O \leftrightarrow CO + 3H_2$ $\Delta H_R = 206$ kJ/mole

Carbon Formation:

$2CO \leftrightarrow CO_2 + C$ $\Delta H_R = -172$ kJ/mole

$CH_4 \leftrightarrow 2H_2 + C$ $\Delta H_R = 75$ kJ/mole

$CO + H_2 \leftrightarrow H_2O + C$ $\Delta H_R = -131$ kJ/mole

$CO_2 + 2H_2 \leftrightarrow 2H_2O + C$ $\Delta H_R = -90$ kJ/mole

Considering the above-stated reactions, glycerol steam reforming reaction occurs at temperatures in the range of 300-900^oC; however, according to studies, the maximum H_2 yield is obtained between 525-725^oC. Although the operating pressure

is generally atmospheric pressure, vacuum pressure is better not only to achieve higher H_2 yield, but also to reduce energy consumption by lowering operating temperatures (Schwengber et al., 2016; Avasthi et al., 2013; Adhikari et al., 2008; Silva et al., 2015). Similar to glycerol steam reforming reaction, glycerol decomposition reaction occurs at wide temperature range of 400-900^{o}C, but its yield increases between 650-750^{o}C at atmospheric pressure (Bagnato et al., 2017; Barker-Hemings et al., 2011). In addition, water gas shift reaction favours the product side up to 450^{o}C, this reaction may also occur at elevated temperature depending on the amount of water in the feed (Pal et al., 2018; Rhodes et al., 1995; Basile et al., 2013). Exothermic methanation reaction generally occurs between 200-550^{o}C at atmospheric pressure (Stangeland et al., 2017; Schaaf et al., 2014). Aside from these reactions, both methane dry reforming and methane steam reforming reactions operate at high temperature in the range of 700-1000^{o}C and at high pressure in the range of 3-20 bar (Idriss et al., 2015; Kahle et al., 2013; Chen et al., 2020). Moreover, while carbon formation reactions may occur at the temperature higher than 400^{o}C, reverse carbon formation reactions (carbon gasification reactions) may occur, particularly at high water/glycerol ratios (Schaaf et al., 2014; Nakoua et al., 2009; Spivey, 2011).

2.1.2 Partial Oxidation

Glycerol reacts with oxygen in the presence or absence of a catalyst in the partial oxidation process that uses an oxygen source to provide the necessary heat internally. In this process, some of the glycerol is oxidized in the presence of the required air energy until the process stabilizes. The global glycerol oxidation reaction is represented as:

$$C_3H_8O_3 + 3/2\ O_2 \leftrightarrow 3CO_2 + 4H_2 \qquad \Delta H_R = -598\ kJ/mole$$

The partial oxidation reaction is an exothermic process whose energy efficiency is directly dependent on the amount of oxygen fed. Since it involves the rapid consumption of oxygen, the reaction causes a parallel reaction as follows: (Adhikari et al., 2009; Vaidya et al., 2009; Schwenger et al.,2011):

$C_3H_8O_3 + O_2 \leftrightarrow CO + 2CO_2 + 4H_2$ $\Delta H_R = -315$ kJ/mole

If excess air is fed, all glycerol is oxidized and mainly carbon dioxide and water are formed. Complete combustion of glycerol is expressed as:

$C_3H_8O_3 + 7/2\ O_2 \leftrightarrow 3CO_2 + 4H_2O$ $\Delta H_R = -1565$ kJ/mole

2.1.3 Autothermal Reforming

Autothermal process combines partial oxidation and steam reforming processes by feeding glycerol, air, and water together and forming mainly carbon dioxide and hydrogen in the presence of a catalyst. This process, where glycerol steam reforming is an endothermic reaction and partial oxidation is an exothermic reaction, is considered promising for temperature management and energy self-sufficiency. Due to the fact that the heat generated by partial oxidation is absorbed by the steam reforming process, the overall autothermal process is exothermic and represented as:

Glycerol Autothermal Reforming:

$C_3H_8O_3 + 3/2\ H_2O + 3/4\ O_2 \rightarrow 3CO_2 + 11/2\ H_2$ $\Delta H_R = -240$ kJ/mole

The main advantage of glycerol autothermal reforming process is that no external heat is required. The addition of oxygen in the process both increases hydrogen production and provides the necessary heat, which is very valuable in terms of energy. However, it is noteworthy that the thermodynamically produced hydrogen in this reaction is less than conventional steam reforming (Adhikari et al., 2009; Vaidya et al., 2009; Schwenger et al.,2011).

Among the above-stated processes, steam reforming of glycerol is the most efficient and widely used one. In addition, the use of glycerol, a by-product of biodiesel, which is a renewable feedstock, in the steam reforming process is considered as renewable and carbon dioxide (CO_2) neutral, offering an environmentally harmless process (Schwengber et al., 2016; Vaidya et al., 2009; Avasthi et al., 2013).

2.2 Thermodynamic Analysis of Glycerol Steam Reforming

In order to accomplish maximum hydrogen yield, one of the most important criteria is to determine the reaction operating conditions. For this reason, the effects of reaction parameters such as water-to-glycerol molar ratio and temperature were thermodynamically investigated at atmospheric pressure.

According to the glycerol steam reforming reactions, the equilibrium mole fractions of each compound were obtained on dry basis with the aid of Aspen HYSYS software. Approximately complete glycerol conversion was achieved at any feed ratio and any temperature value. Therefore, all graphs (Figures 2.1-2.5) were plotted considering the mole fractions of produced gas compounds methane, carbon monoxide, carbon dioxide and hydrogen. The equilibrium graphs for each compound and H_2 yield graph were plotted with respect to varying temperature values (300-1050^oC) at atmospheric pressure with the constant water-to-glycerol molar ratio (0.25, 1, 1.5, 3, 6 & 9).

According to Figure 2.1, mole fraction of CO_2 decreases with an increase in temperature. At about 525^oC the mole fraction of CO_2 displays inverse behaviour with an increase in W/G ratio. After this temperature, increase in water amount in the feed shifts the WGS reaction to the product side, resulting in CO_2 formation.

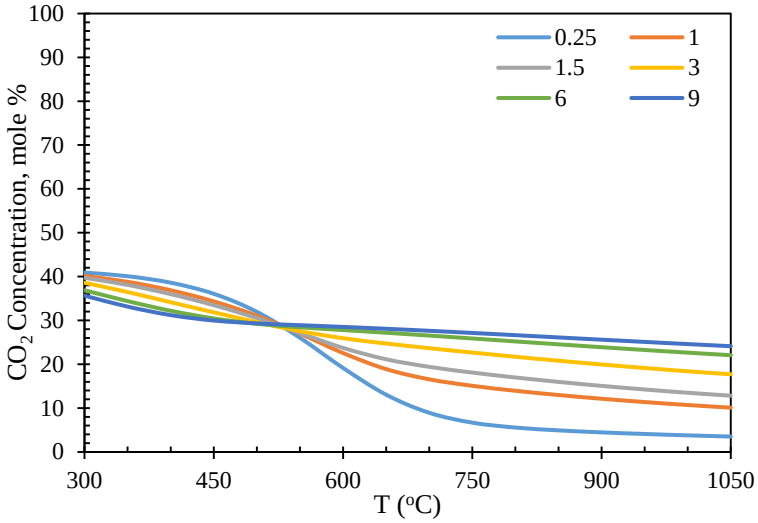

Figure 2.1 Effect of Temperature on CO_2 Concentration at Various W/G Molar Ratios

According to Figure 2.2, the formation of CH_4 decreases with an increase in both temperature and W/G ratio. Particularly at high temperatures, methane formation approaches zero due to the exothermic nature of methanation, reverse methane dry reforming and reverse methane steam reforming reactions. In addition, considering the CO and H_2 mole fraction graphs (Figures 2.3-2.4), it can be deduced that the increase in the amount of water in the feed contributes to H_2 and CO production after 500°C.

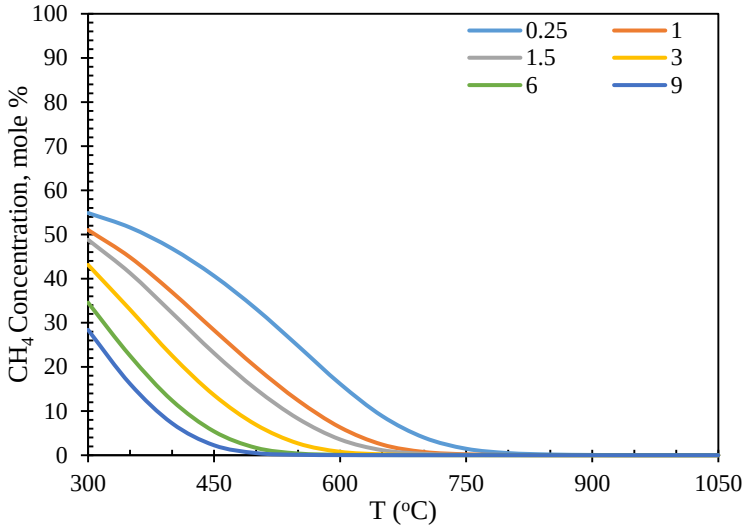

Figure 2.2 Effect of Temperature on CH_4 Concentration at Various W/G Molar Ratios

According to Figure 2.3, the formation of CO increases with an increase in temperature whereas it decreases with an increase in W/G ratio. There is no significant amount of CO before 450°C; however, after this temperature, there is a notable increase in CO formation, attributing to the shift in WGS reaction to the reactant site after this temperature. In addition, increase in the amount of water in the feed decreases the CO formation in contrast to the CO_2 formation (Figure 2.1). Considering these graphs together, the results can be ascribed to the shift in the WGS reaction with the varying amount of water.

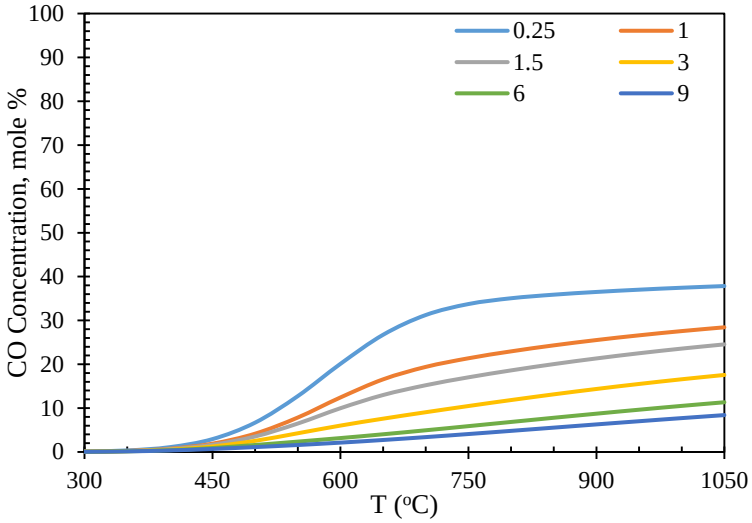

Figure 2.3 Effect of Temperature on CO Concentration at Various W/G Molar Ratios

According to Figure 2.4, mole fraction of H_2 increases with an increase in W/G ratio. Parallel to the H_2 yield % graph (Figure 2.5), there is a slight decrease after 550°C when W/G is 9. Similar behaviour can also be seen in other W/G ratios.

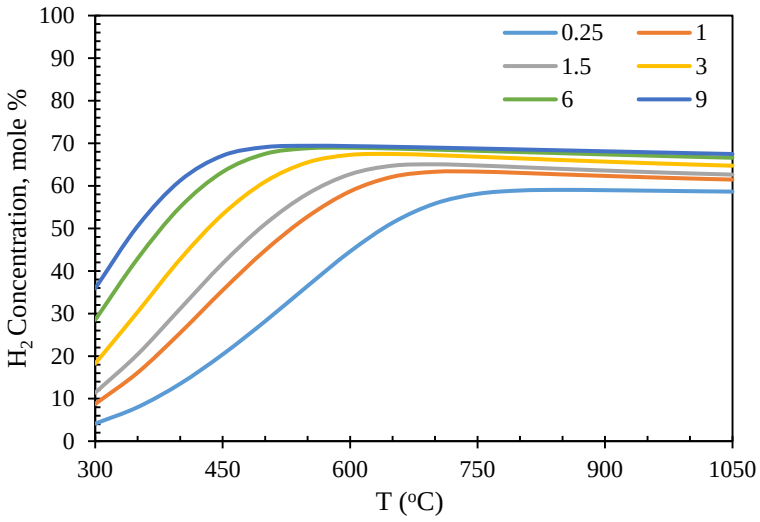

Figure 2.4 Effect of Temperature on H_2 Concentration at Various W/G Molar Ratios

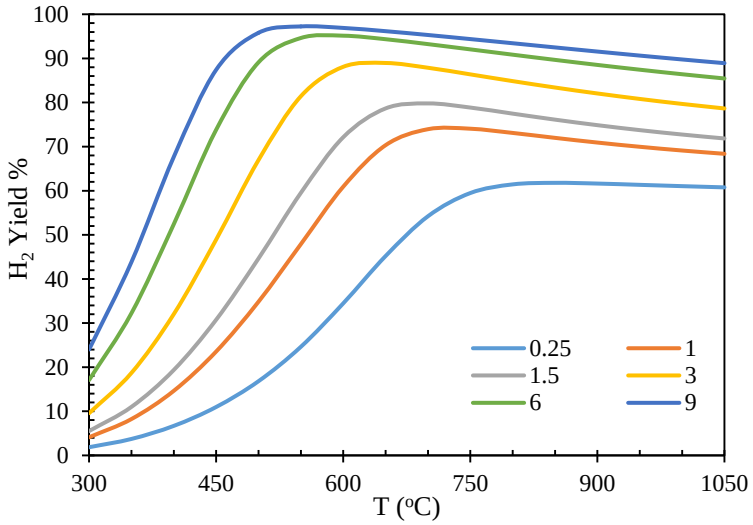

Figure 2.5 Effect of Temperature on H_2 Yield at Various W/G Molar Ratios

According to Figure 2.5, it can be clearly deduced that both temperature and W/G ratio notably affect the H_2 yield. On the one hand, W/G ratio is directly proportional to the H_2 yield %, implying that the H_2 yield increases as the W/G ratio increases. On the other hand, the effect of temperature can be examined in two regions. For instance, when the W/G ratio is 9, the H_2 yields % increases significantly with the increase in temperature to 550°C; however, it decreases slightly after 550°C. Similar effects can be seen in other W/G ratios at different temperatures.

To sum up, the increase in the W/G ratio increases the mole fraction of both H_2 and CO_2 whereas decreases the mole fraction of both CH_4 and CO. In addition, operating at high temperatures favours the H_2 formation. At elevated temperatures, the formation of CO_2 and CH_4 decreases, in fact CH_4 formation approaches zero value, while the CO formation slightly increases. Therefore, the reaction operating conditions were selected by considering higher amount of H_2 formation with lower amount of CH_4, CO and CO_2 formations.

Considering the thermodynamic analysis of glycerol steam reforming reactions, operating condition was determined as 550°C and the W/G molar ratio of 9 in order

to achieve high H_2 yield. In addition, the effect of temperature and W/G molar ratio on H_2 yield were examined at temperatures in the range of 450-1050^oC with the W/G molar ratio between 1-9.

CHAPTER 3

PROPER CATALYSTS FOR GLYCEROL STEAM REFORMING

Catalysts are used in 90% of all commercially produced bulk and fine chemical products through reforming, hydrolysis, hydrogenation, isomerization, halogenation, oxidation processes etc., as well as in the industries such as energy and food processes (Fechete et al., 2012).

The use of catalysts provides an alternative reaction mechanism with a lower activation energy that equally increases the rates of both forward and reverse reactions and reduces the time to reach equilibrium. Catalysts have no effect on equilibrium constants of the reaction. These benefits not only result in less energy use but also save costs in industries by allowing the operating temperature to decrease. In addition, catalysts are reusable and sufficient to catalyse reactions when used even small amounts. It should be also taken into account that catalysts must be non-toxic and/or inexpensive as well as not easily poisoned by waste products or impurities.

According to the industrial applications, catalysts are divided into two: homogeneous and heterogeneous catalysts.

Heterogeneous catalysts are in different phase than reactants. The catalysts provide reactive surface where the reaction can take place by adsorption of reactants. They are used in hydrocarbon reactions such as cracking, reforming, dehydrogenation and isomerization. They can be easily removed from products by filtration that contributes to the recycling of catalysts. Aside from these, they are safe to store and have a long lifetime. However, they are only effective on the surface, resulting in poorly defined reaction mechanisms and active sites of catalyst in general (Farnetti et al., 1999).

Homogeneous catalysts are in the same phase with reactants. The catalysts are consumed at one stage in the mechanism and reformed at a larger stage. They are in liquid phase and used in carbonylation, oxidation, hydrocyanation, metathesis, and hydrogenation, acid-base, metal ions, Lewis acid enzymatic reactions. All catalysts are exposed to the reactant and easily modified. The reaction mechanisms are well understood. In addition, they offer easy process of diffusion, heat transfer and well-defined active sites of catalysts. However, it is difficult to remove from products for reuse (Bravo-suarez et al., 2013).

In addition, the use of support materials in catalysts not only ensures an optimal dispersion of the catalytically active components and stabilizes the catalyst against sintering (loss of active surface area by structural modification of the catalyst), but also creates its physical form, texture, mechanical resistance and certain activity. Using support also prevents the aggregation of the catalytic particles, thus improving catalytic performance. For industrial applications, catalyst supports must have high chemical, mechanical, thermal stability and surface area-to-volume ratio. Commonly used organic solid supports are polymers (e.g. polystyrene), copolymers (e.g. styrene-divinylbenzene) and inorganic supports such as silica, zeolites, alumina, activated carbon, titanium dioxide, graphene (NPTEL, 2014).

One of the most significant points to achieve maximum hydrogen yield in glycerol steam reforming is selection of the proper catalyst. Therefore, catalysts should be selected taking into account the selectivity and yield of the desired product, the ability to operate under appropriate mild or severe conditions, environmental impact, problems caused by catalysts poisoned by impurities, and stability.

3.1 Solid Catalysts

A solid catalyst consists of mainly three components: catalytic agent, support/carrier, promoters or inhibitors.

Catalytic agents are the catalytically active component in the catalyst. These components generate the active sites that participate in the chemical reaction. The activity of any catalyst is proportional to the concentration of these active sites (e.g. Fe, Pt, Ag, etc.).

The supports provide a large surface area for the dispersion of the catalytically active agent and impart their physical form, texture, mechanical resistance and activity to catalysts, particularly for bifunctional catalysts (e.g. alumina, silica, silica-alumina, molecular sieves etc.).

Promoters are generally defined as substances added during preparation of catalysts that improve the activity, selectivity and/or stabilize the catalytic agents. For instance, addition of small quantities of alumina to an iron catalyst in ammonia synthesis prevents sintering of the iron crystallites.

Inhibitors act opposite to promoters, reducing activity, selectivity, or stability, even when added in small amounts. The inhibitor is particularly useful for reducing the activity of a catalyst for undesirable side reactions. For instance, in the oxidation of ethylene, ethylene dichloride is added to inhibit CO_2 formation and thus acts as an inhibitor (NPTEL, 2014).

3.1.1 Preparation of Solid Catalysts

Supported catalysts are prepared in two main steps in which the precursor of the active component is loaded onto the support and catalytically transformed into the active site. The final active component can be in metallic state, oxide form or reduced form, depending on the requirements.

There are various deposition methods. Most of these contains aqueous solutions and liquid solid interface. The one of the most common method is impregnation method because it is faster, inexpensive, and allows the final property and configuration to

be controllable in advance. However, it is more difficult to both prepare a high-concentration catalyst and to ensure an even dispersion of catalyst components on the surface. Depending on the volume of the solution, the methods of contacting the solid with the solution are divided into two: wet impregnation and dry impregnation. On the one hand, in dry impregnation method, the volume of the solution of appropriate concentration is equal or slightly less than the pore volume of the support or other active solid phase. On the other hand, in wet impregnation method, an excess solution is used. After a certain time, the solid is separated and excess solvent is removed by drying. The heat of adsorption is released in a short time. Wet impregnation method provides a great advantage as it is easy to prepare a layer of active matter on the surface of catalyst. However, the impregnation time is much longer than dry impregnation (de Jong et al., 2009; NPTEL, 2014).

In addition to the impregnation method, the precipitation method is frequently used in the synthesis of supported catalysts. Catalysts based on more than one component can be easily prepared by the co-precipitation method. The main advantage of the precipitation process is that it is possible to synthesize pure and homogeneous material, as well as obtain fine and uniform particle size with poorly agglomerated particles at relatively low reaction temperature and low cost. However, major disadvantages include the need to separate the product after precipitation and the formation of solutions containing large volumes of salt. In the precipitation process several processes occur such as liquid mixing/supersaturation, nucleation, crystal growth to form primary products, and aggregation of the primary particles. The initial mixing or dispersion of the components in solution has a significant effect on precipitation. In the co-precipitation method, good mixing results in a more homogeneous product. However, stirring rate affects nucleation and agglomeration of the particles (NPTEL, 2014; Deraz et al., 2018).

3.2 Studies on Glycerol Steam Reforming

According to studies, hydrogen was produced via glycerol steam reforming over mesoporous catalysts whose diameter between 2 and 50 nm. The reactions were carried out at high temperatures and atmospheric pressure with different water/glycerol ratios.

Hirai et al. (2005) tested the catalytic activities of 8-10 group metals (Ni, Ru, Rh, Ir, Co, Pt, Pd & Fe) loaded yttrium oxide, zirconium oxide, cerium oxide, lanthanum oxide, silicon dioxide, magnesium oxide, and aluminium oxide catalysts in a fixed bed quartz reactor. The reactions were carried out at 600°C and atmospheric pressure with the steam-to-carbon molar ratio of 3.3. All catalysts exhibited high CO_2 selectivity. The highest glycerol conversion and hydrogen yield were achieved in ruthenium loaded yttrium oxide and ruthenium loaded zirconium oxide catalysts. However, the lowest glycerol conversion was observed in ruthenium-loaded magnesium oxide catalyst. Among all catalysts, the best results were obtained in ruthenium loaded yttrium oxide catalyst as 88% hydrogen yield and approximately complete glycerol conversion.

Profeti et al. (2009) modified nickel-loaded cerium oxide-aluminium oxide catalyst with noble metals such as platinum, iridium, palladium, and ruthenium. An increase in glycerol conversion and a decrease in carbon deposition were observed with the addition of noble metals. All of the noble metals loaded catalysts exhibited high hydrogen yield and glycerol conversion at 700°C and atmospheric pressure with the water-to-glycerol molar ratio of 6. The highest hydrogen yield and glycerol conversion were obtained in platinum-nickel loaded catalyst as 68% and 98%, respectively. However, the lowest hydrogen yield and glycerol conversion were obtained in nickel loaded aluminium dioxide-cerium dioxide as 31% and 65%, respectively.

Ming et al. (2016) prepared nickel, cobalt and lanthanum loaded aluminium oxide catalysts by impregnation method and tested the activities of these catalysts in a fixed bed quartz reactor at 700°C and atmospheric pressure with the water-to-glycerol (mole/mole) ratio of 9. They reached 47%, 44% and 55% hydrogen yield in the presence of nickel loaded aluminium oxide, cobalt loaded aluminium oxide and lanthanum loaded aluminium oxide catalysts, respectively. Aside from these, under the same conditions, by loading nickel, cobalt and lanthanum together onto the aluminium oxide, they reached both maximum glycerol conversion and hydrogen yield as 96% and 78%, respectively.

Demsash et al. (2018) synthesized nickel loaded aluminium oxide, nickel-loaded aluminium oxide-cerium oxide and nickel-ruthenium-loaded aluminium oxide-cerium oxide catalysts by impregnation method. Then, they tested the performances of these catalysts at 650°C and atmospheric pressure with the water-to-glycerol (mole/mole) ratio of 12. Among the catalysts, the lowest carbon deposition and the highest activity were obtained with nickel-ruthenium loaded aluminium oxide-cerium oxide catalyst. Hydrogen yield, hydrogen selectivity, and glycerol conversion were achieved as 86%, 89% and 100%, respectively, in the presence of this catalyst.

Ebshish et al. (2012) examined the catalytic activity of 10 wt. % Ni loaded alumina xerogel catalyst in a fixed bed reactor at 600°C and atmospheric pressure with the water-to-glycerol molar ratio of 6. Ni is impregnated over alumina xerogel which was pre-treated at different temperatures of 700, 800, 900, and 1000°C. It was deduced that rise in pre-treatment temperature of alumina leads to increase in the amount of hydrogen production. In 10 wt. % Ni loaded alumina xerogel pre-treated at 1000°C, the highest glycerol conversion and hydrogen yield were attained as 100% and 63%, respectively.

Kim and Lee (2013) tested the catalytic activities of Ru and Ru-Fe, Ru-Co, Ru-Ni and Ru-Mo catalysts supported on yttria, ceria-zirconia and ɣ-alumina at elevated temperatures. The ɣ-alumina supported Ru-based catalysts demonstrate a low H_2

production rate with a high CO selectivity. Additionally, these catalysts favour the formation of C_1-C_2 hydrocarbons. The bimetallic catalysts were limited with only small increases in glycerol conversion. Among the synthesized catalysts, Ru-Mo/Y_2O_3 exhibits low carbon formation and superior catalytic stability against deactivation. The highest H_2 selectivity was attained as 71.8% in the presence of 1 wt. % Ru loaded ceria-zirconia catalyst at 600^{o}C and atmospheric pressure with the water-to-glycerol molar ratio of 12.

Adhikari et al. (2007) examined the influence of alumina and ceria-alumina supported Pt, Rh, Ni, Pd, Ir, and Ru catalysts on hydrogen selectivity and glycerol conversion at temperatures ranging from 600^{o}C to 900^{o}C, atmospheric pressure with the water to glycerol molar ratio of 6 and 9. It was deduced that, increase in water-to-glycerol ratio increases hydrogen selectivity and glycerol conversion. CH_4 formation was also completely inhibited at low flow rates such as 0.15 ml/min. Even though, increase in metal loading increased glycerol conversion, it was not necessarily the case for H_2 selectivity. Among the synthesized 14 catalysts, the best catalysts were determined as 2.5Ni/Al_2O_3 and 2.5Rh/CeO_2-Al_2O_3 in terms of hydrogen selectivity and glycerol conversion. Approximately, 80% of H_2 selectivity and 90% of glycerol conversion were obtained with 2.5Ni/Al_2O_3 whereas they were 71% and 93% with 2.5Rh/CeO_2-Al_2O_3, respectively, at 900^{o}C and atmospheric pressure with the water-to-glycerol molar ratio of 9.

Gallo et al. (2012) synthesized Ru loaded Mg(Al)O catalyst by employing wet impregnation method and they used the catalyst for the first time in steam reforming of glycerol. In this case, 0.6 wt. % Ru was doped on Mg(Al)O support and catalytic activity of the catalyst was tested in a wide feed concentration range (10-40 wt. % glycerol in water) and at varying reaction temperature (450-600^{o}C). The best activity results were obtained as 96% glycerol conversion and 90% hydrogen selectivity, respectively, in 10 wt. % glycerol in water, at 550^{o}C and atmospheric pressure.

Surendar et al. (2016) prepared Au, Ag, Cu, Pt doped Co based perovskites ($LaCo_{0.99}X_{0.01}O_3$) by co-precipitation technique and examined their catalytic activities in the temperature range of 400-700°C, at atmospheric pressure and 30 wt. % glycerol in water. The amount of carbon formation was the maximum for $LaCo_{0.99}Au_{0.01}O_3$ catalyst. However, Cu and Pt promoted samples demonstrated similar and the lowest carbon formations. At 700°C, $LaCo_{0.99}Pt_{0.01}O_3$ and $LaCo_{0.99}Cu_{0.01}O_3$ exhibited higher H_2 yields as 78% and 75%, respectively.

Bossola et al. (2017) examined the catalytic performances of Pt/C and Pt-Mn/C in steam reforming and aqueous phase reforming of glycerol. Under steam reforming conditions, addition of Mn to Pt exhibited a significant promoting effect over Pt/C, in terms of glycerol conversion with a higher selectivity toward the glycerol dehydration products. Contrarily, under aqueous phase reforming conditions compared to Pt/C, a slightly higher hydrogen selectivity and solely minimal enhancement in product selectivity were obtained in the presence of Mn. Both steam reforming and aqueous phase reforming reactions operated at 225°C with the feed ratio of 10 wt. % glycerol in water. Consequently, in steam reforming of glycerol, glycerol conversion and hydrogen selectivity were obtained as 26.0% and 36.9% for Pt/C whereas these were 78.2% and 25.2% for Pt-Mn/C. In aqueous phase reforming, glycerol conversion decreased whereas hydrogen selectivity increased compared to steam reforming. In the presence of Pt/C, glycerol conversion and hydrogen selectivity were obtained as 8.6% and 51.3%, respectively. Loading Mn to Pt/C increased both glycerol conversion and hydrogen selectivity to 10.6% and 58%, respectively.

Zamzuri et al. (2017) tested the catalytic activities of Ni loaded Al_2O_3, La_2O_3, ZrO_2, SiO_2, and MgO prepared by wet impregnation method. All synthesized catalysts were used in a fixed bed reactor at 650°C and atmospheric pressure with the water-to-glycerol molar ratio of 6. The catalysts overall activity increases in the following order: $SiO_2<MgO<ZrO_2<La_2O_3<Al_2O_3$. Furthermore, glycerol conversion at these

conditions was in the order: $SiO_2<ZrO_2<La_2O_3<MgO<Al_2O_3$. In the presence of alumina supported Ni catalyst, the highest glycerol conversion and hydrogen selectivity were achieved as 80.0% and 71.5%, respectively. On the other hand, the lowest glycerol conversion and hydrogen selectivity were obtained as 48.0% and 43.7%, respectively, in the presence of silica supported Ni catalyst.

Goula et al. (2016) examined the effect of catalyst synthesis method on hydrogen production. For this purpose, they synthesized nickel doped alumina catalyst via incipient wetness, wet impregnation and modified equilibrium deposition filtration methods. These results revealed that the synthesis method affected the textural, structural and surface properties of the catalysts, differentiating the dispersion and the kind of nickel species on the surface of alumina. Both Ni/Al-wet and Ni/Al-edf catalysts exhibited increasing CO_2 selectivity and almost constant CO selectivity for temperatures above 550^oC. It was also confirmed that the Ni/Al-edf catalyst indicated the highest glycerol conversion, hydrogen yield and the lowest carbon deposition on the catalyst at 650^oC and atmospheric pressure with the feed ratio of 20 wt. % glycerol in water. At these operating conditions, in the presence of 8 wt. % Ni loaded alumina synthesized using equilibrium deposition filtration method, the highest glycerol conversion and H_2 yield were achieved as 87% and 63%, respectively.

Carrero et al. (2017) tested the activities of 15% by weight of nickel loaded SBA-15 and the catalysts promoted by loading 4% by weight of Cu, Co and Cr in a stainless-steel fixed bed reactor at 600^oC and 0.075 ml/min water-glycerol feed flow rate with the water-to-glycerol molar ratio of 6. In the presence of all catalysts, glycerol conversion was above 85 mole % and hydrogen contents were above 50 mole %. To be more specific, H_2 mole contents were achieved as 55%, 51%, 52%, and 61% with 15Ni, 15Ni-4Cu, 15Ni-4Co, and 15Ni-4Cr loaded SBA-15 catalysts, respectively.

Adhikari et al. (2008) examined the catalytic performances of magnesium oxide, titanium dioxide and cerium dioxide supported nickel catalysts in a stainless-steel

reactor at 550, 600, and 650°C and 1.0 ml/min water-glycerol feed flow rate with the water-to-glycerol molar ratio of 6 in the presence of 1.5 g catalyst. The highest hydrogen yield and hydrogen selectivity and approximately complete glycerol conversion were attained in nickel-loaded magnesium at 650°C as 57% and 66%, respectively. However, lower catalytic activity was obtained in the presence of nickel loaded cerium dioxide, i.e., glycerol conversion, hydrogen selectivity, and hydrogen yield decreased to 93%, 54% and 33%, respectively.

Calles et al. (2014) compared the activities of SBA-15 supported 7% by weight of nickel with 10% by weight of magnesium oxide and 10% by weight of calcium oxide modified catalysts at 600°C, atmospheric pressure with the water-to-glycerol molar ratio of 6 at 0.075 ml/min water-glycerol feed flow rate in a fixed bed stainless steel reactor. In the presence of 7Ni/SBA-15, hydrogen yield, and glycerol conversion were attained as 46% and 31%, respectively. The use of modified catalysts increased the glycerol conversion to 98% in both catalysts, and hydrogen yield values of 7Ni/10Mg/SBA-15 and 7Ni/10Ca/SBA-15 to 65% and 70%, respectively.

Thyssen et al. (2013) examined the activities of 10% by weight of nickel doped silica, 10% by weight of nickel doped lanthanum and 10%, 30%, and 50% by weight of lanthanum modified nickel loaded silica catalysts in a fixed bed quartz reactor at 600°C, 2.5 ml/h glycerol-water feed flow rate with the W/G molar ratio of 3. On the one hand, in the presence of $10Ni/SiO_2$, glycerol conversion and H_2 yield were attained as 52% and 31%, respectively. On the other hand, $10Ni/La_2O_3$ showed lower activity compared to silica supported catalyst as 26% glycerol conversion and 4% H_2 yield. However, glycerol conversion and hydrogen yield values were increased with lanthanum modified catalysts. Approximately complete glycerol conversion and 54% hydrogen yield were achieved in the presence of $10Ni/10La_2O_3/SiO_2$. However, the increase in La_2O_3 content decreased the glycerol conversion to 79% and 52% in $10Ni/30La_2O_3/SiO_2$ and $10Ni/50La_2O_3/SiO_2$, respectively. In addition, hydrogen yield values were obtained as 40% in both catalysts.

Dahdah et al. (2020) studied the effect of zirconia support on H_2 production in glycerol steam reforming reaction. Therefore, tetragonal zirconia synthesized via a hydrolysis technique and commercial monoclinic zirconia support were activated with 5% by weight Ni via wet-impregnation method and tested at 400-700^oC with a steam-to-glycerol molar ratio of 9 and a flow rate of 0.025 ml/min. The results revealed that higher glycerol conversion and hydrogen yield were achieved in monoclinic zirconia supported catalyst which remained stable during 24 hours whereas the tetragonal zirconia supported catalyst was deactivated due to the coke deposition after 6 hours. As a result of the activity tests, both catalysts displayed higher selectivity to carbonaceous compounds with low glycerol conversion and low H_2 yield. In the presence of tetragonal zirconia and monoclinic zirconia supported catalysts, the H_2 yields of nearly 16% and 20% were obtained with 12% and 35% glycerol conversions at 550^oC, respectively.

Al-salihi et al. (2020) examined the catalytic activities of SBA-15 and MgO promoted SBA-15 supported Ni and Co based monometallic and bimetallic catalysts synthesized by one-pot hydrothermal and/or incipient wetness impregnation methods at temperatures in the range of 450-700^oC with the water-to-glycerol molar ratio of 12 at 0.2 ml/min glycerol-water liquid mixture flow rate. According to the experimental results, Co-Ni/SBA-15 catalysts synthesized by both one-pot hydrothermal and wet-impregnation methods were resistant to a coke deposition, and both achieved complete glycerol conversion during the 40 h test period. Moreover, it was deduced that the stability and activity of Co/SBA-15 and Ni/SBA-15 increased with MgO loading. The stability performance of catalysts tested decreased in the following order: 10Co-5Ni>10Co-5MgO>10Co-5Ni-IMPG>15Co>10Ni-5MgO >15Ni/SBA-15. In addition, glycerol conversion of the catalysts decreased in the following order: 10Co-5Ni-IMPG≥10Co-5Ni>10Co-5MgO>15Co>15Ni>10Ni-5MgO. All catalysts also exhibited higher H_2 selectivity (>70%) at 650^oC. The

highest hydrogen selectivity was achieved as 83% in the presence of 10Co-5Ni/SBA-15-IMPG with complete glycerol conversion.

Moogi et al. (2020) synthesized 20Co/MgO, 5Cu-20Co/MgO, and 20Co/50MgO-50Al_2O_3 catalysts by co-precipitation method. Among the catalysts, 5Cu-20Co/MgO exhibited higher hydrogen yield of 74.6% with complete glycerol conversion into the gaseous products at 650^{o}C with a feed ratio of 30 wt. % glycerol in water at a feed flow rate of 0.08 ml/h. In addition, coke deposition on the catalyst was attained as 0.05 $mg/g_{cat}h^{-1}$. The yields of H_2 obtained increased in the following order: 20Co/50MgO-50Al_2O_3<20Co/MgO<5Cu-20Co/MgO. The order of coke formation amount decreased in the following order: 20Co/50MgO-50Al_2O_3>20Co/MgO>5Cu-20Co/MgO.

To sum up, hydrogen production via steam reforming of glycerol was carried out in a fixed bed reactor. The reactions operated at 350-900^{o}C and atmospheric pressure with the water-to-glycerol molar ratio of 3-12 in the presence of mesoporous catalysts. As catalysts, nickel, cobalt, ruthenium, platinum, and palladium loaded silicon dioxide, aluminium dioxide, cerium oxide, yttrium oxide, and magnesium oxide were used. In general, higher hydrogen yield was achieved in the presence of ruthenium and nickel loaded catalysts. According to literature review, it is clear that no silica aerogel was used as a catalyst support in glycerol steam reforming. Therefore, the objective of this study was determined as the synthesis and characterization studies of silica aerogel supported catalysts. In addition, determining the effect of the synthesized catalyst types and operating conditions on H_2 yield and developing a laboratory scale setup for this purpose are among the aims of the study.

3.3 Silica Aerogel

The superior properties of silica aerogels such as low bulk density (up to 95% of their volume is air), hydrophobicity, low thermal conductivity, high surface area, optical transparency, high porosity, low dielectric constant and excellent heat insulation have attracted attention in science and technology. Silica aerogels are implemented as a composite, an adsorbent, a sensor, a film material, a catalyst, a template and a thermal insulator in housing, refrigerators, skylights, windows, clothing, apparel, blankets, and space applications.

Silica aerogel as a catalyst support is of great interest due to its high surface area and high porosity. Silica aerogels have all micro (<2 nm), meso (2-50 nm) and macro (>50 nm) pores with a predominance of the mesopore range. The approximate pore size is between 5 and 100 nm, and the BET surface area is between 600 and 1000 m^2. The porosity can be as high as 99%. An important aspect of the aerogel pore network is its open structure and connectivity, which allows liquids or gases to flow through open porous structures with limited restriction from pores to pores and eventually penetrate the entire material. Moreover, silica aerogels are chemically stable, inert and have good thermal stability, and their high surface with open pores ensures good dispersion of catalytically active substances (Soleimani Dorcheh et al., 2007; Gurav et al., 2010; Amiri et al., 2016).

3.3.1 Synthesis of Silica Aerogels

Silica aerogels are generally synthesized by the sol-gel process due to its simplicity, efficiency and feasibility. Sol-gel process is a very prevalent and reliable methodology especially with metal oxides having uniform and small particle sizes, and various morphologies. It involves the transition of a system from a liquid “sol” into a solid “gel” phase.

The synthesis of silica aerogel is divided into 3 general steps:

- **Gel preparation**: The silica gel is obtained by the sol–gel process. The sol is prepared by a silica source solution and gelation is occurred by addition of catalyst. The gels are usually classified according to the dispersion medium used, e.g., hydrogel or aquagel, alcogel and aerogel (for water, alcohol, and air, respectively).

- **Aging of the gel**: The prepared gel is aged in its mother solution. This aging process strengthens the gel so that shrinkage during the drying step is kept to a minimum.

- **Drying of the gel**: In the drying phase, the gel pore liquid is removed to prevent the gel structure from collapsing (Soleimani Dorcheh et al.,2007).

3.3.1.1 Silicon Alkoxide Gelation

Sol-gel processing refers to the synthesis of an inorganic network by a chemical reaction in solution at low temperatures, which forms an amorphous network in the solution. The most prominent feature of this reaction is the transition from a colloidal solution (liquid) to a di- or multiphase gel (solid), leading to the expression "sol-gel process".

The most common technique for producing silica gels involves the reaction of a silicon alkoxide (usually tetramethoxysilane abbreviated as "TMOS" or tetraethoxysilane abbreviated as "TEOS"), which serves as a source of silica, with water, acting as a reactant to help combine the alkoxide molecules together, in the presence of a basic, acidic and/or fluoride-containing catalyst (such as ammonium hydroxide or ammonium fluoride). Since silicon alkoxides are non-polar, ethanol or acetone is used as a solvent to allow the necessary chemical reactions occur in the same phase (Gurav et al., 2010; Pudukudy et al., 2015).

3.3.1.2 Formation of a Sol

Sol can be prepared by two techniques: condensation and dispersion of particles. Condensation proceeds by nucleation growth of particles to the appropriate size, whereas dispersion involves the reduction of large particles down to the colloidal dimensions. The size and properties of the resulting particles depend on the relative rates of these two processes. Sol formation is favoured when the rate of nucleation is high and the rate of crystal growth is low.

When an alkoxide reacts with water, three reactions occur and result in the formation of silica nanoparticles which then interconnect together to form a gel. The first of these reactions is hydrolysis in which a silicon alkoxide reacts with water to form silanol (Si-OH) groups.

Hydrolysis

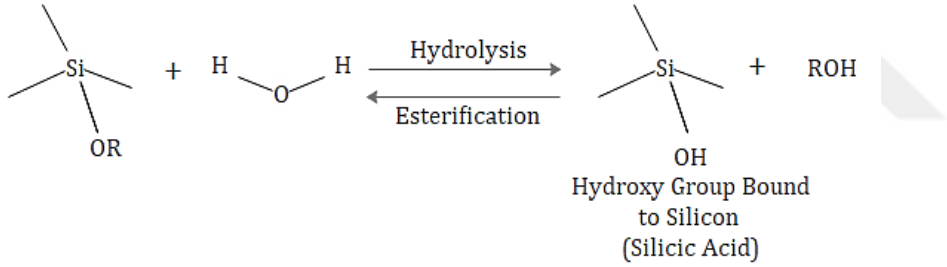

where R= Vinyl, Alkyl, or Aryl groups.

These silanol groups can then react either with each other or an alkoxide group (Si-OR) to form a siloxane bridge (Si-O-Si), forming giant molecules containing thousands of silicon-oxygen bridges called silica nanoparticles.

During the formation of a silicon nanoparticle, some silicon atoms cannot form a siloxane bridge by forming siloxane bonds with hydroxyl (-OH) or alkoxy (-OR) groups. The silanol groups are then condensed in two different reactions to form silicone-oxygen-silicone bridges (Gurav et al., 2010).

Water Condensation

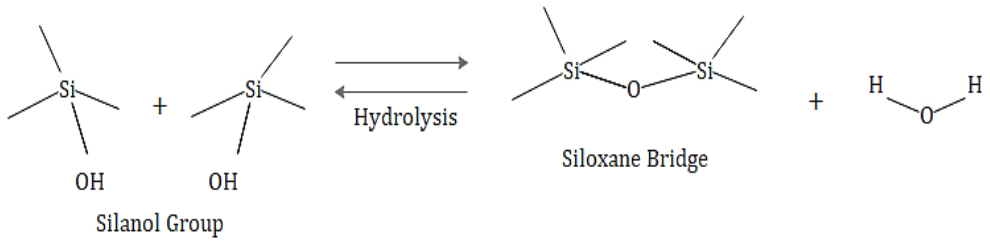

Silanol Group

Alcohol Condensation

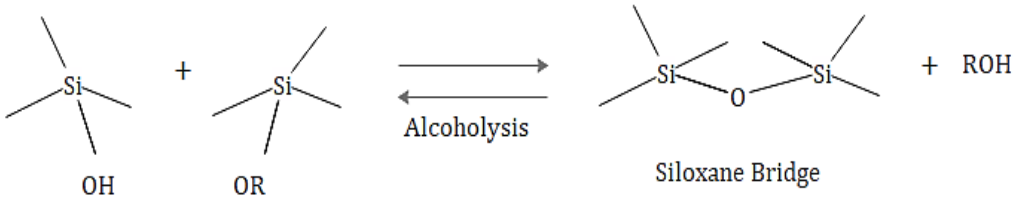

Silanol Group

3.3.1.3 Formation of a Gel from a Sol

At some point, the nanoparticles stop growing in size and instead agglomerate with other particles. The terminal hydroxyl (-OH) groups left over from the hydrolysis of the alkoxide and alkoxy (-OR) groups that are never hydrolysed allow the nanoparticles to bond together. When adequate nanoparticles join together, a gel is formed. There are functional groups along the aerogel and on the surface of the struts that form the sponge-like framework of the aerogel, in which one silicon atom does not share the siloxane bridge with another silicon atom i.e., one of the four bonds do not participate in network bonding (Gurav et al., 2010).

3.3.1.4 Purifying and Aging of Silica Gels

After silica gel is synthesized, the liquid in the pores of the gel usually contains alcohol, water, catalyst and other random organic compounds that cause shrinkage or decrease in transparency and mechanical strength. Therefore, the gel solution is purified by soaking in a pure organic solvent such as methanol, ethanol or acetone. When the gel is treated with pure solvent, impurities are diffused out and the pure solvent is dispersed until the equilibrium concentration of the species is reached. During this purification process, long silica bonds are formed as a result of some final chemical reactions called aging, which contribute to strengthening the structural framework of the gel (Pudukudy et al., 2015).

3.3.1.5 Drying of Alcogel

The process of removing the majority solvent (mainly alcohol and water) from the gel is called drying. Surface silanol groups (Si–OH) on the adjacent silica cluster undergo condensation reactions during drying resulting in an irreversible shrinkage of the gel network. This process can create very low energy surfaces that significantly reduce surface tension. Therefore, it is necessary to modify alcogel surfaces with appropriate modifying agents to render the alcogel hydrophobic. Surface modification is a crucial step in the ambient pressure drying method as the H of the gels is replaced by non-polar alkyl or aryl groups from Si-OH, which prevents the silica clusters from condensation reactions that cause the gel shrink. There are several hydrophobic reagents such as, methyltrimethoxysilane (MTMS), hexamethyldisilazane (HMDZ), dimethylchlorosilane (DMCS), dimethyldichlorosilane (DMDC), trimethylchlorosilane (TMCS), trimethylethoxysilane (TMES), and hexadecyltrimethoxysilane (HDTMS) that can change the wetting properties of the surface (Gurav et al., 2010).

Surface modification is the key process in the preparation of the silica aerogel. The most commonly used silylating reagent is TMCS. In silica modification process, the hydroxyl group (–OH) located on the internal pore surface of the silica gels is reacted with Cl^- in TMCS, resulting in the formation of HCl and attachment of the $–OSi(CH_3)_3$ functional group to the surface of the silica gel. The replacement of –OH and $–CH_3$ groups transforms the initial hydrophilic character of the internal surface of silica network into a hydrophobic state.

The reaction mechanism of silica alcogel and TMCS is represented by following reaction (Wu et al., 2011).

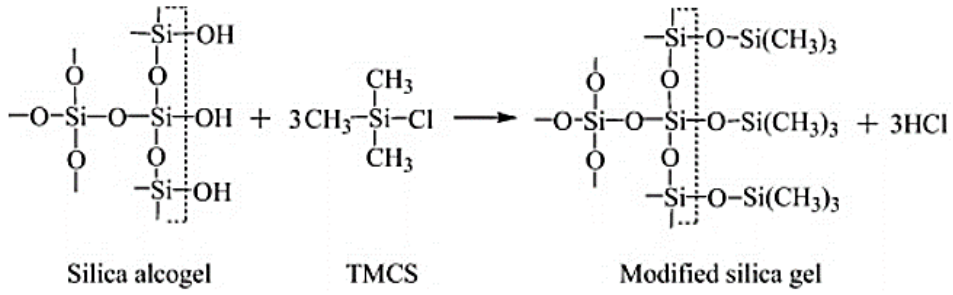

The reaction of TMCS with water within pores simultaneously take place as represented by the following reaction.

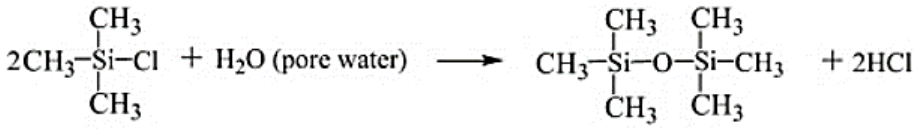

Water is then replaced with n-hexane, a low surface tension solvent, to reduce capillary pressure into the pores. The hexamethyldisiloxane ($(CH_3)_3Si–O–Si(CH_3)_3$) is adsorbed on the surface, which enhances the expel of alcohols/H_2O/HCl phase and entrance of n-Hexane due to the incompatibility between hexamethyldisiloxane/n-Hexane phase and alcohols/H_2O/HCl phase (Wu et al., 2011).

3.4 Metal-Based Catalysts

In this part, general information about the metals used in this study is detailed in the relevant sections.

3.4.1 Nickel-Based Catalysts

Nickel-based catalyst is used in a large number of industrial processes and in organic synthesis due to its stability and high catalytic activity. Ni-based catalysts assure an acceptable catalytic activity and a lower cost. The catalysts offer significant advantages in steam reforming reactions as they have high capability of breaking the C-C, H-O and C-H bonds and thus provide a high H_2 selectivity. However, Ni-based catalysts are prone to sintering at higher temperature causing coke formation, resulting in deactivation of catalyst during the reaction (Llorca et al., 2013; Meloni et al.,2012; Ismailia et al., 2020).

3.4.2 Cobalt-Based Catalysts

Cobalt-based catalysts are extensively applied in desulphurisation reactions, synthesis of polyester precursors, production of aldehydes from alkenes in the OXO reaction and other industrial reactions. The catalysts exhibit higher activity for various C-C bond formations (Ozkal et al., 2015). The main reasons behind the utilization of cobalt are low cost and high activity as well as good functional group tolerance, operability even under mild conditions, and good electrochemical activity (Llorca et al., 2013). In addition, Co-based catalyst might be considered as a good catalyst in steam reforming reactions due to its stability and reduced deposition of carbonaceous species (Konsolakis et al., 2016; Greluk et al., 2020). However, cobalt catalysts may be deactivated by surface oxidation and sintering depending on the interaction with support (Carrero et al., 2017).

3.4.3 Chromium-Based Catalysts

Chromium-based catalysts are the most important ethylene polymerization and oligomerization catalysts widely applied for industrial production of polyethylene and 1-hexene. The Phillips catalyst, a heterogeneous catalyst consisting of a chromium oxide supported on silica gel, is used to produce about half of the world's polyethylene. The chromium-based catalysts have drawn intense attention in the dehydrogenation of light alkanes. The effectivity of chromium-based catalysts is risen by dispersing on supports with high surface areas. In addition, its use as a bimetallic form stabilizes the catalyst. However, it is still unclear that chromium-based catalysts play the most important role in dehydrogenation reactions (Liu et al., 2014; Cheng et al., 2016).

3.4.4 Zirconium-Based Catalysts

Zirconium oxide and compounds containing zirconium are recognized as useful catalytic materials. In particular, zirconia (ZrO_2) is an important support material for catalysis due to its acid-base properties. Zirconia can also act as a catalyst on its own in the hydrogenation of CO, olefins and dienes, as well as the conversion of synthesis gas to isobutane. The use of zirconia as a catalyst or as a support is effective only when the compound has a high surface area that remains stable under process conditions (Calafat et al., 1998).

3.4.5 Silver-Based Catalysts

Silver-based catalysts are of particular interest due to a number of valuable features, such as the ability to activate molecular oxygen, uniform distribution of metal particles/clusters on various supports, and a synergistic effect with a large number of promoters and modifiers. These features laid a ground for the application of Ag-

based catalysts in the industrial gas phase oxidation of methanol to formaldehyde and ethylene glycol to glyoxal. Ag-based catalysts are also of interest due to the optimal redox potential of silver and higher concentration of Lewis acid sites accompanied by the limited Brønsted acidity of the support (Torbina et al., 2018).

3.4.6 Molybdenum-Based Catalysts

Molybdenum-based catalysts have a number of important applications in the petroleum and plastics industries. Its major use is in the hydrodesulfurization of petroleum, petrochemicals and coal-derived liquids. In addition, Mo-based catalysts are resistant to sulphur poisoning and catalyse the conversion of hydrogen and carbon monoxide from the pyrolysis of waste materials to alcohols in the presence of sulphur, under conditions that will poison precious metal catalysts. Mo-based catalysts are abundant and non-noble, possessing superior catalytic activity with their Lewis acid sites and low oxidation potentials in the highest oxidation states. In this regard, interest in Mo-based catalyst increased both in industrial and laboratory (Shen et al., 2019).

3.4.7 Ruthenium-Based Catalysts

One of the cheapest noble metals, ruthenium is frequently used in processes of catalytic hydrogen evolution. Ru-based catalysts offer selective oxidative transformations of various functional groups with environmentally friendly and easily accessible oxidants. Ruthenium catalysis can be a very powerful tool for selective catalysis in synthetic chemistry, such as asymmetric epoxidation of alkenes, production of dioxygen species, dihydroxylation of olefins and oxidative dehydrogenation of alcohols. One of the major reasons of attractiveness is that Ru-based catalysts are responsible not only for the functionalization of C-H bonds but also for the C-O cleavage with dominant Lewis acid sites. However, it is not

economical to use only Ru for catalysis. Thus, lower loadings of Ru on an appropriate support or synthesis bimetallic forms of Ru are better options (Demsash et al.,2018; Sun et al., 2017; Odenkirk et al., 1992).

3.4.8 Iron-Based Catalysts

Iron-based catalysts offer prominent advantages such as low cost, high safety, environmental friendliness and wide-distribution. Iron and/or iron oxide-based catalysts are widely used in fertilizer, refining and chemical industries. Zero valent iron (ZVI), $Fe_2(SO_4)_3$, $FeSO_4$, $FeCl_3$, and FeOOH are used in water and wastewater treatment (Zhang et al., 2018). Iron oxide-based catalyst is also used for well-known large-scale ammonia production, called 'Haber-Bosch method'. In this method, Magnetite (Fe_3O_4) is used as a catalyst that increases the reactivity between nitrogen and hydrogen to produce ammonia (Morlanés et al., 2020). Another well-known process using magnetite is the gas-to-liquid process, which produces synthetic fuel from either natural gas or gasified coal. Moreover, the iron oxide-based catalysts doped with chromium oxide (Cr_2O_3) that prevent sintering of iron oxide crystallites are commercially used in high temperature (350-400°C) water gas shift (WGS) reaction (Bouarab et al., 2014). Besides the oxide forms of iron, metallic iron is also an active catalyst in the Fischer-Tropsch processes to produce longer hydrocarbon chains i.e., olefins, by catalysing CO and H_2, called syngas (de Smit et al., 2009).

3.4.9 Magnesium-Based Catalysts

Magnesium-based catalysts are used for oxidative coupling of methane, dehydrogenation–dehydration of alcohols, dehydrohalogenation of halogenated hydrocarbons, benzylation of aromatics, synthesis of pyranopyrazole derivatives, and Claisen–Schmidt condensation (Elkhalifa et al., 2018). Even though Mg is used as an active catalyst in a number of processes, MgO, the oxide form, is a well-known

catalyst support with specific properties such as cation valence, redox properties, acid-base character, and crystal and electronic structure. MgO is considered as a high-surface-area heterogeneous catalyst support, additive and promoter for various chemical reactions such as dry reforming, dehydrohalogenation, oxidative dehydrogenation of butane, nonoxidative dehydrogenation of ethylbenzene, and decomposition of CCl. In addition, the use of Mg as a support or promoter for Ni-based catalysts provides good metal dispersion on the catalyst surface that offers high catalytic activity and low catalyst deactivation by reducing the amount and rate of carbon deposition on the Ni-active sites (Khairudin et al., 2018; Al-salihi et al., 2020).

3.4.10 Manganese-Based Catalysts

Manganese-based catalysts have remarkable advantages, such as low toxicity, high natural abundance, low cost, and environmental friendliness. Mn-based catalysts are used as the physical template and the chemical oxidative initiator for the aniline polymerization (Ran et al., 2018), in water and wastewater treatment (Wolowiec et al., 2019), and for activating peroxymonosulfate (PMS) and peroxydisulfate (PDS) to degrade many contaminants (Huang et al., 2019). In addition, the use of Mn with magnetite (Fe_3O_4) are envisioned as a candidate for obtaining Cr-free Fe-based WGS catalysts (Meshkani et al., 2014).

In this study, above-stated metals were used as either monometallic or promoting metals. The ability to break H-O bonds in addition to C-C and C-H makes Ni a great candidate for use as a monometallic and bimetallic catalyst in the GSR reaction. However, the major drawback of using Ni is its high sintering tendency and less resistance to carbon formation, resulting in a catalyst poisoning and hence catalyst deactivation (Llorca et al., 2013; Meloni et al.,2012; Ismailia et al., 2020). Therefore, some promoting metals such as Mg and Ru were used to increase the thermal stability

and reduce the coke deposition. According to literature, it was envisioned that due to the high basicity of MgO, it would lead to a reduction in the amount of coke deposits on the catalyst by capturing the CO_2 produced and hence reversing the Boudouard reaction (Dębek, 2016; Calles et al., 2014). In addition, MgO provides good dispersion of particles by preventing pore clogging by agglomeration of Ni particles (Moogi et al., 2020). However, it is also possible to observe a decrease in H_2 yield as the basic nature of MgO may cause a decrease in acidity in the catalyst and thus reduce the cleavage ability of C-C and C-H. Besides Mg, use of Ru as a promoter to Ni offers a great advantage due to its ability to break C-C and C-H bonds as well as C-O bonds. In addition, according to the literature, Ru has a positive effect on reducing coke deposition on the catalyst (Demsash et al.,2018; Sun et al., 2017; Odenkirk et al., 1992). Moreover, iron-oxide based catalysts are commercial catalysts in the high temperature WGS reaction occurring between 350-450^oC (Bouarab et al., 2014). Regardless of the high operating temperature of this study, Fe-oxide was used as a promoting metal to Ni to increase the H_2 yield and then doped with Mn, which was used to prevent the sintering of Fe. As a result of the studies of some authors, a higher CO conversion was achieved in Ni-Fe-Mn catalyst in the WGS reaction with a Fe/Mn weight ratio of 10% (Meshkani et al., 2014). Moreover, some literature has revealed that Co, Cr and Zr promoting Ni-based catalysts display higher catalytic activity compared to Ni-based catalysts. In addition, their higher thermal stability and greater coke resistance have intensified the studies on these catalysts (Carrero et al., 2017; Haryanto et al., 2011; Calafat, 2011; Manfro et al, 2013). Besides these catalysts, relatively inexpensive metals such as Mo and Ag compared to the noble metals were chosen due to possessing predominant Lewis acid sites (Torbina et al., 2018; Shen et al., 2019) that are forecasted to rupture the C-C and C-H bonds and thereby increase the H_2 yield.

CHAPTER 4

EXPERIMENTAL

The experimental studies are divided into three parts: catalyst synthesis, catalyst characterization, and catalyst activity test. Silica aerogel supported mono, bi and trimetallic catalysts were synthesized by loading different amounts of Ni, Co, Cr, Zr, Mo, Ag, Ru, Fe, Mg, and Mn by wet impregnation or co-precipitation methods. Subsequently, the catalysts were calcined under dry air and reduced with hydrogen.

All synthesized catalysts were characterized using N_2 Physisorption, X-Ray Diffractometer (XRD), Scanning Electron Microscopy (SEM), Diffuse Reflectance Infrared Fourier Transform Spectroscopy (DRIFT) and Thermogravimetric Analysis (TGA) methods to examine their physical properties, chemical composition and surface morphology.

The catalysts were tested in a fixed bed quartz reactor at 450-1050^{o}C, under atmospheric pressure with the water-to-glycerol molar ratio of 1, 3, 6 and 9 at 0.8, 0.9 and 1.0 ml/h feed flow rate in the presence of 2.5, 5, 8 and 10 wt. % nickel and 10 wt. % of each cobalt, chromium, molybdenum, silver, and zirconium loaded monometallic, various amounts of nickel-molybdenum, nickel-ruthenium, nickel-iron and nickel magnesium loaded bimetallic and nickel-iron-manganese loaded trimetallic catalysts. Moreover, repeatability of the experiments was performed.

The catalyst synthesis procedure, catalyst characterization techniques, and catalyst activity test were detailed in the following sections.

4.1 Synthesis of the Catalysts

Synthesis of the catalyst was divided into two parts as the synthesis of silica aerogel and the loading of metals onto silica aerogel. The route of synthesis of silica aerogel was followed by the synthesis procedure of Deshpande, (1996) developed by our lab-mate Değirmencioğlu, (2018).

4.1.1 Synthesis of Silica Aerogel

In the synthesis of silica aerogel, in general, pure water and ethanol (Sigma Aldrich) are used as solvents, tetraethylorthosilicate (TEOS, Merck) is used as a silica source, hydrochloric acid (HCl, 37% v/v, Merck) is used as an acidic catalyst, ammonia (NH_3, 25% v/v, Merck) is used as a basic catalyst, and ammonium fluoride (NH_4F, Merck) is used as a gelation agent. Trimethylchlorosilane (TMCS, Merck) is used to modify surface and maintain hydrophobicity to aerogel.

For the preparation of the sol, 1.73 g pure water and 5.63 g absolute ethanol, 10.01 g TEOS and 62µL HCl are placed in an airtight beaker, respectively. The solution is then mixed for 2 hours at room temperature on a magnetic stirrer. After mixing, 3.8 g pure water, 9.9 g ethanol and 650 µL NH_3 are added to the sol. Then, 800 µL NH_4F is added dropwise to the solution and gelation occurs. Absolute ethanol is then added to cover the entire gel, and cap of the beaker is closed to prevent gas entry. The ethanol-covered gel mixture is left at room temperature for 8 hours for the formation of long silica bonds referring to aging. For ambient pressure drying, ethanol is poured from the gel after 8 hours and 30 ml of hexane is added. The gel-hexane mixture is left in a water bath at 45°C for 2 hours. After 2 hours, hexane is decanted from the gel and the gel is washed again with 30 ml of hexane. Then, 5 g of TMCS is slowly added to the gel to provide surface modification and maintain hydrophobicity to aerogel. At this point, water with HCl vapour comes out as a white smoke. After the

HCl vapour has disappeared, a solution of water and hexane is taken into a graduated cylinder. Hexane at the top of the water in graduated cylinder and fresh hexane as much as the volume of water in the graduated cylinder are added back to the gel. Thus, the water is removed from the gel structure and hexane is added to protect the hydrophobic structure and prevent the shrinkage into the pores. The gel-hexane mixture is then left in a water bath at 45°C for 5 hours. This step is repeated once more by pouring hexane and then leaving the gel in a water bath for 5 hours at 45°C. Finally, the hexane is decanted and the gel is allowed to dry in a furnace set at 125°C for 2 hours to evaporate all the hexane.

4.1.2 Synthesis of Metal Loaded Silica Aerogel

Within the scope of this study, various metals were loaded onto silica aerogels by co-precipitation or wet-impregnation techniques to obtain active catalysts. The main reason for using co-precipitation technique is that it provides pure and uniform catalysts as a result of good mixing, while wet impregnation method provides an easy preparation of a layer of an active substance on the catalyst surface for supported catalysts (de Jong et al., 2009; NPTEL, 2014). In this study, nickel, cobalt, chromium, zirconium, molybdenum, silver, nickel-ruthenium, nickel-iron, nickel-molybdenum, nickel-magnesium, and nickel-iron-manganese loaded silica aerogels were synthesized by co-precipitation method. In addition, only 10 wt. % nickel doped silica aerogels were synthesized by following both co-precipitation and wet-impregnation methods.

The synthesis methods of Ni, Mo and 8Ni-2Mo loaded silica aerogels were detailed in relevant sections and the synthesis routes of other catalysts were summarized in Table 4.1.

The amount of metal precursors loaded to achieve the desired metal content was calculated according to the equation given in Appendix A.

4.1.2.1 Monometal Loading

Monometals were loaded onto silica aerogel by co-precipitation or wet-impregnation methods.

To synthesize nickel, cobalt, chromium, and zirconium loaded silica aerogels by co-precipitation method, one gram of silica aerogel is first powdered, placed in a beaker and mixed on a magnetic stirrer with 20 ml absolute ethanol for 30 minutes. At the same time, desired amount of metal precursor is dissolved in absolute ethanol in the other beaker and placed on a magnetic stirrer to mix for 30 min. After the solutions are homogeneously mixed, the metal-containing solution is added dropwise to the silica aerogel solution. The resulting solution is allowed to stand for 24 hours on the magnetic stirrer. At the end of the mixing, the solution is left for drying for 24 hours to evaporate whole ethanol in a furnace previously set to 60°C.

To synthesize molybdenum and silver loaded silica aerogels by co-precipitation method, silica aerogel was first calcined at 700°C with a heating ramp of 1°C/min at 5 bar under dry air flow of 80 ml/min. Then, one-gram calcined silica aerogel placed in a beaker and mixed on a magnetic stirrer with 20 ml distilled water for 30 minutes. At the same time, desired amount of metal precursor is dissolved in distilled water in the other beaker and placed on a magnetic stirrer to mix for 30 min. After the solutions are homogeneously mixed, the metal-containing solution is added dropwise to the silica aerogel solution. The resulting solution is allowed to stand for 24 hours on the magnetic stirrer. At the end of the mixing, the solution is left for drying for 24 hours to evaporate whole distilled water in a furnace previously set to 60°C.

To synthesize nickel loaded silica aerogel by wet impregnation method, distilled water is used instead of ethanol and the synthesis process is carried out following the same routes as in the co-precipitation process. The reason for using distilled water is

that silica aerogel, unlike nickel precursor, is insoluble in water due to its hydrophobic nature.

4.1.2.2 Bimetal Loading

Ni-containing bimetals were loaded onto silica aerogels by co-precipitation method with two-step metal loading and simultaneous metal loading.

In two-step metal loading path (abbreviated as I), one-gram silica aerogel is powdered, placed in a beaker and mixed on a magnetic stirrer with 20 ml absolute ethanol for 30 minutes. At the same time, desired amount of nickel precursor, is dissolved in absolute ethanol in the other beaker and placed on a magnetic stirrer to mix for 30 min. After the solutions are homogeneously mixed, the nickel-containing solution is added dropwise to the silica aerogel solution. The resulting solution is allowed to stand for 24 hours on the magnetic stirrer. At the end of the mixing, the solution is left for drying for 24 hours to evaporate whole ethanol in a furnace previously set to 60°C. After drying, nickel doped silica aerogel is calcined at 700^{o}C for 5 h under dry air of 80 ml/min. Subsequently, it is placed in a beaker and mixed on a magnetic stirrer with distilled water for 30 minutes. At the same time, desired amount of promoting metals such as molybdenum, iron, magnesium, and ruthenium are dissolved in distilled water in the other beaker and placed on a magnetic stirrer to mix for 30 min. After the solutions are homogeneously mixed, the promoting metals-containing solution is added dropwise to the nickel-loaded silica aerogel solution. The resulting solution is allowed to stand for 24 hours on the magnetic stirrer. At the end of the mixing, the solution is left for drying for 24 hours to evaporate whole water in a furnace previously set to 60°C.

In simultaneous metal loading path (abbreviated as II), one-gram calcined silica aerogel placed in a beaker and mixed on a magnetic stirrer with 20 ml distilled water for 30 minutes. At the same time, both desired amount of nickel precursor and

promoting metal (molybdenum) precursor are dissolved in distilled water in two different beaker and placed on a magnetic stirrer to mix for 30 min. After the solutions are homogeneously mixed, the nickel-containing and molybdenum-containing solution are simultaneously added dropwise to the silica aerogel solution. The resulting solution is allowed to stand for 24 hours on the magnetic stirrer. At the end of the mixing, the solution is left for drying for 24 hours to evaporate whole water in a furnace previously set to 60°C.

4.1.2.3 Trimetal Loading

In this study, Ni-Fe-Mn loaded trimetallic catalyst was synthesized by co-precipitation method.

In the synthesis of trimetallic catalyst, firstly, one-gram silica aerogel is powdered, placed in a beaker and mixed on a magnetic stirrer with 20 ml absolute ethanol for 30 minutes. At the same time, desired amount of nickel precursor is dissolved in absolute ethanol in the other beaker and placed on a magnetic stirrer to mix for 30 min. After the solutions are homogeneously mixed, the nickel-containing solution is added dropwise to the silica aerogel solution. The resulting solution is allowed to stand for 24 hours on the magnetic stirrer. At the end of the mixing, the solution is left for drying for 24 hours to evaporate whole ethanol in a furnace previously set to 60°C. After drying, nickel doped silica aerogel is calcined at 700^{o}C for 5 h under dry air of 80 ml/min. Subsequently, it is placed in a beaker and mixed on a magnetic stirrer with distilled water for 30 minutes. At the same time, both desired amount of iron precursor and manganese precursor are dissolved in distilled water in two different beaker and placed on a magnetic stirrer to mix for 30 min. After the solutions are homogeneously mixed, the iron-containing and manganese-containing solutions are simultaneously added dropwise to the nickel-loaded silica aerogel solution. The resulting solution is allowed to stand for 24 hours on the magnetic

stirrer. At the end of the mixing, the solution is left for drying for 24 hours to evaporate whole water in a furnace previously set to 60°C.

In all catalyst synthesis, the amount of solvent containing metal precursor was arranged with respect to the amount of metal precursor loaded. The synthesis paths of catalysts were detailed in Table 4.1.

Table 4.1 Catalyst Synthesis Paths

Metal	***Support***	***Method***	***Solvent***	***Metal Precursor***	***Metal Precursor Amount, g***	***Metal Content, wt. %***
Ni	SA	Co-precipitation	Ethanol	$(Ni(NO_3)_2 \cdot 6H_2O$, Acros Organics, 99%)	0.125	2.5
					0.250	5
					0.400	8
	SA	Wet-impregnation	Water		0.500	10
Co	SA	Co-precipitation	Ethanol	$(Co(C_2H_3O_2)_2 \cdot 4H_2O$, Sigma Aldrich, 98%)	0.420	
Cr				$(Cr(NO_3)_3 \cdot 9H_2O$, Sigma Aldrich, 98%)	0.770	

Table 4.1 (cont'd) Catalyst Synthesis Paths

Metal	***Support***	***Method***	***Solvent***	***Metal Precursor***	***Metal Precursor Amount, g***	***Metal Content, wt. %***
Zr	SA	Co-precipitation	Ethanol	($ZrO(NO_3)_2 \cdot xH_2O$, Sigma Aldrich, 99%)	0.250	10
Mo	Calcined SA		Water	$(NH_4)_6Mo_7O_{24} \cdot 4H_2O$, Fluka Analytical, 99%	1.290	
Ag				$AgNO_3$, Merck, 99%	0.160	

Table 4.1 (cont'd) Catalyst Synthesis Paths

Metal	***Support***	***Method***	***Solvent***	***Metal Precursor***	***Metal Precursor Amount, g***	***Metal Content, wt. %***
Ni & Mo	SA (Ni) & Calcined SA (Mo)	Two-step co-precipitation	Ethanol (Ni) & Water (Mo)	$(Ni(NO_3)_2 \cdot 6H_2O$, Acros Organics, 99%) & $(NH_4)_6 Mo_7O_{24} \cdot 4H_2O$, Fluka Analytical, 99%	0.400 & 0.260	8 & 2
	Calcined SA	Simultaneous co-precipitation	Water			
Ni & Mg	SA & Calcined SA	Two-step co-precipitation	Ethanol (Ni) & Water (Mg)	$(Ni(NO_3)_2 \cdot 6H_2O$, Acros Organics, 99%) & $(Mg(NO_3)_2 \cdot 6H_2O$, Merck, 99%)	0.500 & 0.316	10 & 3

Table 4.1 (cont'd) Catalyst Synthesis Paths

Metal	***Support***	***Method***	***Solvent***	***Metal Precursor***	***Metal Precursor Amount, g***	***Metal Content, wt. %***
Ni & Fe	SA & Calcined SA	Two-step co-precipitation	Ethanol (Ni) & Water (Fe-Ru)	$(Ni(NO_3)_2 \cdot 6H_2O$, Acros Organics, 99%) & $Fe(NO_3)_3 \cdot 9H_2O$, Merck, 98%	0.500 & 0.217	10 & 3
Ni & Ru				$(Ni(NO_3)_2 \cdot 6H_2O$, Acros Organics, 99%) & $Cl_3Ru \cdot xH_2O$, Acros Organics, 35-40%	0.500 & 0.062	10 & 3
					0.500 & 0.041	10 & 2
					0.500 & 0.021	10 & 1

Table 4.1 (cont'd) Catalyst Synthesis Paths

Metal	***Support***	***Method***	***Solvent***	***Metal Precursor***	***Metal Precursor Amount, g***	***Metal Content, wt. %***
Ni & Fe & Mn	SA & Calcined SA	Two-step co-precipitation	Ethanol (Ni) & Water (Fe & Mn)	$(Ni(NO_3)_2 \cdot 6H_2O$, Acros Organics, 99%) & $Fe(NO_3)_3 \cdot 9H_2O$, Merck, 98% & $Mn(NO_3)_2 \cdot 4H_2O$, Merck, 98.5%	0.500 & 0.217 & 0.001	10 & 3 & 0.3

4.2 Naming of the Catalysts

The metal loaded silica aerogels were synthesized by wet-impregnation or co-precipitation method, calcined under dry air and reduced with H_2 flow. They were named in the XY/SA(Z)(T) format where X indicates the metal percent in weight, Y is the type of loaded metal, SA stands for silica aerogel, Z is calcination temperature and T is reduction temperature. For instance, 10Ni/SA(700)(1035) indicates that the catalyst is 10 wt. % nickel loaded silica aerogel, calcined at 700°C under dry air and reduced at 1035°C with H_2 flow. In addition, 10Ni/SA(700)(1035)-wet indicates the catalyst synthesized following wet impregnation method, 10 wt. % nickel loaded

silica aerogel, calcined at 700°C under dry air and reduced at 1035°C with H_2 flow. The synthesized catalysts were given in Table 4.2.

Table 4.2 Synthesized Catalysts

<table>
<tr><th>Catalyst</th><th>Metal Type</th><th>Metal Amount, wt.%</th><th>Calcination Temperature, °C</th><th>Reduction Temperature, °C</th></tr>
<tr><td>2.5Ni/SA</td><td rowspan="5">Ni</td><td>2.5</td><td rowspan="3">700</td><td rowspan="11">1035</td></tr>
<tr><td>5Ni/SA</td><td>5</td></tr>
<tr><td>8Ni/SA</td><td>8</td></tr>
<tr><td>10Ni/SA</td><td rowspan="8">10</td><td>700, 1035</td></tr>
<tr><td>10Ni/SA-wet</td><td rowspan="7">700</td></tr>
<tr><td>10Co/SA</td><td>Co</td></tr>
<tr><td>10Cr/SA</td><td>Cr</td></tr>
<tr><td>10Zr/SA</td><td>Zr</td></tr>
<tr><td>10Mo/SA</td><td>Mo</td></tr>
<tr><td>10Ag/SA</td><td>Ag</td></tr>
<tr><td>8Ni-2Mo/SA</td><td>Ni, Mo</td><td>8, 2</td></tr>
<tr><td>10Ni-3Fe/SA</td><td>Ni, Fe</td><td>10, 3</td><td rowspan="2">550</td><td rowspan="2">550</td></tr>
<tr><td>10Ni-3Fe-0.3Mn/SA</td><td>Ni, Fe, Mn</td><td>10, 3, 0.3</td></tr>
<tr><td>10Ni-3Mg/SA</td><td>Ni, Mg</td><td>10, 3</td><td rowspan="4">700</td><td rowspan="4">700</td></tr>
<tr><td>10Ni-1Ru/SA</td><td rowspan="3">Ni, Ru</td><td>10, 1</td></tr>
<tr><td>10Ni-2Ru/SA</td><td>10, 2</td></tr>
<tr><td>10Ni-3Ru/SA</td><td>10, 3</td></tr>
</table>

4.2.1 Calcination & Reduction of the Synthesized Catalysts

In metal-loaded catalysts, calcination and reduction must be performed respectively to obtain an active phase. In this study, the catalysts were calcined under dry air and then reduced with hydrogen flow.

Calcination is a heat treatment that aims to stabilize textural and structural properties of catalysts during the reaction, remove impurities, and oxidize metal precursor under controlled environment and temperature (NPTEL, 2014). For calcination, metal loaded silica aerogels are placed in a fixed bed quartz reactor and heated from room temperature to 550, 700, and 1035°C with a heating ramp of 1°C/min at 5 bar under dry air flow at 50 ml/min. When the desired calcination temperature is reached, the catalyst is kept at this temperature for 5 hours. At the end of 5 h, the dry air flow is turned off and furnace is allowed to cool.

After calcination, the catalysts are reduced under hydrogen flow for generating active sites of catalysts. For reduction, the catalysts are placed in the fixed bed quartz reactor and heated from room temperature to 550, 700, and 1035°C with a heating ramp of 10°C/min at 5 bar under argon flow of 80 ml/min. When the temperature reaches to desired point, the catalysts are treated with H_2 flow of 50 ml/min at 5 bar for half an hour. At the end of half an hour, Ar is allowed to pass through the catalyst at the same flow rate of 80 ml/min for an hour to sweep all the hydrogen gas.

In both calcination and reduction processes, it is aimed to ensure the stability of the textural and structural properties of the catalysts during the reaction.

4.3 Characterization of the Catalysts

Chemical composition, surface area and porosity, bulk solid structure, surface morphology, particle size, crystallite size, activity, selectivity and stability of the catalysts were examined with the aid of some of characterization techniques, such as

N_2 Physisorption, X-Ray Diffraction (XRD), Scanning Electron Microscopy (SEM), Diffuse Reflectance Infrared Fourier Transform Spectroscopy (DRIFTS) and Thermogravimetric Analysis (TGA).

4.3.1 N_2 Physisorption Analysis

Nitrogen physisorption at boiling temperature (77 K) is the most widely used technique to determine the catalyst surface area and to characterize its porous texture (Gregg and Sing, 1982). In this context, adsorption isotherm curves, which is nitrogen adsorbed volume against its relative pressure, was determined under the relative pressure range of $0.0001<P/Po<0.99$ using Micromeritics Tristar II 3020. Prior to the analysis, catalysts were degassed at 110°C for 3h.

4.3.2 X-Ray Diffraction Analysis (XRD)

The degree of crystallinity and the phases of the synthesized catalysts were identified with the aid of XRD analysis for their reduced forms (Lavina et al., 2014). Average crystallite sizes of metals or metal oxides were calculated using Scherrer Equation. XRD pattern was obtained by setting Bragg angle values in the range of 10°-90° with a step size of 1°/min. The XRD analysis was performed using Rigaku Ultima-IV diffractometer with CuKα anode ($\lambda = 0.1542$ nm) operating at 40 kV and 30 mA.

4.3.3 Scanning Electron Microscopy (SEM)

A scanning electron microscope (SEM) is a type of electron microscope that produces images of a sample by scanning the surface with a focused beam of electrons. The electrons interact with atoms in the sample, producing various signals that contain information about the surface texture, morphology and composition of

the sample (Goula et al., 2016). Prior to SEM analysis, the catalysts were covered with Au/Pd for avoiding to interaction of electrons with the catalysts. SEM analyses were performed by using QUANTA 400F field-emission scanning Electron microscope.

4.3.4 Thermogravimetric Analysis (TGA)

TGA analysis measures the amount of weight change of a material, either as a function of increasing temperature or as a function of time at isothermal condition in an atmosphere of nitrogen, helium, air, other gas, or in vacuum. The measurements are generally used in temperature and weight change of decomposition reactions that allow quantitative composition analysis. The technique can characterize materials that exhibit weight loss or gain due to decomposition, oxidation, or dehydration (Sundari et al., 2012). TGA analysis was performed under air flow with a flow rate of 50 ml/min and a heating rate of 10°C/min in the temperature range of 25°C-1050°C to determine the amount of deposited coke on the used catalyst by using Shimadzu DTG-60H.

4.3.5 Diffuse Reflectance Infrared Fourier Transform Spectroscopy (DRIFTS)

DRIFTS analysis examines the surface chemistry of high surface area powders, particularly heterogeneous catalysis, where the temperature and environment of the catalyst can be controlled in-situ in the DRIFTS cell (Fuller et al., 1978; Accardo et al., 2014). Pyridine adsorption technique is used to determine the nature of acidity i.e., Lewis or Brønsted acid sites of the catalyst. Prior to the analysis, the catalysts are dried at 110℃, then all catalysts are left in the desiccator with approximately 30 ml of pyridine for 9 days for adsorption of pyridine vapour by the catalysts. After background KBr spectra are obtained, spectra of both fresh and pyridine adsorbed

catalysts are recorded in the mid-IR region (4000 – 450 cm^{-1}) by collecting 100 scans at 4 cm^{-1} resolution using a mirror velocity of 0.2 cm/s. The final spectra of the catalysts are obtained based on the differences between the fresh and pyridine adsorbed spectra. DRIFT analyses were performed by using Perkin Elmer Instruments Spectrum One FT-IR Spectrometer.

4.4 Activity Test of the Catalysts

In this section, the reaction system in which activity tests are carried out is detailed.

4.4.1 The Reaction System

A schematic diagram of the reaction system is demonstrated in Figure 4.1. The experimental setup consists of two stages: preparation of the catalysts for the reaction and the activity test of the catalyst. Catalysts are prepared for the reaction by performing the calcination and reduction steps with dry air and H_2 gases fed to the reactor using the bypass stream where the gas passes directly to vent without including condenser and gas chromatography (GC). On the other hand, the activity test of the catalyst is carried out using the reaction stream. Catalytic activity tests for glycerol steam reforming are performed in a conventional fixed-bed quartz reactor. The glycerol-water mixture is fed into the evaporator using a syringe pump. The mixture is heated in the evaporator to evaporate the mixture and subsequently mixed with 100% Ar flow. Heating tapes are used in the inlet and outlet streams of the reactor to prevent condensation of the feed and products. The bed temperature is heated by an electric furnace surrounding the reactor tube to reach the reaction temperature with 100% Ar flow as carrier gas. The gas products are cooled in the condenser with the water bath and then the liquid products are collected. The overall flow rate is measured using a soap bubble meter during the reaction, and the gas composition of the reactor's effluent is analysed online at the same time interval

using gas chromatography (GC) (Schimadzu GC-2010 Plus) equipped with a thermal conductivity detector (TCD) (Carboxen 1010 Plot column with 0.53 mm inside diameter (ID) and 30 m length). Ar was used as a carrier gas in GC. Liquid products in the condensate are manually identified in GC using Rt- Q-Bond column with 0.53 mm inside diameter (ID) and 30 m length by using He as a carrier gas. Finally, all the gases produced are sent to the atmosphere.

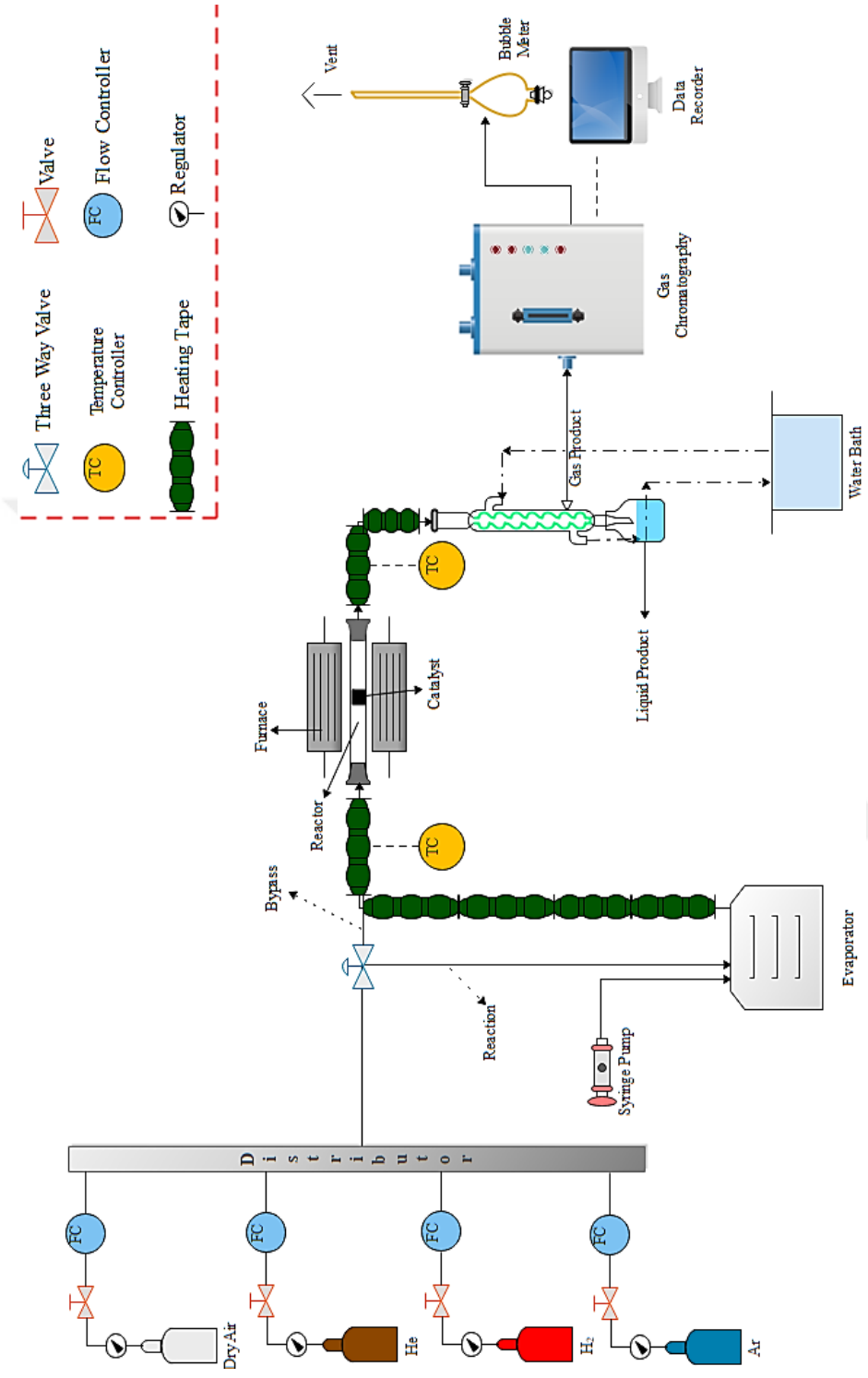

Figure 4.1 Schematic Representation of Glycerol Steam Reforming Experimental Setup

4.4.1.1 Experimental Procedure

First, 0.15 g of catalyst is weighed and placed inside the quartz reactor, and supported by ceramic wool. The reactor is inserted in a tubular furnace. Then, the setup is controlled for leakage with 100% Ar flow. The catalyst bed is heated by an electric furnace enclosed the reactor tube with 100% Ar flow to reach the reaction temperature with a heating rate of 10°C/min. Then, the condenser is set to -10^{o}C and the heating tapes of reactor outlet stream to 190^{o}C. When the furnace and heating tapes of the reactor outlet stream reach to the set temperatures, heating tapes of reactor inlet stream and evaporator are set to 300^{o}C and at the same time the analysis method is loaded into GC. The glycerol-water mixture is then fed to the evaporator by a syringe pump and mixed with %100 Ar flow in the evaporator. Liquid products are collected from the bottom of the condenser while gas products are analysed in GC with the same time interval (21.85 min) during the reaction and then sent to the atmosphere. At the end of the experiment period (5 h), the final volume is set in the syringe pump and turned off, then the shutdown method is loaded into GC and gas and liquid detectors are allowed to cool down to 50^{o}C. Then GC, He flow, condenser and furnace are turned off. Subsequently, the evaporator and heating tapes are turned off. Finally, the Ar flow is turned off.

The experimental conditions for glycerol steam reforming were given in Table 4.3.

The method conditions in GC for gas and liquid analyses were given in Table 4.4 and Table 4.5, respectively.

Table 4.3 All Parameters Tested in GSR

Catalyst	***T_{rxn} (^oC)***	***W/G (molar)***	***FFR (ml/h)***
10Ni/SA(1035)(1035)	965	3	0.8
			0.9
			1.0
10Ni/SA(700)(1035)	470	3	0.9
	500		
	540		
	610		
	680	1	
		3	
		6	
		9	
	755	3	
	825		
	895		
	965		
	1035		
	470	9	
	550		
10Ni/SA(700)(1035)-wet	470		
	550		
	680		
Metal Loaded Catalysts	550		

Table 4.4 Analysis conditions of GC for gaseous products

Column Oven Temperature (ºC)	250
Injection Temperature (ºC)	200
Detector Type and Temperature (ºC)	TCD-250
Column Pressure (psi)	3.89
Analysis Time (min)	21.85
Carrier Gas and Flow Rate (ml/min)	Ar-50
Split Ratio	1/1

Table 4.5 Analysis conditions of GC for liquid products

Column Oven Temperature (ºC)	250
Injection Temperature (ºC)	200
Detector Type and Temperature (ºC)	TCD-250
Column Pressure (psi)	3.89
Analysis Time (min)	21.85
Carrier Gas and Flow Rate (ml/min)	He-258
Split Ratio	1/50

The analysis in GC is completed by starting the oven temperature at 35ºC, keeping it at this temperature for 7.50 minutes and then reaching 250ºC at 21.85 minutes with a heating rate of 23ºC/min.

CHAPTER 5

RESULTS AND DISCUSSION

Within the scope of this study, the experiments were carried out considering both thermodynamic analysis and studies related to glycerol steam reforming. On the one hand, considering the effect of W/G ratio according to thermodynamic analysis, it is deduced that as the W/G ratio increases, the mole fractions of both hydrogen and carbon monoxide increase whereas mole fractions of both methane and carbon dioxide decrease. Furthermore, high operating temperatures favour the hydrogen formation. Increase in temperature decreases the formation of CO_2 and CH_4, while slightly increases the CO formation. According to the thermodynamic analysis, the reaction operating conditions were selected considering the high amount of hydrogen formation and low amount of methane, carbon monoxide and carbon dioxide formation. There are various operating conditions to achieve this goal. Thus, the experiments were carried out at 450-1050^oC with the W/G molar ratios of 1, 3, 6, & 9 at 0.8, 0.9, & 1.0 ml/h water-glycerol feed flow rates and 30 ml/min Ar flow rate in the presence of 0.15 g catalyst under atmospheric pressure. The effect of reaction parameters such as temperature, feed ratio, and feed flow rate on H_2 yield were examined in the presence of 10% by weight nickel loaded silica aerogel synthesized by co-precipitation technique. Moreover, the effect of catalyst synthesis technique on H_2 yield was examined in the presence of 10% by weight nickel loaded silica aerogels synthesized by both co-precipitation and wet-impregnation techniques. In addition, the effects of metal amount and mono, bi & trimetal type on H_2 yield were also examined. For this reason, 2.5, 5, 8 and 10% by weight of Ni loaded silica aerogels were tested to examine the effect of metal amount. In addition to Ni, promising active metals such as Co, Cr, Zr, Mo and Ag were loaded onto silica

aerogel by 10% by weight in order to examine the effect of metal type on H_2 yield. To examine the bi & trimetal effect, Ni-Ru, Ni-Mo, Ni-Mg, Ni-Fe and Ni-Fe-Mn loaded silica aerogels were synthesized in dominance of Ni following co-precipitation technique. All the catalysts were calcined under dry air for 5h and reduced under H_2 flow for half an hour and then tested. The activity performances of various metal loaded catalysts were performed at 550^oC with a W/G molar ratio of 9, which is the highest H_2 yield conditions according to thermodynamic analysis. On the other hand, according to the studies on glycerol steam reforming, there is no evidence that silica aerogel is used as a catalyst support, which makes the study unique. In other words, silica aerogel was used as a catalyst support for the first time in glycerol steam reforming.

In all experiments, the outlet gas stream contained hydrogen, carbon monoxide, carbon dioxide and methane whereas the liquid products, collected from the bottom of the condenser, generally contained almost solely water. The conversion of glycerol and hydrogen yield were obtained based on the analysis of both gas and liquid products. Apart from these, coke deposition in the catalyst and purity of produced hydrogen were taken into consideration as crucial factors.

In addition, chemical and physical properties of fresh and used catalysts were determined using some characterization techniques such as N_2 Physisorption, XRD, SEM, DRIFTS, and TGA.

5.1 Characterization Results of the Catalysts

Surface area and porosity, bulk solid structure, surface morphology, particle size, mechanical strength, crystallite size, activity, selectivity and stability of the catalysts were examined with the aid of some of characterization techniques, such as N_2 Physisorption, X-Ray Diffraction (XRD), Scanning Electron Microscopy (SEM) and Diffuse Reflectance Infrared Fourier Transform Spectroscopy (DRIFTS).

5.1.1 N_2 Physisorption Analysis

In this part, N_2 Physisorption analyses of silica aerogel and various metal loaded silica aerogels were examined.

5.1.1.1 Silica Aerogel and Nickel Loaded Silica Aerogels

N_2 Physisorption isotherms and pore size distributions of pure silica aerogel and 2.5%, 5%, 8%, and 10% by weight of nickel loaded silica aerogels were depicted in Figures 5.1-5.2.

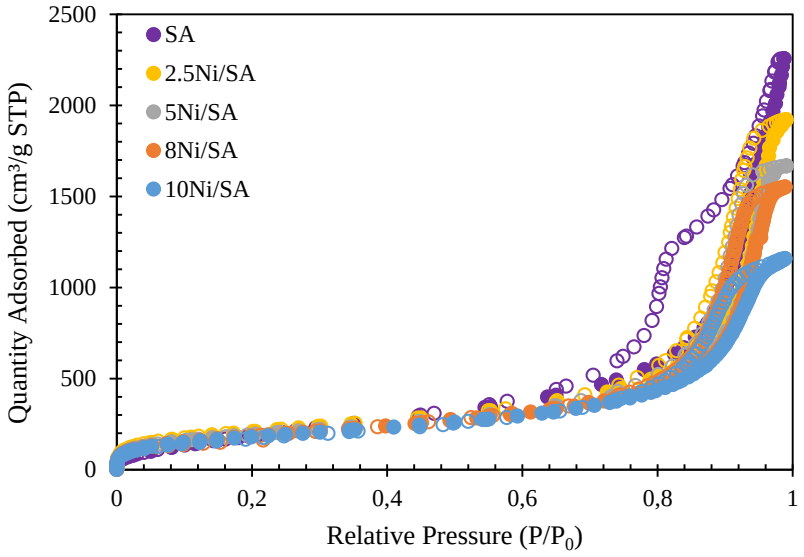

Figure 5.1 N_2 Physisorption Isotherms of Pure SA and Ni Loaded Silica Aerogels (Filled Symbols: Adsorption Branch, Empty Symbols: Desorption Branch)

According to Figure 5.1, it is clear that nickel loaded silica aerogels exhibited similar behaviour, unlike pure silica aerogel. Pure silica aerogel exhibited type IV isotherm with H3 type hysteresis loop according to the Brunauer-Deming-Deming-Teller (BDDT) classification in accordance with the literature (Sivri et al., 2019), which is characteristic of mesoporous materials (Lowell, 2006; Wang et al., 2020). However,

the adsorbed volume of N_2 decreased with an increase in metal amount. Nickel loading also changed the pore structure, resulting in a change in hysteresis loops from H3 to H1, expressing a narrower pore size distribution range. However, there was no change in the shape of isotherm representing type IV.

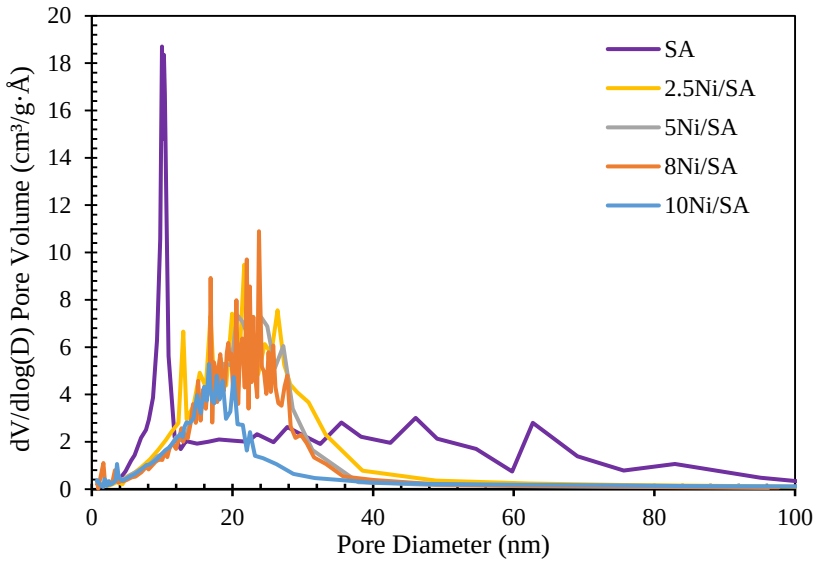

Figure 5.2 Pore Size Distributions of Pure SA and Ni Loaded Silica Aerogels

According to Figure 5.2, silica aerogel contains both mesopores and macropores. However, when nickel was loaded onto the silica aerogel, the macropores vanished, only mesopores remained. This is due to the fact that nickel accommodates into the pores of silica aerogel, which resulted not only in a reduction in the pore size of the macropores but also in the clogging of the pores. The physical properties of pure silica aerogel, 2.5Ni/SA, 5Ni/SA, 8Ni/SA and 10Ni/SA catalysts were given in Table 5.1. Additionally, due to the location of Ni particles into meso and macropores of silica aerogel the increase in nickel amount decreases the BET surface area, pore diameter and pore volume of the catalysts, which may result in an increase in microporosity.

Table 5.1 Physical Properties of Ni Loaded Silica Aerogels

Catalyst	Multi-point BET Surface Area (m^2/g)	BJH Desorption Cumulative Volume of Pores (cm^3/g)	BJH Desorption Average Pore Diameter (nm)	Microporosity (%)
SA	806±46	3.56±0.18	10.9±0.4	3.65±0.14
2.5Ni/SA	749	2.98	10.2	6.90
5Ni/SA	698	2.58	9.3	6.63
8Ni/SA	670	2.40	9.6	7.05
10Ni/SA	602	1.64	7.1	8.12

5.1.1.2 Monometal Loaded Silica Aerogels

Besides nickel, 10% by weight of cobalt, chromium, zirconium, molybdenum and silver were loaded onto the silica aerogel by co-precipitation method.

N_2 physisorption isotherms and pore size distributions of 10% by weight of Co, Zr and Cr loaded silica aerogels were shown in Figures 5.3-5.4.

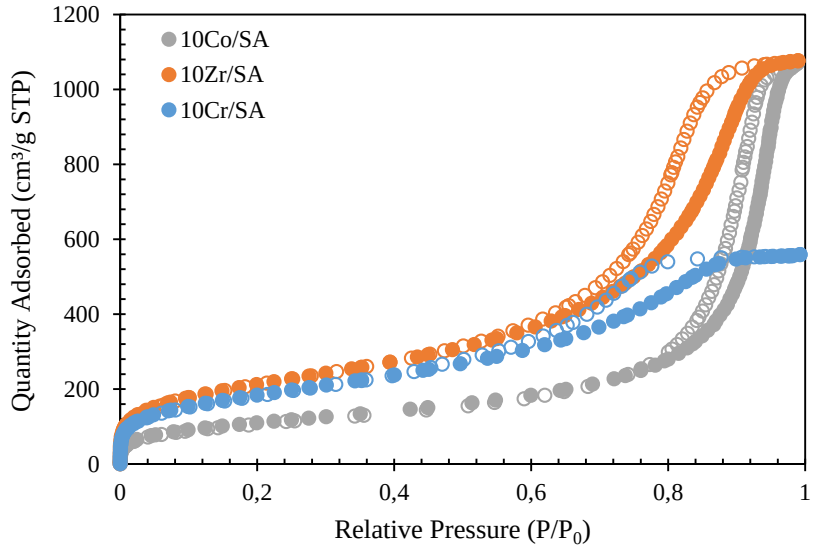

Figure 5.3 N_2 Physisorption Isotherms of 10Co/SA, 10Zr/SA and 10Cr/SA (Filled Symbols: Adsorption Branch, Empty Symbols: Desorption Branch)

According to Figure 5.3, Co, Zr and Cr loaded silica aerogels exhibited type IV isotherm, which is characteristic of mesoporous materials. All catalysts displayed similar behaviour with nickel-based catalysts as changing the hysteresis loop of pure silica aerogel from H3 to H1, expressing a narrower pore size distribution range.

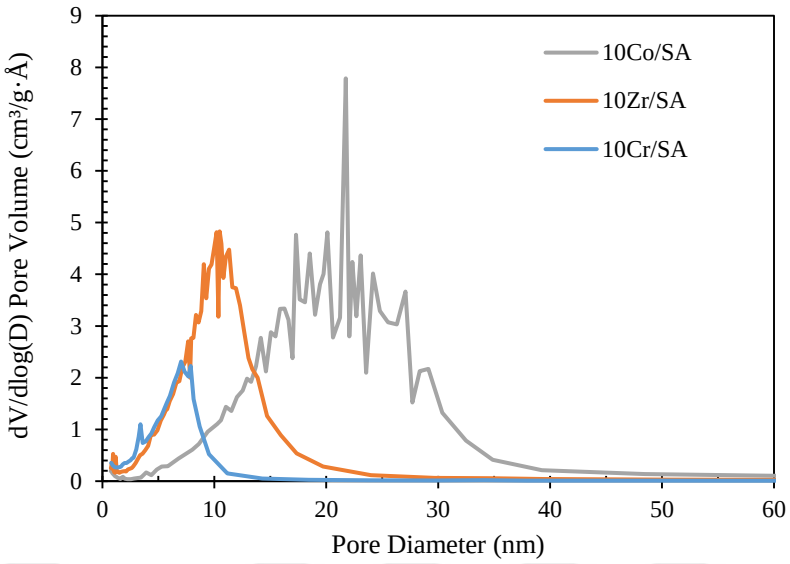

Figure 5.4 Pore Size Distributions of 10Co/SA, 10Zr/SA and 10Cr/SA

According to Figure 5.4, Co, Zr and Cr-based catalysts mainly contain mesopores. The physical properties of pure SA, 10Co/SA, 10Cr/SA and 10Zr/SA catalysts were given in Table 5.2. Compared to pure silica aerogel, the presence of metals decreased the BET surface area, pore volume and pore diameter of the catalysts, indicating that the clogging of the pores by the accommodation of the metals into the pores of silica aerogel.

Table 5.2 Physical Properties of 10Co/SA, 10Zr/SA and 10Cr/SA

Catalyst	Multi-point BET Surface Area (m^2/g)	BJH Desorption Cumulative Volume of Pores (cm^3/g)	BJH Desorption Average Pore Diameter (nm)	Microporosity (%)
SA	806±46	3.56±0.18	10.9±0.4	3.65±0.14
10Co/SA	398	1.66	10.6	5.82
10Zr/SA	763	1.67	5.6	10.12
10Cr/SA	663	0.88	3.5	17.11

N_2 physisorption isotherms and pore size distributions of calcined silica aerogel and 10% by weight of Mo and Ag loaded silica aerogels were depicted in Figures 5.5-5.8.

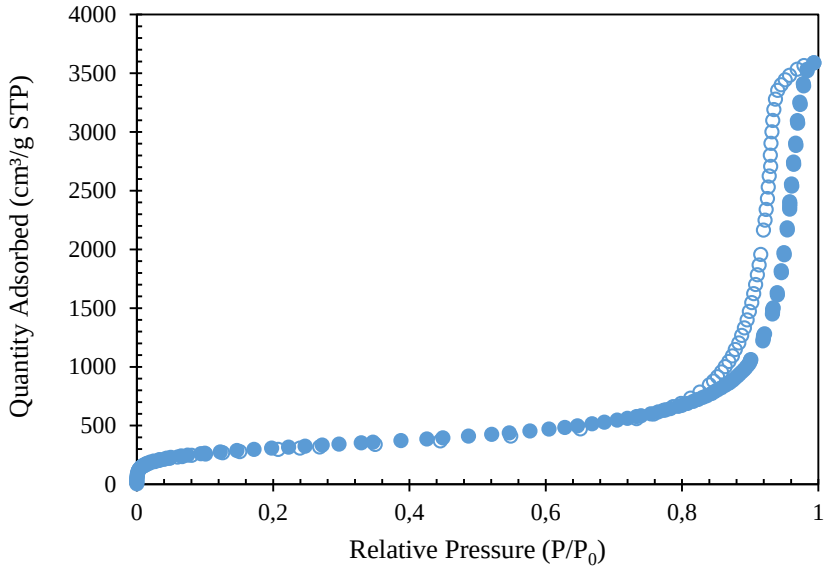

Figure 5.5 N_2 Physisorption Isotherm of Calcined SA

(Filled Symbols: Adsorption Branch, Empty Symbols: Desorption Branch)

According to Figure 5.5, calcined silica aerogel exhibited type IV isotherm representing mesoporous materials. Different from uncalcined silica aerogel (Figure 5.1), calcined silica aerogel indicated H1 hysteresis loop in accordance with the literature (Sivri et al., 2019). The reason for the change in hysteresis type in silica aerogel was ascribed to change in the pore structure due to the removal of methyl (CH_3) groups in the aerogel structure during the heat treatment in the calcination process.

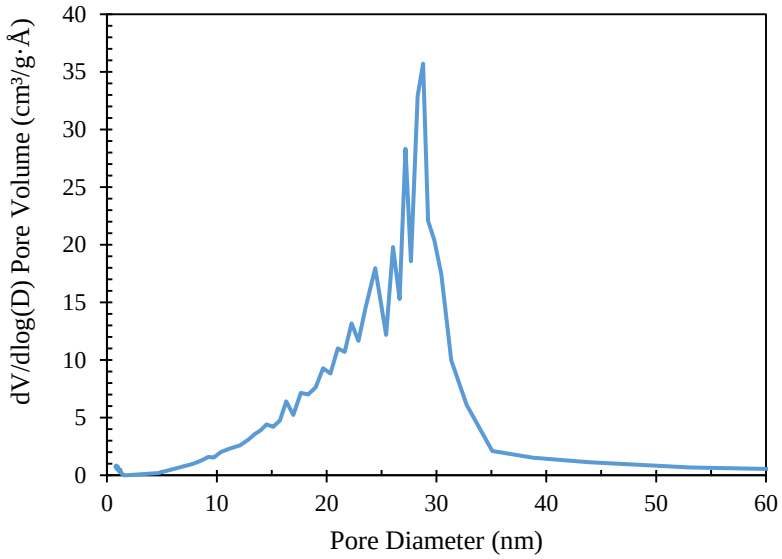

Figure 5.6 Pore Size Distributions of Calcined SA

According to Figure 5.6, it is clear that calcination process leads to an increase in pore diameter of the silica aerogel compared to the uncalcined silica aerogel (Figure 5.2).

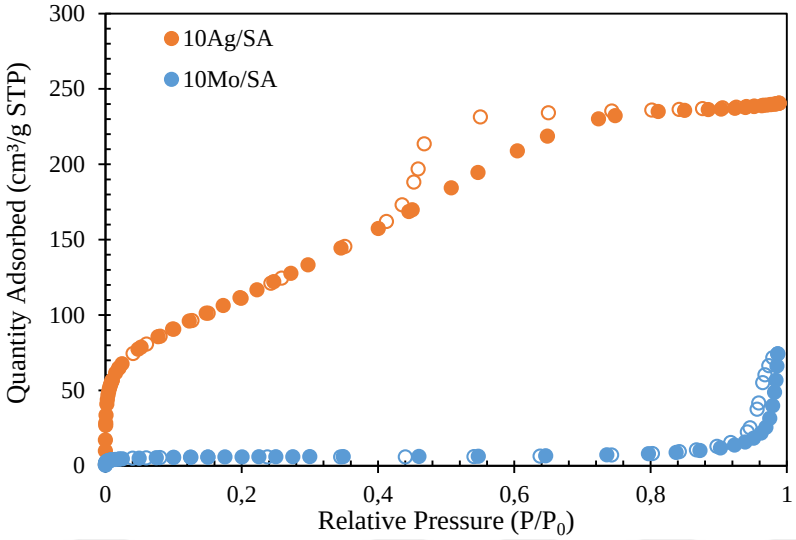

Figure 5.7 N_2 Physisorption Isotherms of 10Mo/SA and 10Ag/SA
(Filled Symbols: Adsorption Branch, Empty Symbols: Desorption Branch)

According to Figure 5.7, molybdenum and silver loaded silica aerogels exhibited type IV isotherm, representing mesoporous materials. Loading of silver and molybdenum precursors onto calcined silica aerogels resulted in a change in the pore structure of the catalysts. The hysteresis loops of Ag and Mo-based catalysts refer to H2 and H3 hysteresis loops, respectively.

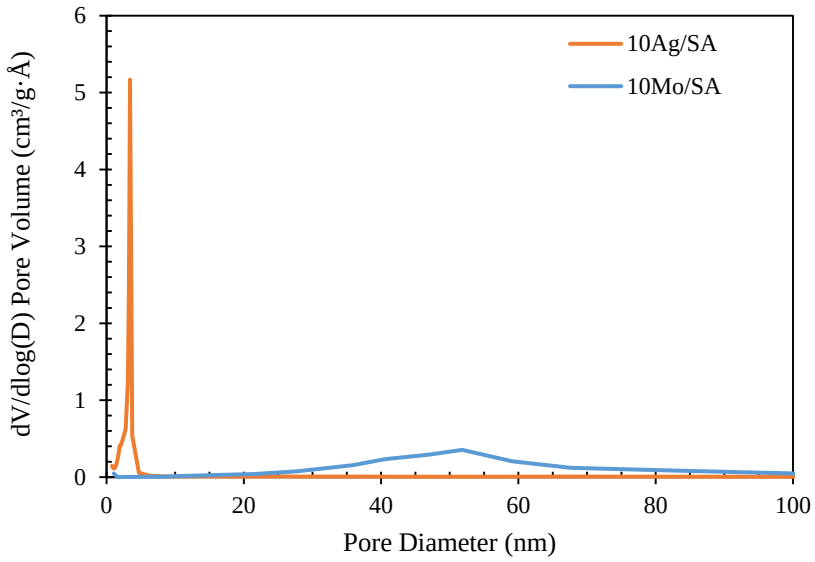

Figure 5.8 Pore Size Distributions of 10Mo/SA and 10Ag/SA

According to Figure 5.8, pore size distributions of Ag and Mo-based catalysts vary. On the one hand, Ag loading reduces the pore size of the silica aerogel and contains mainly mesopores, on the other hand, Mo loading increases the pore size and contains both meso and macropores. The physical properties of calcined silica aerogel, 10Ag/SA and 10Mo/SA were given in Table 5.3. The unexpected behaviour of the Mo-based catalyst is ascribed to its high tendency to sinter, resulting in a decrease in BET surface area and an increase in BJH pore diameter. It is also said that loading of metals causes a significant decrease in pore volume, attributed to the clogging of pores.

Table 5.3 Physical Properties of Calcined SA, 10Mo/SA and 10Ag/SA

Catalyst	Multi-point BET Surface Area (m^2/g)	BJH Desorption Cumulative Volume of Pores (cm^3/g)	BJH Desorption Average Pore Diameter (nm)	Microporosity (%)
Calcined SA	1080	5.53	13.2	8.27
10Mo/SA	18	0.12	15.5	20.73
10Ag/SA	423	0.38	2.4	23.76

5.1.1.3 Bi and Trimetal Loaded Silica Aerogels

In addition to the monometal-based catalysts, nickel-dominated Ni-Mo, Ni-Ru, Ni-Mg, Ni-Fe and Ni-Fe-Mn loaded bi and trimetals were loaded onto silica aerogels by co-precipitation method.

N_2 physisorption isotherms and pore size distributions of 8% by weight of nickel and 2% by weight of molybdenum loaded silica aerogels were shown in Figures 5.9-5.10.

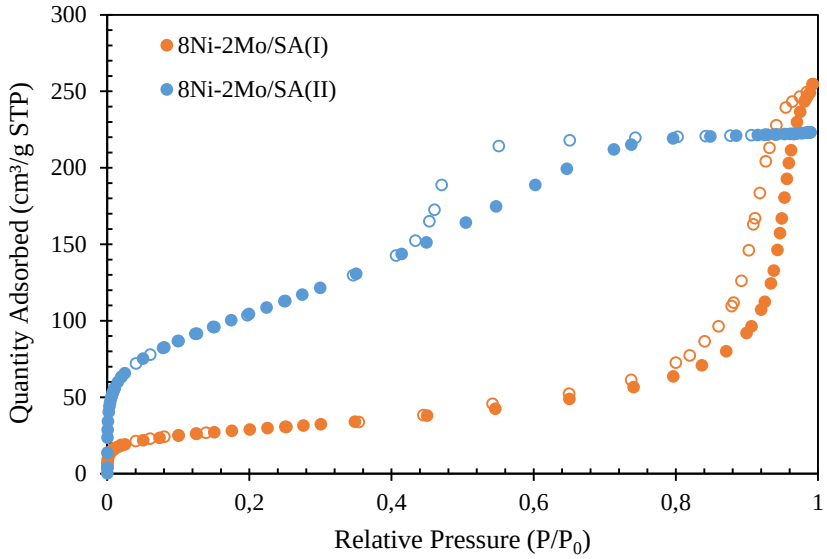

Figure 5.9 N_2 Physisorption Isotherms of 8Ni-2Mo/SA(I) and 8Ni-2Mo/SA(II) (Filled Symbols: Adsorption Branch, Empty Symbols: Desorption Branch)

According to Figure 5.9, Ni-Mo bimetallic catalysts synthesized by two different metal loading paths exhibited type IV isotherm representing mesoporous materials. Due to the metal loading paths of the catalysts, the hysteresis loops differed. 8Ni-2Mo/SA(I) exhibited H1 hysteresis loop whereas 8Ni-2Mo/SA(II) exhibited H2 hysteresis loop. Although, the same metal type and metal amount are loaded onto silica aerogels, the reason for the hysteresis types difference is attributed to the change in pore structure along the synthesis paths. In two-step metal loading path (I), Ni was first placed into the pores of the silica aerogel and then Mo was placed into the pores of calcined Ni loaded silica aerogel. However, in simultaneous metal loading path (II), the metals were simultaneously loaded onto calcined silica aerogel, causing the two metals to accommodate in the pores together or separately.

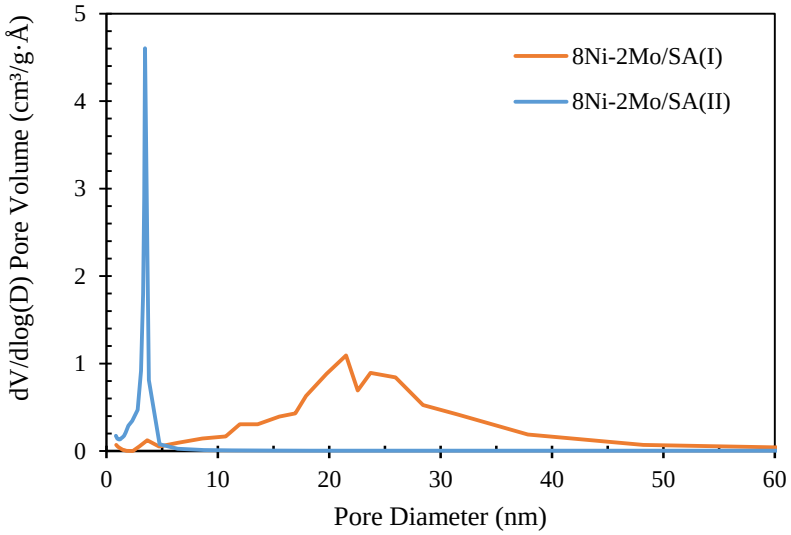

Figure 5.10 Pore Size Distributions of 8Ni-2Mo/SA(I) and 8Ni-2Mo/SA(II)

According to Figure 5.10, both catalysts mainly contained mesopores, but in different sizes due to the following of different metal loading paths. Larger diameter and smaller area were obtained in path I compared to path II. The physical properties of 8Ni-2Mo/SA(I) and 8Ni-2Mo/SA(II) were given in Table 5.4.

Table 5.4 Physical Properties of 8Ni-2Mo/SA(I) and 8Ni-2Mo/SA(II)

Catalyst	**Multi-point BET Surface Area (m^2/g)**	**BJH Desorption Cumulative Volume of Pores (cm^3/g)**	**BJH Desorption Average Pore Diameter (nm)**	**Microporosity (%)**
8Ni-2Mo/SA(I)	101	0.40	10.8	9.01
8Ni-2Mo/SA(II)	383	0.36	2.5	25.14

N_2 physisorption isotherms and pore size distributions of 10% by weight of nickel and 3% by weight of magnesium, 10% by weight of nickel and 3% by weight of iron, and 10% by weight of nickel, 3% by weight of iron and 0.3% by weight of manganese loaded silica aerogels were indicated in Figures 5.11-5.12.

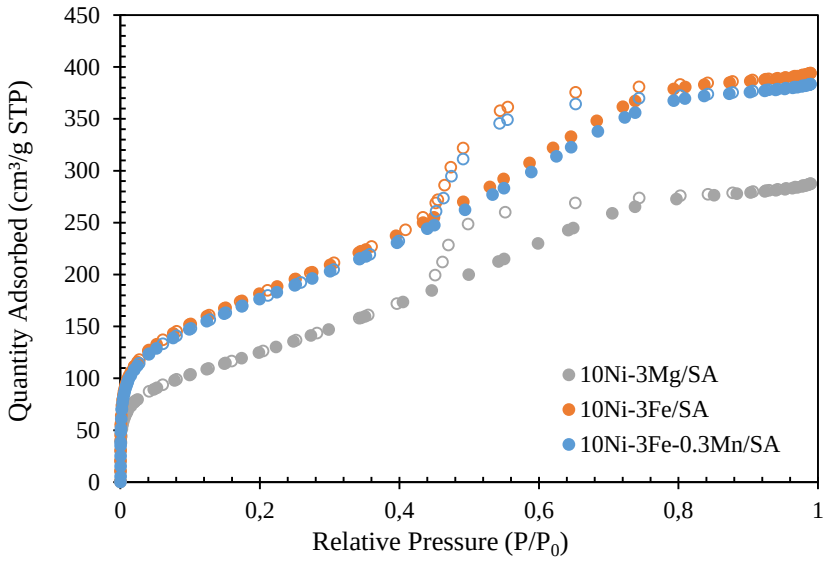

Figure 5.11 N_2 Physisorption Isotherms of 10Ni-3Mg/SA, 10Ni-3Fe/SA and 10Ni-3Fe-0.3Mn/SA

(Filled Symbols: Adsorption Branch, Empty Symbols: Desorption Branch)

According to Figure 5.11, 10Ni-3Mg/SA, 10Ni-3Fe/SA, and 10Ni-3Fe-0.3Mn/SA bi and trimetallic catalysts synthesized by following Path I of Ni-Mo metal loading, exhibited type IV isotherms, which is characteristic of mesoporous material. All catalysts displayed H2 hysteresis loops. Moreover, the almost identical isotherms of 10Ni-3Fe and 10Ni-3Fe-0.3Mn were attributed to the fact that the addition of a small amount of Mn did not significantly affect the properties of 10Ni-3Fe/SA.

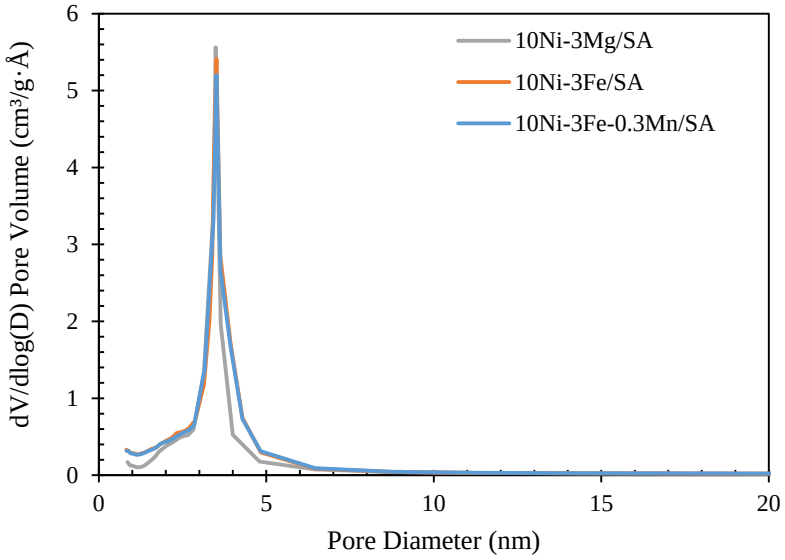

Figure 5.12 Pore Size Distributions of 10Ni-3Mg/SA, 10Ni-3Fe/SA and 10Ni-3Fe-0.3Mn/SA

According to Figure 5.12, pore size distributions of the catalysts are quite similar and mostly contain mesopores. The physical properties of 10Ni-3Mg/SA, 10Ni-3Fe/SA and 10Ni-3Fe-0.3Mn/SA were given in Table 5.5.

Table 5.5 Physical Properties of 10Ni-3Mg/SA, 10Ni-3Fe/SA and 10Ni-3Fe-0.3Mn/SA

Catalyst	**Multi-point BET Surface Area (m^2/g)**	**BJH Desorption Cumulative Volume of Pores (cm^3/g)**	**BJH Desorption Average Pore Diameter (nm)**	**Microporosity (%)**
10Ni-3Mg/SA	463	0.46	2.8	24.26
10Ni-3Fe/SA	657	0.63	2.6	25.35
10Ni-3Fe-0.3Mn/SA	638	0.61	2.6	25.31

N_2 Physisorption isotherms and pore size distributions of 10% by weight of nickel and 1-3% by weight of ruthenium loaded silica aerogels were depicted in Figures 5.13-5.14.

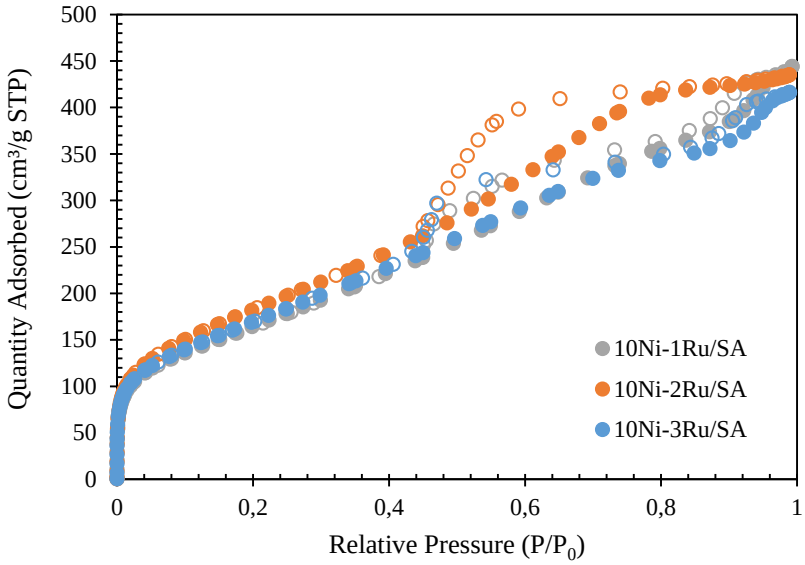

Figure 5.13 N_2 Physisorption Isotherms of 10Ni-1Ru/SA, 10Ni-2Ru/SA and 10Ni-3Ru/SA

(Filled Symbols: Adsorption Branch, Empty Symbols: Desorption Branch)

According to Figure 5.13, 10Ni-1Ru/SA, 10Ni-2Ru/SA and 10Ni-3Ru/SA bimetallic catalysts exhibited type IV isotherms, which is characteristic of mesoporous material. 10Ni-2Ru/SA displayed H2 hysteresis loop, while 10Ni-1Ru/SA and 10Ni-3Ru/SA displayed both H1 and H2 hysteresis loops, indicating bimodal pore size distribution. H1 hysteresis loop can be associated with exhibiting non-constrictions in pore channels containing relatively uniform pores, whereas the H2 hysteresis type occurs in a network of ink-bottle pores where capillary condensate evaporates from an ink-bottle network. This means that desorption from the pore body may only occur after the neck has been emptied. This type of hysteresis loop is generally regarded as a sign of a percolation process occurring during the emptying of disordered porous material consisting of cavities connected by constrictions (Grosman et al., 2008). In

addition, the H2 type can be observed in a network where the neck size distribution is much narrower than the size distribution of the main cavities. The two-step desorption isotherm is consistent with a structure of both open and blocked mesopores, indicating that both equilibrium evaporation/desorption and pore blocking/cavitation effects occur (Thommes 2010).

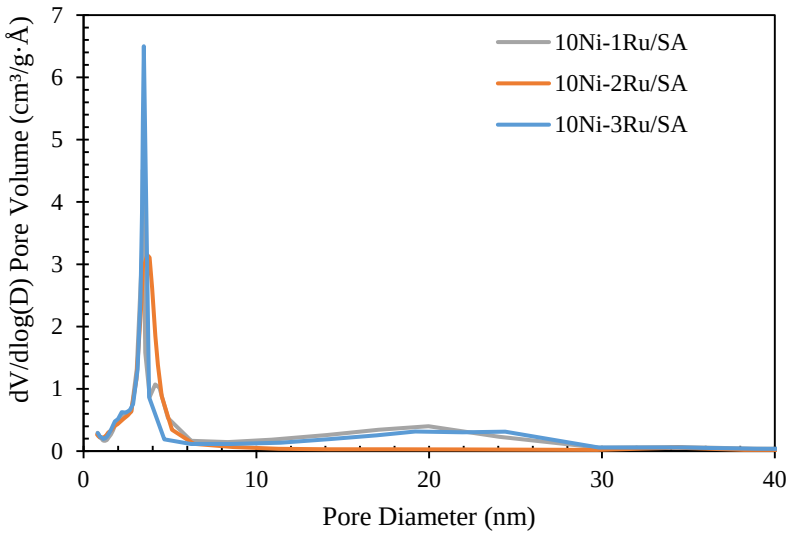

Figure 5.14 Pore Size Distributions of 10Ni-1Ru/SA, 10Ni-2Ru/SA and 10Ni-3Ru/SA

According to Figure 5.14, pore size distributions of Ni-Ru-based catalysts mainly contain mesopores. Existence of two types of hysteresis in both 10Ni-1Ru/SA and 10Ni-3Ru/SA is consistent with pore size distribution. The existence of two peaks in the pore size distribution curve can be attributed to the different mechanisms of pore structure formation (Zhang et al., 2019) consistent with the presence of two distinct hysteresis loops consisting of both narrower and wider pores. The physical properties of 10Ni/SA, 10Ni-1Ru/SA, 10Ni-2Ru/SA and 10Ni-3Ru/SA were given in Table 5.6. The presence of additional metals decreased the pore volume and pore diameter of the catalysts compared to 10Ni/SA.

Table 5.6 Physical Properties of 10Ni/SA, 10Ni-1Ru/SA, 10Ni-2Ru/SA and 10Ni-3Ru/SA

Catalyst	Multi-point BET Surface Area (m^2/g)	BJH Desorption Cumulative Volume of Pores (cm^3/g)	BJH Desorption Average Pore Diameter (nm)	Microporosity (%)
10Ni/SA	603	1.64	7.1	8.12
10Ni-1Ru/SA	606	0.69	3.2	21.03
10Ni-2Ru/SA	669	0.69	2.8	22.11
10Ni-3Ru/SA	624	0.66	2.9	22.81

Among all catalysts, the highest BET surface area was obtained in 10Zr/SA, while the lowest BET surface area was obtained in 10Mo/SA. The BET surface areas of all catalysts increase in the following order:

10Mo<8Ni-2Mo(I)<8Ni-2Mo(II)<10Co<10Ag<10Ni-3Mg<10Ni<10Ni-1Ru <10Ni-3Ru<10Ni-3Fe-0.3Mn<10Ni-3Fe<10Cr<10Ni-2Ru<8Ni<5Ni<2.5Ni<10Zr.

In addition, considering the desorption average pore diameter of the catalysts, the highest pore diameter was obtained in 10Mo/SA; however, the lowest desorption average pore diameter was obtained in 10Ag/SA. The BJH desorption average pore diameter of all catalysts increases in the following order:

10Ag<8Ni-2Mo(II)<10Ni-3Fe<10Ni-3Fe-0.3Mn<10Ni-2Ru<10Ni-3Mg<10Ni-3Ru <10Ni-1Ru<10Cr<10Zr <10Ni<5Ni<8Ni<2.5Ni<10Co<8Ni-2Mo(II)<10Mo.

5.1.2 X-Ray Diffraction (XRD) Analysis of the Catalysts

In this part, XRD analysis of various metal loaded silica aerogels was examined. According to the XRD patterns, the phases of catalysts were identified using PDF Cards of the metal and/or metal oxide and/or bimetallic forms given in Appendix B. In addition, the crystallite sizes of metals were calculated using Scherrer Equation, explicitly explained in Appendix C.

5.1.2.1 Nickel Loaded Silica Aerogels

XRD patterns of various amounts of Ni loaded silica aerogels were depicted in Figure 5.15. Around 22.0º silica appears as a broad peak due to its amorphous structure (Sarıyer, 2018; Musić et al., 2011). The peaks at 2Θ value of 44.4, 51.7, 76.1º in 2.5Ni/SA, the peaks at 2Θ value of 44.5, 51.9, 76.2º in 5Ni/SA, the peaks at 2Θ value of 44.5, 51.5, 76.4º in 8Ni/SA, the peaks at 2Θ value of 44.6, 51.9, 76.6º in 10Ni/SA and the peaks at 2Θ value of 44.4, 51.8, 76.3º in 10Ni/SA-wet correspond to metallic-nickel in accordance with Ni PDF Card (No: 00-004-0850) (Table B.1 in Appendix B). In addition to the metallic-nickel phase, the peaks at 2Θ value of 37.6, 43.6 and 62.5º in 8Ni/SA and the peaks at 2Θ value of 37.2, 43.2 and 62.9º in 10Ni/SA-wet correspond to nickel oxide in accordance with NiO PDF Card (No: 01-089-5881) (Table B.2 in Appendix B).

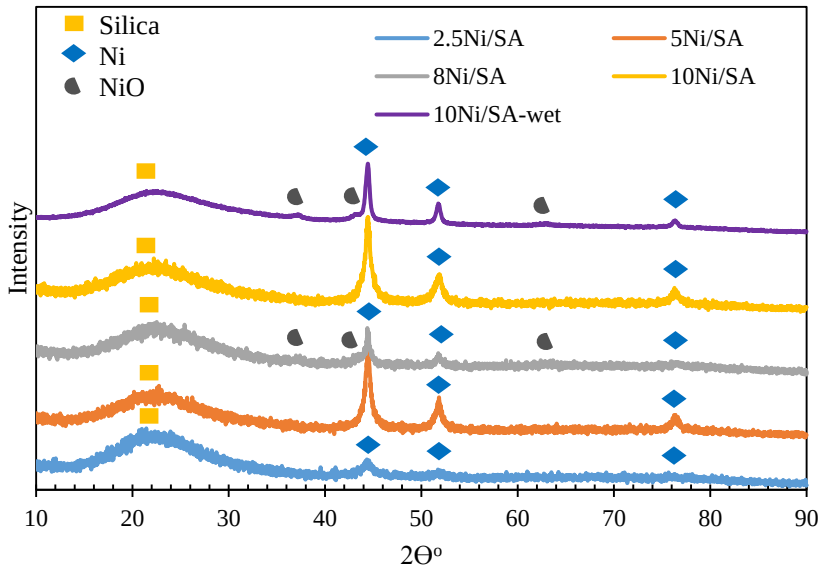

Figure 5.15 XRD Patterns of Various Amounts of Ni Loaded Silica Aerogels

Crystallite sizes of the catalysts were calculated using Scherrer Equation at d_{100} peak of each and tabulated in Table 5.7.

Table 5.7 Crystallite Sizes of Ni Loaded Silica Aerogels

Catalyst	**2θ (°)**	**Phase**	**$t_{crystallite\ size}$ (nm)**
2.5Ni/SA	44.4	Ni^o	7.2
5Ni/SA	44.5	Ni^o	8.8
8Ni/SA	44.5	Ni^o	16.8
10Ni/SA	44.6	Ni^o	12.3
10Ni/SA-wet	44.4	Ni^o	19.0

5.1.2.2 Monometal Loaded Silica Aerogels

XRD patterns of various metal loaded silica aerogels were indicated in Figure 5.16. In all catalysts, around 22.2º silica appears as a broad peak due to its amorphous structure (Sarıyer, 2018; Musić et al., 2011). In 10Ni/SA, the peaks at 2Θ value of 44.6, 51.9, 76.6º correspond to metallic-nickel in accordance with Ni PDF Card (No: 00-004-0850) (Table B.1 in Appendix B). Similar to Ni, in 10Co/SA, the peaks at 2Θ value of 44.3, 51.6, 75.9º correspond to metallic-cobalt in accordance with Co PDF Card (No: 00-015-0806) (Table B.3 in Appendix B). In 10Zr/SA, only peak was observed at 2Θ value of 30.7º referring to ZrO_2 in accordance with ZrO_2 PDF Card (No: 00-002-0733) (Table B.8 in Appendix B). In 10Ag/SA, the peaks at 2Θ value of 38.1, 44.3, 64.4, 77.4 and 81.7º refer to metallic-silver in accordance with Ag PDF Card (No: 00-004-0783) (Table B.11 in Appendix B). In 10Cr/SA, the peaks at 2Θ value of 24.5, 33.6, 36.2, 41.5, 50.1, 54.8, 63.4 and 65.1º correspond to Cr_2O_3 in accordance with Cr_2O_3 PDF Card (No: 00-038-1479) (Table B.6 in Appendix B). In Mo/SA, the peaks at 2Θ value of 26.0, 37.0 and 53.4º correspond to MoO_2 in accordance with MoO_2 PDF Card (No: 01-086-0135) (Table B.10 in Appendix B) whereas at 40.5, 58.6, 73.6 and 87.6º correspond to metallic-molybdenum in accordance with Mo PDF Card (No: 00-042-1120) (Table B.9 in Appendix B).

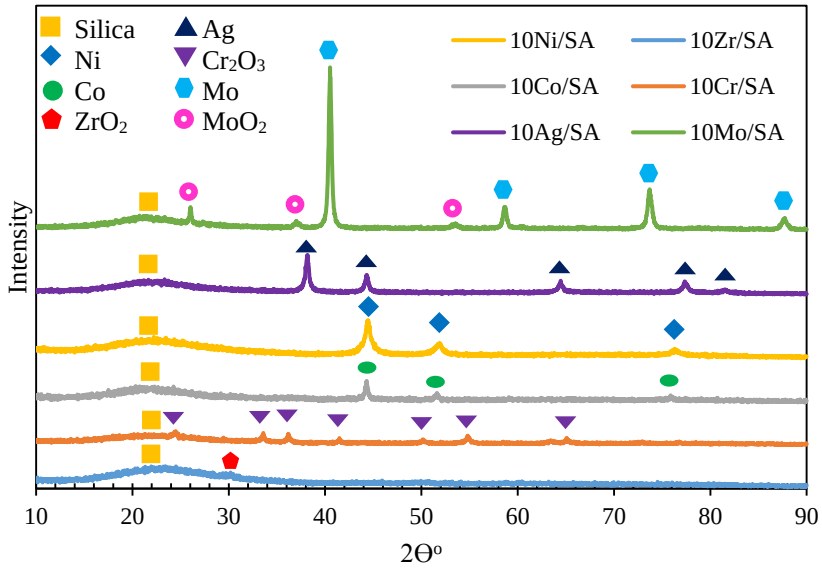

Figure 5.16 XRD Patterns of Monometal Loaded Silica Aerogels

Crystallite sizes of the catalysts were calculated using Scherrer Equation at d_{100} peak of each and tabulated in Table 5.8.

Table 5.8 Crystallite Sizes of Monometal Loaded Silica Aerogels

Catalyst	**2θ (°)**	**Phase**	**$t_{crystallite\ size}$ (nm)**
10Ni/SA	44.6	Ni^o	12.3
10Co/SA	44.3	Co^o	30.3
10Ag/SA	38.1	Ag^o	22.3
10Mo/SA	40.5	Mo^o	25.0

5.1.2.3 Bi and Trimetal Loaded Silica Aerogels

XRD patterns of Ni&Mo loaded silica aerogels synthesized by two-step metal loading (I) and simultaneous metal loading (II) paths were indicated in Figure 5.17.

In both catalysts, around 21.8º silica appears as a broad peak due to its amorphous structure (Sarıyer, 2018; Musić et al., 2011). In 8Ni-2Mo/SA(I), the peaks at 2Θ value of 40.6, 58.6, 73.7 and 88.2º and in 8Ni-2Mo/SA(II), the peaks at 2Θ value of 40.6, 58.6, 73.8 and 87.7º correspond to metallic-molybdenum in accordance with Mo PDF Card (No: 00-042-1120) (Table B.9 in Appendix B). In addition, the peaks at 2Θ value of 43.4 and 51.0º in 8Ni-2Mo/SA(I) and the peaks at 2Θ value of 43.4 and 50.6º in 8Ni-2Mo/SA(I) correspond to molybdenum-nickel in accordance with $MoNi_4$ PDF Card (No: 03-065-1533) (Table B.10 in Appendix B).

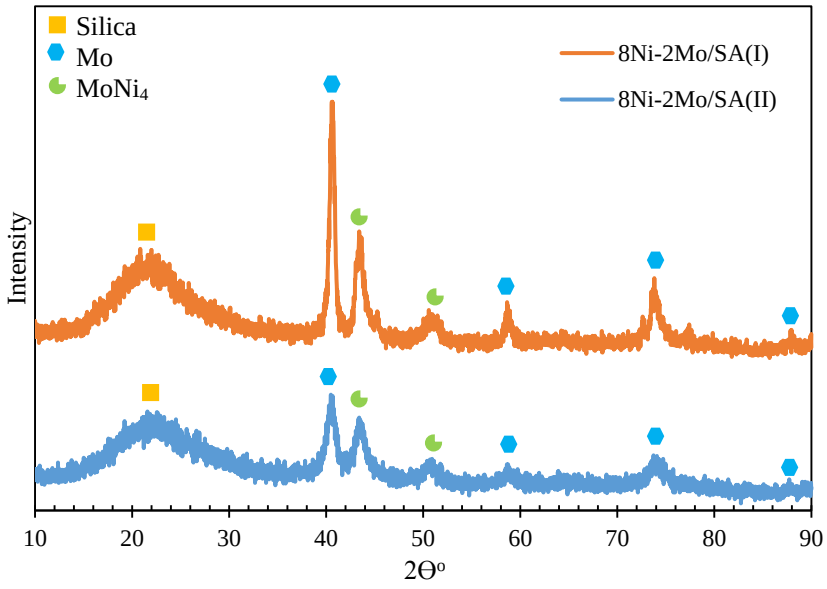

Figure 5.17 XRD Patterns of 8Ni-2Mo/SA(I) and 8Ni-2Mo/SA(II)

Crystallite sizes of the catalysts were calculated using Scherrer Equation at d_{100} peak of each and tabulated in Table 5.9.

Table 5.9 Crystallite sizes of 8Ni-2Mo/SA(I) and 8Ni-2Mo/SA(II)

Catalyst	**2θ (°)**	**Phase**	**$t_{crystallite\ size}$ (nm)**
8Ni-2Mo/SA(I)	40.6	Mo^o	14.6
8Ni-2Mo/SA(II)	40.6	Mo^o	7.3

According to Table 5.9., the crystallite size of 8Ni-2Mo/SA(II) synthesized following path II (simultaneous metal loading) is lower than that synthesized following path I (two-step metal loading).

XRD patterns of 10Ni-3Mg/SA, 10Ni-3Fe/SA and 10Ni-3Fe-0.3Mn/SA were depicted in Figure 5.18. In all catalysts, around 22.3º silica appears as a broad peak due to its amorphous structure (Sarıyer, 2018; Musić et al., 2011). In 10Ni-3Mg/SA, the peaks at 2Θ value of 44.7, 52.0 and 76.6º correspond to metallic-nickel in accordance with Ni PDF Card (No: 00-004-0850) (Table B.1 in Appendix B) and at 2Θ value of 37.0, 42.9, 62.7 and 78.4º correspond to magnesium oxide in accordance with MgO PDF Card (No: 01-075-1525) (Table B.15 in Appendix B). The XRD analysis of 10Ni-3Fe/SA and 10Ni-3Fe-0.3Mn/SA are quite similar, attributing to insignificant effect of including very small amount of manganese. The peaks at 2Θ value of 37.1, 43.1 and 62.6º in 10Ni-3Fe/SA and the peaks at 2Θ value of 37.1, 42.8 and 62.8º in 10Ni-3Fe-0.3Mn/SA refer to nickel oxide in accordance with NiO PDF Card (No: 01-089-5881) (Table B.2 in Appendix B), while in both catalysts, the peaks at 2Θ value of 35.7, 42.8 and 61.1º refer to iron-oxide in accordance with $Fe_{0.925}O$ PDF Card (No: 01-089-0686) (Table B.16 in Appendix B).

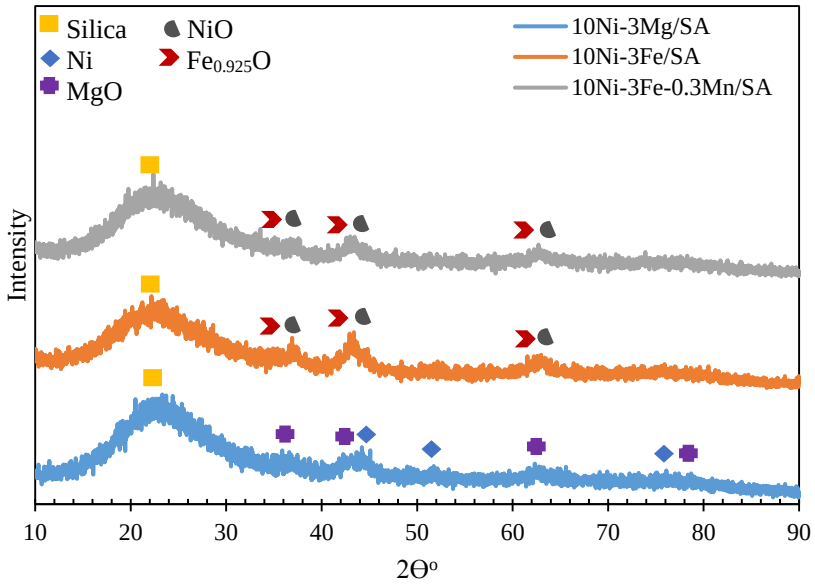

Figure 5.18 XRD Patterns of 10Ni-3Mg/SA, 10Ni-3Fe/SA and 10Ni-3Fe-0.3Mn/SA

XRD patterns of Ni&Ru loaded silica aerogels were shown in Figure 5.19. In all catalysts, around 22.7º silica appears as a broad peak due to its amorphous structure (Sarıyer, 2018; Musić et al., 2011). The peaks at 2Θ value of 38.5, 42.1, 44.1, 58.4, 70.1, 78.7 and 85.2º in 10Ni-1Ru/SA, the peaks at 2Θ value of 38.4, 42.1, 44.0, 58.2, 70.0, 78.6 and 85.2º in 10Ni-2Ru/SA and the peaks at 2Θ value of 38.4, 42.4, 44.1, 58.5, 70.2, 78.8 and 85.3º in 10Ni-3Ru/SA correspond to metallic-ruthenium in accordance with Ru PDF Card (No: 03-065-1863) (Table B.13 in Appendix B). In addition, the peaks at 2Θ value of 44.4, 51.7 and 76.2º in 10Ni-1Ru/SA, the peaks at 2Θ value of 44.2, 51.7 and 76.2º in 10Ni-2Ru/SA and the peaks at 2Θ value of 44.4, 51.7 and 76.3º in 10Ni-3Ru/SA correspond to metallic-nickel in accordance with Ni PDF Card (No: 00-004-0850) (Table B.1 in Appendix B). There is no evidence of the presence of a nickel-ruthenium phase in the catalysts.

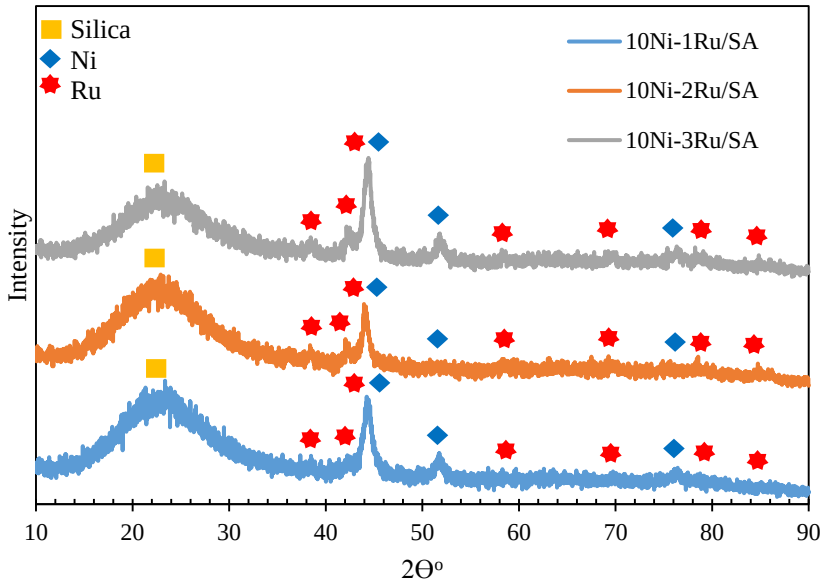

Figure 5.19 XRD Patterns of 10Ni-1Ru/SA, 10Ni-2Ru/SA and 10Ni-3Ru/SA

According to XRD analysis, different sizes of crystallite sizes were obtained. Crystallite sizes are influenced by the dispersion of metals on the support, agglomeration of metals and/or being in various forms as well as metallic phases (Slowik et al., 2016). Among the catalysts, the lowest crystallite size was obtained in 2.5Ni/SA, attributing the lowest amount of metal loaded. However, the highest crystallite size was obtained in the presence of 10Co/SA, attributing to not well dispersed of Co particles on the support. The crystallite sizes increase in the following order: 2.5Ni<8Ni-2Mo(I)<5Ni<10Zr<10Ni<8Ni-2Mo(II)<8Ni<10Ni-wet <10Ag<10Cr<10Mo<10Co.

5.1.3 Diffuse Reflectance Infrared Fourier Transform Spectroscopy (DRIFTS) Analyses

In this part, nature of acidity of the various metal loaded silica aerogels were examined with the aid of pyridine adsorption technique. Lewis and Bronsted acidity

of the catalysts are determined with respect to the adsorption bands between 1400-1700 cm^{-1} wavenumbers. Lewis acidity is observed between 1632-1580 cm^{-1}, around 1575 cm^{-1} (Kooli et al., 2000; Chen et al., 2017) and between 1455-1438 cm^{-1}, while Bronsted acidity is observed around 1640, 1608 and 1540 cm^{-1} (Busca et al., 1998). In addition, the band around 1490 cm^{-1} corresponds to both Lewis and Bronsted acid site (Khalil et al., 2020; Güner Ö., 2007; Dinçer B. Y., 2019; Obalı et al., 2011).

Herein, Lewis-to-(Lewis+Bronsted) acid ratio L/(L+B) was determined by proportionating the intensities of Lewis acid site in the region of 1632-1580 cm^{-1} to Lewis+Bronsted acid site around 1490 cm^{-1}.

5.1.3.1 Nickel Loaded Silica Aerogels

The nature of acidities of 2.5%, 5%, 8% and 10% by weight of nickel loaded silica aerogels were determined with respect to the adsorption bands wavenumbers shown in Figure 5.20.

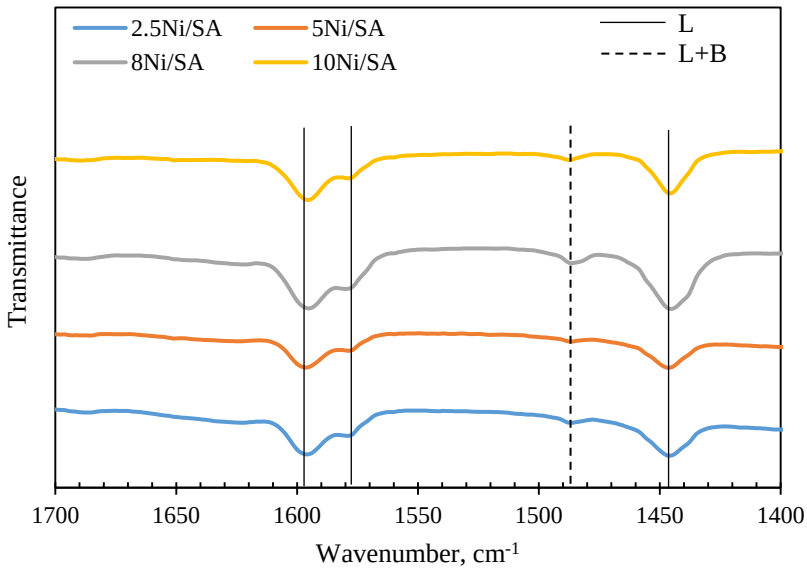

Figure 5.20 DRIFT Spectra of Adsorbed Pyridine on Ni Loaded Silica Aerogels

According to Figure 5.20, all nickel loaded silica aerogels exhibited intense bands at similar wavenumber. In nickel loaded silica aerogels, the intense bands around 1596, 1577, and 1445 cm^{-1} correspond to Lewis acid sites, while the broad band at 1486 cm^{-1} refers to both Lewis and Bronsted acid sites. Therefore, it was deduced that all Ni doped silica aerogels contain both Lewis and Bronsted acid sites in which Lewis acid sites are predominant. The L/(L+B) ratios of 2.5Ni, 5Ni, 8Ni and 10Ni doped silica aerogels were found to be 8.10, 9.47, 15.82 and 17.52, respectively, by proportioning the intensities at 1596 and 1486 cm^{-1}. This indicates that the L/(L+B) ratio increased with an increase in Ni content.

5.1.3.2 Monometal Loaded Silica Aerogels

The nature of acidities of 10% by weight of silver, chromium, zirconium, cobalt, nickel and molybdenum loaded silica aerogels were determined with respect to the adsorption bands wavenumbers depicted in Figure 5.21.

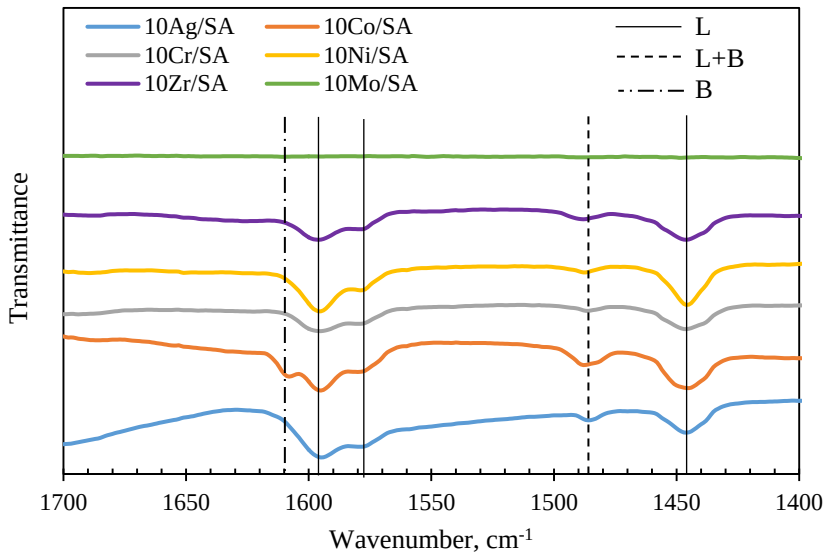

Figure 5.21 DRIFT Spectra of Adsorbed Pyridine on Monometal Loaded Silica Aerogels

According to Figure 5.21, 10% by weight Ni, Cr, Zr and Ag loaded silica aerogels exhibited intense bands at similar wavenumber. In these catalysts, the intense bands around 1596, 1577, and 1445 cm^{-1} correspond to Lewis acid sites, while the broad band at 1486 cm^{-1} refers to both Lewis and Bronsted acid sites. In addition to these bands, the broad band at 1609 cm^{-1} in 10Co/SA refers to Bronsted acid site. Thus, all monometal doped silica aerogels contain both Lewis and Bronsted acid sites in which Lewis acid sites are predominant, with the exception of the Mo doped SA. Although Mo contains Lewis acid sites (Shen et al., 2019), the reason for the absence of both Lewis and Bronsted acid sites in 10Mo/SA in the DRIFTS analysis may be due to the inability of Mo to adsorb pyridine vapour due to its sintering. The L/(L+B) ratios of 10Co, 10Cr, 10Zr, 10Ni and 10Ag doped silica aerogels were found to be 4.08, 6.90, 3.63, 17.52 and 4.37 respectively, by proportioning the intensities at 1596 and 1486 cm^{-1}. This indicates that the L/(L+B) ratio is affected by the properties of the metals regardless of the amount of metals.

5.1.3.3 Bi and Trimetal Loaded Silica Aerogels

The nature of acidities of bi and trimetal loaded silica aerogels were determined with respect to the adsorption bands wavenumbers indicated in Figures 5.22-5.24

In Figure 5.22, DRIFT spectra of 8Ni-2Mo/SA(I) and 8Ni-2Mo/SA(II) were depicted.

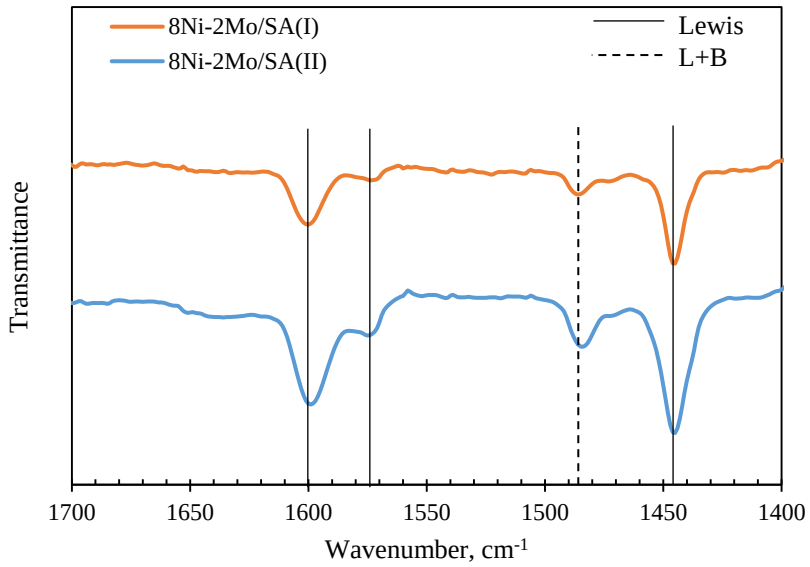

Figure 5.22 DRIFT Spectra of Adsorbed Pyridine on 8Ni-2Mo/SA(I) & 8Ni-2Mo/SA(II)

According to Figure 5.22, 8% by weight of Ni and 2% by weight of Mo loaded silica aerogels synthesized following two distinct paths described in section 4.1.2.7 Nickel-Molybdenum Loading, exhibited intense bands around 1599, 1571 and 1445 cm^{-1} correspond to Lewis acid sites, while the broad band at 1485 cm^{-1}. Therefore, it was concluded that 8Ni-2Mo doped silica aerogels contain both Lewis and Bronsted acid sites in which Lewis acid sites are predominant. The L/(L+B) ratios of 8Ni-2Mo(I) and 8Ni-2Mo(II) doped silica aerogels were found to be 3.96 and 3.94, respectively, by proportioning the intensities at 1599 and 1486 cm^{-1}. The close values of the L/(L+B) ratios indicate that the L/(L+B) ratio was not affected by the synthesis path of the bimetallic catalysts. However, the L/(L+B) ratio of these catalysts was significantly reduced compared to solely 8% by weight Ni doped SA with the L/(L+B) ratio of 15.82. The notable decrease in the L/(L+B) ratio might be attributed to the presence of $MoNi_4$ phase according to XRD analyses.

In Figure 5.23, DRIFT spectra of 10Ni-3Mg/SA, 10Ni-3Fe/SA and 10Ni-3Fe-0.3Mn/SA were depicted.

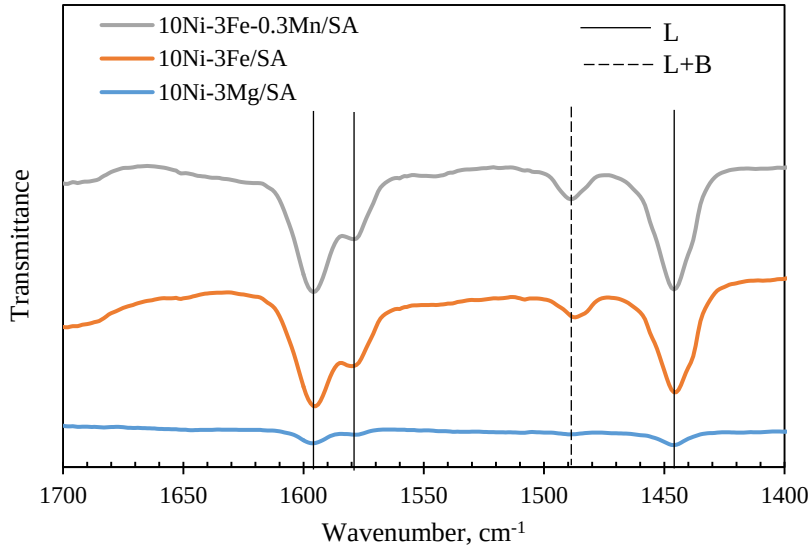

Figure 5.23 DRIFT Spectra of Adsorbed Pyridine on 10Ni-3Mg/SA, 10Ni-3Fe/SA & 10Ni-3Fe-0.3Mn/SA

According to Figure 5.23., 10% by weight of Ni – 3% by weight of magnesium, 10% by weight of Ni – 3% by weight of iron and 10% by weight of Ni – 3% by weight of iron – 0.3% by weight of manganese loaded silica aerogels exhibited intense bands at similar wavenumber. In these catalysts, the intense bands around 1596, 1578 and and 1445 cm^{-1} correspond to Lewis acid sites. However, the broad bands around 1487 cm^{-1} correspond to both Lewis and Bronsted acid sites. Among the catalysts, it is clear that the Mg containing catalysts exhibit less intense bands. The reason for this is that according to XRD analysis, magnesium is in the form of oxide with basic structure, which causes a decrease in acidity compared to the catalysts containing Fe and Fe-Mn. However, it is clear that the catalysts contain both Lewis and Bronsted acid sites in which Lewis acid sites are predominant. The L/(L+B) ratios of 10Ni-3Mg, 10Ni-3Fe and 10Ni-3Fe-0.3Mn doped silica aerogels were found to be 2.48, 7.43 and 6.29, respectively, by proportioning the intensities at 1596 and 1486 cm^{-1}.

Among these catalysts, the lowest L/(L+B) ratio was obtained in Mg containing SA, ascribing to the reduction of the acidity of the catalyst due to the basic nature of the oxide form. It is also clear that the presence of Mn causes a decrease in the L/(L+B) ratio compared to the non-containing.

In Figure 5.24, DRIFT spectra of 10Ni-1Ru/SA, 10Ni-2Ru/SA and 10Ni-3Ru/SA were depicted.

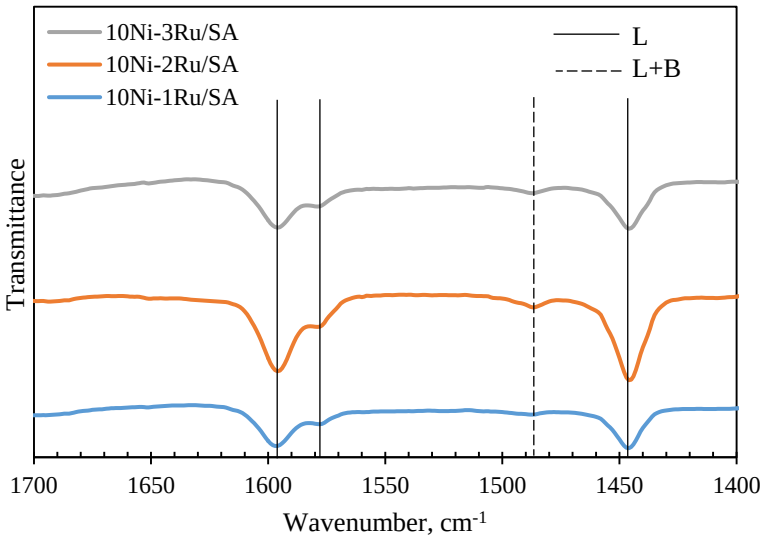

Figure 5.24 DRIFT Spectra of Adsorbed Pyridine on 10Ni-1Ru/SA, 10Ni-2Ru/SA & 10Ni-3Ru/SA

According to Figure 5.24, 10% by weight Ni and 1%, 2% and 3% by weight of Ru loaded silica aerogels exhibited intense bands at similar wavenumber. In these catalysts, the intense bands around 1596, 1577 and 1445 cm^{-1} correspond to Lewis acid sites, while the broad band at 1486 cm^{-1} refers to both Lewis and Bronsted acid sites. Therefore, it was deduced that all Ni-Ru bimetallic catalysts contain both Lewis and Bronsted acid sites in which Lewis acid sites are predominant. The L/(L+B) ratios of 10Ni-1Ru, 10Ni-2Ru and 10Ni-3Ru doped silica aerogels were found to be 19.01, 20.02 and 23.26, respectively, by proportioning the intensities at 1596 and 1486 cm^{-1}. It is clear that the presence of Ru leads to an increase in L/(L+B) ratio

compared to other catalysts. Further, the increase in Ru content in the bimetallic catalysts led to an increase in the L/(L+B) ratio.

Considering the L/L+B ratios in the catalysts, it was seen that the acid sites differ due to the diversity in the properties and phases of the doped metals. The L/(L+B) acid ratios in the catalysts increase in the following order: 10Mo<10Ni-3Mg <10Zr<8Ni-2Mo(II)<8Ni-2Mo(I)<10Co<10Ag<10Ni-3Fe-0.3Mn<10Cr<10Ni-3Fe <2.5Ni<5Ni<8Ni<10Ni<10Ni-1Ru<10Ni-2Ru<10Ni-3Ru.

5.1.4 Scanning Electron Microscopy (SEM) Analysis

SEM Analysis was performed for pure silica aerogels and all synthesized mono, bi and trimetallic catalysts to examine the surface texture, morphology and composition of catalysts.

5.1.4.1 Silica Aerogel and Nickel Loaded Silica Aerogels

In this part, SEM and back scattered electron images of pure silica aerogel, 2.5Ni/SA, 5Ni/SA, 8Ni/SA, 10Ni/SA and 10Ni/SA-wet were examined.

Figure 5.25 depicts the SEM images of pure SA at 100000X and 300000X magnifications.

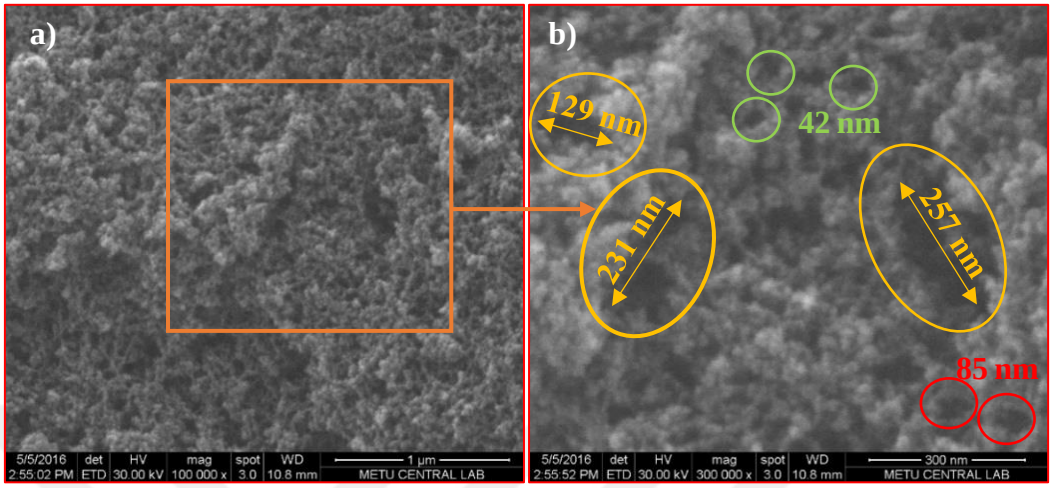

Figure 5.25 SEM Images of Pure SA a) 100000X and b) 300000X Magnifications

According to Figure 5.25, it is clear that silica aerogel has sponge like framework and porous morphology. The gaps in the structure represent both macro and mesopores in sizes 42, 85, 129, 231 and 257 nm, consistent with N_2 physisorption analysis.

Figure 5.26 shows the SEM and backscattered electron images of 2.5% by weight of nickel loaded silica aerogel at different magnifications.

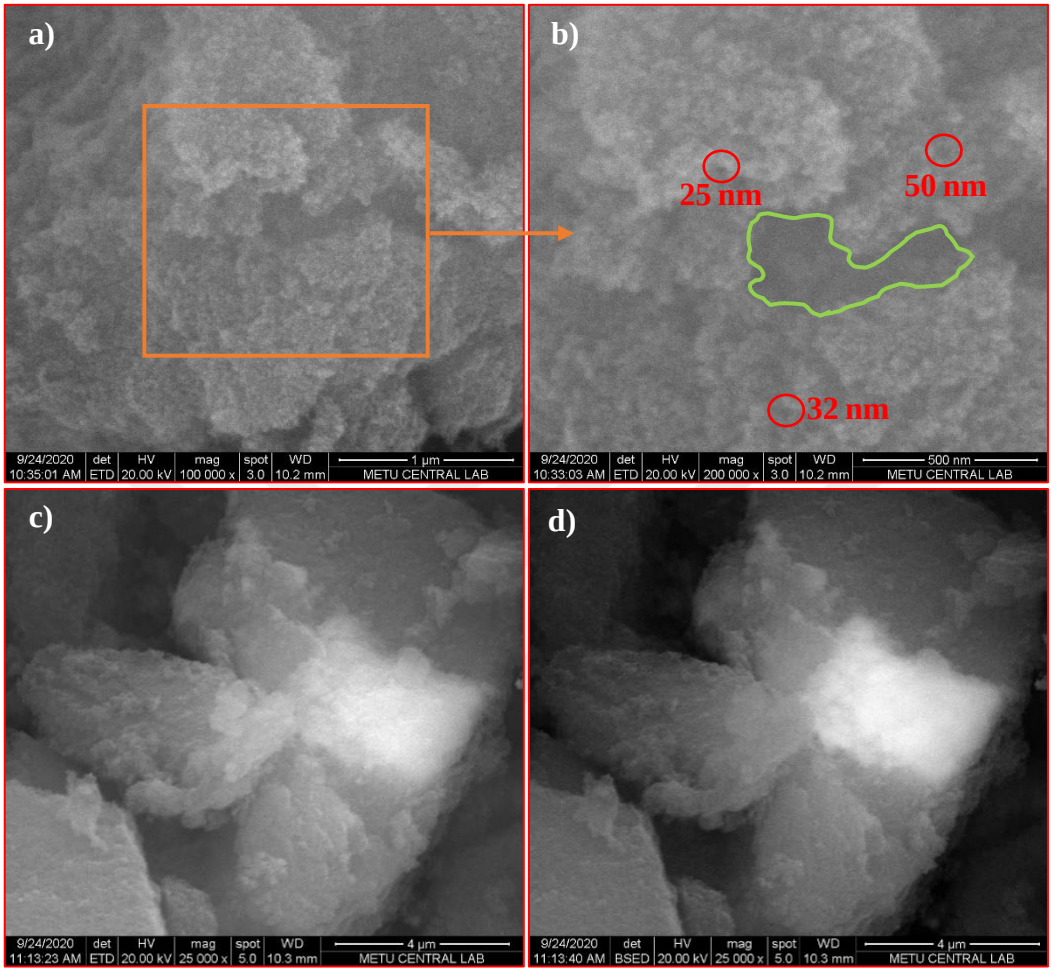

Figure 5.26 SEM (a,b,c) (100000X, 200000X, 25000X) and Back Scattered (d) Electron Images of 2.5Ni/SA

According to Figure 5.26 (a,b), the mesoporous morphology of 2.5% by weight of Ni loaded silica aerogel is observed with the sizes of 25, 32, and 50 nm in accordance with N_2 physisorption analysis. Despite the green circle shows the shift, it seems that the surface morphology and texture of the silica aerogel is preserved after Ni loading.

According to Figure 5.26 (c,d), the presence of Ni particles can be easily distinguished by the white and shiny particles indicating that Ni has been loaded into SA. However, the presence of the white and shiny particle can be interpreted as an agglomeration of Ni particles, implying that the Ni particles are not well dispersed in the silica aerogel.

SEM and back scattered electron images of 5% by weight of nickel loaded silica aerogel at 25000X magnification are shown in Figure 5.27.

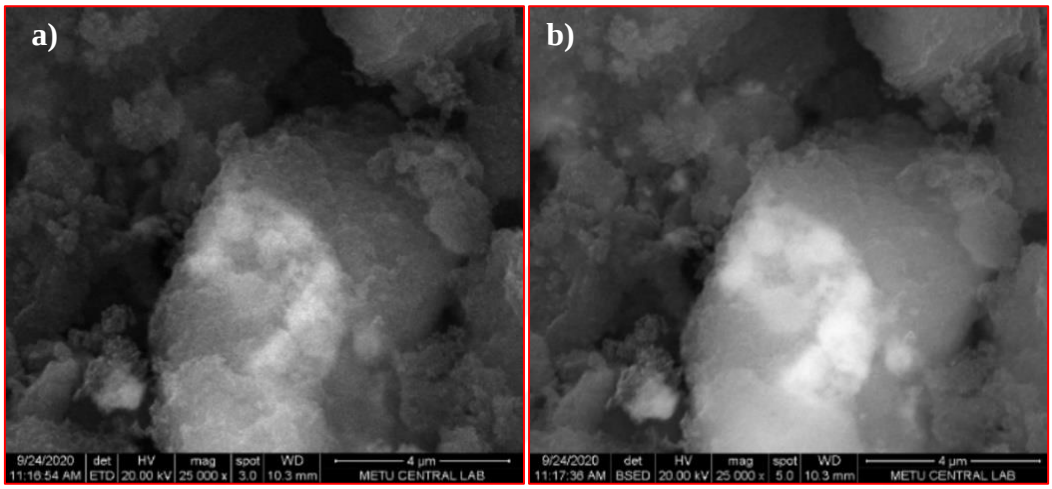

Figure 5.27 a) SEM and b) Back Scattered Electron Images of 5Ni/SA at 25000X Magnification

According to Figure 5.27, the white and shiny particles indicate the presence of Ni particles. However, Ni particles do not appear to be well dispersed in silica aerogel. According to the backscattered image, the white and shiny particle proves the agglomeration of Ni particles.

Figure 5.28 demonstrates the SEM and back scattered electron images of 8% by weight of nickel loaded silica aerogel at 10000X magnification.

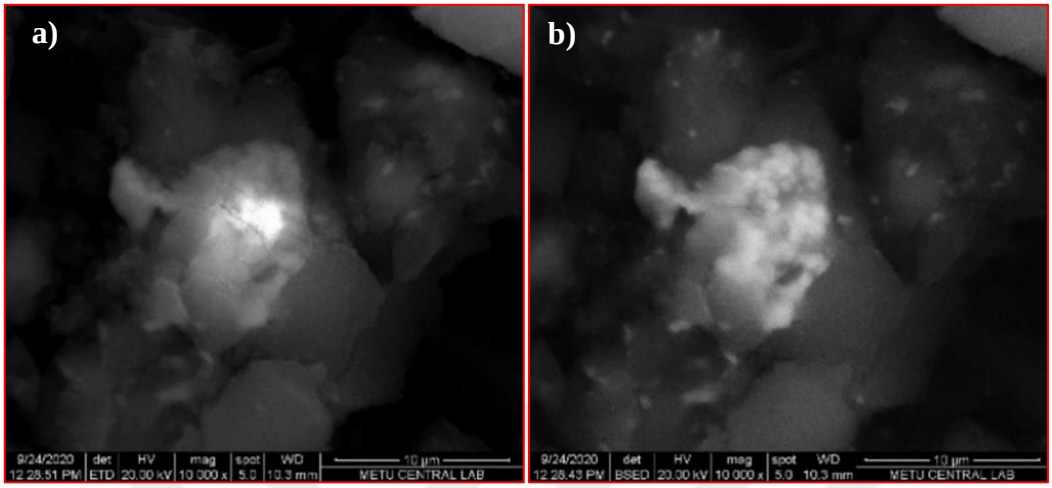

Figure 5.28 a) SEM and b) Back Scattered Electron Images of 8Ni/SA at 10000X Magnification

According to Figure 5.28, Ni particles can be seen as white and shiny particles. However, poor dispersion and agglomeration of Ni particles are more clearly observed in the backscattered image.

Figure 5.29 depicts the SEM images of 10% by weight of nickel loaded silica aerogel at different magnifications.

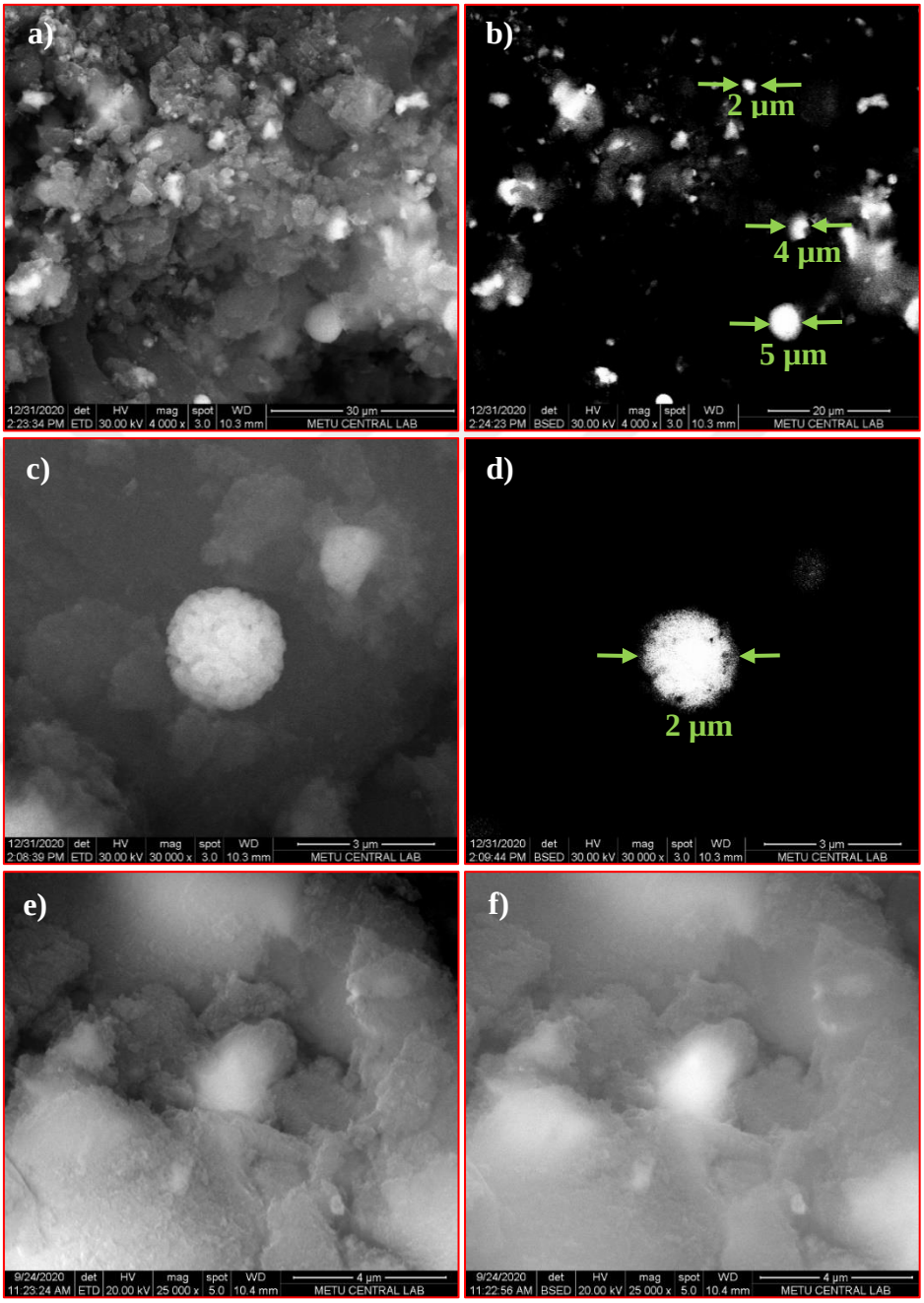

Figure 5.29 SEM (a,c,e) (4000X, 30000X, 25000X) and Back Scattered Electron (b,d,f) Images of 10Ni/SA

According to Figure 5.29 (a,b) the presence of Ni particles appears as white and shiny particles with the sizes of about 2, 4 and 5 µm, indicating that Ni has been loaded into SA. However, the sizes of Ni particles are not compatible with the literature (Liu et al., 2018; Roselina et al., 2012; Jian et al., 2014) and hence are interpreted as agglomeration of Ni particles as sphere cluster with a size of 2 µm as seen in Figure 5.29 (c,d). Although the particles appear to be better dispersed compared to 2.5Ni/SA, 5Ni/SA and 8Ni/SA, the agglomeration of particles is more clearly seen in Figure 5.29 (e,f).

In Figure 5.30 EDX spectrum of 10Ni/SA was given.

(EDX analyses of 10Ni/SA of different regions were given in Figures D.1-D.3 in Appendix D.)

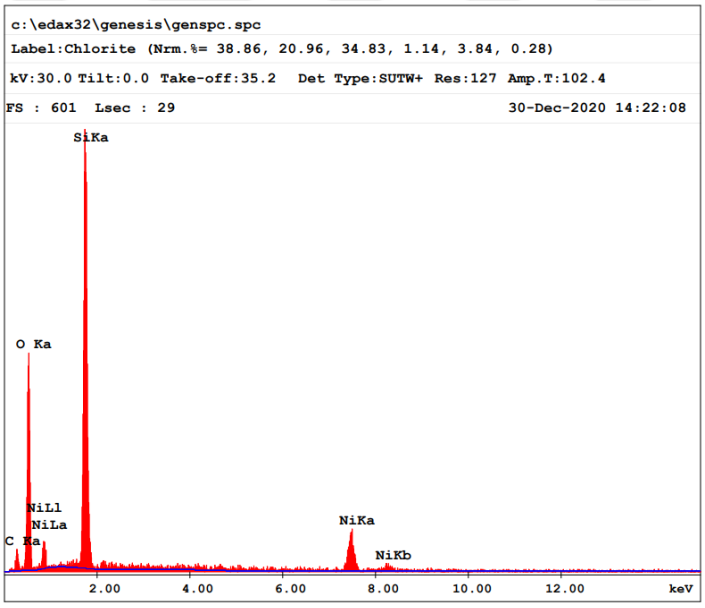

Figure 5.30 EDX Analysis of 10Ni/SA

According to EDX analysis, 10Ni/SA contains Si, O, C and Ni elements. The presence of C is due to the carbon tape. In this region of the catalyst Ni content is 7.17 wt. %. In addition, the average Ni content in different regions of the catalyst is 10.14 wt. %, which is very close to the amount of metal loaded.

Figure 5.31 shows the SEM and back scattered electron images of 10% by weight of nickel loaded silica aerogel by wet impregnation method at 60000X and 120000X magnifications.

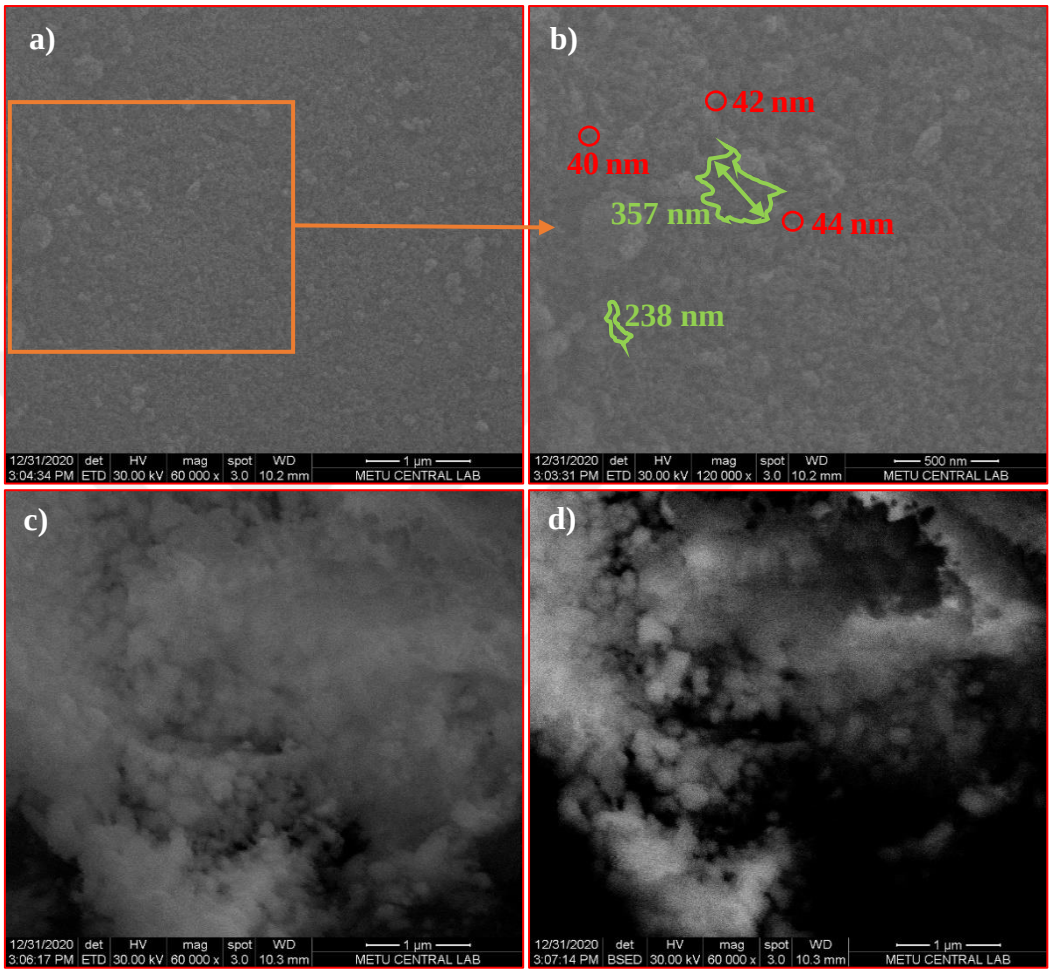

Figure 5.31 SEM (a,b,c) (60000X, 120000X, 60000X) and Back Scattered Electron (d) Images of 10Ni/SA-wet

According to Figure 5.31 (a,b), it is clear that 10Ni/SA-wet has different sized porous morphology. The gaps in the structure represent both meso and macropores in sizes of 40, 42, 44, 238, and 357 nm. It is also observed that the surface morphology and texture of silica aerogel is preserved after Ni loading. According to Figure 5.31 (c,d), the presence of Ni particles can be easily distinguished by the white and shiny

particles indicating that Ni has been loaded into SA. Ni particles appear well dispersed in SA.

In Figure 5.32 EDX analysis of 10Ni/SA-wet was given.

(EDX analyses of 10Ni/SA-wet different regions of were given in Figures D.4-D.5 in Appendix D)

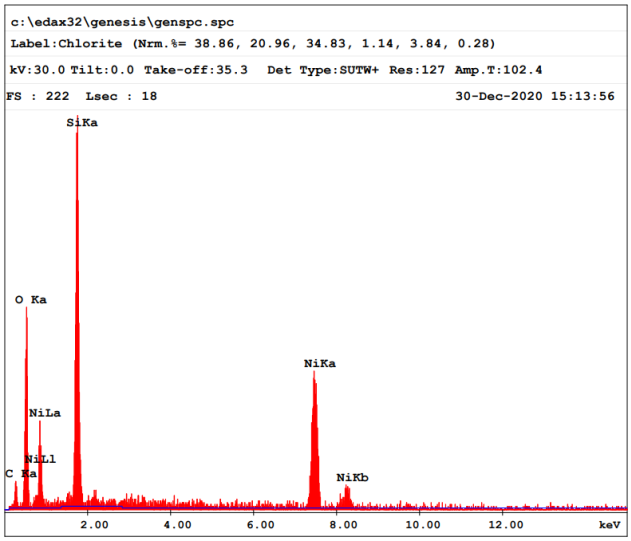

Figure 5.32 EDX Analysis of 10Ni/SA-wet

According to EDX analysis, 10Ni/SA-wet contains Si, O, C and Ni elements. The presence of C is due to the carbon tape. In this region of the catalyst, Ni content is 20.93 wt.%. However, the average Ni content in different regions of the catalyst is 16.74 wt.%, indicating that the poor dispersion of Ni particles in silica aerogel.

5.1.4.2 Monometal Loaded Silica Aerogels

In this part, SEM and back scattered electron images of 10Co/SA, 10Cr/SA, 10Zr/SA, 10Ag/SA and 10Mo/SA were examined.

Figure 5.33 depicts the SEM and back scattered electron images of 10% by weight of cobalt loaded silica aerogel at 25000X magnification.

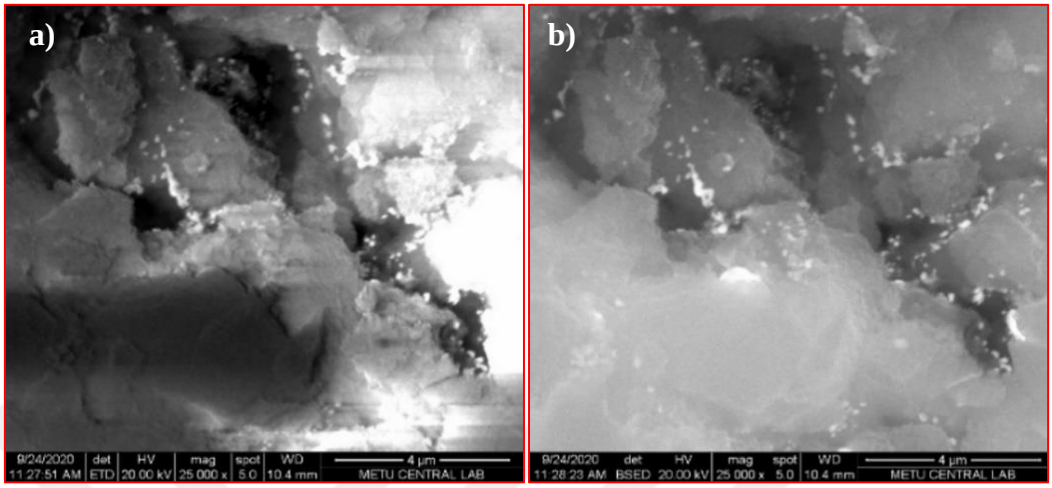

Figure 5.33 a) SEM and b) Back Scattered Electron Images of 10Co/SA at 25000X Magnification

According to Figure 5.33, the presence of small sized white and shiny particles represents Co particles, indicating that Co has been loaded into SA. It is also observed that the surface morphology and texture of the silica aerogel is not preserved after Co loading.

Figure 5.34 shows the SEM images of 10% by weight of chromium loaded silica aerogel at 25000X and 50000X magnifications.

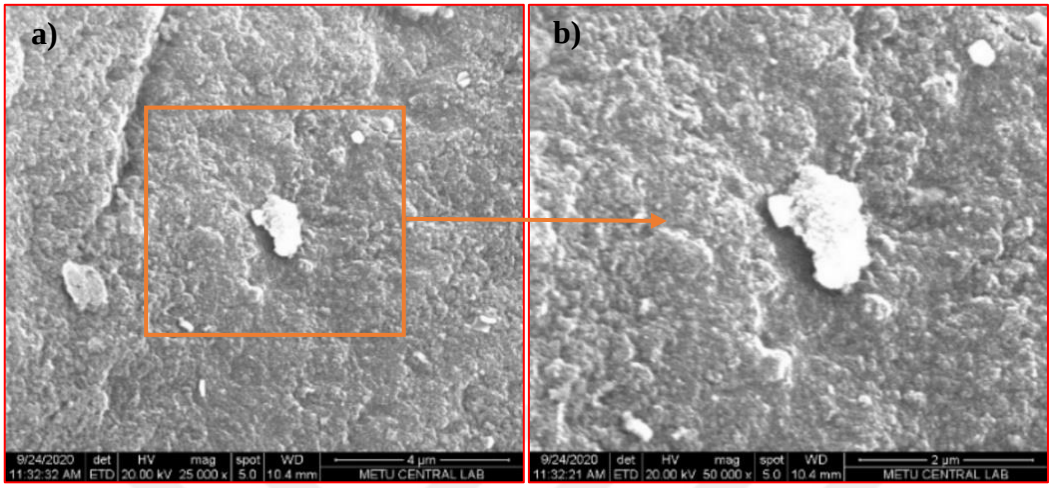

Figure 5.34 SEM Images of 10Cr/SA at a) 25000X and b) 50000X Magnifications

According to Figure 5.34, the surface morphology and texture of pure SA is not preserved after loading of Cr. In addition, agglomeration of Cr particles is observed in magnified image.

Figure 5.35 demonstrates the back scattered electron images of 10% by weight of zirconium loaded silica aerogel at 25000X and 50000X magnifications.

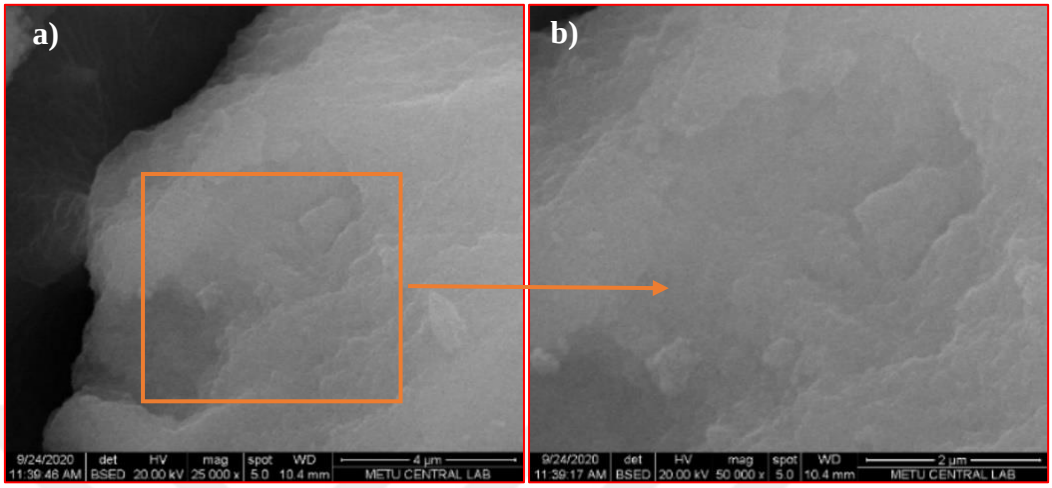

Figure 5.35 Back Scattered Electron Images of 10Zr/SA at a) 25000X and b) 50000X Magnifications

According to Figure 5.35, it is seen that loading of 10% by weight of Zr into the silica aerogel changes the morphology of silica aerogel. There is also no evidence of the presence of Zr particles in the region of the catalyst, indicating that the Zr particles are not well-dispersed in silica aerogel.

Figure 5.36 depicts the back scattered electron images of 10% by weight of silver loaded silica aerogel at 5000X and 25000X magnifications.

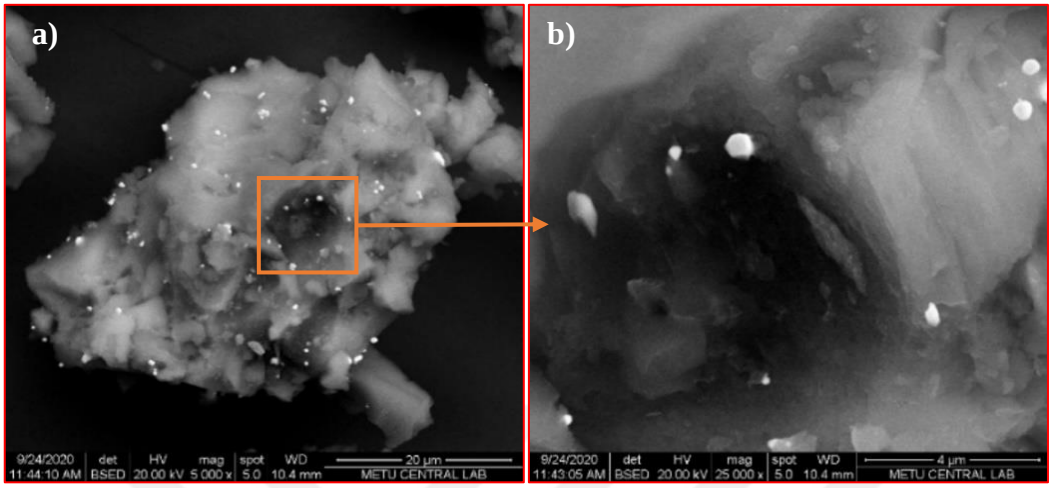

Figure 5.36 Back Scattered Electron Images of 10Ag/SA at a) 5000X and b) 25000X Magnifications

According to Figure 5.36, Ag particles appear as small sized white and shiny particles. However, loading of Ag appears to cause a change in surface texture and morphology of pure SA.

SEM and back scattered electron images of 10% by weight of molybdenum loaded silica aerogel at different magnifications are shown in Figure 5.37.

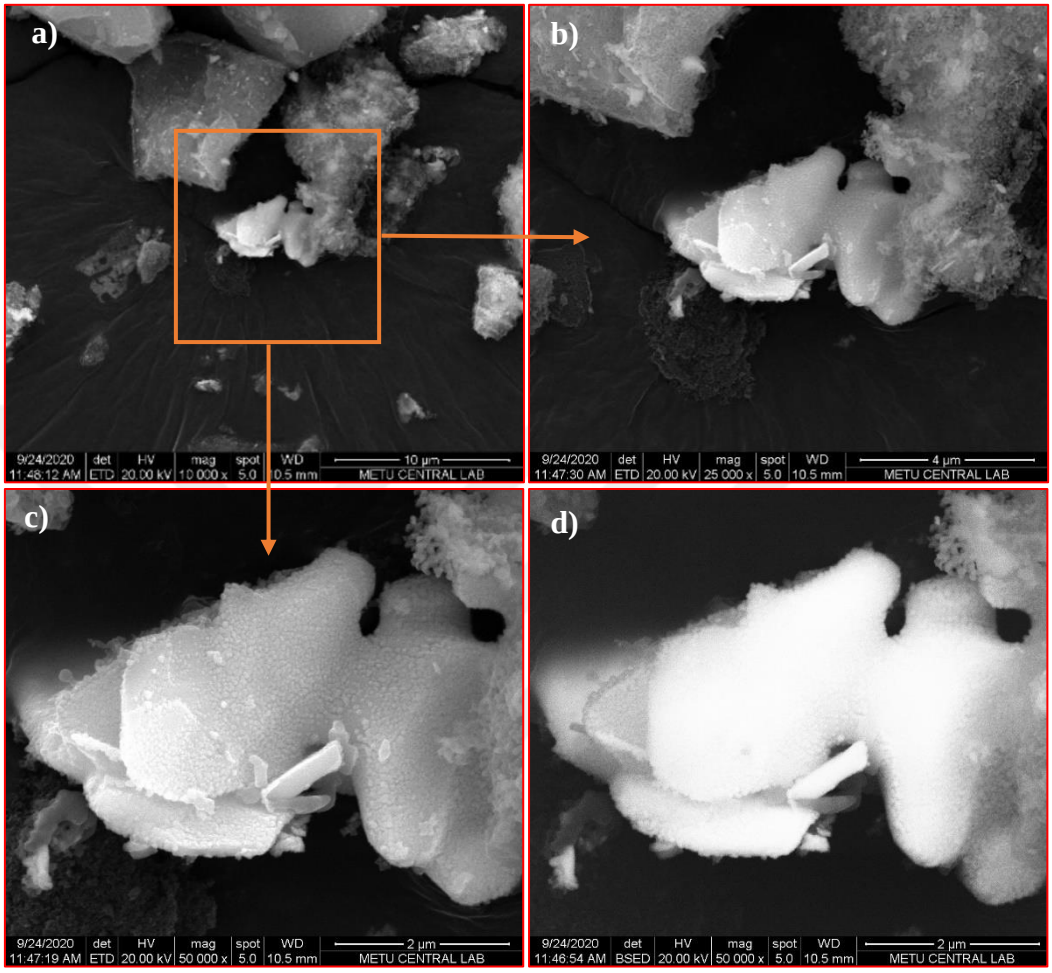

Figure 5.37 SEM (a,b,c) (10000, 25000X, 50000X) and Back Scattered (d) Electron Images of 10Mo/SA

According to Figure 5.37, it is clear that agglomeration of Mo particles causes a change in surface morphology and texture of pure SA.

5.1.4.3 Bi and Trimetal Loaded Silica Aerogel

In this part, SEM and back scattered electron images of 8Ni-2Mo/SA(I), 8Ni-2Mo/SA(II), 10Ni-3Mg/SA, 10Ni-3Fe/SA, 10Ni-3Fe-0.3Mn/SA, 10Ni-1Ru/SA, 10Ni-2Ru/SA, and 10Ni-3Ru/SA were examined.

Figure 5.38 demonstrates the SEM and back scattered electron images of 8% by weight of nickel and 2% by weight of molybdenum loaded silica aerogel at 10000X and 25000X magnifications.

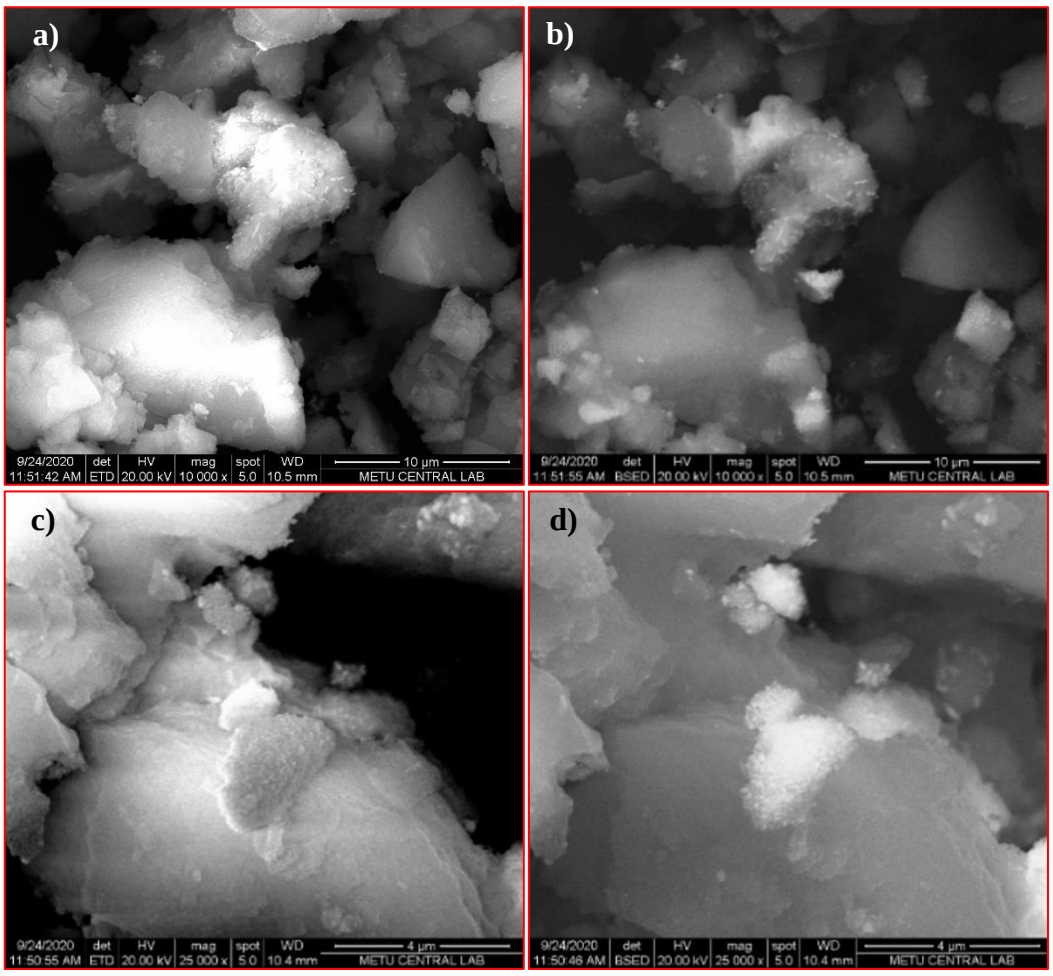

Figure 5.38 SEM (a,c) (10000X, 25000X) and Back Scattered Electron (b,d) Images of 8Ni-2Mo/SA(I)

According to Figure 5.38, it is clear that the presence of Mo, despite the low loading amount, notably affects the surface morphology and texture of pure SA. In addition, Ni and Mo particles do not appear to be well dispersed in silica aerogel, as evidenced by the presence of white and shiny particles of agglomeration of these particles.

Figure 5.39 depicts the SEM images of 8% by weight of nickel and 2% by weight of molybdenum loaded silica aerogel at different magnifications.

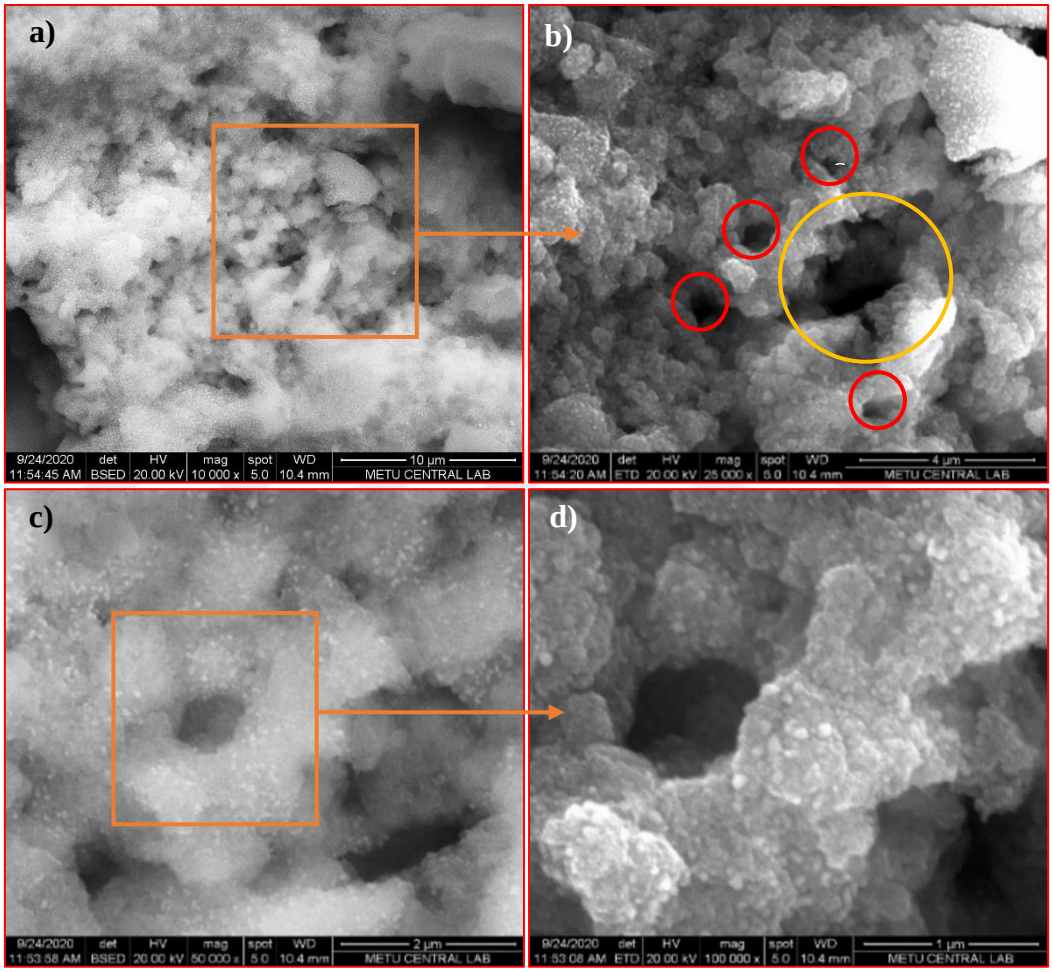

Figure 5.39 Back Scattered Electron (a,c) (10000X and 50000X) and SEM (b,d) (25000X and 100000X) Images of 8Ni-2Mo/SA(II)

According to Figure 5.39, it is clear that 8% by weight of Ni and 2% by weight of Mo loaded silica aerogel has different sized porous network represented in circles (Figure 5.39 (b)), consistent with N_2 physisorption analysis. According to the images, Ni and Mo particles are seen as white and shiny particles that appear well dispersed into SA.

Figure 5.40 indicates the back scattered images of 10% by weight of nickel and 3% by weight of magnesium loaded silica aerogel at 10000X and 50000X magnifications

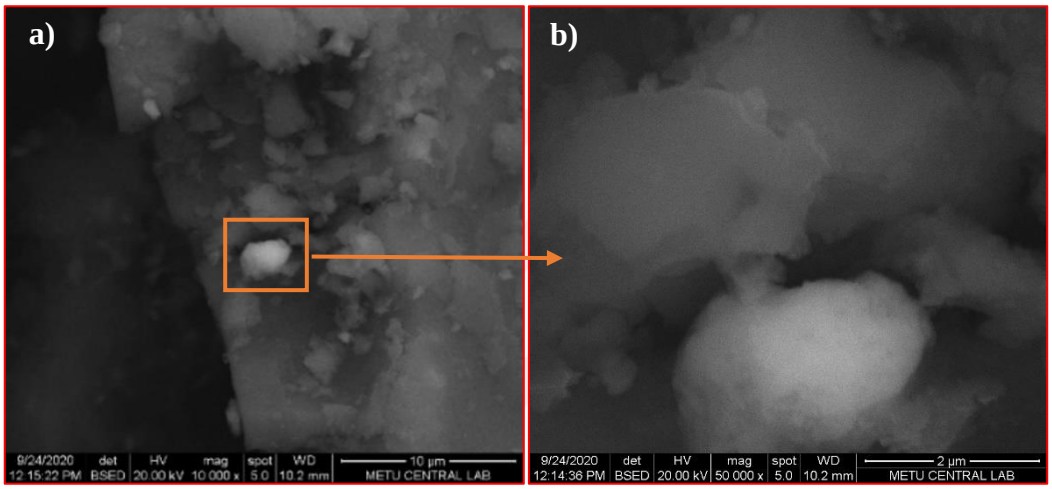

Figure 5.40 Back Scattered Electron Images of 10Ni-3Mg/SA a) 10000X and b) 50000X Magnifications

According to Figure 5.40, the surface morphology of pure SA was deformed after loading of Ni and Mg particles. The agglomeration of these particles is more clearly seen in the magnified image.

Figure 5.41 depicts the back scattered electron images of 10% by weight of nickel and 3% by weight of iron loaded silica aerogel at 10000X and 25000X magnifications.

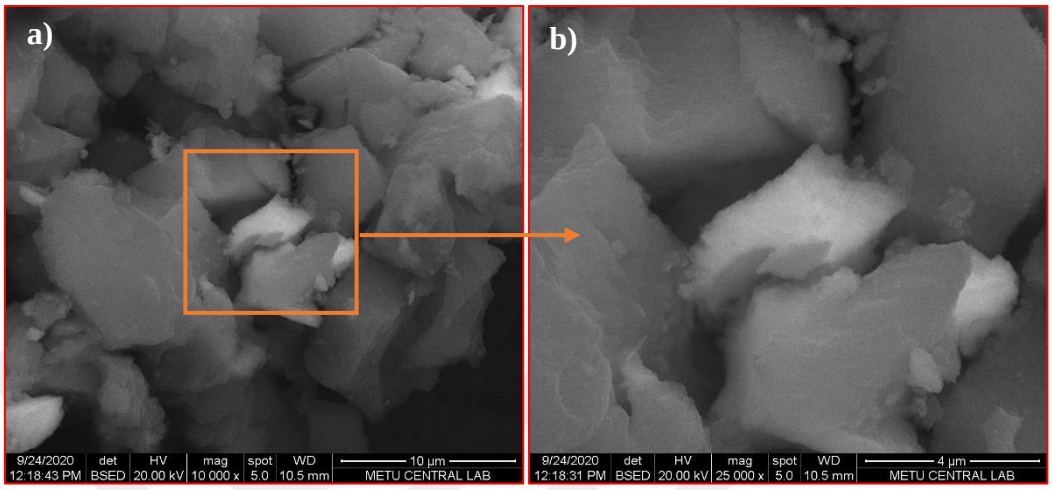

Figure 5.41 Back Scattered Electron Images of 10Ni-3Fe/SA a) 10000X and b) 250000X Magnifications

According to Figure 5.41, the surface texture and morphology of pure SA changed after Ni and Fe loading. In addition, the white and shiny particles refer to the agglomeration of these particles, indicating that the metals are not well dispersed into SA.

EDX analysis of 10Ni-3Fe/SA was given in Figure 5.42.

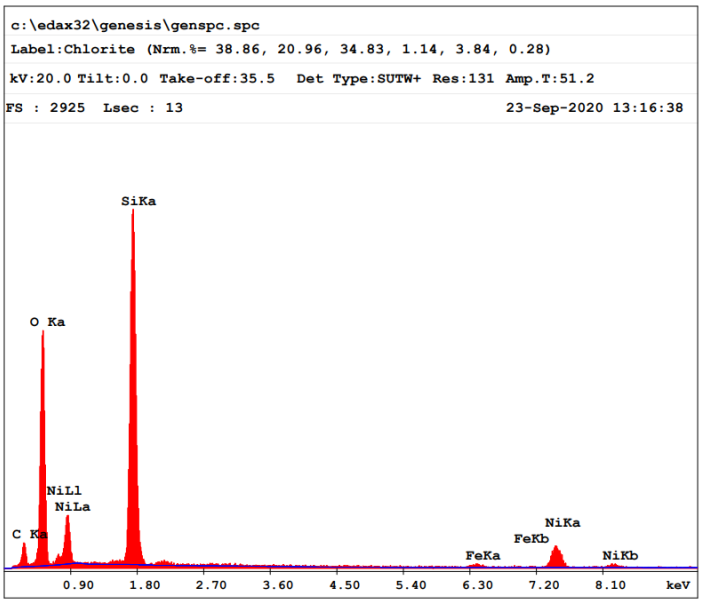

Figure 5.42 EDX Analysis of 10Ni-3Fe/SA

According to EDX analysis, 10% by weight of Ni and 3% by weight of Mg loaded silica aerogel contains Si, O, C, Ni and Fe elements. The presence of C element is due to the carbon tape. In this region of the catalyst Ni and Fe contents are 11.03% by weight and 1.02% by weight, respectively. In addition, presence of high amount of O elements is due to the presence of nickel and iron in the form of oxide in accordance with XRD analysis.

Figure 5.43 shows the SEM and back scattered electron images of 10% by weight of nickel, 3% by weight of iron and 0.3% by weight of manganese loaded silica aerogel at 10000X and 100000X magnifications.

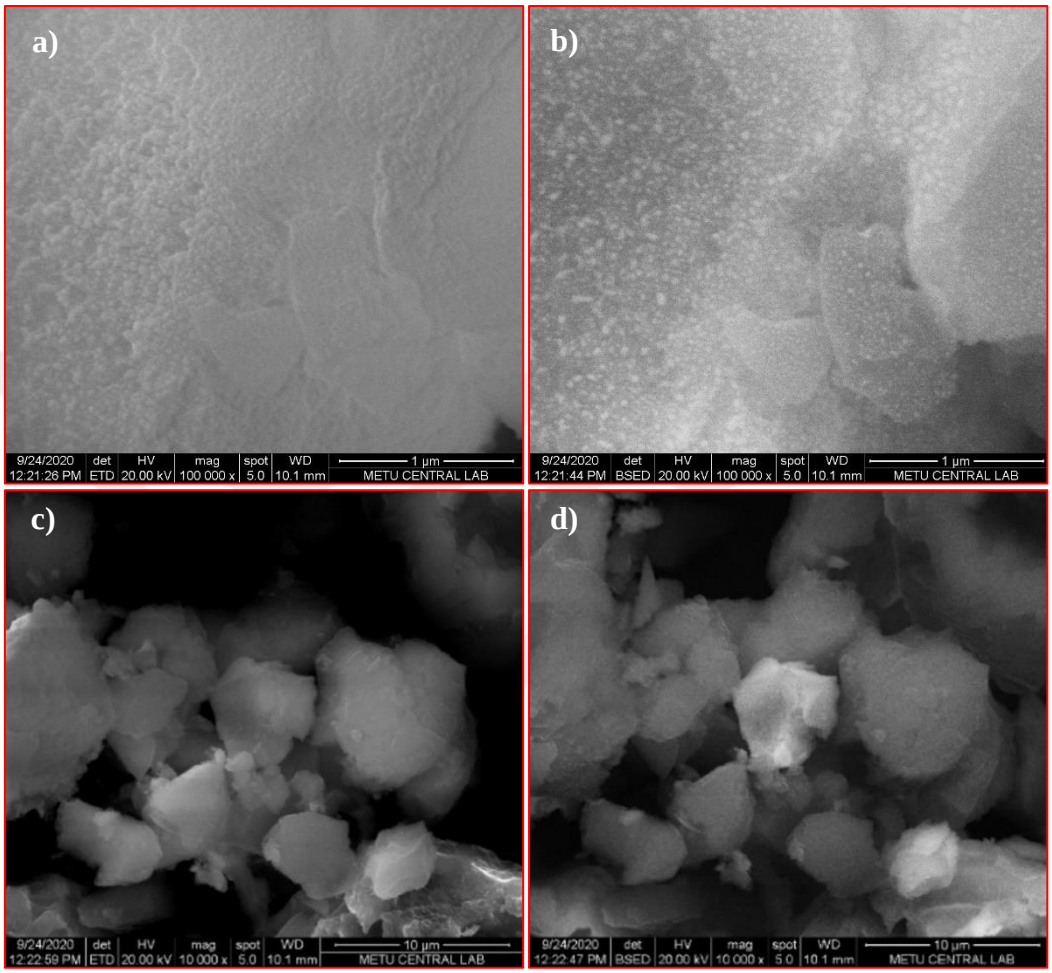

Figure 5.43 SEM (a,c) (100000X, 10000X) and Back Scattered Electron (b,d) Images of 10Ni-3Fe-0.3Mn/SA

According to Figure 5.43, the surface texture and morphology of pure SA is not preserved after loading of Ni, Fe and Mn. These particles appear as white and shiny particles in Figure 5.43 (b), indicating that the metals have been loaded into SA.

However, the agglomeration of these particles is seen more clearly in Figure 5.43 (c,d).

EDX analysis of 10Ni-3Fe-0.3Mn/SA was given in Figure 5.42.

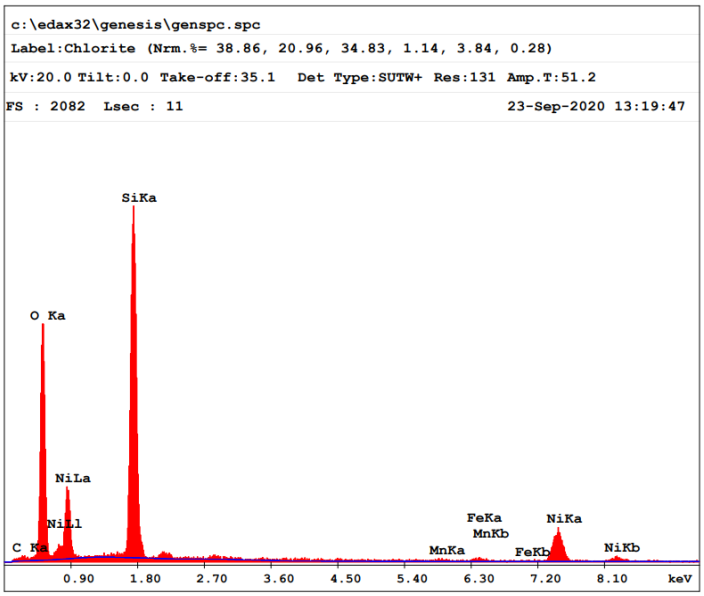

Figure 5.44 EDX Analysis of 10Ni-3Fe-0.3Mn/SA

According to EDX analysis, 10% by weight of Ni, 3% by weight of Fe and 0.3% by weight of Mn loaded silica aerogel contains Si, O, C, Ni, Fe, and Mn elements. The presence of C element is due to the carbon tape. In this region of the catalyst Ni, Fe and Mn contents are 18.43%, 1.20% and 0.77% by weight, respectively. In addition, presence of high amount of O elements is due to the presence of nickel and iron in the form of oxide in accordance with XRD analysis.

Figure 5.45 indicates the SEM and back scattered electron images of 10% by weight of nickel and 1% by weight of ruthenium loaded silica aerogel at 10000X magnifications.

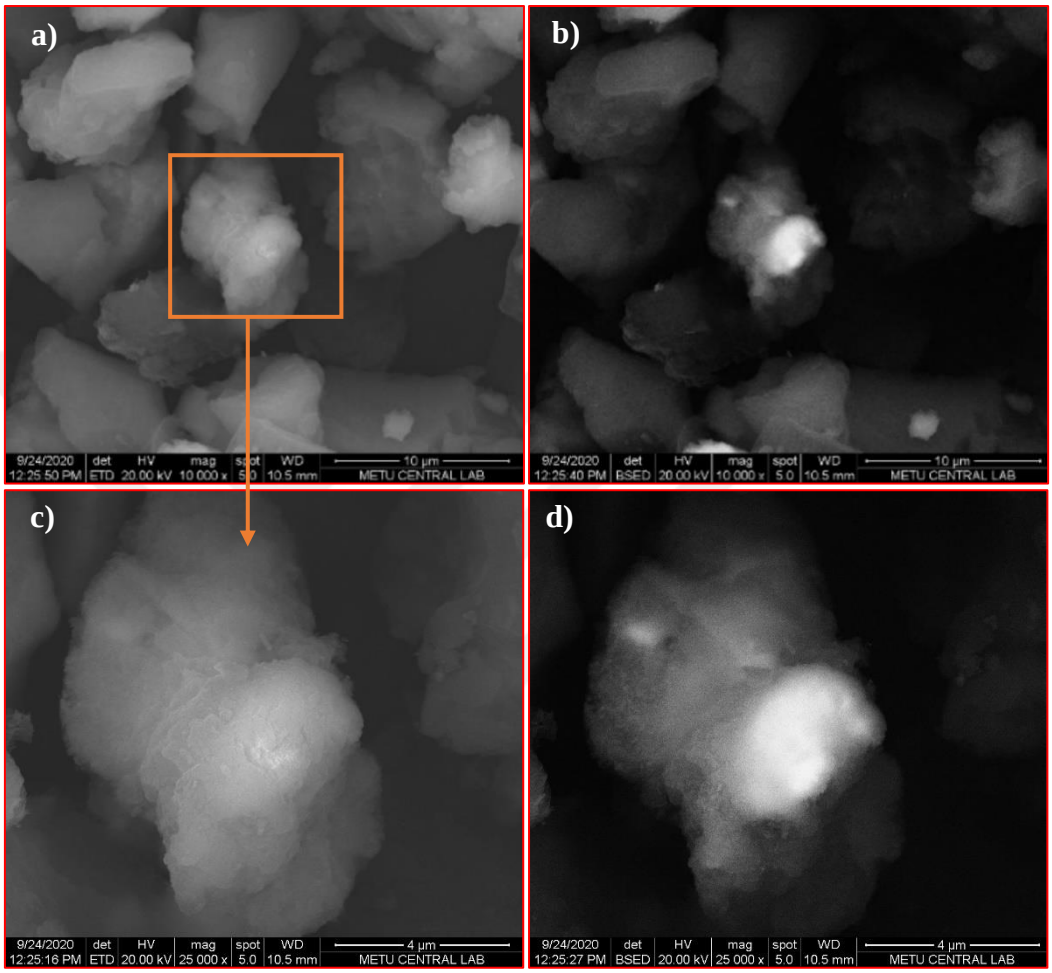

Figure 5.45 SEM (a,c) (10000X, 25000X) and Back Scattered Electron (b,d) Images of 10Ni-1Ru/SA

According to Figure 5.45, Ni and Ru particles do not appear to be well dispersed in silica aerogel, as evidenced by the presence of white and shiny particles of agglomeration of these particles.

SEM and back scattered electron images of 10% by weight of nickel and 2% by weight of ruthenium loaded silica aerogel at different magnifications are shown in Figure 5.46.

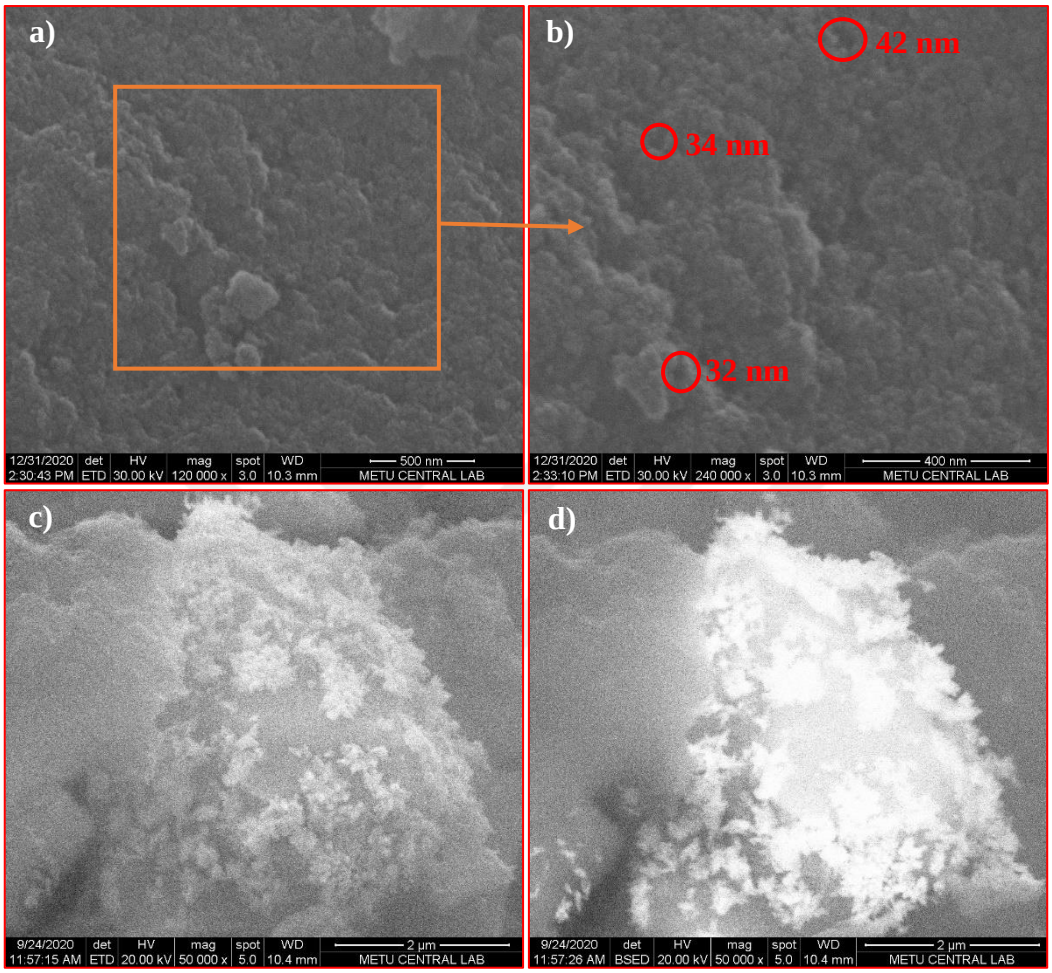

Figure 5.46 SEM (a,b,c) (120000X, 240000X, 50000X) and Back Scattered Electron (d) Images of 10Ni-2Ru/SA

According to Figure 5.46 (a,b), it is observed that 10Ni-2Ru/SA has different sized mesoporous morphology in sizes 32, 34 and 42 nm, consistent with N_2 physisorption analysis. It is also indicated that the surface morphology and texture of the silica aerogel is not deformed after metal loading. However, the poor dispersion of Ni and

Ru particles into SA is interpreted based on agglomerated white and shiny particles in some regions of the catalyst in Figure 5.46 (c,d).

In Figure 5.47 EDX analysis of 10Ni-2Ru/SA was given.

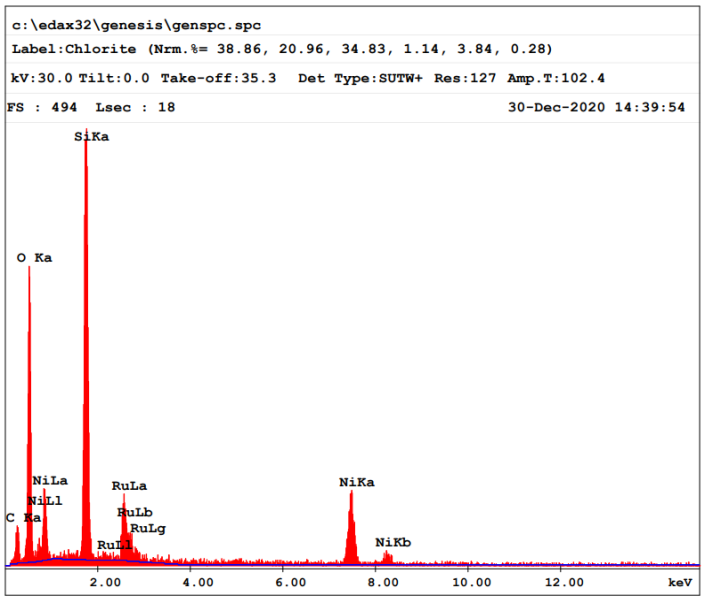

Figure 5.47 EDX Analysis of 10Ni-2Ru/SA

According to EDX analysis, 10Ni-2Ru/SA contains Si, O, C and Ni elements. The presence of C is due to the carbon tape. In this region of the catalyst Ni and Ru contents are 8.49 wt. % and 6.19 wt. %, respectively.

Figure 5.48 depicts the SEM images of 10% by weight of nickel and 3% by weight of ruthenium loaded silica aerogel at different magnifications.

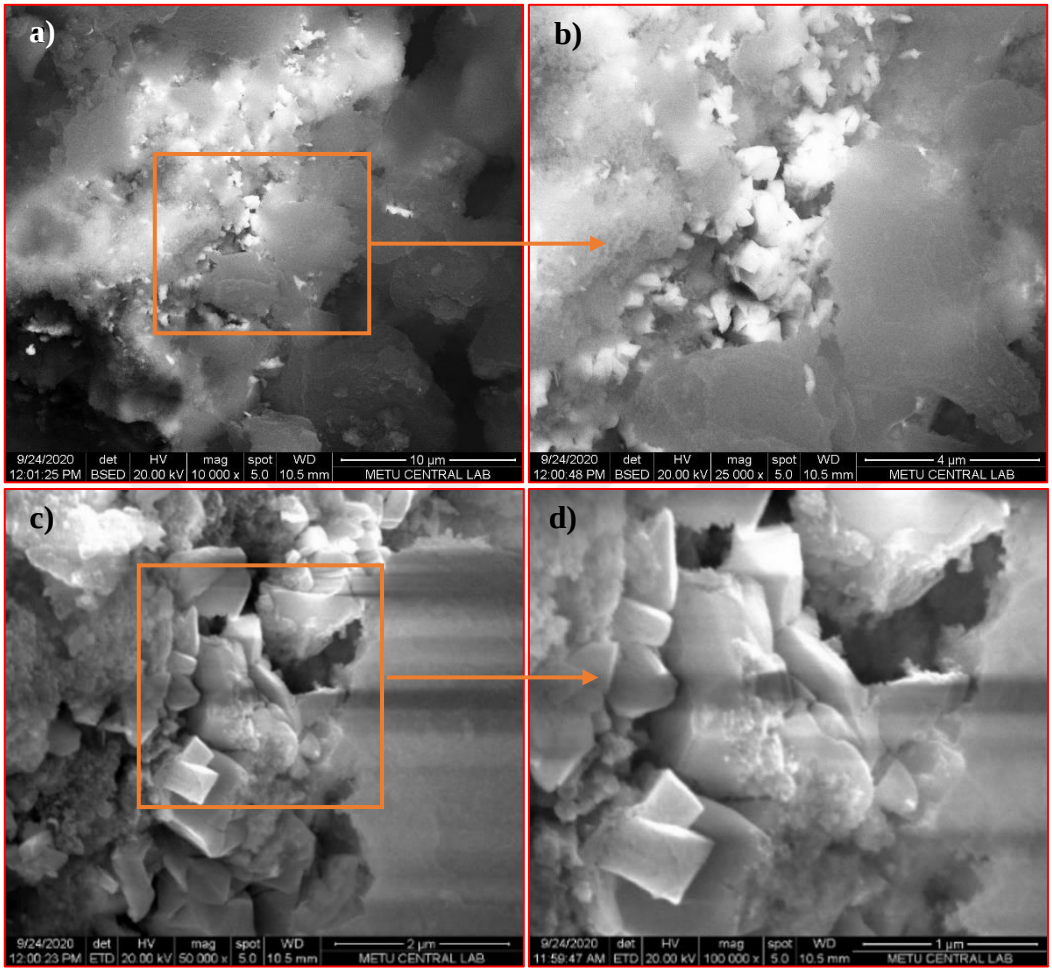

Figure 5.48 Back Scattered (a,b) (10000X, 25000X) and SEM (c,d) Images (50000X, 100000X) of 10Ni-3Ru/SA

According to Figure 5.48 (a,b), agglomeration of Ni and Ru particles are seen as white and shiny particles. In addition, the rectangular shaped particles are observed after Ni and Ru loading in Figure 5.48 (c,d).

5.2 Activity Results of the Catalysts

The activity tests of the catalysts were performed in a fixed bed quartz reactor system under continuous flow. The reactions were performed at 450-1050^{o}C, atmospheric pressure, and water-glycerol feed flow rate of 0.8, 0.9 and 1.0 ml/h, under 30 ml/min argon flow rate with the W/G molar ratio of 1, 3, 6 and 9 in the presence of 0.15 g mono, bi and trimetal loaded catalysts. Prior to each experiment, all catalysts were calcined under 50 ml/min dry air at 5 bar for 5 hours and then reduced under 50 ml/min H_2 flow for half an hour. The produced gases were analysed online during the reaction time, 5 h, with the same time interval, 30 min, and the collected liquid products were analysed manually using a gas chromatograph (GC).

The compositions of the gas and liquid products were calculated with the aid of calibration (beta) factor detailed in Appendix E.

The composition of the produced compounds and activity of the catalysts were given in terms of mole compositions of the gas compounds, glycerol conversion and hydrogen yield in the following sections. The calculations of compositions of compounds, glycerol conversion and H_2 yield were detailed in Appendix F.

In this study, grey hydrogen was produced in each experiment and the activity test results of the catalysts were divided into 5 parts: the effect of feed flow rate, the effect of temperature, the effect of feed ratio, the effect of catalyst synthesis method, and the effect of catalyst type on H_2 yield. The repeatability experiments were also performed to ensure the consistency and reliability in the experiments. Detailed information and experimental results were given in the following sections.

5.2.1 Repeatability Experiments

To ensure the consistency and reliability of the experiments, the experiments were performed under the same conditions for 2-3 times. Herein, the repeatability

experiments were carried out at 550°C, under atmospheric pressure with the W/G molar ratio of 9 at 0.9 ml/h glycerol-water feed flow rate and 30 ml/min Ar flow rate over 0.15 g 10Ni-3Ru/SA(700)(700) catalyst. Prior to experiments, the catalysts were calcined under dry air for 5 h and reduced with H_2 flow for half an hour.

In both experiments, four compounds, H_2, CO_2, CO, and CH_4 were produced with approximately complete glycerol conversions (99%). The product distribution and H_2 yield results of each experiments were given in Figures 5.49-5.50, respectively.

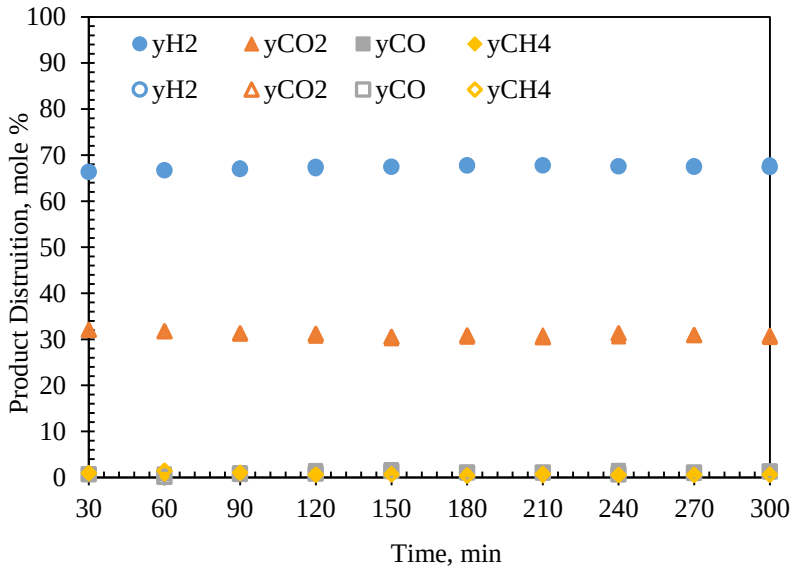

Figure 5.49 Product Distribution of GSR
(Catalyst:10Ni-3Ru/SA(700)(700), T_{rxn}:550°C, FFR:0.9ml/h, WGMR:9)
(Filled symbols: experiment 1, empty symbols: experiment 2)

According to Figures 5.49, it is clear that after 60 minutes, the gas compounds were produced with approximately the same mole percent in a time interval of 30 minutes. This indicates that the product distribution remained steady during the reaction time, 5h. In the experiment 1, the average mole percent of the produced H_2, CO_2, CO, and CH_4 are 65.7%, 32.6%, 0.9% and 0.8%, respectively. The product distribution of experiment 2 is also quite similar to experiment 1, with the average mole percent of 65.8%, 32.4%, 1.1%, and 0.6%, respectively. In addition, the average mole percent

of the produced H_2, CO_2, CO, and CH_4 in both experiments are 65.8±0.1%, 32.5±0.1%, 1.0±0.2%, and 0.7±0.1%, respectively.

Depending on the product distribution, high amounts of H_2 and CO_2 formations may be attributed to glycerol steam reforming reaction. Operating at high temperature favours the glycerol steam reforming reaction due to its endothermic nature and contributes to CO_2 and H_2 formation.

Glycerol Steam Reforming:

$C_3H_8O_3 + 3H_2O \leftrightarrow 3CO_2 + 7H_2$ $\Delta H_R = 128$ kJ/mole

In addition, the low amount of CO and CH_4 formations may be ascribed to water gas shift and reverse methanation reactions, resulting in an increase in CO_2 and H_2 compatible with the product distribution.

Water Gas Shift Reaction:

$CO + H_2O \leftrightarrow CO_2 + H_2$ $\Delta H_R = -41$ kJ/mole

Methanation:

$CO_2 + 4H_2 \leftrightarrow CH_4 + 2H_2O$ $\Delta H_R = -165$ kJ/mole

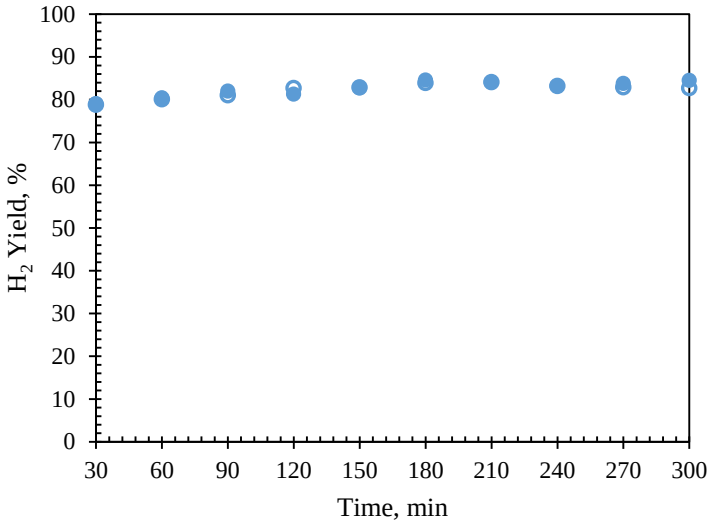

Figure 5.50 H_2 Yield of GSR
(Catalyst:10Ni-3Ru/SA(700)(700), T_{rxn}:550°C, FFR:0.9ml/h, WGMR:9)
(Filled symbols: experiment 1, empty symbols: experiment 2)

Similar to the gas products, as depicted in Figure 5.50, H_2 yield was also steadily obtained in both experiments with an average value of 82.4±0.2 % with the H_2 yields of 82.2 and 82.6% in experiment 1 and 2, respectively.

The consistency between the values and low standard deviation indicate that repeatable results were obtained in the experiments.

5.2.2 The Effect of Feed Flow Rate on H_2 Yield

To examine the effect of feed flow rate on H_2 yield, the reactions were carried out at 965°C, at 30 ml/min Ar flow rate under atmospheric pressure with the W/G molar ratio of 3 over 0.15 g 10Ni/SA(1035)(1035). Prior to experiments, the catalysts were calcined under dry air for 5 h and reduced with H_2 flow for half an hour. At these reaction conditions, 4 compounds, H_2, CO_2, CO and CH_4 were produced with approximately complete glycerol conversions in all experiments. The product

distribution and H_2 yield results at 0.9 ml/h were given in Figures 5.51-5.52, respectively.

The product distributions and H_2 yield values as a function of time at 0.8 and 1.0 ml/h feed flow rates were given in Figures G.1-G.4 in Appendix G.

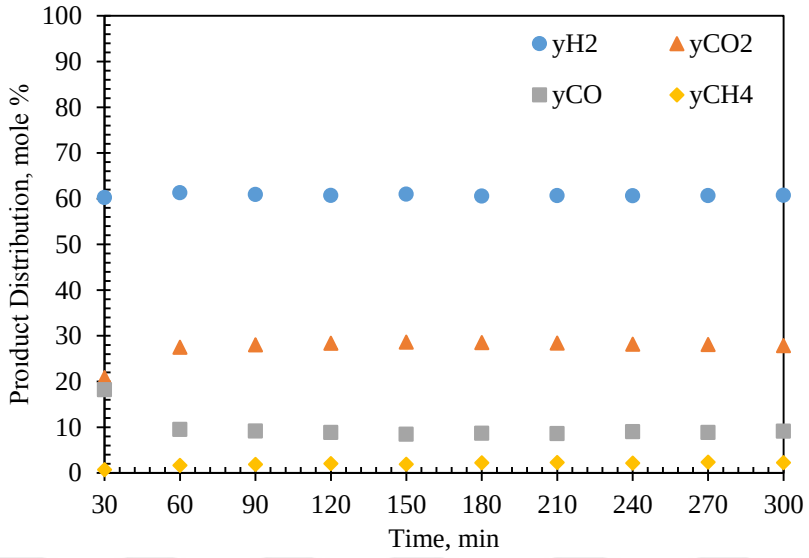

Figure 5.51 Product Distribution of GSR

(Catalyst:10Ni/SA(1035)(1035), T_{rxn}:965°C, FFR:0.9ml/h, WGMR:3)

According to Figure 5.51, it is clear that after 60 minutes, the gas compounds were produced with approximately the same mole percent in a time interval of 30 minutes. This indicates that the product distribution remained steady during the reaction time, 5h. The average mole percent of the produced H_2, CO_2, CO, and CH_4 are 60.7±0.5%, 27.5±1.4%, 9.8±0.9%, and 2.0±0.1%, respectively.

Considering the average mole compositions of gas compounds both glycerol steam reforming, glycerol decomposition and reverse water gas shift reactions may occur, resulting in the formation of H_2, CO_2, and CO.

Glycerol Steam Reforming:

$C_3H_8O_3 + 3H_2O \leftrightarrow 3CO_2 + 7H_2$ $\Delta H_R = 128$ kJ/mole

Glycerol Decomposition:

$C_3H_8O_3 \rightarrow 3CO + 4H_2$ $\Delta H_R = 250$ kJ/mole

Reverse Water Gas Shift Reaction:

$CO_2 + H_2 \leftrightarrow CO + H_2O$ $\Delta H_R = 41$ kJ/mole

In addition, the low formation of CH_4 may be attributed to the conversion of CH_4 into CO_2 and H_2 by reverse methanation reaction, which forms in reverse methane dry reforming and reverse methane steam reforming reactions. (Idriss et al., 2015; Kahle et al., 2013; Chen et al., 2020)

Reverse Methanation:

$CH_4 + 2H_2O \leftrightarrow CO_2 + 4H_2$ $\Delta H_R = 165$ kJ/mole

Reverse Methane Dry Reforming:

$2CO + 2H_2 \leftrightarrow CH_4 + CO_2$ $\Delta H_R = -259$ kJ/mole

Reverse Methane Steam Reforming:

$CO + 3H_2 \leftrightarrow CH_4 + H_2O$ $\Delta H_R = -206$ kJ/mole

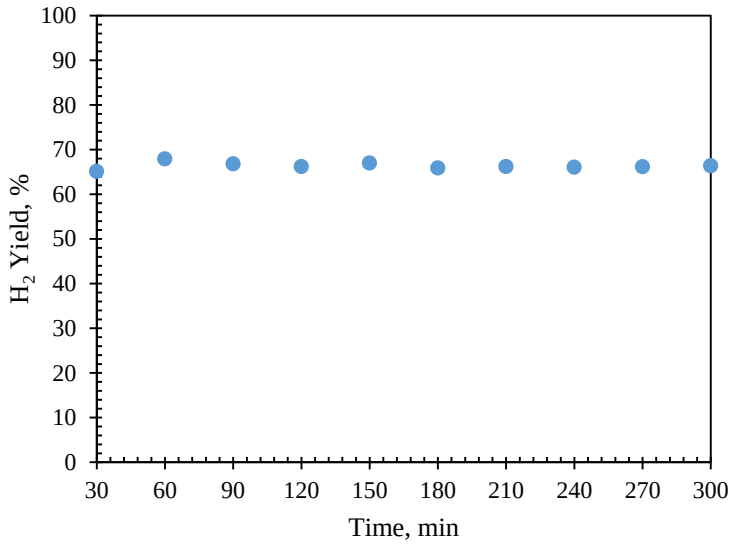

Figure 5.52 H_2 Yield of GSR (Catalyst:10Ni/SA(1035)(1035), T_{rxn}:965ºC, FFR:0.9ml/h, WGMR:3)

Similar to the gas products, H_2 yield was also steadily obtained with an average value of 66.4±1.2%.

The comparative results of the performed feed flow rates were given in Figures 5.53-5.54.

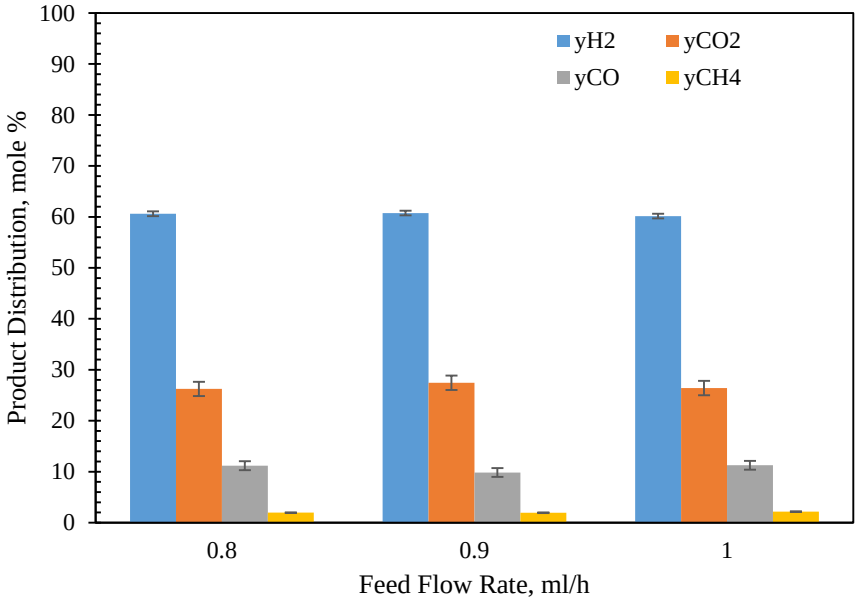

Figure 5.53 The Effect of Feed Flow Rate on Product Distribution (Catalyst:10Ni/SA(1035)(1035), T_{rxn}:965°C, WGMR:3)

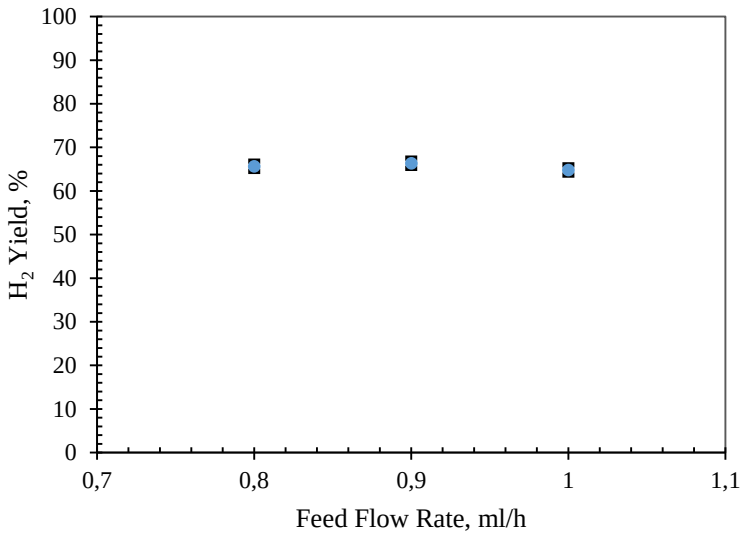

Figure 5.54 The Effect of Feed Flow Rate on H_2 Yield (Catalyst:10Ni/SA(1035)(1035), T_{rxn}:965°C, WGMR:3)

According to results of the feed flow rate experiments (Figures 5.53-5.54), both mole compositions of the produced gases and H_2 yield values are similar. The H_2 yield values were attained as 65.7%, 66.4% and 64.8% with a standard deviation of 1.2, at 0.8, 0.9 and 1.0 ml/h feed flow rates, respectively. Therefore, it is clearly deduced that the effect of feed flow rate is insignificant in the flow rate range tested.

5.2.3 The Effect of Temperature on H_2 Yield

To examine the effect of temperature on H_2 yield, the experiments were carried out between 450°C and 1050°C with the W/G molar ratio of 3 and at 0.9 ml/h glycerol-water feed flow rate and 30 ml/min Ar flow rate under atmospheric pressure over 10Ni/SA(700)(1035). At these reaction conditions, 4 compounds, H_2, CO_2, CO and CH_4 were produced with approximately complete glycerol conversions in all experiments, except for the reaction carried out at 540°C with a glycerol conversion of 96.5%. The product distributions and H_2 yield results at 680°C were demonstrated in Figures 5.55-5.56.

The product distributions and H_2 yield values as a function of time at the other temperatures were given in Figures G.5-G.22 in Appendix G.

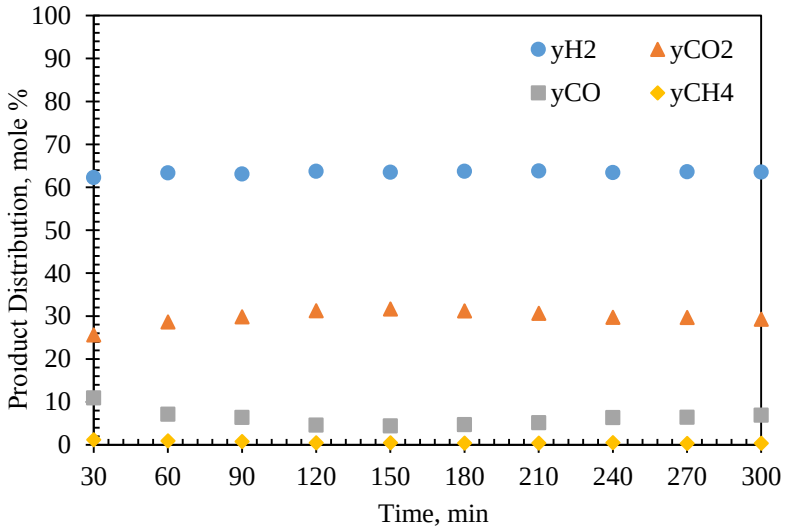

Figure 5.55 Product Distribution of GSR

(Catalyst:10Ni/SA(700)(1035), T_{rxn}:680°C, FFR:0.9ml/h, WGMR:3)

According to Figure 5.55, it is clear that after 90 minutes, the gas compounds were produced with approximately the same mole percent in a time interval of 30 minutes. This indicates that the product distribution remained steady during the reaction time, 5h. Under these reaction conditions, the average mole percent of the produced H_2, CO_2, CO, and CH_4 are 63.4±0.1%, 29.7±1.8%, 6.3±2.1%, and 0.6±0.2%, respectively.

Considering the average mole compositions of gas compounds, glycerol steam reforming, glycerol decomposition, reverse water gas shift reactions may occur, resulting in the formations of H_2, CO_2 and CO.

Glycerol Steam Reforming:

$C_3H_8O_3 + 3H_2O \leftrightarrow 3CO_2 + 7H_2$ $\Delta H_R = 128$ kJ/mole

Glycerol Decomposition:

$C_3H_8O_3 \rightarrow 3CO + 4H_2$ $\Delta H_R = 250$ kJ/mole

Reverse Water Gas Shift Reaction:

$CO_2 + H_2 \leftrightarrow CO + H_2O$ $\Delta H_R = 41$ kJ/mole

However, low amount of CH_4 formation may be attributed to methanation, reverse methane dry reforming and reverse methane steam reforming reactions.

Methanation:

$CO_2 + 4H_2 \leftrightarrow CH_4 + 2H_2O$ $\Delta H_R = -165$ kJ/mole

Reverse Methane Dry Reforming:

$2CO + 2H_2 \leftrightarrow CH_4 + CO_2$ $\Delta H_R = -259$ kJ/mole

Reverse Methane Steam Reforming:

$CO + 3H_2 \leftrightarrow CH_4 + H_2O$ $\Delta H_R = -206$ kJ/mole

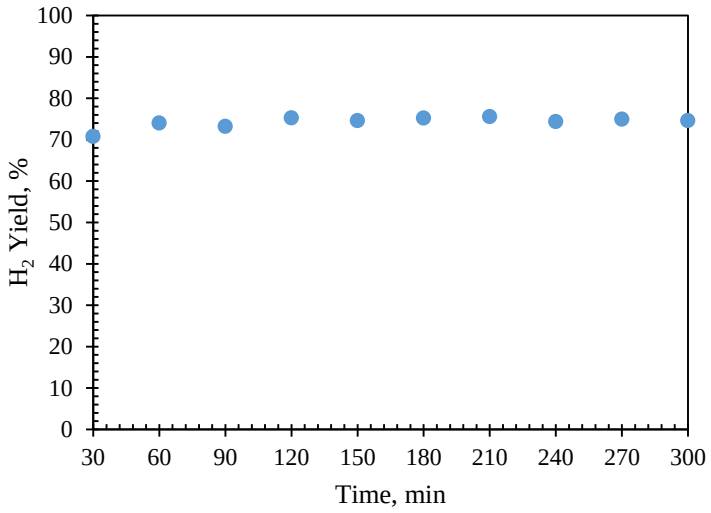

Figure 5.56 H_2 Yield of GSR
(Catalyst:10Ni/SA(700)(1035), T_{rxn}:680°C, FFR:0.9ml/h, WGMR:3)

Similar to the gaseous products, as depicted in Figure 5.56, H_2 yield was also steadily obtained with an average value of 74.2±0.2%.

Figure 5.57 indicates the product distribution with respect to temperature values performed and Figure 5.58 indicates the experimental and equilibrium values of H_2 yield.

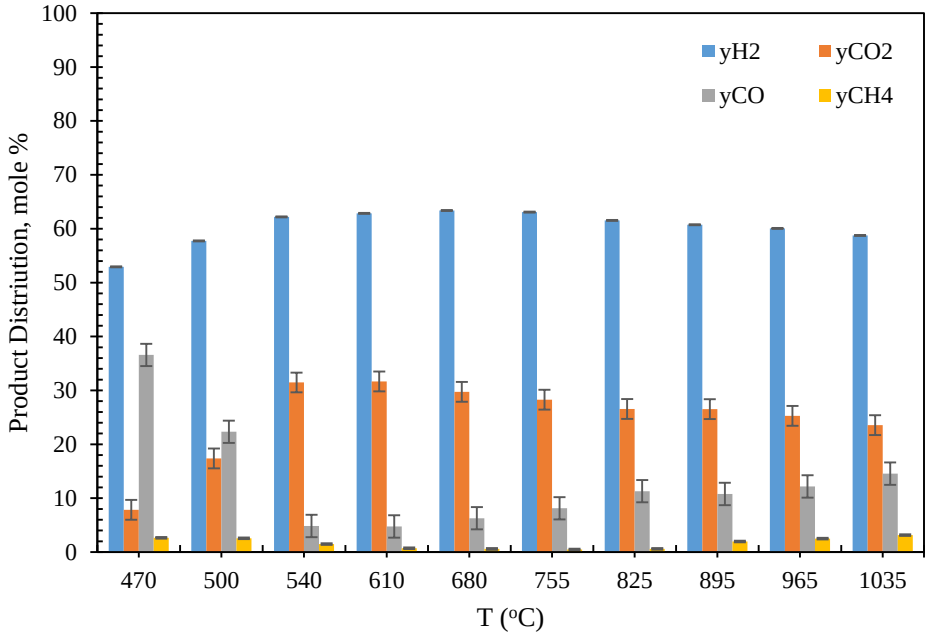

Figure 5.57 The Effect of Temperature on Product Distribution
(Catalyst:10Ni/SA(700)(1035), FFR:0.9ml/h, WGMR:3)

According to Figure 5.57, before 540°C, there is a notable increase in both H_2 and CO_2 formation and decrease in CO formation with an increase in temperature. After this temperature, the formation of CO instead of CO_2 increases, which may be ascribed to the reverse water gas shift reaction, may also occur before 540°C, and results in high CO formation with low H_2 and CO_2 formations. After this temperature, there is a slight increase in H_2 formation. Due to the endothermic nature of glycerol steam reforming and glycerol decomposition reactions, H_2 formation rises at elevated temperature. Low CH_4 formation can be attributed to the methanation, reverse methane steam reforming and reverse methane dry reforming reactions.

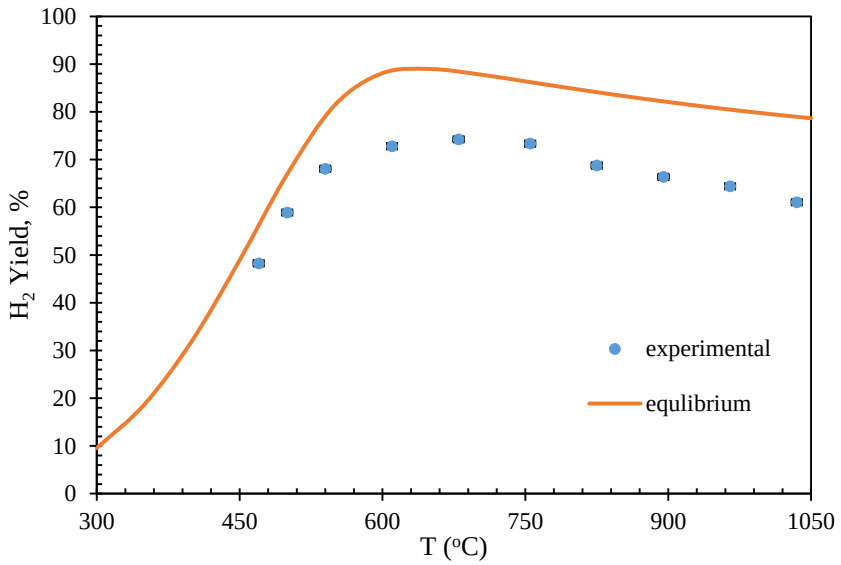

Figure 5.58 The Effect of Temperature on H_2 Yield
(Catalyst:10Ni/SA(700)(1035), FFR:0.9ml/h, WGMR:3)

As depicted in Figure 5.58, the highest H_2 yield were attained as 74.2% at 680°C with a standard deviation of 0.2. The decrease in H_2 yield is observed before and after 680°C; this is consistent with the equilibrium values, which implies that the experimental results of the temperature studies displayed a similar trend to the equilibrium curve.

To sum up, at 680°C with the W/G molar ratio of 3 (mole/mole ratio is 12), 5.20 moles of H_2 were produced and 74.2% H_2 yield and approximately complete conversion were achieved in the presence of 10Ni/SA(700)(1035). In addition, at 610°C and at the same above-stated conditions, 5.12 moles of H_2 were produced, approximately complete glycerol conversion and 73.1% H_2 yield were achieved in the presence of same catalyst. Compared to literature, Demsash et al. (2018) achieved approximately complete conversion and H_2 yields of 79% and 86% in the presence of 10Ni/Al_2O_3-5CeO_2 and 10Ni-1Ru/Al_2O_3-5CeO_2, respectively, at 650°C, atmospheric pressure with the W/G (mole/mole) ratio of 12. In addition, Thyssen et

al. (2014) obtained 52% glycerol conversion and produced 2.2 moles of H_2 at 600°C with the W/G molar ratio of 3 in the presence of 10Ni/SiO_2. They also reached approximately complete conversion at the same conditions in the presence of 10Ni/10La_2O_3-SiO_2 and increased the moles of H_2 produced to 3.8.

5.2.4 The Effect of Feed Ratio on H_2 Yield

To examine the effect of feed ratio on H_2 yield, the experiments were performed at 680°C, at 0.9 ml/h glycerol-water feed flow rate and 30 ml/min Ar flow rate under atmospheric pressure with the W/G molar ratio of 1, 3, 6 and 9 over 10Ni/SA(700)(1035). At these reaction conditions, 4 compounds, H_2, CO_2, CO and CH_4 were produced with approximately complete glycerol conversions in all experiments, except for the reaction carried out at W/G molar ratio of 1 with a glycerol conversion of 91.1%. The product distributions and H_2 yield results at 680°C with the W/G molar ratio of 9 in Figures 5.59-5.60.

The product distributions and H_2 yield values as a function of time at W/G molar ratio of 1 & 6 were given in Figures G.23-G.26 in Appendix G. (The product distributions and H_2 yield values as a function of time at W/G molar ratio of 3 were given in section 5.2.3 The Effect of Temperature on H_2 Yield)

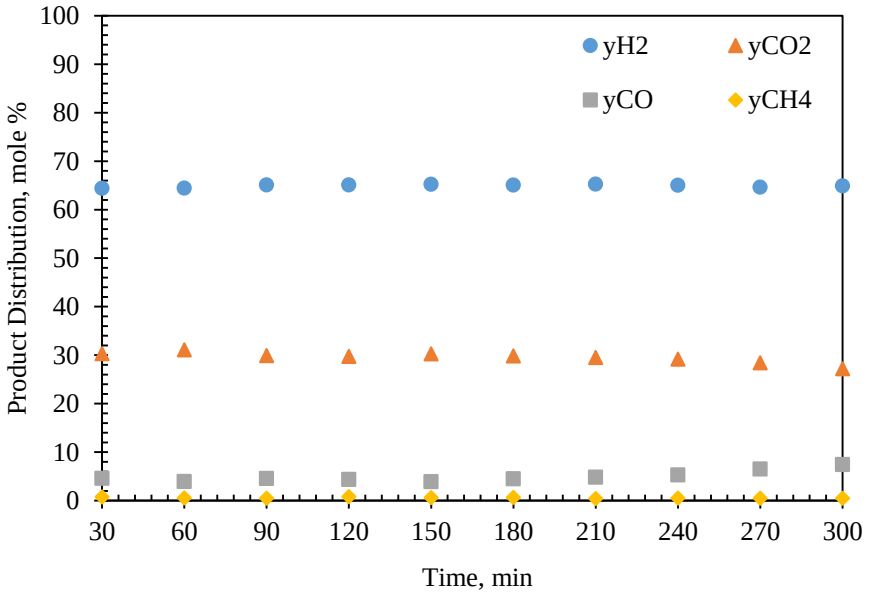

Figure 5.59 Product Distribution of GSR
(Catalyst:10Ni/SA(700)(1035), T_{rxn}:680°C, FFR:0.9ml/h, WGMR:9)

According to Figure 5.59, it is clear that after 90 minutes, the gas compounds were produced with approximately the same mole percent in a time interval of 30 minutes. This indicates that the product distribution remained steady during the reaction time, 5h. Under these reaction conditions, the average mole percent of the produced H_2, CO_2, CO, and CH_4 are 64.9±0.3%, 29.5±0.7%, 5.0±0.5%, and 0.6±0.4%, respectively.

Depending on the product mole distribution, following reactions may occur:

Glycerol Steam Reforming:

$C_3H_8O_3 + 3H_2O \leftrightarrow 3CO_2 + 7H_2$ $\Delta H_R = 128$ kJ/mole

Water Gas Shift Reaction:

$CO + H_2O \leftrightarrow CO_2 + H_2$ $\Delta H_R = -41$ kJ/mole

However, a low amount of CH_4 may be formed in reverse methane steam reforming and reverse methane dry reforming reactions, which is then convert into CO_2 and H_2 by reverse methanation reaction.

Reverse Methanation:

$CH_4 + 2H_2O \leftrightarrow CO_2 + 4H_2$ $\Delta H_R = 165$ kJ/mole

Reverse Methane Dry Reforming:

$2CO + 2H_2 \leftrightarrow CH_4 + CO_2$ $\Delta H_R = -259$ kJ/mole

Reverse Methane Steam Reforming:

$CO + 3H_2 \leftrightarrow CH_4 + H_2O$ $\Delta H_R = -206$ kJ/mole

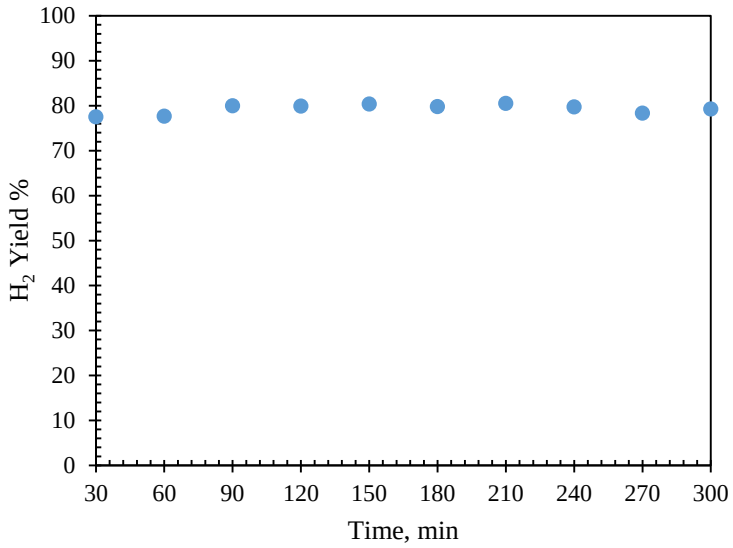

Figure 5.60 H_2 Yield of GSR
(Catalyst:10Ni/SA(700)(1035), T_{rxn}:680°C, FFR:0.9ml/h, WGMR:9)

Similar to the gas compounds, as depicted in Figure 5.60, H_2 yield was also steadily obtained with an average value of 79.3±1.0%.

The comparative results of the performed feed ratios with the equilibrium values were demonstrated in Figures 5.61-5.62, respectively.

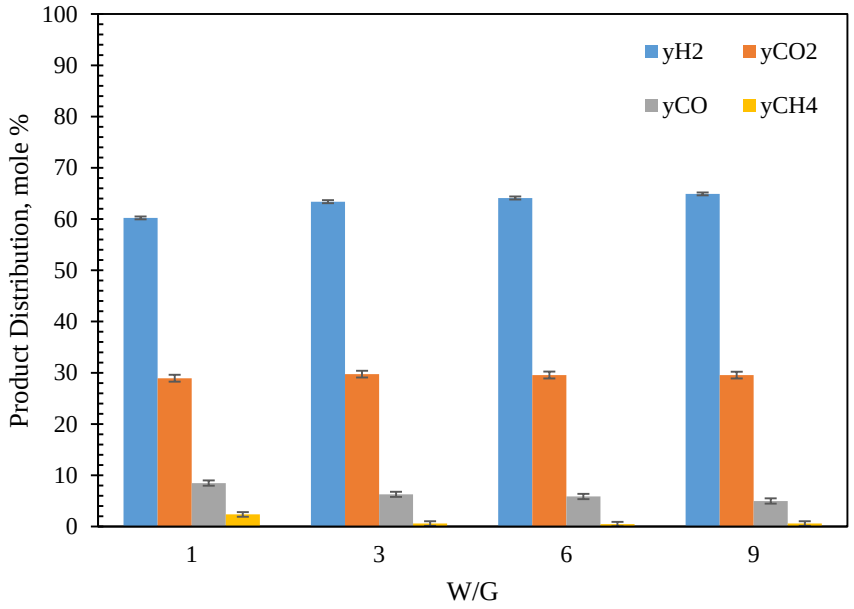

Figure 5.61 The Effect of Molar Feed Ratio on Product Distribution (Catalyst:10Ni/SA(700)(1035), T_{rxn}:680°C, FFR:0.9ml/h)

According to Figure 5.61, increase in water amount increases the H_2 formation, while decreases the CO formation. The reason behind the positive effect of high W/G molar ratio on H_2 formation is ascribed to the shift in WGS reaction to the product side which leads to high conversion of CO into H_2.

However, increase in CO and CH_4 formations with a decrease in W/G molar ratio may be ascribed to glycerol decomposition, reverse methane steam reforming and reverse methane dry reforming reactions.

Glycerol Decomposition:

$C_3H_8O_3 \rightarrow 3CO + 4H_2$ $\Delta H_R = 250$ kJ/mole

Reverse Methane Dry Reforming:

$2CO + 2H_2 \leftrightarrow CH_4 + CO_2$ $\Delta H_R = -259$ kJ/mole

Reverse Methane Steam Reforming:

$CO + 3H_2 \leftrightarrow CH_4 + H_2O$ $\Delta H_R = -206$ kJ/mole

It is also seen that increase in water amount decreases the formation of CH_4, which may be attributed to the conversion of CH_4 formed in reverse methane steam reforming and reverse methane dry reforming reactions into CO_2 and H_2 in reverse methanation reaction.

Reverse Methanation:

$CH_4 + 2H_2O \leftrightarrow CO_2 + 4H_2$ $\Delta H_R = 165$ kJ/mole

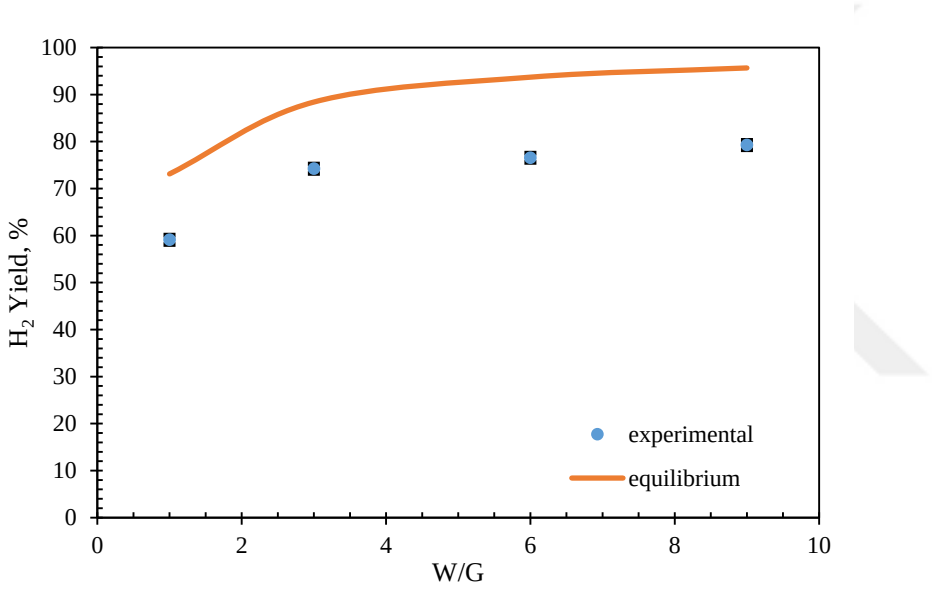

Figure 5.62 The Effect of Molar Feed Ratio on H_2 Yield
(Catalyst:10Ni/SA(700)(1035), T_{rxn}:680°C, FFR:0.9ml/h, WGMR:9)

According to Figure 5.62, it is clearly deduced that increase in W/G ratio increases the H_2 yield consistent with the equilibrium values. The highest H_2 yield was obtained as 79.3% at the W/G molar ratio of 9 with a standard deviation of 1.0. In addition, 5.36 moles of H_2 were produced referring to 76.6% of H_2 yield with approximately complete glycerol conversion at the W/G molar ratio of 6.

Compared to literature, Adhikari et al., (2008) reached approximately complete conversion and 57% of H_2 yield at 650^oC with the W/G molar ratio of 6 in the presence of 15Ni/MgO.

Furthermore, Profeti et al., (2009) tested the activities of 5Ni/Al_2O_3-10CeO_2 and 0.3Ru-5Ni/Al_2O_3-10CeO_2 at 700^oC, atmospheric pressure with the W/G molar ratio of 6. At these conditions, in the presence of 5Ni/Al_2O_3-10CeO_2, glycerol conversion and the number of moles of H_2 produced as 65% and 2.20, respectively. They also increased the glycerol conversion and the number of moles of H_2 produced to 89% and 2.36, respectively, using 0.3Ru-5Ni/Al_2O_3-10CeO_2.

5.2.5 The Effect of Catalyst Synthesis Method on H_2 Yield

To examine the effect of synthesis method on H_2 yield, the experiments were performed at 470, 550 and 680^oC, at 0.9 ml/h glycerol-water feed flow rate and 30 ml/min Ar flow rate under atmospheric pressure with the W/G molar ratio of 9 over 10Ni/SA(700)(1035) and 10Ni/SA(700)(1035)-wet. At these reaction conditions, 4 compounds, H_2, CO_2, CO, and CH_4 were produced with approximately complete glycerol conversions in all experiments. The product distributions and H_2 yield results of 10Ni/SA(700)(1035) at 550^oC with the W/G molar ratio of 9 were demonstrated in Figures 5.63-5.64, respectively.

The product distributions and H_2 yield values of 10Ni/SA(700)(1035) at 470^oC and *10Ni/SA(700)(1035)-wet at 470^oC, 550^oC and 680^oC as a function of time were given in Figures G.27-G.34 in Appendix G. (The product distributions and H_2 yield values of 10Ni/SA(700)(1035) at 680^oC were given in section 5.2.4 The Effect of Feed Ratio on H_2 Yield)*

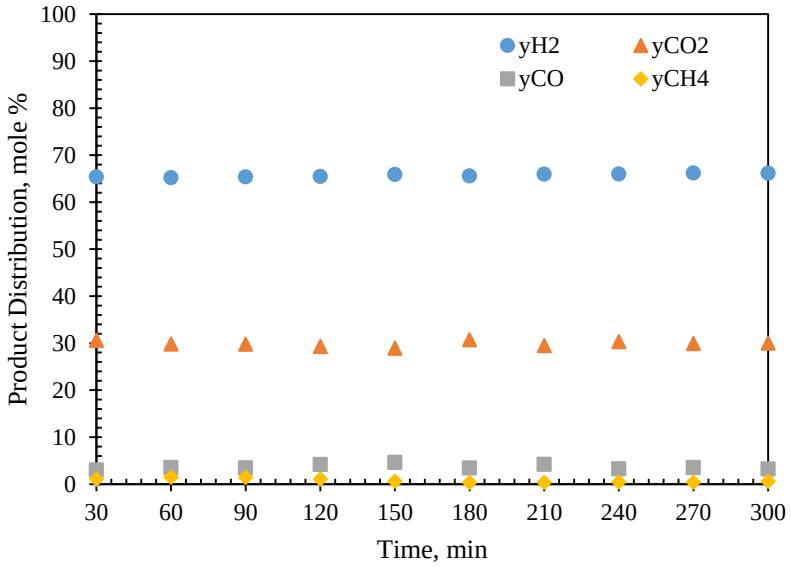

Figure 5.63 Product Distribution of GSR

(Catalyst:10Ni/SA(700)(1035), T_{rxn}:550°C, FFR:0.9ml/h, WGMR:9)

According to Figure 5.63, it is clear that after 90 minutes, the gas compounds were produced with approximately the same mole percent in a time interval of 30 minutes. This indicates that the product distribution remained steady during the reaction time, 5h. Under these reaction conditions, the average mole percent of the produced H_2, CO_2, CO, and CH_4 are 65.7±0.3%, 29.9±0.7%, 3.6±0.5%, and 0.8±0.4%, respectively.

According to the product mole distribution, following reactions may occur:

Glycerol Steam Reforming:

$C_3H_8O_3 + 3H_2O \leftrightarrow 3CO_2 + 7H_2$ $\Delta H_R = 128$ kJ/mole

Water Gas Shift Reaction:

$CO + H_2O \leftrightarrow CO_2 + H_2$ $\Delta H_R = -41$ kJ/mole

In addition, low amount of CH_4 formation may be attributed to methanation, reverse methane dry reforming and reverse methane steam reforming reactions.

Methanation:

$CO_2 + 4H_2 \leftrightarrow CH_4 + 2H_2O$ ΔH_R = -165 kJ/mole

Reverse Methane Dry Reforming:

$2CO + 2H_2 \leftrightarrow CH_4 + CO_2$ ΔH_R = -259 kJ/mole

Reverse Methane Steam Reforming:

$CO + 3H_2 \leftrightarrow CH_4 + H_2O$ ΔH_R = -206 kJ/mole

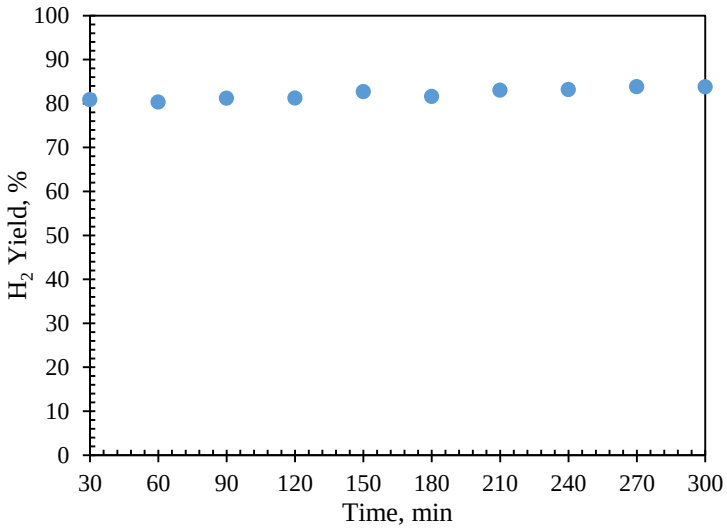

Figure 5.64 H_2 Yield of GSR
(Catalyst:10Ni/SA(700)(1035), T_{rxn}:550°C, FFR:0.9ml/h, WGMR:9)

Similar to the gas compounds, H_2 yield was also steadily obtained with an average value of 82.1±1.0%.

The comparative results of the performed temperatures of the catalysts with the equilibrium values were demonstrated in Figures 5.65-5.66, respectively.

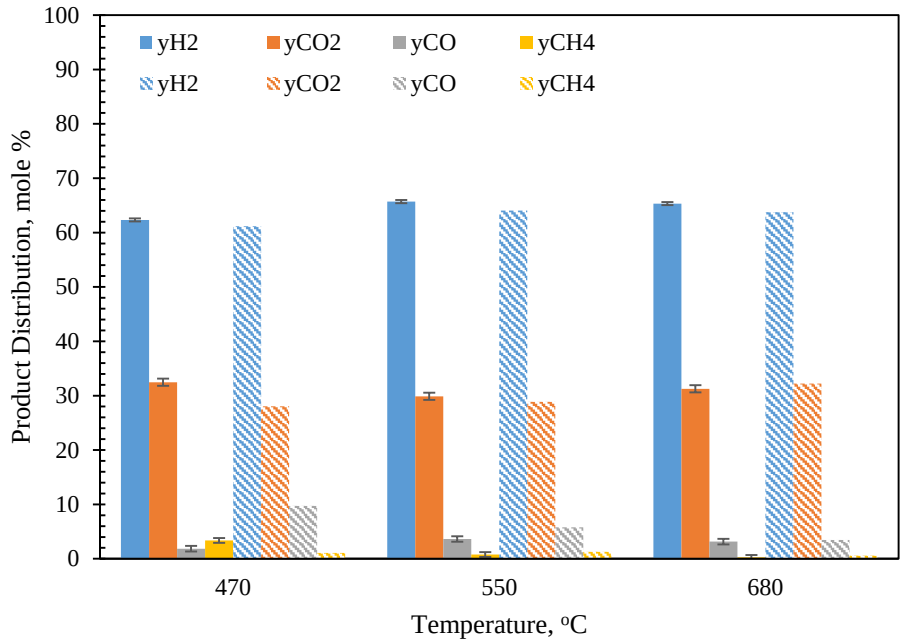

Figure 5.65 The Effect of Catalyst Synthesis Method on Product Distribution (Filled Symbols: Co-precipitation, Patterned Symbols: Wet-impregnation) (Catalyst: 10Ni/SA(700)(1035), FFR:0.9ml/h, WGMR:9)

According to Figure 5.65, when each reaction temperature was examined separately, higher H_2, CO_2 and CH_4 formations were achieved in the presence of 10Ni/SA synthesized by co-precipitation method in experiments performed at 470°C; on the contrary, CO formation was quite low compared to the catalyst synthesized by the wet-impregnation method. Although the mole product distributions were similar at 550°C, H_2 formation was higher in the presence of catalyst synthesized by co-precipitation method. In addition, when the product distributions are compared in the presence of both catalyst at 680°C, it is clear that H_2 and CO formations are higher in the presence of catalyst synthesized by co-precipitation method. However, CO_2 formation was higher in the presence of catalyst synthesized by wet-impregnation method. Apart from these, CH_4 formations were quite similar in both catalysts. Nonetheless, it is clear that the product distributions in both catalysts are quite close.

As depicted in Figure 5.66, the highest H_2 yield were attained as 82.1% in the presence of 10Ni/SA synthesized by co-precipitation technique at 550°C with a standard deviation of 1.0. The decrease in H_2 yield is observed before and after 550°C; this is consistent with the equilibrium values, which implies that the experimental results of the temperature studies at the W/G molar ratio of 9 displayed a similar trend to the equilibrium curve. In addition, the synthesis method slightly affected the H_2 yield by decreasing the value to 76.4% at 550°C in the presence of 10Ni/SA synthesized by the wet-impregnation method.

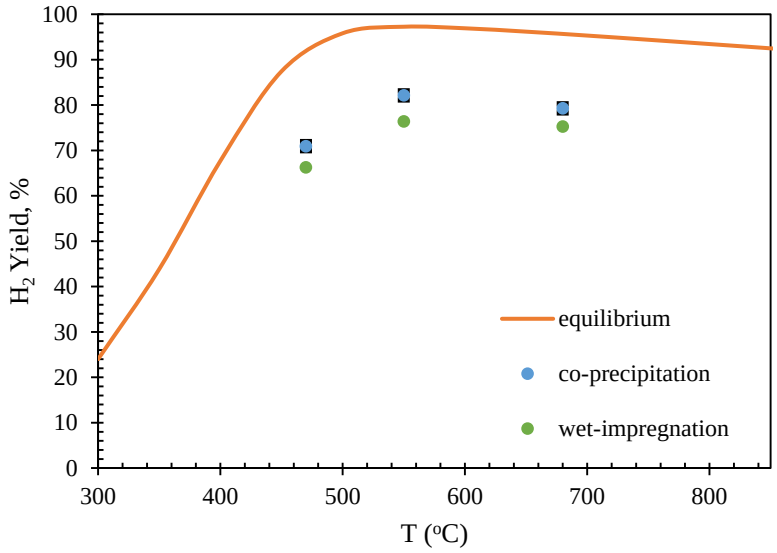

Figure 5.66 The Effect of Catalyst Synthesis Method on H_2 Yield
(Filled Symbols: Co-precipitation, Patterned Symbols: Wet-impregnation)
(Catalyst: 10Ni/SA(700)(1035), FFR:0.9ml/h, WGMR:9)

5.2.6 The Effect of Catalyst Type on H_2 Yield

The effect of catalyst type on H_2 yield was examined in 3 parts: effect of metal amount, effect of monometal type, and effect of bi and trimetal type on H_2 yield. Detailed catalytic activity test results were given in the relevant sections.

5.2.6.1 The Effect of Metal Amount on H_2 Yield

To examine the effect of metal amount on H_2 yield, 2.5, 5, 8 and 10 % by weight of Ni doped silica aerogels were tested at 550°C, at 0.9 ml/h glycerol-water feed flow rate and 30 ml/min Ar flow rate under atmospheric pressure with the W/G molar ratio of 9. Prior to experiments, all catalysts were calcined under dry air at 700°C for 5 h and then reduced by H_2 flow at 1035°C for half an hour. At these reaction conditions, 4 compounds, H_2, CO_2, CO, and CH_4 were produced with approximately complete glycerol conversions in all experiments. The comparative results of the metal amount experiments were demonstrated in Figures 5.67-5.68, respectively.

The product distributions and H_2 yield values of 2.5, 5 and 8 % by weight of Ni doped silica aerogels as a function of time were given in Figures G.35-G.40 in Appendix G. (The experimental results of 10 % by weight Ni doped silica aerogel was given in section 5.2.4 The Effect of Feed Ratio)

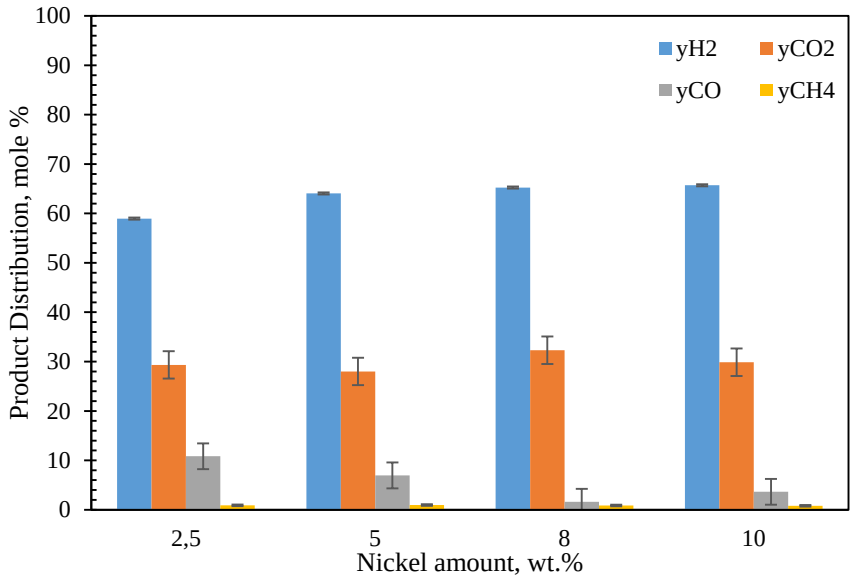

Figure 5.67 The Effect of Nickel Amount Loaded onto Silica Aerogel on Product Distribution

(T_{rxn}:550°C, FFR:0.9ml/h, WGMR:9)

According to Figure 5.67, it is clear that increase in the metal amount from 2.5 % to 5% leads to a notable increase in H_2 formation; however, H_2 formation slightly increases with an increase in metal amount from 5% to 10%. In addition, as the amount of metal increased, CO formation decreased; however, both CO_2 and CH_4 formations were not affected by this increase and obtained similarly in all metal amounts tested.

According to Figure 5.68, the highest H_2 yield was obtained in the presence of 10% by weight nickel doped silica aerogel, which may be ascribed to increase in active sites with an increase in metal amount. Under these reaction conditions, H_2 yield was attained as 82.1% with a standard deviation of 1.0.

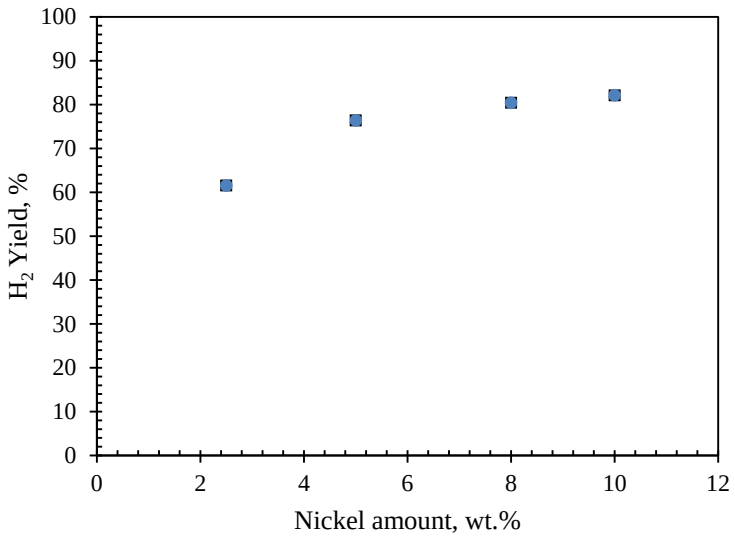

Figure 5.68 The Effect of Nickel Amount Loaded onto Silica Aerogel on H_2 Yield (T_{rxn}:550^{o}C, FFR:0.9ml/h, WGMR:9)

5.2.6.2 The Effect of Monometal Type on H_2 Yield

To examine the effect of metal type on H_2 yield, promising metals such as Co, Cr, Zr, Mo, and Ag in addition to Ni were loaded 10 % by weight on silica aerogel. All

synthesized catalysts were calcined under dry air at 700°C for 5h and subsequently reduced by H_2 flow at 1035°C for half an hour. The catalytic activities of all catalysts were tested at 550°C, at 0.9 ml/h glycerol-water feed flow rate and 30 ml/min Ar flow rate under atmospheric pressure with the WGMR of 9. At these reaction conditions, 4 compounds, H_2, CO_2, CO and CH_4 were produced with approximately complete glycerol conversions in all experiments. The comparative results of the metal type experiments were demonstrated in Figures 5.69-5.70, respectively.

The product distributions and H_2 yield values of Zr, Co, Cr, Mo and Ag loaded silica aerogels as a function of time were given in Figures G.41-G.50 in Appendix G. (The experimental results of 10 % by weight Ni doped silica aerogel was given in section 5.2.4 The Effect of Catalysts Synthesis Method on H_2 Yield)

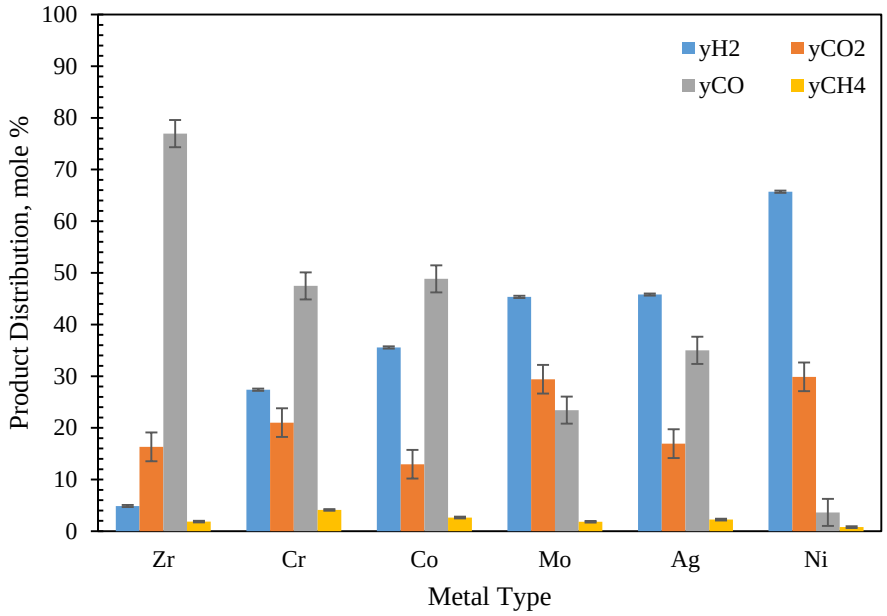

Figure 5.69 The Effect of 10% by wt. Metal Type Loaded onto Silica Aerogel on Product Distribution
(T_{rxn}:550°C, FFR:0.9ml/h, WGMR:9)

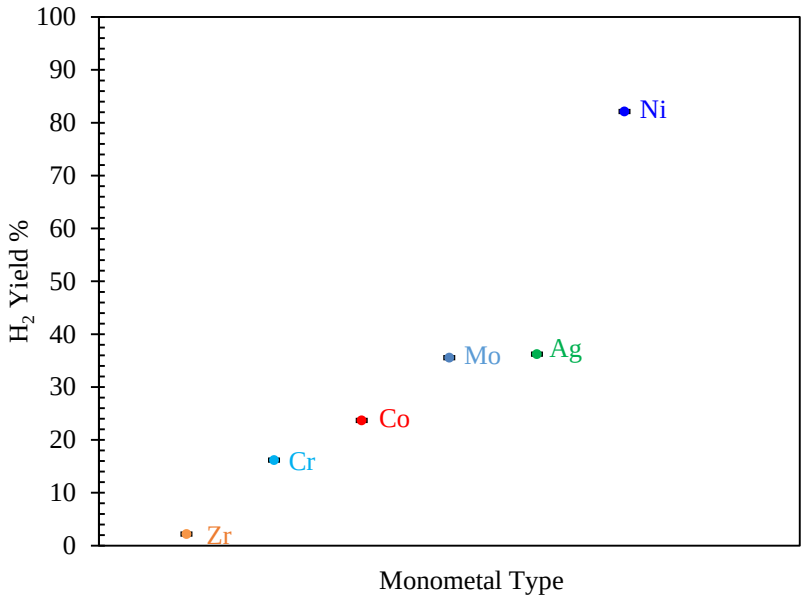

Figure 5.70 The Effect of 10% by wt. Metal Type Loaded onto Silica Aerogel on H_2 Yield

(T_{rxn}:550°C, FFR:0.9ml/h, WGMR:9)

According to Figure 5.69, Mo loaded SA exhibits similar behaviour with Ni as producing CO_2 more than CO, which may be attributed to GSR and WGSR. However, high amount of CO formation with low amount of CH_4 formation may be interpreted by reverse methane steam reforming and reverse methane dry reforming reactions.

Besides Ni and Mo, CO formation is higher than the CO_2 formation in the presence of Ag loaded SA that may be ascribed to the reverse WGSR. Furthermore, methanation, reverse methane steam reforming and reverse methane dry reforming may occur, resulting in low amount of CH_4 formation.

In Co, Cr and Zr loaded SA high amount of CO formation with low amount of CO_2 and H_2 formations may be attributed to reverse WGSR. It may be also said that, CO_2 and H_2 may convert into CH_4 in methanation reaction.

To sum up, among all tested metals, the highest H_2 formation with the lowest CO and CH_4 formations were achieved in the presence of Ni loaded SA. The reason behind the superior catalytic activity of Ni is its high ability to break the C-C, C-H and H-O bonds, promoting to both GSR and WGS reactions and thus increase the hydrogen formation. In addition, Mo loaded SA displayed a similar behaviour to Ni despite the low H_2 formation. In the presence of monometallic Ni and monometallic Mo, CO_2 was formed more than CO, indicating that both catalysts promoted the WGSR to the product side. Nevertheless, H_2 formation is quite low compared to Ni. Moreover, Ag catalysts exhibited almost the same H_2 formation as Mo, while CO formation was much higher in Ag than Mo, indicating that Ag favoured the reactant side in WGSR. The rest of the metals, Co, Cr and Zr displayed much lower activity; in fact, in the presence of Zr, the H_2 formation is the lowest with the mole fraction of around 5%, while CO formation is much higher compared to other metals. Aside from these, Co exhibited higher H_2 formation with lower CO_2 formation compared to Cr. However, in the presence of both catalysts, the H_2 formations are quite low and CO formations are very high. Despite the highest CH_4 formation is observed in Cr loaded SA, all CH_4 formations are quite low, varying between 1% and 4%.

As depicted in Figure 5.70, the highest H_2 yield was obtained in the presence of Ni as 82.1% with a standard deviation of 0.8. However, the lowest H_2 Yield was obtained as 2.2% with a standard deviation of 0.8 in the presence of Zr. The overall activity of all tested catalysts increases in the following order: Zr<Cr<Co<Mo<Ag<Ni. Considering the activities of all monometallic catalysts, it is clear that Ni is the most active and appropriate catalyst for GSR.

Compared to some catalysts with literature, Carrero et al (2017) tested the activities of bimetallic catalysts as 15Ni-4Co/SBA-15 and 15Ni-4Cr/SBA-15 at 600^oC with the W/G molar ratio of 6. At these conditions, 92% glycerol conversion was achieved and 52% by mole H_2 was produced in the presence of 15Ni-4Co/SBA-15. They also increased the both glycerol conversion and amount of produced H_2 to 94% and 61%

by mole, respectively, using 15Ni-4Cr/SBA-15. In this study, the activities of Co and Cr monometallic catalysts loaded on SA as 10% by weight were tested at 550°C with the W/G molar ratio of 9. In the presence of both catalysts, approximately complete glycerol conversions were achieved, while mole compositions of H_2 were quite low, 27.4±0.2% and 35.6±0.2% in 10Cr/SA(700)(1035) and 10Co/SA(700)(1035), respectively.

5.2.6.3 The Effect of Bi and Trimetal Type on H_2 Yield

To examine the effect of additional metal type on H_2 yield, Ni and different metals such as Mo, Ru, Fe, Mg and Fe-Mn were loaded onto silica aerogel by co-precipitation method. Ni-Mo loaded silica aerogels were synthesized following two different routes explained in detail in section 4.1.2.2 Bimetal Loading. According to the experimental results of nickel-molybdenum loaded catalysts, other metal loaded catalysts were synthesized by the two-step metal loading path, namely the path I of Nickel-Molybdenum loading, due to the higher H_2 yield in the synthesis path. The synthesized catalysts were calcined under dry air for 5h and subsequently reduced by H_2 flow for half an hour. The loaded metal amounts and calcination & reduction temperatures were given in detail in Tables 4.1-4.2. All catalysts used in the reaction at 550°C, at 0.9 ml/h glycerol-water feed flow rate and 30 ml/min Ar flow rate under atmospheric pressure with the W/G molar ratio of 9. At these reaction conditions, 4 compounds, H_2, CO_2, CO, and CH_4 were produced with approximately complete glycerol conversions in all experiments.

The product distributions and H_2 yield % values as a function of time in the presence of 10Ni-2Ru/SA(700)(700) were demonstrated in Figures 5.71-5.72.

The product distributions and H_2 yield values of 8Ni-2Mo (I), 8Ni-2Mo (II), 10Ni-3Mg, 10Ni-3Fe, 10Ni-3Fe-0.3Mn, 10Ni-3Ru and 10Ni-1Ru loaded silica aerogels as a function of time were given in Figures G.51-G.64 in Appendix G.

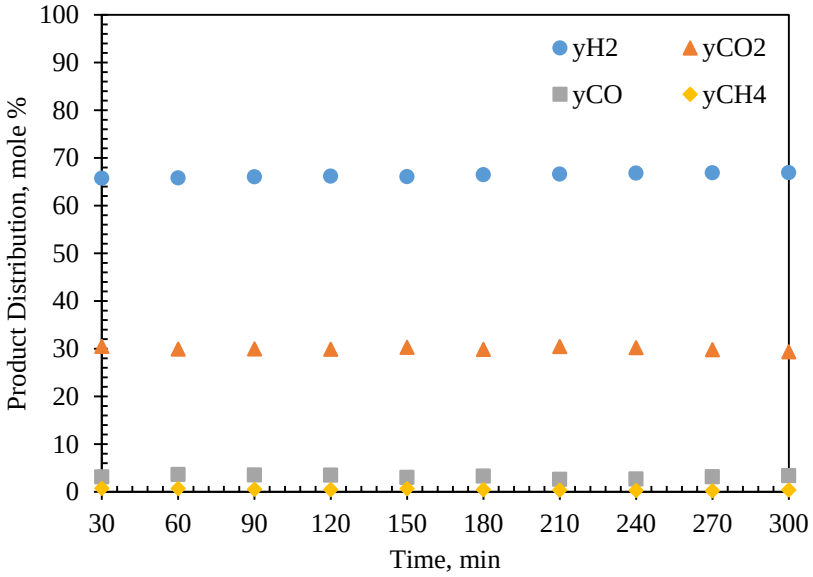

Figure 5.71 Product Distribution of GSR

(Catalyst:10Ni-2Ru/SA(700)(700), T_{rxn}:550°C, FFR:0.9ml/h, WGMR:9)

According to Figure 5.71, it is clear that after 30 minutes, the gas compounds were produced with approximately the same mole percent in a time interval of 30 minutes. This indicates that the product distribution remained steady during the reaction time, 5h. Under these reaction conditions, the average mole percent of the produced H_2, CO_2, CO, and CH_4 are 66.3±0.1%, 30.0±0.1%, 3.2±0.2%, and 0.5±0.1%, respectively.

Considering the product mole distribution, high amount of H_2 and CO_2 formations may be ascribed to glycerol steam reforming reaction.

Glycerol Steam Reforming:

$C_3H_8O_3 + 3H_2O \leftrightarrow 3CO_2 + 7H_2$ $\Delta H_R = 128$ kJ/mole

In addition, reverse WGS reaction may occur, resulting in CO formation.

Reverse Water Gas Shift Reaction:

$CO_2 + H_2 \leftrightarrow CO + H_2O$ $\Delta H_R = 41$ kJ/mole

The low amount of CH_4 formation may be interpreted as CH_4 may be formed by reverse methane dry reforming and reverse methane steam reforming and then converting into CO_2 and H_2 in reverse methanation reaction.

Reverse Methanation:

$CH_4 + 2H_2O \leftrightarrow CO_2 + 4H_2$ $\Delta H_R = 165$ kJ/mole

Reverse Methane Dry Reforming:

$2CO + 2H_2 \leftrightarrow CH_4 + CO_2$ $\Delta H_R = -259$ kJ/mole

Reverse Methane Steam Reforming:

$CO + 3H_2 \leftrightarrow CH_4 + H_2O$ $\Delta H_R = -206$ kJ/mole

Besides these reactions, CH_4 might also be converted into H_2 and carbon by the following reaction:

Carbon Formation:

$CH_4 \leftrightarrow 2H_2 + C$ $\Delta H_R = 75$ kJ/mole

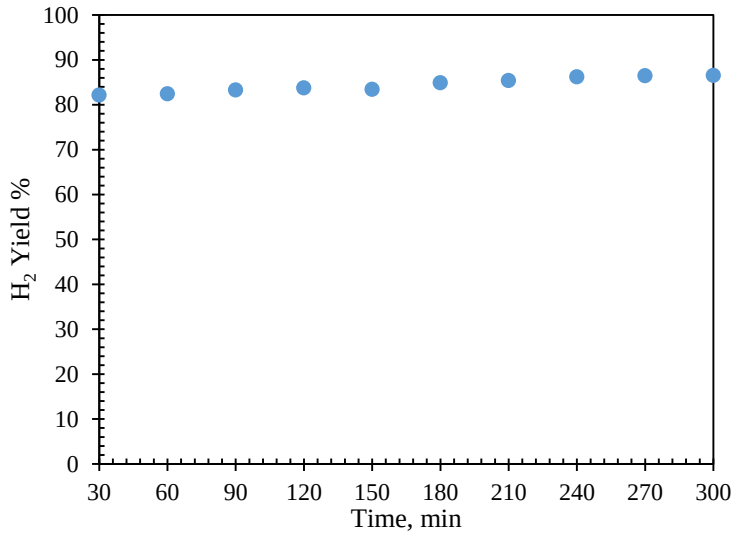

Figure 5.72 H_2 Yield of GSR

(Catalyst:10Ni-2Ru/SA(700)(700), T_{rxn}:550°C, FFR:0.9ml/h, WGMR:9)

Similar to the gas compounds, H_2 yield was also steadily obtained with an average value of 84.5±0.2%.

The comparative results of the bi & trimetal type experiments were demonstrated in Figures 5.73-5.74, respectively.

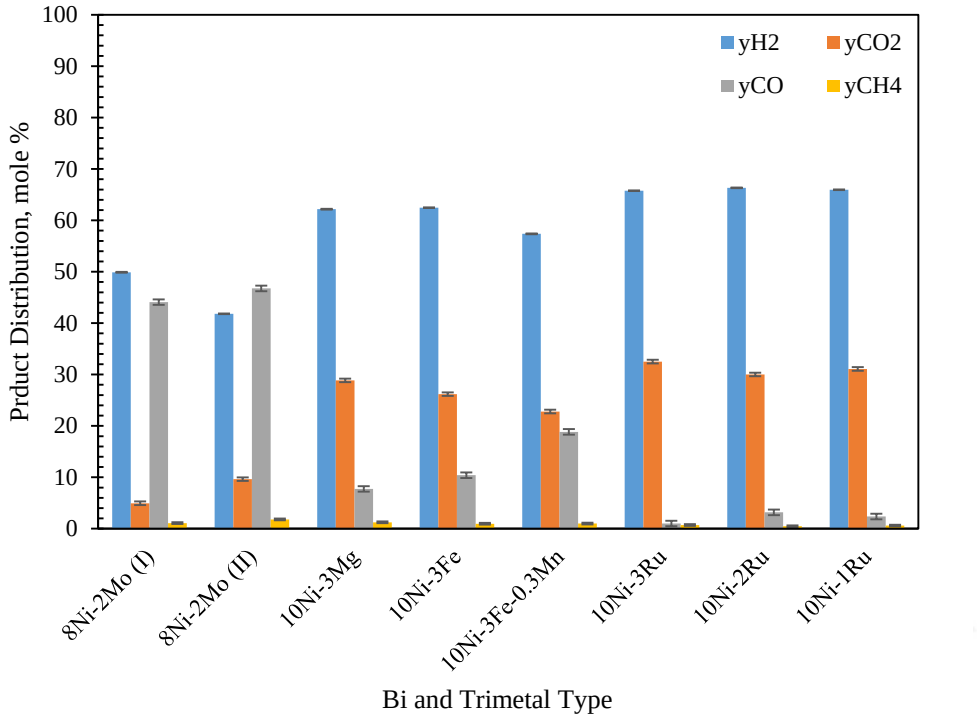

Figure 5.73 The Effect of Bi and Trimetal Type on Product Distribution (T_{rxn}:550°C, FFR:0.9ml/h, WGMR:9)

The low amount of H_2 formation with high amount of CO formation in the presence of 8Ni-2Mo/SA(I) and 8Ni-2Mo/SA(II) may be attributed to the reverse WGS reaction.

Reverse Water Gas Shift Reaction:

$CO_2 + H_2 \leftrightarrow CO + H_2O$ $\Delta H_R = 41$ kJ/mole

In addition, glycerol steam reforming, reverse methane dry reforming, reverse methane steam reforming and methanation reactions may occur, resulting in H_2, CO_2 and CH_4 formations.

Glycerol Steam Reforming:

$C_3H_8O_3 + 3H_2O \leftrightarrow 3CO_2 + 7H_2$ $\Delta H_R = 128$ kJ/mole

Reverse Methane Dry Reforming:

$2CO + 2H_2 \leftrightarrow CH_4 + CO_2$ $\Delta H_R = -259$ kJ/mole

Reverse Methane Steam Reforming:

$CO + 3H_2 \leftrightarrow CH_4 + H_2O$ $\Delta H_R = -206$ kJ/mole

Methanation:

$CO_2 + 4H_2 \leftrightarrow CH_4 + 2H_2O$ $\Delta H_R = -165$ kJ/mole

Besides Ni-Mo catalysts, same reactions may occur in 10Ni-3Mg, 10Ni-3Fe and 10Ni-3Fe-0.3Mn loaded silica aerogels. In the presence of both catalysts, H_2 and CH_4 formations were quite similar, while the formations of CO and CO_2 are different. Compared to other compounds, higher amount of H_2 formations may be ascribed to GSR. However, in the presence of 10Ni-3Fe, lower CO_2 and higher CO formed than in 10Ni-3Mg. This is ascribed to the presence of Fe promoting the WGSR to the reactant site (Bouarab et al., 2014) at high temperature due to the exothermic nature of WGSR. In addition, low CH_4 formations in both catalysts may be ascribed to methanation, reverse methane dry reforming and reverse methane steam reforming reactions. In addition, presence of Mn in 10Ni-3Fe resulted in a remarkable reduction in H_2 formation, despite its small amount loading i.e., 0.3 % by weight.

In the presence of Ni-Ru bimetallic catalysts, the highest H_2 formations were attained, ascribing to glycerol steam reforming and water gas shift reaction. The highest H_2 formation and the lowest CO_2 formation were obtained in the presence of

moderate Ru amount i.e., 2% by weight Ru. On the one hand, an increase in the amount of Ru from 2% to 3% resulted in an increase in CO_2 formation from 30.0±0.1% to 32.5±0.1% and a decrease in CO formation from 3.2±0.2% to 1.0±0.2. On the other hand, a decrease in the amount of Ru from 2% to 1% causes a slight increase in CO_2 formation from 30.0±0.1% to 31.1±0.1% and a decrease in CO formation from 3.2±0.2% to 2.4±0.2%. Among the Ru-loaded bimetallic catalysts, the lowest CO_2 and the highest CO formation were attained in the presence of catalyst containing 2% by weight Ru. The disproportionate change in CO_2 and CO formations may be attributed to the carbon formation reactions in addition to WGSR.

Carbon Formation:

$2CO \leftrightarrow CO_2 + C$ $\Delta H_R = -172$ kJ/mole

$CO + H_2 \leftrightarrow H_2O + C$ $\Delta H_R = -131$ kJ/mole

$CO_2 + 2H_2 \leftrightarrow 2H_2O + C$ $\Delta H_R = -90$ kJ/mole

In addition, CH_4 formations are close to zero in all Ni-Ru loaded catalyst, ascribing to produced CH_4 in methanation, reverse methane steam reforming and reverse methane dry reforming reactions may also convert into C by following reaction:

$CH_4 \leftrightarrow 2H_2 + C$ $\Delta H_R = 75$ kJ/mole

According to Figure 5.73, among all bi and trimetals tested, the highest H_2 formations were achieved in the presence of 10% by weight Ni and 1%, 2% and 3% by weight Ru loaded silica aerogels. The reason behind the positive effect of presence of Ru is its high ability to cleavage the C-C, C-H and C-O bonds, which increases the H_2 formation and thereby H_2 yield. (Demsash et al.,2018; Sun et al., 2017; Odenkirk et al., 1992)

Besides Ru loaded silica aerogels, Ni-Mg bimetallic catalysts showed moderate activity which may be due to Mg being in oxide form according to the XRD analysis

(Figure 5.18) (Lopez et al., 1998), which may reduce the ability of C-C and C-H bond rupture, and hence a decrease in H_2 yield compared to monometallic Ni.

In addition, presence of Fe, which is commercially used in WGS reactions (Bouarab 2014), also decreases the H_2 yield by shifting the WGS reaction to the reactant side. Furthermore, the addition of Mn increases CO formation and decreases the H_2 formation compared to non-containing, as the presence of Mn may prevent the sintering of Fe by increasing the thermal stability of the catalyst. Therefore, it may be said that both catalysts are more appropriate for low temperature WGS reactions.

However, it is clear that loading of Mo by following two different paths affected to H_2 formation quite negatively. The lowest H_2 formation and thereby lowest H_2 yield were obtained in the presence of these catalysts. In fact, the formation of CO is higher than H_2 formation by using 8Ni-2Mo synthesized following simultaneous metal loading explicitly described in section 4.1.2.7 Bimetal Loading. The reason of the lowest H_2 formations by using these catalysts might be ascribed to sintering of Mo, which causes a change in the surface structure, resulting in collapse of the pores and thus loss of catalyst activity (Bartholomew 2001). On the other hand, lower H_2 yield obtained in the presence of 8Ni-2Mo/SA(II) may be ascribed to the clogging of the pores by metal loading and/or the formation of inactive metallic-compounds and/or the agglomeration of metals causing a decrease in activity of the catalyst. In addition, the fact that 8Ni-2Mo/SA(II) has much smaller pore diameter compared to 8Ni-2Mo/SA(I), it might be deduced that the synthesis route of bimetallic catalysts affects the physical properties of these catalysts, resulting in a decrease in H_2 yield.

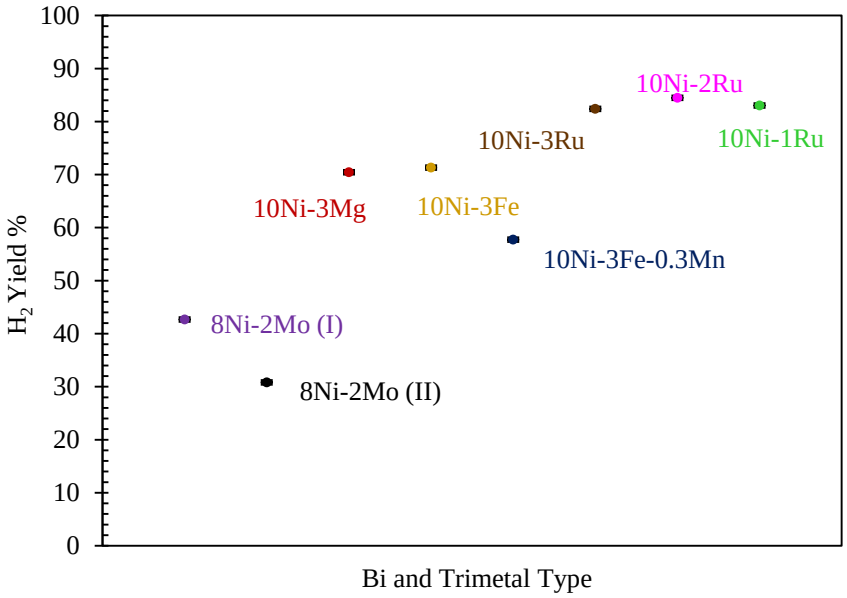

Figure 5.74 The Effect of Bi and Trimetal Type on H_2 Yield (T_{rxn}:550°C, FFR:0.9ml/h, WGMR:9)

As seen in Figure 5.74, the highest H_2 yield was obtained in the presence of 10Ni-2Ru as 84.5 % with a standard deviation of 0.2. However, the lowest H_2 yield was obtained as 30.8 % with a standard deviation of 0.2 in the presence of 8Ni-2Mo(II). The overall activity of all tested catalysts increases in the following order:

8Ni-2Mo(II)<8Ni-2Mo(I)<10Ni-3Fe-0.3Mn<10Ni-3Mg<10Ni-3Fe<10Ni-3Ru <10Ni-1Ru<10Ni-2Ru.

Considering the activities of all catalysts, it is clearly deduced that 10Ni-2Ru/SA is the most active and appropriate catalyst for GSR.

To sum up, the highest H_2 yield was achieved in the presence of 10Ni-2Ru/SA as 84.5% whereas the lowest H_2 yield was obtained as 2.2% in the presence of 10Zr/SA. In addition, the H_2 yield values of 10Ni-1Ru/SA, 10Ni-3Ru/SA, 10Ni/SA, and 8Ni/SA are quite acceptable and close to the yield obtained in 10Ni-2Ru/SA with the values of 83.0%, 82.4%, 82.1% and 80.4%, respectively.

Figure 5.75 shows all H_2 yields obtained from all synthesized catalysts.

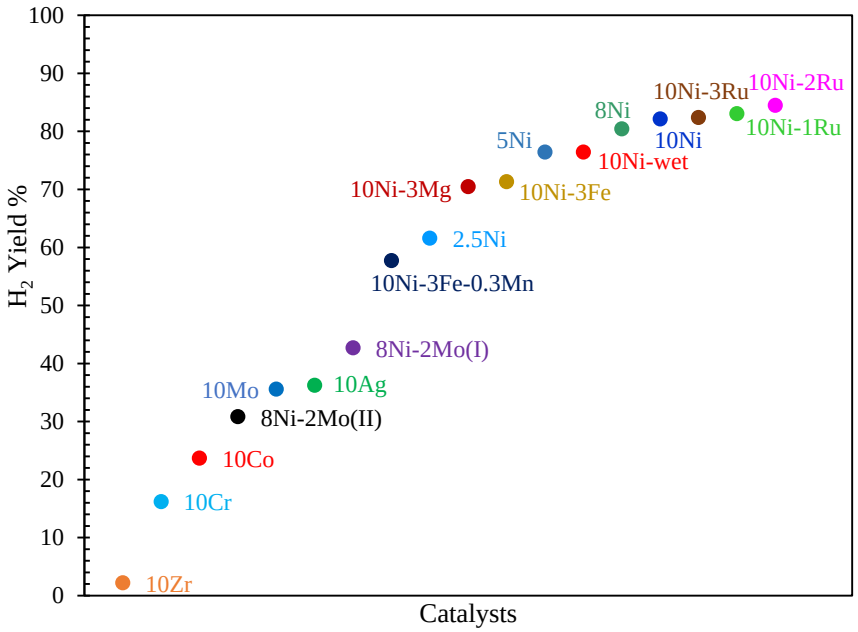

Figure 5.75 Comparison of All Catalysts

(T_{rxn}:550°C, FFR:0.9ml/h, WGMR:9)

Figure 5.76 depicts the comparison of the Lewis-to-(Lewis+Bronsted) acid sites of the catalysts calculated by the intensities of the Lewis and Lewis+Bronsted acid sites in DRIFT analysis of the fresh catalysts.

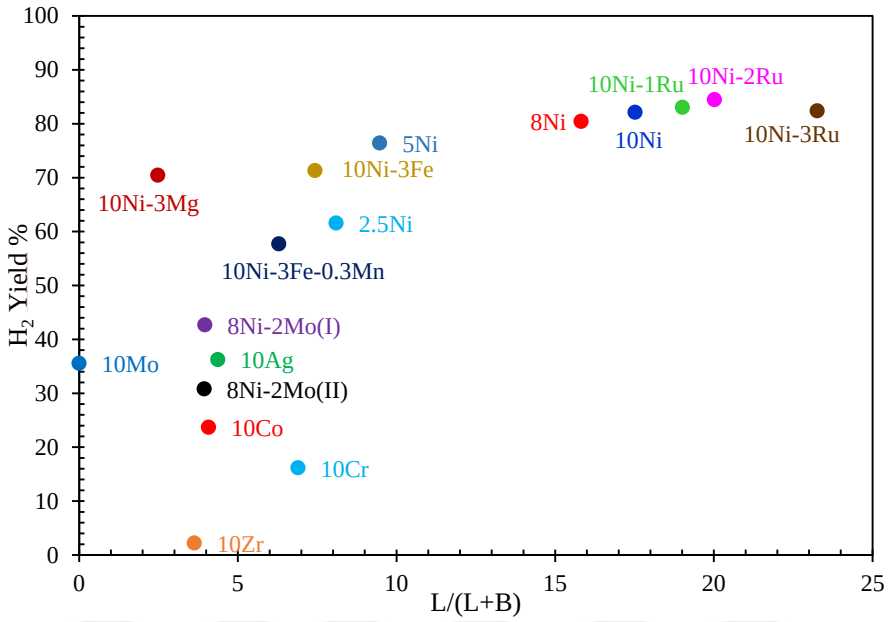

Figure 5.76 Comparison of H_2 Yield and L/(L+B) Acid Sites Ratio of the Catalysts (T_{rxn}:550°C, FFR:0.9ml/h, WGMR:9)

According to Figure 5.76, it is clear that, there is an almost direct proportion between H_2 yield and Lewis-to-(Lewis+Bronsted) acid sites ratio. The highest L/(L+B) ratio was obtained in 10Ni-3Ru/SA in which H_2 yield was quite high; however, the lowest L/(L+B) ratio was obtained in 10Mo/SA in which H_2 yield was moderate value. The zero value of L/(L+B) ratio may be due to the inability of 10Mo to adsorb to pyridine vapour; however, the presence of Lewis acid sites in addition to literature (Shen et al., 2019) is consistent with obtaining moderate H_2 yield value. In addition, low L/(L+B) ratios were obtained in 8Ni-2Mo(I), 8Ni-2Mo(II), 10Co and 10Zr loaded silica aerogels, in which H_2 yields were quite low. Despite the fact that both 8Ni-2Mo/SA(I) and 8Ni-2Mo/SA(II) have the same L/(L+B) values, the higher H_2 yield in 8Ni-2Mo/SA(I) may be ascribed to its higher pore diameter, which may be interpreted as reducing the pore clogging in the catalyst leading to an increase in catalytic activity. Therefore, it is clear that high L/(L+B) ratios are much better to achieve higher H_2 yield.

5.3 Characterization Results of Used Catalysts

In this part, surface area and porosity, crystallite size, amount of deposited coke and surface morphology of used mono, bi and trimetallic catalysts used in the reaction at the best operating conditions were examined with the aid of some characterization techniques such as N_2 Physisorption, XRD, TGA and SEM analysis.

5.3.1 N_2 Physisorption Analysis

N_2 physisorption analysis results of fresh & used 10Ni/SA, 10Ni-1Ru/SA, 10Ni-2Ru/SA and 10Ni-3Ru/SA were depicted in Figures 5.77-5.84. According to figures, there is a decrease in adsorbed pore volume of each used catalyst compared to fresh catalysts. This might be attributed to the fact that Ni is a suitable catalyst for carbon formation (Zhao et al.,2007; Lee et al., 2016; Charisiou et al., 2019; Susi et al., 2008; Wu et al., 2016), causing coke deposition during the reaction, resulting in a reduction in surface area, pore volume and pore diameter. In addition, the physical properties of fresh and used 10Ni/SA, 10Ni-1Ru/SA, 10Ni-2Ru/SA and 10Ni-3Ru/SA were given in Tables 5.10-5.14.

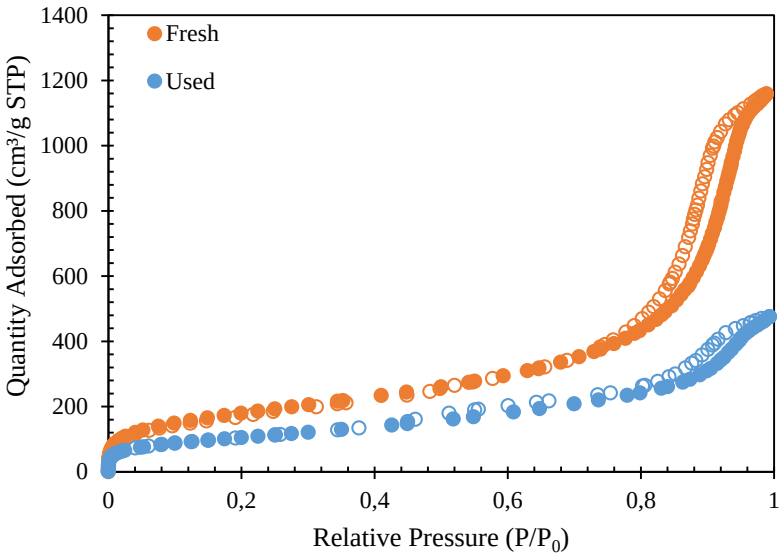

Figure 5.77 N_2 Physisorption Isotherms of Fresh & Used 10Ni/SA Catalysts (Filled Symbols: Adsorption Branch, Empty Symbols: Desorption Branch)

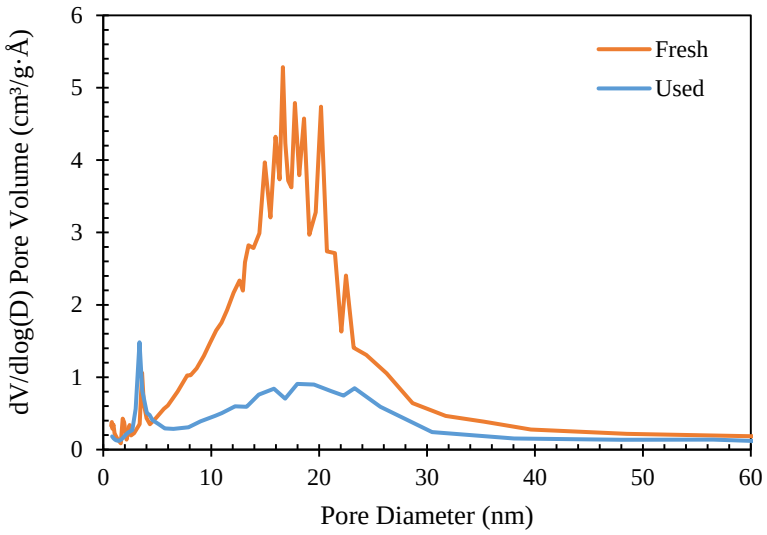

Figure 5.78 Pore Size Distributions of Fresh & Used 10Ni/SA Catalysts

Table 5.10 Physical Properties of Fresh & Used 10Ni/SA Catalysts

Catalyst	Multi-point BET Surface Area (m^2/g)	BJH Desorption Cumulative Volume of Pores (cm^3/g)	BJH Desorption Average Pore Diameter (nm)	Microporosity (%)
10Ni/SA	602	1.64	7.1	8.12
10Ni/SA(used)	381	0.74	5.1	13.24

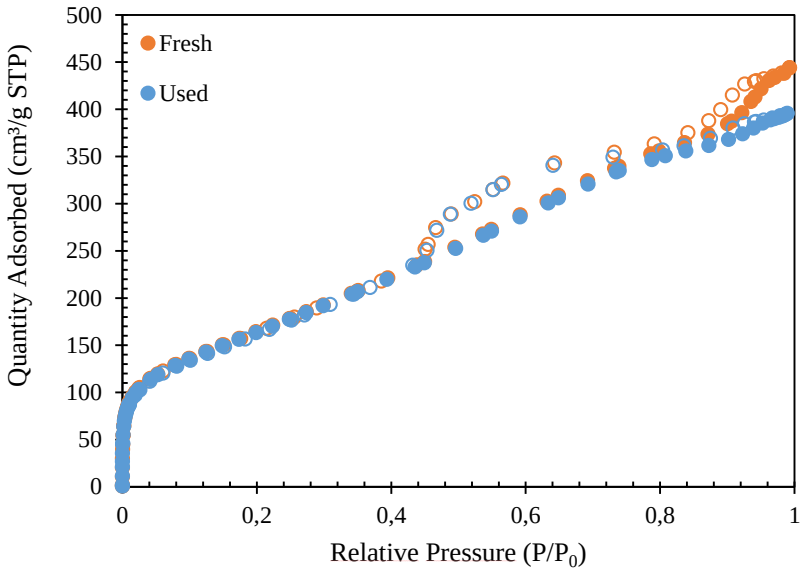

Figure 5.79 N_2 Physisorption Isotherms of Fresh and Used 10Ni-1Ru/SA Catalysts (Filled Symbols: Adsorption Branch, Empty Symbols: Desorption Branch)

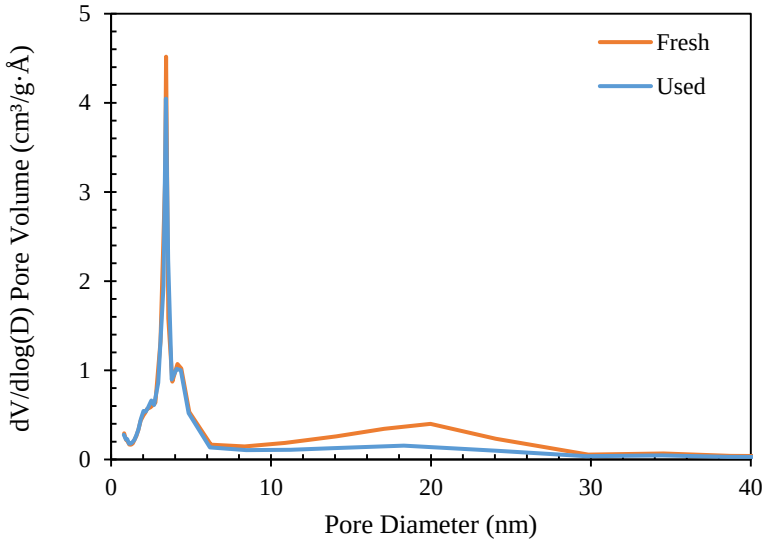

Figure 5.80 Pore Size Distributions of Fresh & Used 10Ni-1Ru/SA Catalysts

Table 5.11 Physical Properties of Fresh & Used 10Ni-1Ru/SA Catalysts

Catalyst	Multi-point BET Surface Area (m^2/g)	BJH Desorption Cumulative Volume of Pores (cm^3/g)	BJH Desorption Average Pore Diameter (nm)	Microporosity (%)
10Ni-1Ru/SA	606	0.69	3.2	21.03
10Ni-1Ru/SA (used)	603	0.63	2.9	22.75

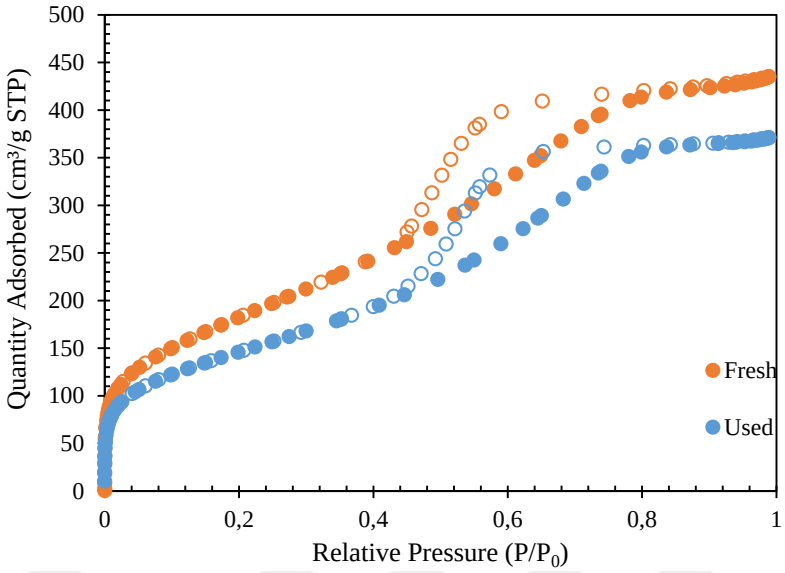

Figure 5.81 N_2 Physisorption Isotherms of Fresh & Used 10Ni-2Ru/SA Catalysts (Filled Symbols: Adsorption Branch, Empty Symbols: Desorption Branch)

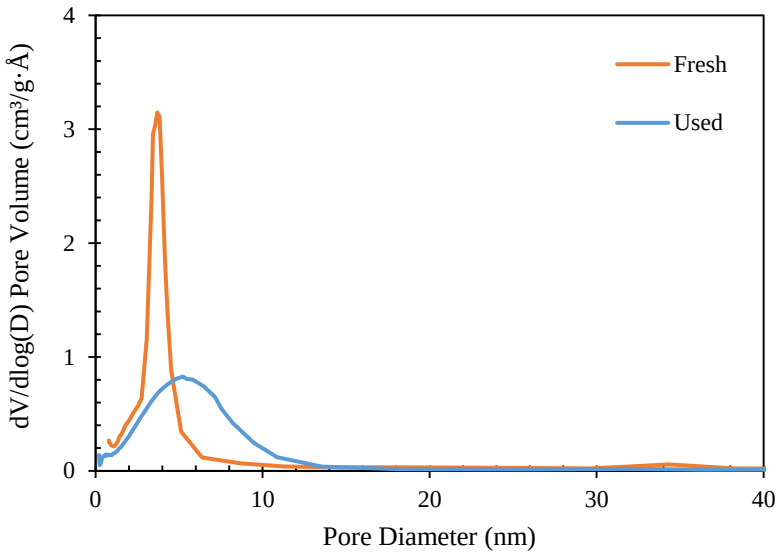

Figure 5.82 Pore Size Distributions of Fresh & Used 10Ni-2Ru/SA Catalysts

Table 5.12 Physical Properties of Fresh & Used 10Ni-2Ru/SA Catalysts

Catalyst	Multi-point BET Surface Area (m^2/g)	BJH Desorption Cumulative Volume of Pores (cm^3/g)	BJH Desorption Average Pore Diameter (nm)	Microporosity (%)
10Ni-2Ru/SA	669	0.69	2.8	22.11
10Ni-2Ru/SA (used)	527	0.59	3.0	21.50

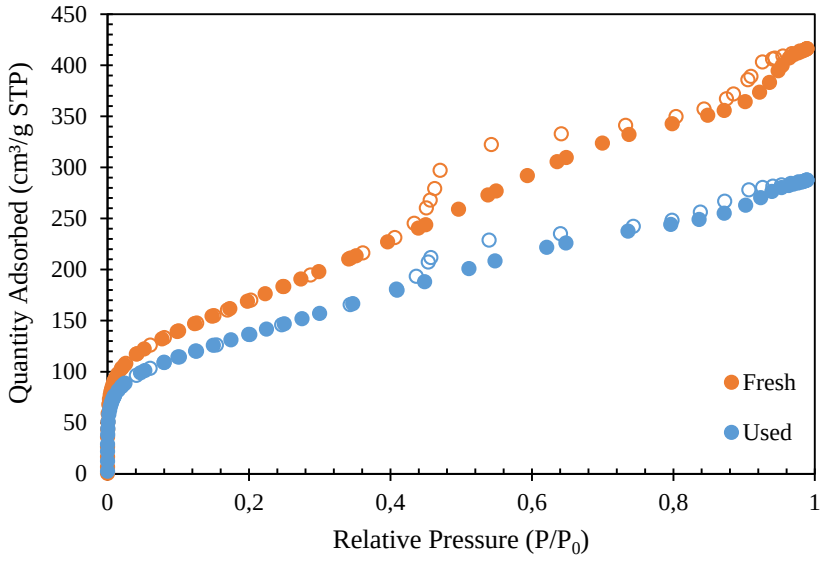

Figure 5.83 N_2 Physisorption Isotherms of Fresh & Used 10Ni-3Ru/SA Catalysts (Filled Symbols: Adsorption Branch, Empty Symbols: Desorption Branch)

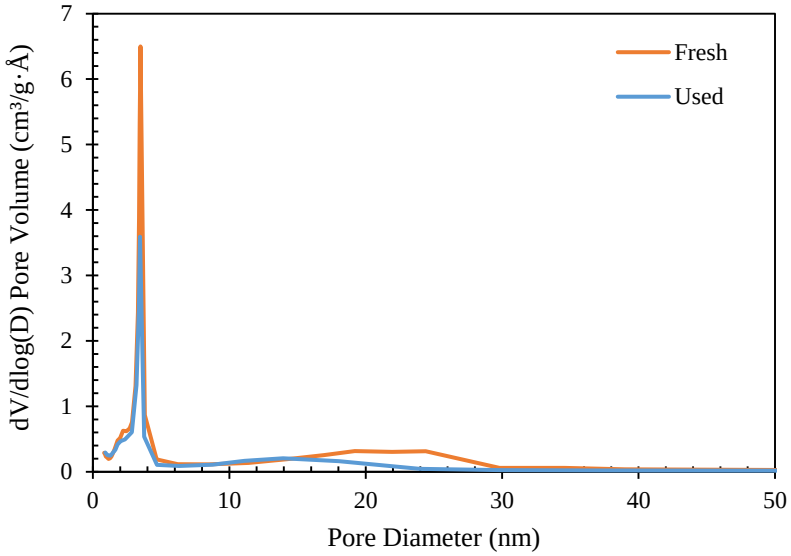

Figure 5.84 Pore Size Distributions of Fresh & Used 10Ni-3Ru/SA Catalysts

Table 5.13 Physical Properties of Fresh & Used 10Ni-3Ru/SA Catalysts

Catalyst	Multi-point BET Surface Area (m^2/g)	BJH Desorption Cumulative Volume of Pores (cm^3/g)	BJH Desorption Average Pore Diameter (nm)	Microporosity (%)
10Ni-3Ru/SA	624	0.66	2.9	22.81
10Ni-3Ru/SA (used)	492	0.46	2.6	27.19

5.3.2 X-Ray Diffraction (XRD) Analysis

In this part, fresh & used 10Ni/SA, 10Ni/SA-wet and 10Ni-2Ru/SA were compared to identify the metal phases and formation of carbon and/or carbon containing compounds after reaction. According to Figures 5.85-5.87, in addition to silica,

metalic-nickel, nickel oxide and metallic-ruthenium peaks, the peaks at 2Θ value of 26.2, 44.7 and 54.5° correspond to carbon in accordance with C PDF Card (No:00-041-1487) (Table B.18 in Appendix B). In addition, the peaks at 2Θ value of 37.1, 43.9 and 61.9° in used 10Ni/SA catalyst correspond to nickel oxide in accordance with NiO PDF Card (No: 01-089-5881) (Table B.2 in Appendix B).

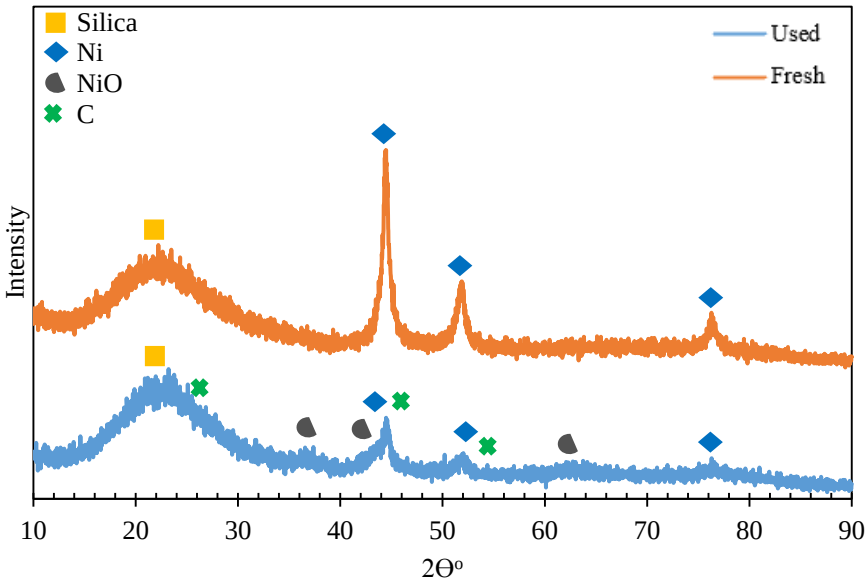

Figure 5.85 XRD Patterns of Fresh & Used 10Ni/SA Catalysts

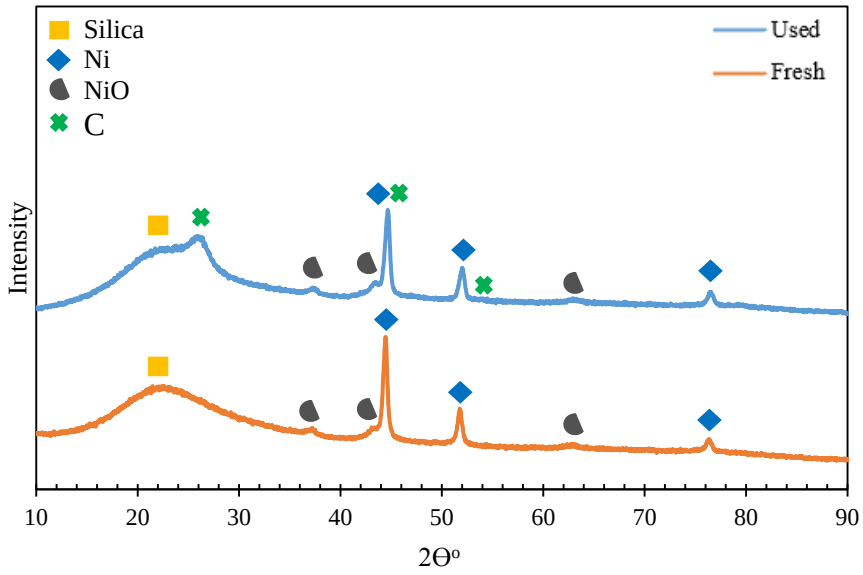

Figure 5.86 XRD Patterns of Fresh & Used 10Ni/SA-wet Catalysts

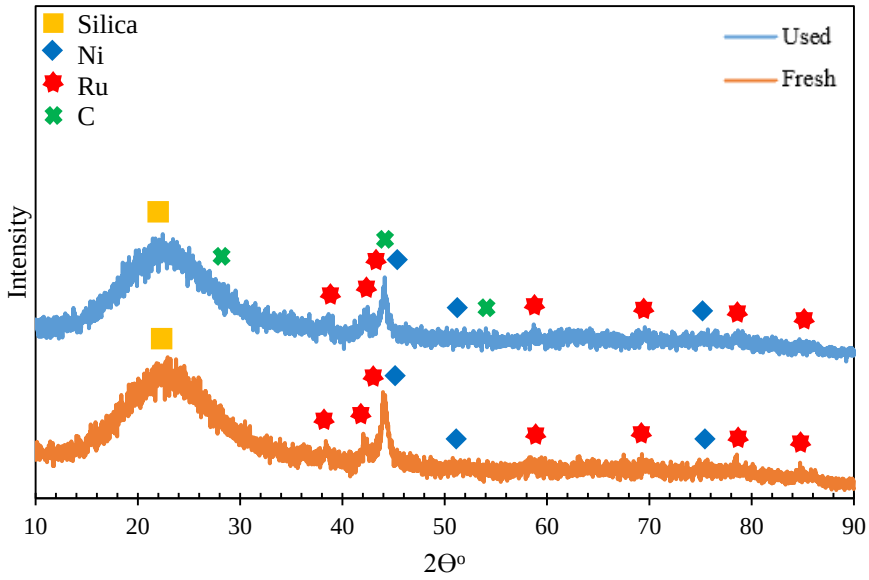

Figure 5.87 XRD Patterns of Fresh & Used 10Ni-2Ru/SA Catalysts

5.3.3 Thermogravimetric Analysis (TGA)

In this part, the amount of coke deposited in the catalysts was examined using TGA. The amount of carbon formation in the catalysts was obtained according to the weight loss in the catalysts as a result of the reaction of the carbon in the catalysts with the oxygen in the air. TGA results of the catalysts used were given in Figures 5.88-5.94. While, the weight loss of the catalysts up to 100^{o}C was due to the moisture in the catalysts, the weight loss at high temperatures was due to the carbon formation in catalysts. For this reason, amounts of deposited coke were calculated with respect to weight loss between the temperatures of 350-750^{o}C. Detailed calculation was given in Appendix H.

The effect of reaction conditions and metal types on carbon formation in the catalysts was discussed in following sections.

5.3.3.1 The Effect of Feed Flow Rate on Carbon Deposition

The effect of feed flow rate on carbon formation was examined in the presence of 10Ni/SA(1035)(1035), performed at 965^{o}C, atmospheric pressure with the W/G molar ratio of 3 and at the feed flow rate of 0.8, 0.9 and 1.0 ml/h. The comparative TGA analysis results with respect to feed flow rates were depicted in Figure 5.88.

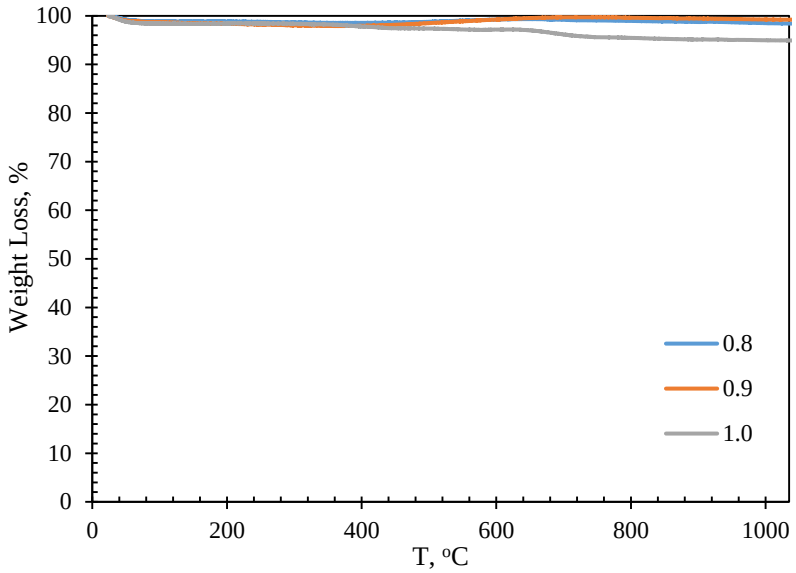

Figure 5.88 The Effect of Feed Flow Rate on Carbon Deposition

According to Figure 5.88, there is no significant weight loss in the catalysts used in the reaction at 0.8, 0.9 and 1.0 ml/h feed flow rates. Low weight loss is ascribed to the high reaction temperature that prevents carbon formation in the catalysts due to the exothermic nature of the carbon formation reactions:

Carbon Formation Reactions:

$2CO \leftrightarrow CO_2 + C$ ΔH_R = -172 kJ/mole

$CH_4 \leftrightarrow 2H_2 + C$ ΔH_R = 75 kJ/mole

$CO + H_2 \leftrightarrow H_2O + C$ ΔH_R = -131 kJ/mole

$CO_2 + 2H_2 \leftrightarrow 2H_2O + C$ ΔH_R = -90 kJ/mole

The weight loss of the catalysts was 0%, 0% and 1.31% corresponding to 0, 0 and 0.04 g_C/g_{cat}-h^{-1} at the feed flow rates of 0.8, 0.9 and 1.0 ml / h, respectively.

5.3.3.2 The Effect of Temperature on Carbon Deposition

The effect of temperature on carbon formation was examined in the presence of 10Ni/SA(700)(1035), performed at 450-1050°C, atmospheric pressure with the W/G molar ratio of 3 and at the feed flow rate of 0.9 ml/h. The comparative TGA analysis results with respect to temperature were depicted in Figure 5.89.

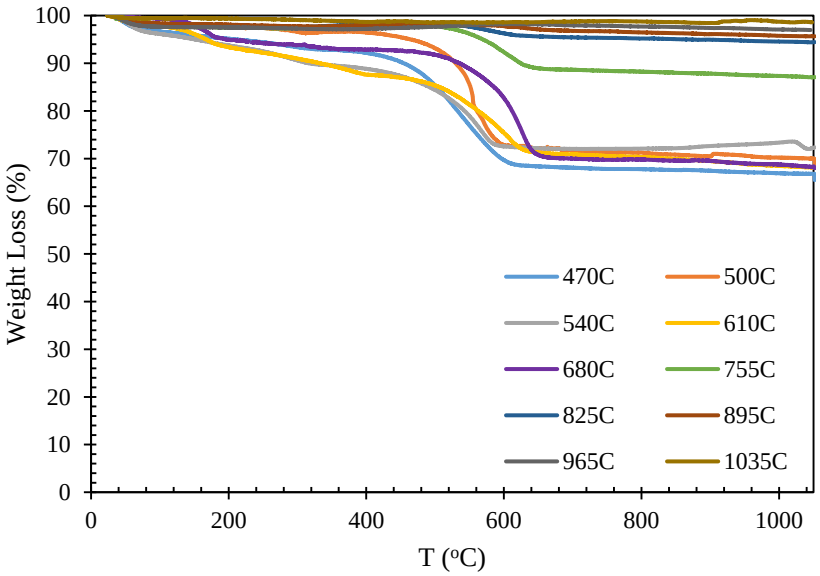

Figure 5.89 The Effect of Temperature on Carbon Deposition

According to Figure 5.89, the amount of weight loss decreases with an increase in temperature. This indicates that exothermic carbon formation reactions were inhibited at elevated temperatures.

Carbon Formation Reactions:

$2CO \leftrightarrow CO_2 + C$ $\Delta H_R = -172$ kJ/mole

$CH_4 \leftrightarrow 2H_2 + C$ $\Delta H_R = 75$ kJ/mole

$CO + H_2 \leftrightarrow H_2O + C$ $\Delta H_R = -131$ kJ/mole

$CO_2 + 2H_2 \leftrightarrow 2H_2O + C$ $\Delta H_R = -90$ kJ/mole

In the activity tests performed between 470-755°C, weight loss is observed in the range of 450-650°C, indicating that the formation of carbon fibre (Xu et al., 2018) during the glycerol steam reforming reaction. The weight loss of the catalysts was 21.83%, 20.88%, 17.58%, 17.00%, 19.55%, 8.93%, 1.89%, 0.89%, 0% and 0% corresponding to 0.65, 0.63, 0.53, 0.51, 0.59, 0.27, 0.06, 0.03, 0 and 0 $g_C/g_{cat}h^{-1}$at 470, 500, 540, 610, 680, 755, 825, 895, 965 and 1035°C, respectively.

5.3.3.3 The Effect of Feed Ratio on Carbon Deposition

The effect of W/G molar ratio on carbon formation was examined in the presence of 10Ni/SA(700)(1035), performed at 680°C, atmospheric pressure with the W/G molar ratio of 1, 3, 6 & 9 and at the feed flow rate of 0.9 ml/h. The comparative TGA analysis results with respect to feed ratio were shown in Figure 5.90.

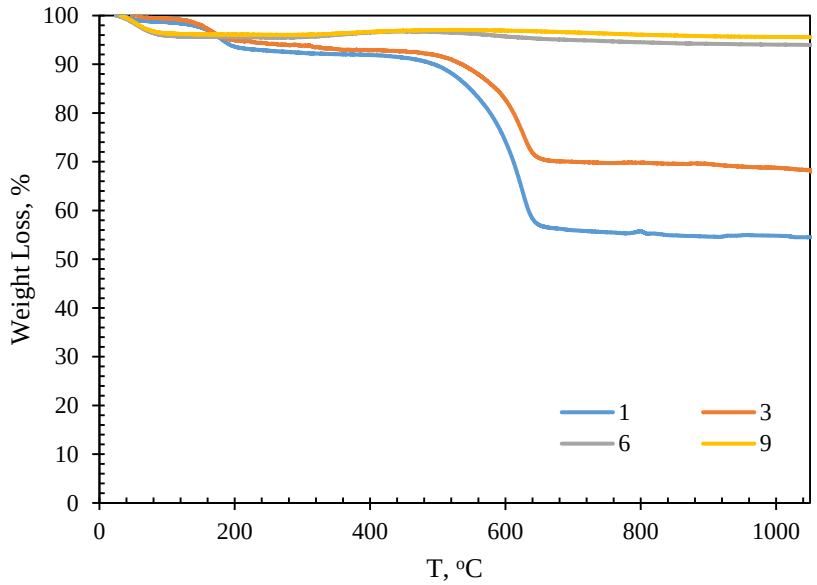

Figure 5.90 The Effect of W/G Molar Ratio on Carbon Deposition

According to Figure 5.90, amount of weight loss varies with respect to the performed W/G ratios. The increase in W/G ratio leads to decrease in amount of coke formation

in the catalysts. The reason of this may be that the increase in water content in the feed yields the reverse carbon formation (carbon gasification) reactions, thus reducing the formation of carbon in the catalysts that increases the both CO and CO_2 formations. (Spivey 2011; Charisiou et al., 2020)

Carbon Gasification Reactions:

$C + H_2O \leftrightarrow CO + H_2$ $\Delta H_R = 131$ kJ/mole

$C + 2H_2O \leftrightarrow CO_2 + 2H_2$ $\Delta H_R = 90$ kJ/mole

However, carbon formation may be assigned to the following reactions, particularly in activity tests performed at the W/G molar ratio of 1 & 3:

Carbon Formation Reactions:

$2CO \leftrightarrow CO_2 + C$ $\Delta H_R = -172$ kJ/mole

$CH_4 \leftrightarrow 2H_2 + C$ $\Delta H_R = 75$ kJ/mole

$CO + H_2 \leftrightarrow H_2O + C$ $\Delta H_R = -131$ kJ/mole

$CO_2 + 2H_2 \leftrightarrow 2H_2O + C$ $\Delta H_R = -90$ kJ/mole

As seen in Figure 5.90, weight loss is observed in the range of 450-650^oC, ascribing to the formation of carbon fibre (Xu et al., 2018) during the activity tests. The weight loss of the catalysts was 35.16%, 19.55%, 1.03% and 0.44% corresponding to 1.05, 0.59, 0.03 and 0.01 $g_C/g_{cat}h^{-1}$ at W/G molar ratio of 1, 3, 6 and 9, respectively.

5.3.3.4 The Effect of Catalyst Synthesis Method on H_2 Yield

The effect of both catalyst synthesis method and temperature at the W/G molar ratio of 9 was examined in 10Ni/SA(700)(1035) and 10Ni/SA(700)(1035)-wet, performed at 470-680^oC, atmospheric pressure and at the feed flow rate of 0.9 ml/h. The comparative TGA analysis results with respect to temperature were demonstrated in Figure 5.91.

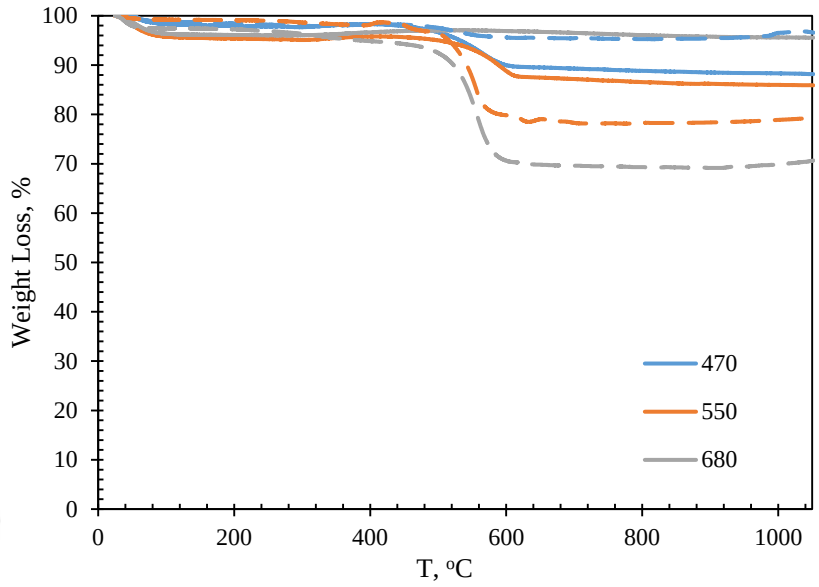

Figure 5.91 The Effect of Catalyst Synthesis Method on Carbon Deposition (Solid Line: Co-precipitation Method & Dashed Line: Wet-impregnation Method)

According to Figure 5.91, while the amount of weight loss decreases as the temperature increases in the presence of 10Ni/SA synthesized by co-precipitation method, the opposite behaviour is observed in the 10Ni/SA-wet synthesized by wet-impregnation method, that is, the amount of coke deposited increases as the temperature increases. This may be ascribed to the interactions between the active metal and the support that cause differences in a change in structural properties of catalysts and thus affect the catalytic activity, thermal stability and coke resistance (Greluk et al., 2020). In the presence of both catalysts, carbon may be formed through the carbon formation reactions:

Carbon Formation Reactions:

$2CO \leftrightarrow CO_2 + C$ $\Delta H_R = -172$ kJ/mole

$CH_4 \leftrightarrow 2H_2 + C$ $\Delta H_R = 75$ kJ/mole

$CO + H_2 \leftrightarrow H_2O + C$ $\Delta H_R = -131$ kJ/mole

$CO_2 + 2H_2 \leftrightarrow 2H_2O + C$ $\Delta H_R = -90$ kJ/mole

In the presence of these catalyst, weight loss between 500-625^oC might be attributed to carbon fibre formation (Xu et al., 2018). At 470, 550 and 680^oC, the weight loss in 10Ni/SA is 8.46%, 7.95% and 0.44%, which corresponds to 0.25, 0.24 and 0.01 $g_C/g_{cat}h^{-1}$, respectively, while in 10Ni/SA-wet it is 1.80%, 16.52% and 21.89%, which corresponds to 0.05, 0.50 and 0.66 $g_C/g_{cat}h^{-1}$, respectively.

5.3.3.5 The Effect of Catalyst Type on Carbon Deposition

The effect of catalyst type on carbon deposition was divided into 3: effect of metal amount, effect of monometal type and effect of bi and trimetal type on carbon deposition. Detailed TGA results were given in the following sections.

5.3.3.5.1 The Effect of Metal Amount on Carbon Deposition

The effect of metal amount in the catalysts on carbon formation was examined in the presence of 2.5Ni/SA(700)(1035), 5Ni/SA(700)(1035), 8Ni/SA(700)(1035), and 10Ni/SA(700)(1035) performed at 550^oC, atmospheric pressure with the W/G molar ratio of 9 and at the feed flow rate of 0.9 ml/h. The comparative TGA analysis results with respect to metal amount were depicted in Figure 5.92.

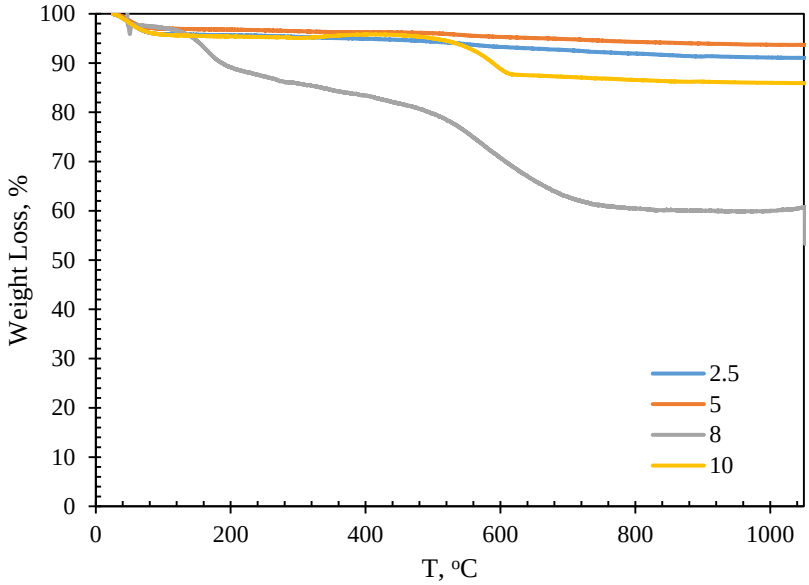

Figure 5.92 The Effect of Nickel Amount Loaded onto Silica Aerogel on Carbon Deposition

According to Figure 5.92, amount of weight loss increases with an increase in metal content in the catalysts except for 8Ni/SA. In the presence of these catalyst, carbon fibre (Xu et al., 2018) may be formed depending on the weight loss is between 500-725°C. The weight loss of the catalysts was 1.19%, 1.20%, 16.37%, and 7.95% corresponding to 0.04, 0.04, 0.49, and 0.24 $g_C/g_{cat}h^{-1}$ in the presence of 2.5%, 5%, 8%, and 10% by weight Ni loaded silica aerogels, respectively.

5.3.3.5.2 The Effect of Monometal Type on Carbon Deposition

The effect of monometal type on carbon formation was examined in 10Ni/SA(700)(1035), 10Co/SA(700)(1035), 10Cr/SA(700)(1035), 10Zr/SA(700)(1035), 10Mo/SA(700)(1035), and 10Ag/SA(700)(1035) performed at 550°C, atmospheric pressure with the W/G molar ratio of 9 and at the feed flow rate

of 0.9 ml/h. The comparative TGA analysis results with respect to monometal types were indicated in Figure 5.93.

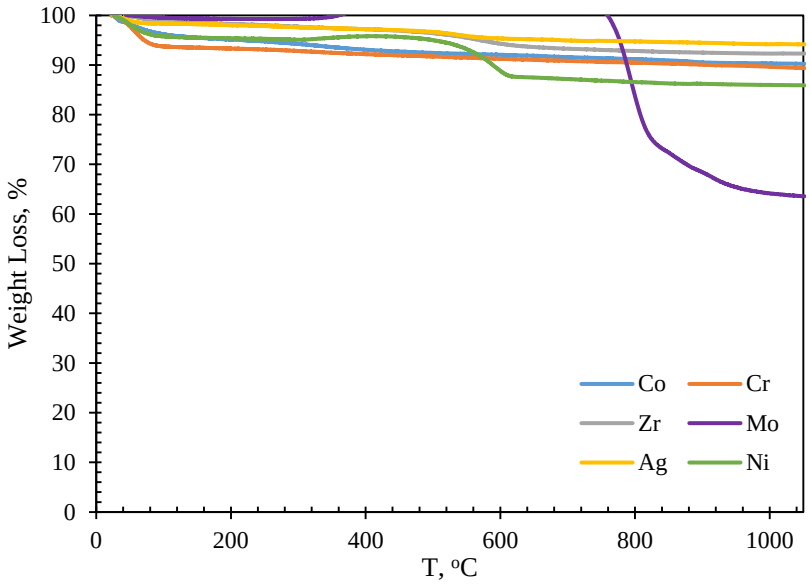

Figure 5.93 The Effect of 10% by wt. Metal Type Loaded onto Silica Aerogel on Carbon Deposition

According to Figure 5.93, the amount of weight loss varies with respect to the monometal types catalysts used in the reaction due to the morphology, texture and activity of the metals. The weight loss of the catalysts was 0.81%, 0.89%, 2.52%, 1.34%, 29.44%, and 7.95% corresponding to 0.02, 0.03, 0.08, 0.04, 0.88, and 0.24 $g_C/g_{cat}h^{-1}$ in the presence of 10% by weight Co, Cr, Zr, Ag, Mo, and Ni, respectively. The amount of deposited carbon in the catalysts used in the reaction increases in the following order: Co<Cr<Ag<Zr<Ni<Mo. An observation of the highest carbon formation in Mo loaded SA can be attributed to the surface morphology and texture of the catalyst. Aside from the other catalysts in which carbon fibre formation may be observed depending on the weight loss between 500-650°C (Xu et al., 2018), the weight loss between 700-800°C may be attributed to carbon nanotube formation (Chen et al.,2014) in the presence of Mo.

5.3.3.5.3 The Effect of Bi and Trimetal Type on Carbon Deposition

The effect of bi and trimetal type on carbon formation was examined in 8Ni-2Mo/SA(I)(700)(1035), 8Ni-2Mo/SA(II)(700)(1035), 10Ni-1Ru/SA(700)(700), 10Ni-2Ru/SA(700)(700), 10Ni-3Ru/SA(700)(700), 10Ni-3Mg/SA(700)(700), 10Ni-3Fe/SA(550)(550), and 10Ni-3Fe-0.3Mn/SA(550)(550) performed at 550^{o}C, atmospheric pressure with the W/G molar ratio of 9 and at the feed flow rate of 0.9 ml/h. The comparative TGA analysis results with respect to bi and trimetal catalyst types were depicted in Figure 5.94.

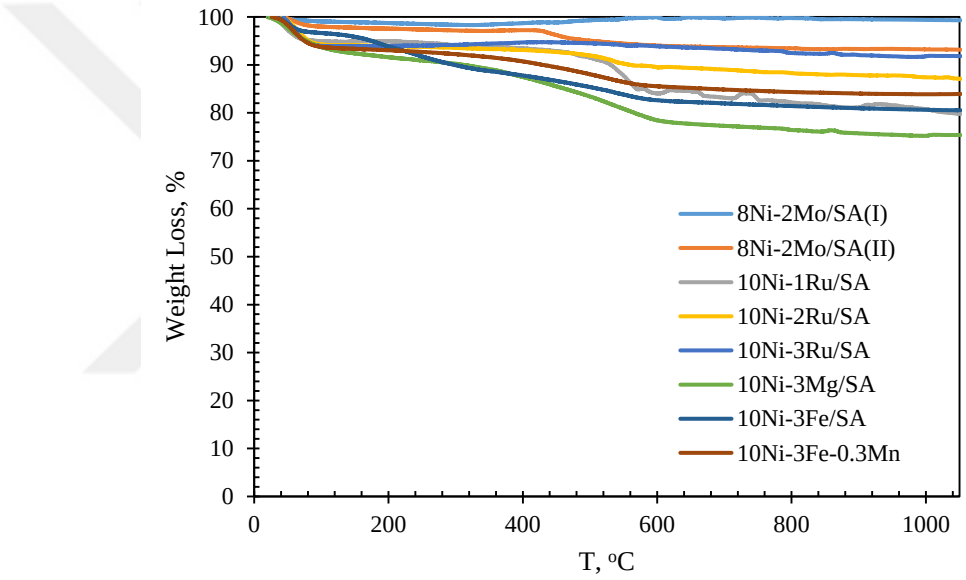

Figure 5.94 The Effect of Bi and Trimetal Type on Carbon Deposition

According to Figure 5.94, the amount of weight loss varies with respect to the bi and trimetal types used in the reaction due to the morphology, texture and activity of the metals. The weight loss of the catalysts was 0%, 2.03%, 6.17%, 2.12%, 0.74%, 11.79%, 6.20%, and 4.67% corresponding to 0, 0.06, 0.19, 0.06, 0.02, 0.35, 0.19, and 0.14 $g_C/g_{cat}h^{-1}$ in the presence of 8Ni-2Mo(I), 8Ni-2Mo(II), 10Ni-1Ru, 10Ni-2Ru, 10Ni-3Ru, 10Ni-3Mg, 10Ni-3Fe, and 10Ni-3Fe-0.3Mn, respectively. It is

clearly deduced that, synthesize route of bimetallic catalyst does not have a considerable effect on coke deposition. Despite loading of same amounts Mo and Ni in 8Ni-2Mo(I) and 8Ni-2Mo(II), the paths of adding metals leads to change in surface morphology and texture of the catalysts resulting in different amounts of coke deposition into the pores. In addition, increase in Ru content has a positive effect on coke deposition by decreasing the formed coke from 0.19 to 0.02 $g_C/g_{cat}h^{-1}$. This behaviour is consistent with the literature (Hirai et al., 2005; Gallo et al., 2012). It is also clear that Mn loading leads to a decrease in coke formation from 0.19 to 0.14 $g_C/g_{cat}h^{-1}$, even with a small amount of loading. The weight loss temperatures are in the range of 450-650^{o}C in the presence of the catalysts, which may be interpreted as carbon fibre (Xu et al., 2018) formation during the activity tests. The amount of deposited carbon in the bi and trimetallic catalysts used in the reactions increases in the following order:

8Ni-2Mo(I)<10Ni-3Ru<8Ni-2Mo(II)<10Ni-2Ru<10Ni-1Ru<0Ni-3Fe<10Ni-3Mg <10Ni-3Fe-0.3Mn.

The amount of coke deposited in all catalysts tested at 550^{o}C, atmospheric pressure, at 0.9 ml/h glycerol-water feed flow rate with the W/G molar ratio of 9, increases in the following order:

8Ni-2Mo(I)<10Ni-3Ru<10Co<10Cr<2.5Ni<5Ni<10Ag<8Ni-2Mo(II)<10Ni-2Ru <10Zr<10Ni-3Fe-0.3Mn<10Ni-1Ru<10Ni-3Fe<10Ni <10Ni-3Mg<8Ni<10Mo.

Figure 5.95 indicates the comparison of H_2 yield percent values and the amount of coke deposition in the catalysts tested at 550^{o}C, atmospheric pressure with the W/G molar ratio of 9 and at the glycerol-water feed flow rate of 0.9 ml/h.

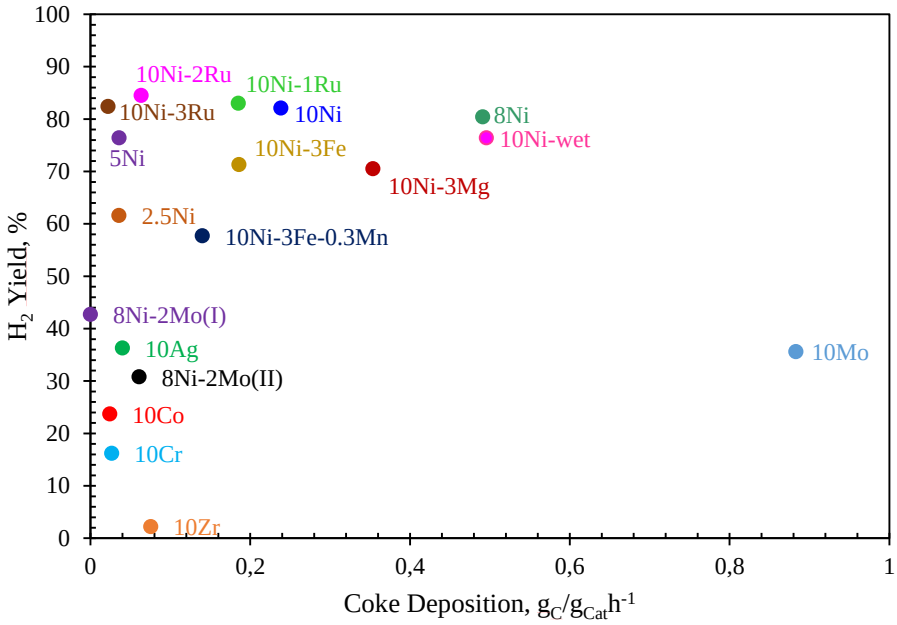

Figure 5.95 Comparison of H_2 Yield and Coke Deposition of the Catalysts

According to Figure 5.95, the highest coke formation was observed in the presence of 10Mo/SA, while the lowest coke deposition was observed in 8Ni-2Mo/SA(I); however, the H_2 yield values of these catalysts are quite close to each other. On the other hand, the highest H_2 yield was achieved in the presence of 10Ni-2Ru/SA, while the lowest H_2 yield was obtained in 10Zr/SA; however, when comparing the amount of carbon formation in the catalysts, it is clear that 10Ni-2Ru/SA and 10Zr/SA are quite close whereas the H_2 yields achieved in the presence of these catalysts are quite far from each other. However, 10Ni-2Ru/SA was determined as the best catalyst in terms of the highest H_2 yield and low carbon formation.

5.3.4 Scanning Electron Microscopy (SEM) Analysis

In this part, surface texture, morphology and composition of 10Ni/SA, 10Ni/SA-wet and 10Ni-2Ru/SA used in the reaction at 550°C, atmospheric pressure with the W/G molar ratio of 9 and at the feed flow rate of 0.9 ml/h were examined by SEM analysis.

Figure 5.96 depicts the SEM images of used 10% by weight of nickel loaded silica aerogel at different magnifications.

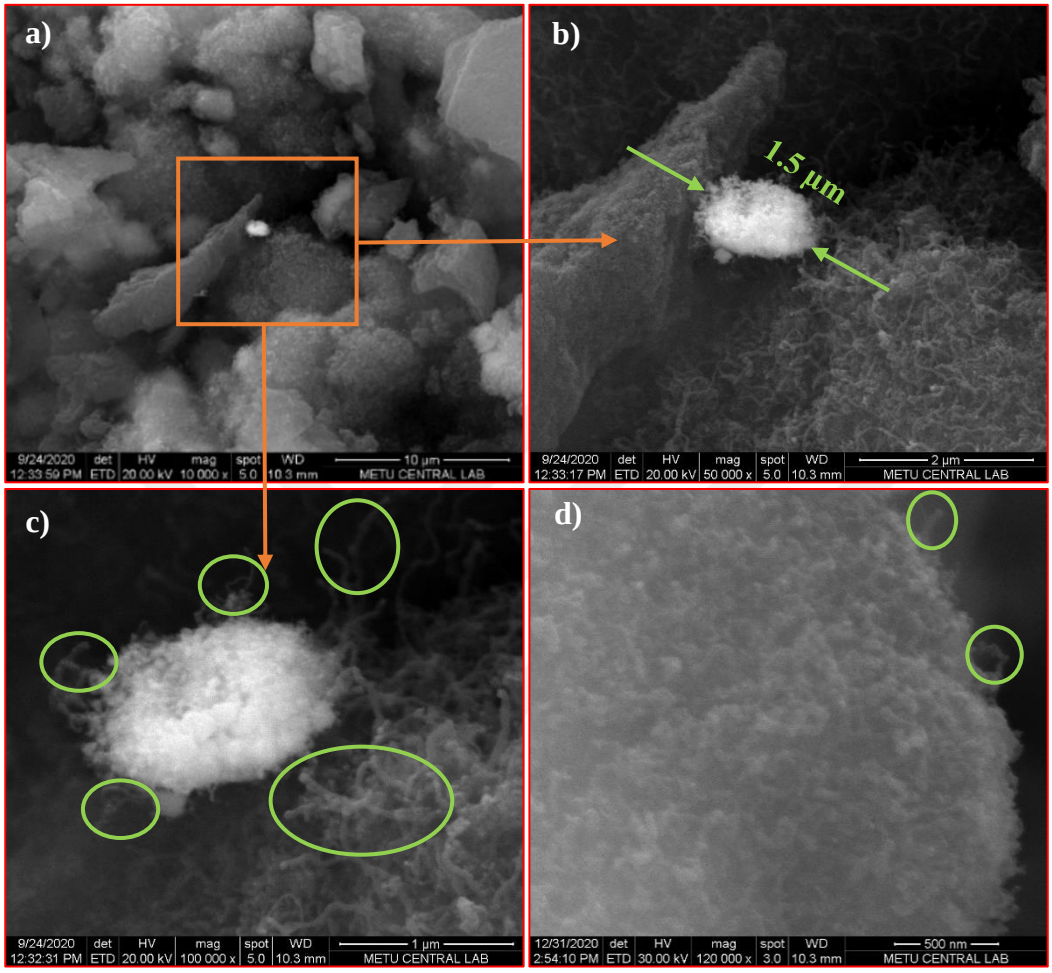

Figure 5.96 SEM Images of Used 10Ni/SA Catalyst a) 10000X, b) 50000X, c) 100000X and d) 120000X Magnifications

According to Figure 5.96 (a,b,c), it is observed that agglomerations of Ni particles in different parts of catalyst appear as white and shiny particle with a size of 1.5 µm. In addition, especially in Figure 5.96 (c,d), carbon fibre formation as aggregate clumps is observed after the catalyst used in the reaction in accordance with TGA analysis. In fact, the Ni particle is covered with carbon fibre as seen in Figure 5.96 (c). It may also be said that Ni particles are appropriate catalysts for carbon formation

(Zhao et al., 2007; Lee et al., 2016; Charisiou et al., 2019; Susi et al., 2008; Wu et al., 2016).

EDX analysis of used 10Ni/SA was given in Figure 5.97.

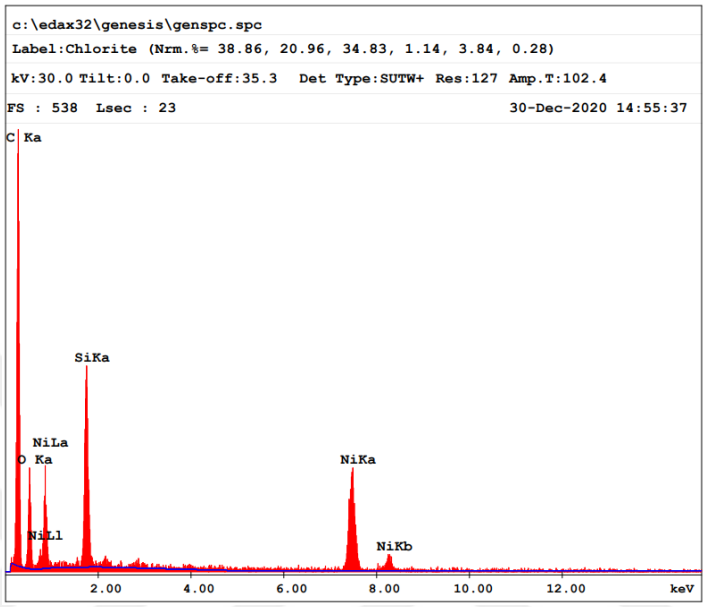

Figure 5.97 EDX Analysis of Used 10Ni/SA

According to EDX analysis, the used 10Ni/SA catalyst contains Si, O, C, and Ni elements. The presence of high amount of C element is due to the formation of carbon during the activity test of the catalyst, resulting in a decrease in multi-point BET surface area (Table 5.10) according to the N_2 physisorption analysis (Figure 5.77). In this region of the catalyst Ni content is 7.75 wt. %

Figure 5.98 depicts the SEM and back scattered electron images of used 10Ni/SA-wet at different magnifications.

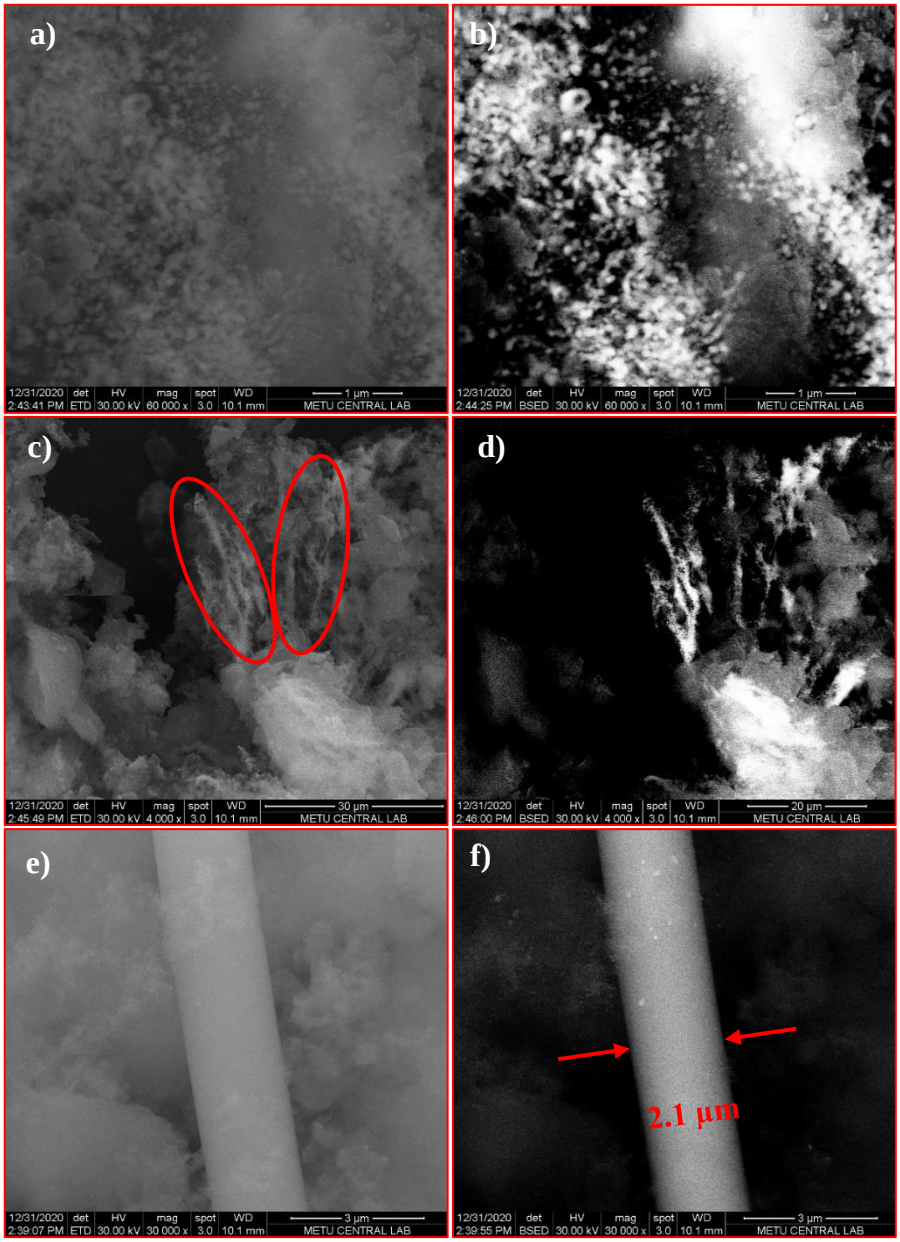

Figure 5.98 SEM (a,c,e) (60000X, 4000X, 30000X) and Back Scattered Electron Images of Used 10Ni/SA-wet

According to Figure 5.98 (a,b), the presence of Ni particles is seen as well-dispersed white and shiny particles; however, Figure 5.98 (c,d) reveals the agglomeration of Ni particles in different parts of the catalyst and the formation of carbon fibre as aggregate clumps after the reaction, consistent with the XRD analysis. Carbon fibre is particularly better seen in Figure 5.98 (e,f) with a size of 2.1 µm.

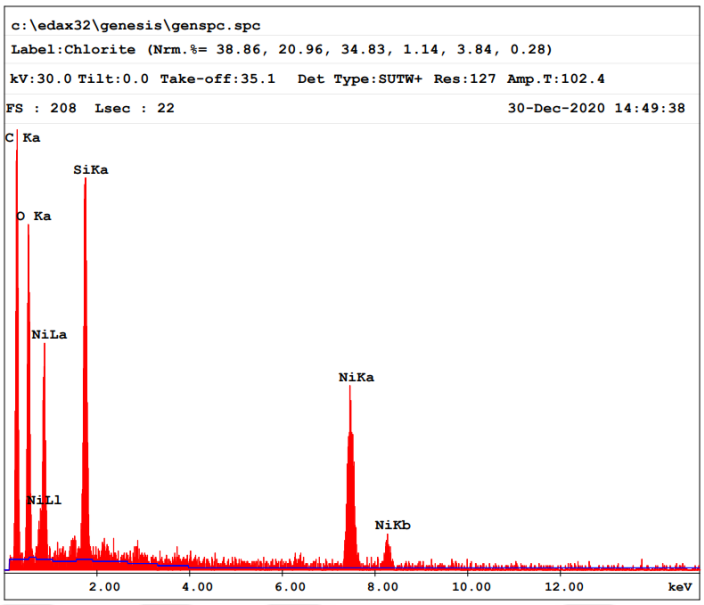

Figure 5.99 EDX Analysis of Used 10Ni/SA-wet

According to EDX analysis, the used 10Ni/SA-wet catalyst contains Si, O, C, and Ni elements. The presence of high amount of C element is due to the formation of carbon throughout the activity test of the catalyst in accordance with the XRD analysis. In this region of the catalyst Ni content is 8.49% by weight.

Figure 5.100 depicts the SEM and back scattered electron images of 10% by weight of nickel and 2% by weight of ruthenium loaded silica aerogel at different magnifications.

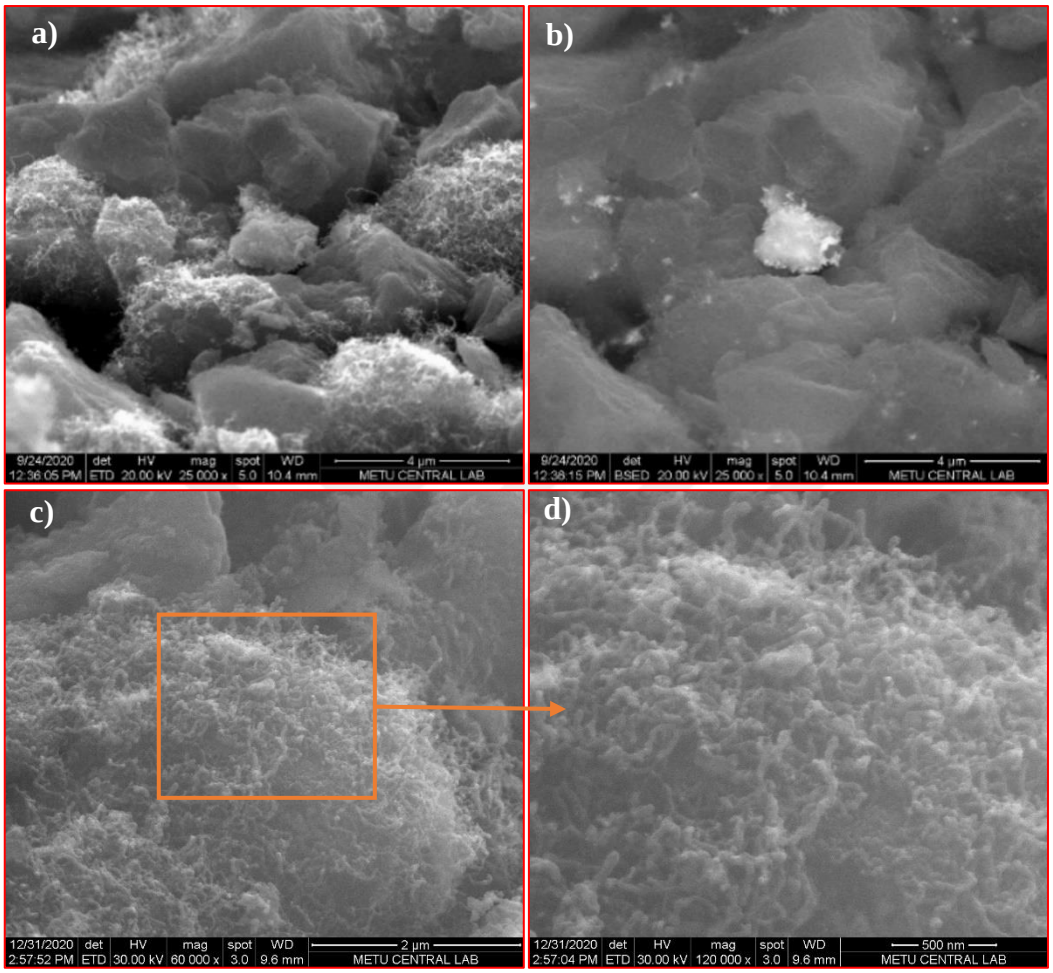

Figure 5.100 SEM (a,c,d) (25000X, 60000X, 120000X) and Back Scattered Electron (b) Images of Used 10Ni-2Ru/SA

According to Figure 5.100 (a,b), Ni and Ru appear as agglomerated small white and shiny particles. In addition, formation of carbon fibre in the form of aggregate clumps is observed especially in Figure 5.100 (c,d) compatible with N_2 physisorption and TGA analysis.

EDX Analysis of used 10Ni-2Ru/SA was given in Figure 5.101.

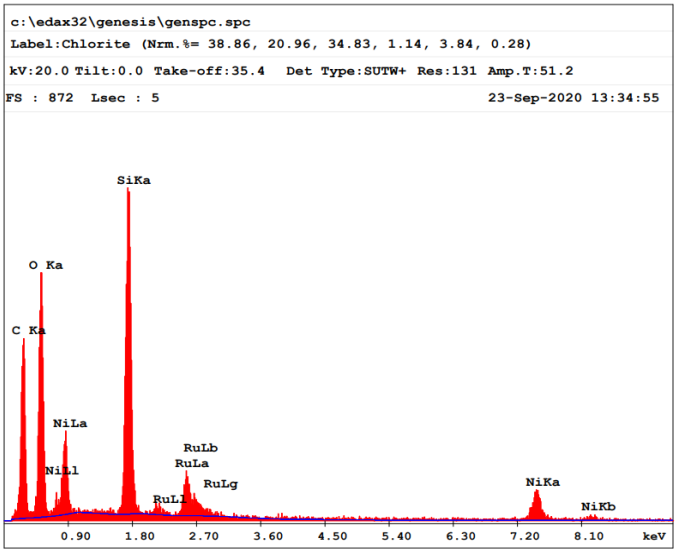

Figure 5.101 EDX Analysis of Used 10Ni-2Ru/SA

According to EDX analysis, the used 10Ni-2Ru/SA catalyst contains Si, O, C, Ni, and Ru elements. The presence of high amount of C element is due to the formation of carbon throughout the activity test of the catalyst. In this region of the catalyst Ni and Ru contents are 7.51 wt. % and 4.56 wt. %, respectively.

CHAPTER 6

CONCLUSIONS AND RECOMMENDATIONS

Within the scope of this study, silica aerogel was used as a catalyst support synthesized by sol-gel method and activated by loading of various amounts of Ni, Co, Cr, Zr, Mo, and Ag monometals, Ni-Mo, Ni-Fe, Ni-Mg, and Ni-Ru bimetals and Ni-Fe-Mn trimetals by co-precipitation or wet-impregnation method to be used in glycerol steam reforming reaction.

The activity of the catalysts and best operating conditions were obtained in the experiments carried out between 450-1050^{o}C, atmospheric pressure, at 0.8, 0.9 and 1.0 ml/h glycerol-water feed flow rate with the W/G molar ratio of 1, 3, 6 and 9 in the presence of 0.15 g catalysts, at 30 ml/min Ar flow rate in conventional fixed-bed quartz reactor. As a result of the experiments, the best operating condition and the most appropriate catalyst were determined in terms of glycerol conversion, H_2 yield and amount of coke deposited in the catalysts attained using TGA.

Herein, the characterization analysis, experimental results of the catalysts and recommendations in this context were stated.

- Silica aerogels synthesized by sol-get method exhibited type IV isotherm and H3 hysteresis loop with the multi-point BET surface area of 806±46 m^2/g, BJH desorption average pore diameter of 10.9±0.4 nm and BJH desorption cumulative pore volume of 3.56±0.18 cm^3/g. The loading of metals changed the hysteresis loop to H1 and/or H2 while the isotherm type remained the same, representing type IV, and decreased the multi-point BET surface area to 18-763 m^2/g, BJH desorption average pore diameter to 2.5-15.53 nm and BJH desorption cumulative pore volume to 0.12-2.98 cm^3/g.

- The catalysts contain predominantly Lewis acid sites regardless of the number of L/(L+B) ratios. It was concluded that increase in L/(L+B) ratio, increases the formation of H_2 and thus the yield of H_2. In fact, more than 80% H_2 yield was achieved in the presence of 8Ni/SA with the L/(L+B) ratio of 15.82. Comparing the experimental results with DRIFT analysis, the highest H_2 yields were achieved in the presence of catalysts having more Lewis acid sites with the L/(L+B) ratios ranging from 15.82 to 23.26.

- According to SEM images, it was observed that silica aerogel has sponge-like framework containing different sizes of pores consistent with N_2 physisorption analysis. In addition, it was seen that all metals tend to agglomeration and are not well dispersed in the catalysts.

- The best operating conditions were determined in the presence of 10Ni/SA(700)(1035) synthesized by co-precipitation method at the temperature varying between 450-1050^oC, atmospheric pressure, at 0.8, 0.9 and 1.0 ml/h glycerol-water feed flow rate with the W/G molar ratio of 1, 3, 6 and 9. As a result of the experiments, the best operating conditions were determined as 550^oC, 0.9 ml/h glycerol-water feed flow rate and W/G molar ratio of 9. At these conditions, H_2 yield was achieved as 82.1% with approximately complete glycerol conversion and the mole compositions of H_2, CO_2, CO and CH_4 as 65.7%, 29.9%, 3.6% and 0.8%, respectively. In addition, the amount of coke deposited in the catalyst was attained as 0.24 $g_C/g_{Cat}h^{-1}$.

- According to TGA results, the highest amount of carbon formed in 10Mo/SA(700)(1035) as 0.88 $g_C/g_{Cat}h^{-1}$, while there is no carbon formation in 8Ni-2Mo/SA(I)(700)(1035), referring to the total weight loss in the catalyst varying from 29.44% to 0% at the best operating conditions stated above.

- As a result of the experiments performed at the operating conditions stated above, the best catalyst was determined as 10Ni-2Ru/SA(700)(700). In the presence

of this catalyst, H_2 yield was achieved as 84.5% with approximately complete glycerol conversion and the mole compositions of H_2, CO_2, CO and CH_4 as 66.3%, 30.0%, 3.2% and 0.5%, respectively. In addition, the amount of coke deposited in the catalyst was attained as 0.06 $g_C/g_{Cat}h^{-1}$.

- In this study, the colour of hydrogen produced is grey due to the release of CO_2 to the atmosphere. However, blue hydrogen can be produced by capturing CO_2 using sorbent-enhanced systems. For instance, the use of CaO as a sorbent increases H_2 production and hence H_2 yield by inhibiting the reverse WGS reaction by capturing CO_2 and converting it into $CaCO_3$, i.e., promoting the conversion of CO and H_2O into H_2 based on Le Chatelier's principle, and reduces C formation formed by the conversion of CO and CO_2 in the series of carbon formation reactions. This process allows the catalyst life to be extended by preventing deactivation of the catalyst as a result of catalyst poisoning due to coke deposition.

- As storage of H_2 is one of the main issues, H_2 can be produced on-board and fed directly to the fuel cell without being stored using conventional fixed bed or membrane reactors. Conventional fixed bed reactor system can be modified into fuel cell-derived vehicles by using a regeneration system to prevent deactivation and/or poisoning of the catalyst due to coke deposition by oxidizing the carbon formed with O_2 in the air atmosphere. Since Proton Exchange Membrane (PEM) fuel cells have zero tolerance to CO and CO_2, H_2 should be separated using micro-scale modified pressure swing adsorption or cryogenic distillation units. The separated H_2 should then pass through the heat exchangers and its temperature should be brought to 60-90^oC before being fed into the PEM fuel cell. In addition, use of membrane reactor instead of fixed-bed reactor provides high H_2 purity and combines separation and reaction in a single unit. In both processes, laboratory scale fuel cells and micro reactors can be used to fix this process on vehicles. The necessary energy for the reaction can be supplied to the reactor by hydropower or other renewable sources. In addition, glycerol filling stations should be built due to the lack of refuelling

infrastructure. These processes seem promising since hydrogen energy provides to diminish fossil fuel dependency, reduce greenhouse gas production, mitigate environmental concerns, offer sustainable energy produced by renewable resources, and contribute to the development of fuel cell technology.

REFERENCES

Accardo, G., Cioffi, R., Colangelo, F., d'Angelo, R., De Stefano, L., & Paglietti, F. (2014). Diffuse reflectance infrared fourier transform spectroscopy for the determination of asbestos species in bulk building materials. Materials, 7(1), 457–470. https://doi.org/10.3390/ma7010457

Adeniyi, A. G., & Ighalo, J. O. (2019). A review of steam reforming of glycerol. Chemical Papers, 73(11), 2619–2635. https://doi.org/10.1007/s11696-019-00840-8

Adhikari, S., & Fernando, S. (2006). Hydrogen membrane separation techniques. Industrial and Engineering Chemistry Research, 45(3), 875–881. https://doi.org/10.1021/ie050644l

Adhikari, S., Fernando, S., & Haryanto, A. (2007). Production of hydrogen by steam reforming of glycerin over alumina-supported metal catalysts. Catalysis Today, 129(3–4), 355–364. https://doi.org/10.1016/j.cattod.2006.09.038

Adhikari, S., Fernando, S. D., & Haryanto, A. (2008). Hydrogen production from glycerin by steam reforming over nickel catalysts. Renewable Energy, 33(5), 1097–1100. https://doi.org/10.1016/j.renene.2007.09.005

Adhikari, S., Fernando, S. D., & Haryanto, A. (2009). Hydrogen production from glycerol: An update. Energy Conversion and Management, 50(10), 2600–2604. https://doi.org/10.1016/j.enconman.2009.06.011

Adris, A. M., Pruden, B. B., Lim, C. J., & Grace, J. R. (1996). On the reported attempts to radically improve the performance of the steam methane reforming

reactor. The Canadian Journal of Chemical Engineering, 74(2), 177-186. doi:10.1002/cjce.5450740202

Ahmed, S., & Krumpelt, M. (2001). Hydrogen from hydrocarbon fuels for fuel cells. International Journal of Hydrogen Energy, 26(4), 291–301. https://doi.org/10.1016/S0360-3199(00)00097-5

Al-salihi, S., Abrokwah, R., Dade, W., Deshmane, V., & Hossain, T. (2020). Renewable hydrogen from glycerol steam reforming using Co-Ni-MgO based SBA-15 nanocatalysts. International Journal of Hydrogen Energy, 45(28), 14183–14198. https://doi.org/10.1016/j.ijhydene.2020.03.149

Amiri, Y. T., Moghaddas, J., & Khajeh, S. R. (2016). Silica aerogel-supported copper catalyst prepared via ambient pressure drying process. Journal of Sol-Gel Science and Technology, 77(3), 627–635. https://doi.org/10.1007/s10971-015-3892-0

Avasthi, K. S., Narasimha, R., & Patel, S. (2013). Challenges in the production of hydrogen from glycerol-a biodiesel byproduct via steam reforming process. Procedia Engineering, 51, 423–429. https://doi.org/10.1016/j.proeng.2013.01.059

Ayabe, S., Omoto, H., Utaka, T., Kikuchi, R., Sasaki, K., Teraoka, Y., & Eguchi, K. (2003). Catalytic autothermal reforming of methane and propane over supported metal catalysts. Applied Catalysis A: General, 241(1-2), 261-269. https://doi.org/10.1016/S0926-860X(02)00471-4

Bagnato, G., Iulianelli, A., Sanna, A., & Basile, A. (2017). Glycerol Production and Transformation: A Critical Review with Particular Emphasis on Glycerol Reforming Reaction for Producing Hydrogen in Conventional and Membrane Reactors. Membranes, 7(2), 17. https://doi.org/10.3390/membranes7020017

Barker-Hemings, E., Cavallotti, C., Cuoci, A., Faravelli, T., & Ranzi, E. (2012). A Detailed Kinetic Study of Pyrolysis and Oxidation of Glycerol (Proane-1,2,3-triol). Combustion Science and Technology, 184(7-8), 1164–1178. https://doi.org/10.1080/00102202.2012.664006

Bartholomew, Calvin H (2001). Mechanisms of catalyst deactivation. Applied Catalysis A: General. 212 (1–2), 17–60. https://doi:10.1016/S0926-860X(00)00843-7.

Basile, A., Tong, J., & Millet, P. (2013). Inorganic membrane reactors for hydrogen production: An overview with particular emphasis on dense metallic membrane materials. In Handbook of Membrane Reactors (Vol. 1). https://doi.org/10.1533/9780857097330.1.42

Bernholz, J. J. (2018). RWE's former, current and possible future energy storage applications (PDF). RWE Technology International GmbH.

Bossola, F., Pereira-Hernández, X. I., Evangelisti, C., Wang, Y., & Dal Santo, V. (2017). Investigation of the promoting effect of Mn on a Pt/C catalyst for the steam and aqueous phase reforming of glycerol. Journal of Catalysis, 349, 75–83. https://doi.org/10.1016/j.jcat.2017.03.002

Bouarab, R., Bennici, S., Mirodatos, C., & Auroux, A. (2014). Hydrogen Production from the Water-Gas Shift Reaction on Iron Oxide Catalysts. Journal of Catalysts, 2014, 6. https://doi.org/doi.org/10.1155/2014/612575

Bravo-suárez, J. J., & Chaudhari, R. V. (2013). Design of heterogeneous catalysts for the conversion of biomass-derived compounds into fuels and chemicals. In Novel Materials for Catalysis and Fuels Processing (Vol. 1132, pp. 3–68). https://doi.org/10.1021/bk-2013-1132.ch001

Busca, G. (1998). Spectroscopic characterization of the acid properties of metal oxide catalysts. Catalysis Today, 41(1–3), 191–206. https://doi.org/10.1016/S0920-5861(98)00049-2

Calafat, A. (1998). The influence of preparation conditions on the surface area and phase formation of zirconia. In Studies in Surface Science and Catalysis (Vol. 118, pp. 837–843). https://doi.org/10.1016/s0167-2991(98)80251-6

Calles, J. A., Carrero, A., & Vizcaíno, A. J. (2014). Hydrogen production by glycerol steam reforming over SBA-15-supported nickel catalysts : Effect of alkaline earth promoters on activity and stability. Catalysis Today, 227, 198–206. https://doi.org/10.1016/j.cattod.2013.11.006

Carrero, A., Calles, J. A., García-Moreno, L., & Vizcaíno, A. J. (2017). Production of renewable hydrogen from glycerol steam reforming over bimetallic Ni-(Cu,Co,Cr) catalysts supported on SBA-15 silica. Catalysts, 7(2), 55. https://doi.org/10.3390/catal7020055

Carrero, A., Vizcaíno, A. J., Calles, J. A., & García-Moreno, L. (2017). Hydrogen production through glycerol steam reforming using Co catalysts supported on SBA-15 doped with Zr, Ce and La. Journal of Energy Chemistry, 26(1), 42–48. https://doi.org/10.1016/j.jechem.2016.09.001

Charisiou, N. D., Douvartzides, S. L., Siakavelas, G. I., Tzounis, L., Polychronopoulou, K., & Goula, M. A. (2019). The Relationship between Reaction Temperature and Carbon Deposition on Nickel Catalysts Based on Al_2O_3, ZrO_2 or SiO_2 Supports during the Biogas Dry Reforming Reaction. Catalysts, 9(8), 676. https://doi.org/10.3390/catal9080676

Charisiou, N. D., Siakavelas, G. I., Papageridis, K. N., Motta, D., Dimitratos, N., Sebastian, V., Polychronopoulou, K., & Goula, M. A. (2020). The effect of

noble metal (M: Ir, Pt, Pd) on M/Ce_2O_3-γ-Al_2O_3 catalysts for hydrogen production via the steam reforming of glycerol. Catalysts, 10(7), 790. https://doi.org/10.3390/catal10070790

Checa, M., Nogales-Delgado, S., Montes, V., & Encinar, J. M. (2020). Recent Advances in Glycerol Catalytic Valorization : A Review. Catalysts, 10(1279), 1–41. https://doi.org/10.3390/catal10111279

Chen, J., Duan, Z., Song, Z., Zhu, L., Zhou, Y., Xiang, Y., & Xia, D. (2017). Relationship between surface property and catalytic application of amorphous NiP/Hβ catalyst for n-hexane isomerization. Applied Surface Science, 425(2017), 448–460. https://doi.org/10.1016/j.apsusc.2017.07.019

Chen, L., Qi, Z., Zhang, S., Su, J., & Somorjai, G. A. (2020). Catalytic hydrogen production from methane: A review on recent progress and prospect. Catalysts, 10(8), 858. https://doi.org/10.3390/catal10080858

Chen, S., Xin, Y., Zhou, Y., Zhang, F., Ma, Y., Zhou, H., & Qi, L. (2014). Branched CNT@SnO_2 nanorods@carbon hierarchical heterostructures for lithium ion batteries with high reversibility and rate capability. Journal of Materials Chemistry A, 2(37), 15582–15589. https://doi.org/10.1039/c4ta03218g

Cheng, C. K. (2011). Synthesis Gas Production from Glycerol Steam Reforming over Alumina Supported Bimetallic Co-Ni Catalyst Doctor of Philosophy. The University of New South Wales, Sydney, Australia.

Cheng, Y., Zhou, L., Xu, J., Miao, C., Hua, W., Yue, Y., & Gao, Z. (2016). Chromium-based catalysts for ethane dehydrogenation: Effect of SBA-15 support. Microporous and Mesoporous Materials, 234, 370–376. https://doi.org/10.1016/j.micromeso.2016.07.031

Colella, W. G., Jacobson, M. Z., & Golden, D. M. (2005). Switching to a U.S. hydrogen fuel cell vehicle fleet: The resultant change in emissions, energy use, and greenhouse gases. Journal of Power Sources, 150(1–2), 150–181. https://doi.org/10.1016/j.jpowsour.2005.05.092

Crowl, D. A., & Jo, Y. Do. (2007). The hazards and risks of hydrogen. Journal of Loss Prevention in the Process Industries, 20(2), 158–164. https://doi.org/10.1016/j.jlp.2007.02.002

Dahdah, E., Estephane, J., Gennequin, C., Aboukaïs, A., Abi-Aad, E., & Aouad, S. (2020). Zirconia supported nickel catalysts for glycerol steam reforming: Effect of zirconia structure on the catalytic performance. International Journal of Hydrogen Energy, 45(7), 4457–4467. https://doi.org/10.1016/j.ijhydene.2019.12.019

Davis, R. A., & Patel, N. M. (2004). Refining: Refinery hydrogen management. Petroleum Technology Quarterly, 9(3), 29–35. Retrieved from https://silo.tips/download/hydrogen-management-has

de Jong, K. P. (2009). Basic Principles and Tools. In Synthesis of Solid Catalysts (pp. 3–8). Wiley-VCH Verlag, Weinheim.

de Smit, E., & Weckhuysen, B. M. (2008). The renaissance of iron-based Fischer-Tropsch synthesis: On the multifaceted catalyst deactivation behaviour. Chemical Society Reviews, 37(12), 2758–2781. https://doi.org/10.1039/b805427d

Dębek, R. (2016). Novel catalysts for chemical CO_2 utilization Doctor of Philosophy. University Pierre and Marie Currie, Institut Jean Le Rond D'Alembert and on Faculty of Energy and Fuels at AGH University of Science and Technology, Krakow, Poland.

Değirmencioğlu, P. (2018). Methanol Steam Reforming over Silica Aerogel Supported Catalyst for Hydrogen Production Master of Science. Middle East Technical University, Ankara, Turkey.

Demsash, H. D., Kondamudi, K. V. K., Upadhyayula, S., & Mohan, R. (2018). Ruthenium doped nickel-alumina-ceria catalyst in glycerol steam reforming. Fuel Processing Technology, 169, 150–156. https://doi.org/10.1016/j.fuproc.2017.09.017

Deraz, N. M. (2018). The comparative jurisprudence of catalysts preparation methods : I . precipitation and impregnation methods . Journal of Industrial and Environmental Chemistry, 2(1), 19–21.

Deshpande, R., D. M. Smith, and C. J. Brinker (1992). Preparation of High Porosity Xerogels by Chemical Surface Modification. US Patent No. 5565142A

Dinçer, B. Y. (2019). Synthesis and Characterization of Metal Loaded New Generation Meso Porous Silica Pillared Catalyst Master of Science. Gazi University, Ankara, Turkey.

Dincer, I., & Acar, C. (2014). Review and evaluation of hydrogen production methods for better sustainability. International Journal of Hydrogen Energy, 40(34), 11094–11111. https://doi.org/10.1016/j.ijhydene.2014.12.035

Docekal, J. (1986). Hydrogen production from hydrocarbons. International Journal of Hydrogen Energy, 11(11), 709-714. doi:10.1016/0360-3199(86)90139-4

Eberle, U., Müller, B., & Von Helmolt, R. (2012). Fuel cell electric vehicles and hydrogen infrastructure: Status 2012. Energy and Environmental Science, 5(10), 8780–8798. https://doi.org/10.1039/c2ee22596d

Ebshish, A., Yaakob, Z., Narayanan, B., Bshish, A., & Wan Daud, W. R. (2012). Steam reforming of glycerol over Ni supported alumina xerogel for hydrogen

production. Energy Procedia, 18, 552–559. https://doi.org/10.1016/j.egypro.2012.05.067

Eftekhari, A., & Fang, B. (2017). Electrochemical hydrogen storage: Opportunities for fuel storage, batteries, fuel cells, and supercapacitors. International Journal of Hydrogen Energy, 42(40), 25143–25165. https://doi.org/10.1016/j.ijhydene.2017.08.103

Elkhalifa, E. A., & Friedrich, H. B. (2018). Magnesium oxide as a catalyst for the dehydrogenation of n-octane. Arabian Journal of Chemistry, 11(7), 1154–1159. https://doi.org/10.1016/j.arabjc.2014.10.002

Farnetti, E., Monte, R. Di, & Kašpar, J. (1999). Homogenous and Heterogenous Catalysis. In Encyclopedia of Life Support Systems: Vol. II.

Farrauto, R., Hwang, S., Shore, L., Ruettinger, W., Lampert, J., Giroux, T., Liu, Y., & Ilinich, O. (2003). New Material Needs for Hydrocarbon Fuel Processing: Generating Hydrogen for the PEM Fuel Cell. Annual Review of Materials Research, 33(1), 1–27. https://doi.org/10.1146/annurev.matsci.33.022802.091348

Fasolini, A., Cespi, D., Tabanelli, T., Cucciniello, R., & Cavani, F. (2019). Hydrogen from renewables: A case study of glycerol reforming. Catalysts, 9(9), 722. https://doi.org/10.3390/catal9090722

Fechete, I., Wang, Y., & Védrine, J. C. (2012). The past, present and future of heterogeneous catalysis. 189, 2–27. https://doi.org/10.1016/j.cattod.2012.04.003

Fernandez, E., Helmi, A., Medrano, J. A., Coenen, K., Arratibel, A., Melendez, J., de Nooijer, N. C.A., Spallina, V., Viviente, J. L., Zuñiga, J., van Sint Annaland, M., Pacheco Tanaka, D. A. & Gallucci, F. (2017). Palladium based membranes

and membrane reactors for hydrogen production and purification: An overview of research activities at Tecnalia and TU/e. International Journal of Hydrogen Energy, 42(19), 13763–13776. https://doi.org/10.1016/j.ijhydene.2017.03.067

Fuller, M. P., & Griffiths, P. R. (1978). Diffuse Reflectance Measurements by Infrared Fourier Transform Spectrometry. Analytical Chemistry, 50(13), 1906–1910. https://doi.org/10.1021/ac50035a045

Gallo, A., Pirovano, C., Ferrini, P., Marelli, M., Psaro, R., Santangelo, S., Giuliana, F., & Dal Santo, V. (2012). Influence of reaction parameters on the activity of ruthenium based catalysts for glycerol steam reforming. Applied Catalysis B: Environmental, 121–122, 40–49. https://doi.org/10.1016/j.apcatb.2012.03.013

Goula, M. A., Charisiou, N. D., Papageridis, K. N., & Siakavelas, G. (2016). Influence of the synthesis method parameters used to prepare nickel-based catalysts on the catalytic performance for the glycerol steam reforming reaction. Cuihua Xuebao/Chinese Journal of Catalysis, 37(11), 1949–1965. https://doi.org/10.1016/S1872-2067(16)62518-4

Gregg, S. J., & Sing, K. S. W. (1982). Adsorption, Surface Area and Porosity. In Academic Press (2nd ed., Vol. 86). https://doi.org/10.1002/bbpc.19820861019

Greluk, M., Rotko, M., & Turczyniak-surdacka, S. (2020). Applied Catalysis A , General Comparison of catalytic performance and coking resistant behaviors of cobalt- and nickel based catalyst with different Co/Ce and Ni/Ce molar ratio under SRE conditions. Applied Catalysis A, General, 590. 117334. https://doi.org/10.1016/j.apcata.2019.117334

Grosman, A., & Ortega, C. (2008). Capillary Condensation in Porous Materials. Hysteresis and Interaction without Pore Blocking/Percolation Process.

Langmuir, American Chemical Society, 24(8), 3977–3987. HAL Id: hal-00290441 https://hal.archives-ouvertes.fr/hal-00290441

Gurav, J. L., Jung, I.-K., Park, H.-H., Kang, E. S., & Nadargi, D. Y. (2010). Silica Aerogel: Synthesis and Applications. Journal of Nanomaterials, 2010, 11. https://doi.org/10.1155/2010/409310

Güler Şentürk, İ., & Büyükgüngör, H. (2010). An Examination of Used Different Waste Materials and Biohydrogen Production Methods. Journal of Engineering and Natural Sciences, 28(362), 369–395.

Güner, Ö. (2007). Acidity Characterization and Adsorption Characteristics of Cobalt and Lead Doped SBA-15 Mesoporous Materials Master of Science. Middle East Technical University, Ankara, Turkey.

Haryanto, A., Fernando, S. D., Filip To, S. D., Steele, P. H., & Pordesimo, L. (2011). High Temperature Water Gas Shift Reaction over Nickel Catalysts for Hydrogen Production: Effect of Supports, GHSV, Metal Loading, and Dopant Materials. Journal of Thermodynamics & Catalysis, 2(1). https://doi.org/10.4172/2157-7544.1000106

Hirai, T., Ikenaga, N. O., Miyake, T., & Suzuki, T. (2005). Production of hydrogen by steam reforming of glycerin on ruthenium catalyst. Energy and Fuels, 19(4), 1761–1762. https://doi.org/10.1021/ef050121q

Hohn, K. L., & Schmidt, L. D. (2001). Partial oxidation of methane to syngas at high space velocities over Rh-coated spheres. Applied Catalysis A: General, 211(1), 53–68. https://doi.org/10.1016/S0926-860X(00)00835-8

Honig, J. M. (2003). Physical and Chemical Properties of Surfaces. Annual Review of Physical Chemistry, 10(1), 77–102. https://doi.org/10.1146/annurev.pc.10.100159.000453

Hosseini, S. E., & Wahid, M. A. (2016). Hydrogen production from renewable and sustainable energy resources: Promising green energy carrier for clean development. Renewable and Sustainable Energy Reviews, 57, 850–866. https://doi.org/10.1016/j.rser.2015.12.112

Huang, J., & Zhang, H. (2019). Mn-based catalysts for sulfate radical-based advanced oxidation processes: A review. Environment International, 133. 105141 https://doi.org/10.1016/j.envint.2019.105141

Idriss, H., Scott, M., & Subramani, V. (2015). Introduction to hydrogen and its properties. In Compendium of Hydrogen Energy (pp. 3–19). https://doi.org/10.1016/b978-1-78242-361-4.00001-7

Ismaila, A., Chen, H., Shao, Y., Xu, S., Jiao, Y., Chen, X., Gao, X., Fan, X. (2020). Renewable hydrogen production from steam reforming of glycerol (SRG) over ceria-modified γ-alumina supported Ni catalyst. Chinese Journal of Chemical Engineering, 28(9), 2328–2336. https://doi.org/10.1016/j.cjche.2020.06.025

Jian, X., Zhou, Z., Wu, S., Chen, L., Zeng, Q., & Wang, C. (2014). Controllable preparation of Ni nanoparticles for catalysis of coiled carbon fibers growth. Nanoscale Research Letters, 9, 370. https://doi.org/10.1186/1556-276X-9-370

Kahle, L. C. S., Roussière, T., Maier, L., Herrera Delgado, K., Wasserschaff, G., Schunk, S. A., & Deutschmann, O. (2013). Methane dry reforming at high temperature and elevated pressure: Impact of gas-phase reactions. Industrial and Engineering Chemistry Research, 52(34), 11920–11930. https://doi.org/10.1021/ie401048w

Kent, J. E. (2013). Steam Reforming of Biodiesel By-Product Glycerol Bachelor of Science, Worcester Polytechnic Institute, Worcester, Massachusetts, USA.

Khairudin, N. F., Sukri, M. F. F., Khavarian, M., & Mohamed, A. R. (2018). Understanding the performance and mechanism of Mg-containing oxides as support catalysts in the thermal dry reforming of methane. Beilstein Journal of Nanotechnology, 9(1), 1162–1183. https://doi.org/10.3762/bjnano.9.108

Khalil, I., Celis-Cornejo, C. M., Thomas, K., Bazin, P., Travert, A., Pérez-Martínez, D. J., Baldovino-Medrano, V. G., Paul, J. F., & Maugé, F. (2020). In Situ IR-ATR Study of the Interaction of Nitrogen Heteroaromatic Compounds with HY Zeolites: Experimental and Theoretical Approaches. ChemCatChem, 12(4), 1095–1108. https://doi.org/10.1002/cctc.201901560

Kim, J., & Lee, D. (2013). Glycerol steam reforming on supported Ru-based catalysts for hydrogen production for fuel cells. International Journal of Hydrogen Energy, 38(27), 11853–11862. https://doi.org/10.1016/j.ijhydene.2013.06.141

Kirubakaran, A., Jain, S., & Nema, R. K. (2009). A review on fuel cell technologies and power electronic interface. Renewable and Sustainable Energy Reviews, 13(9), 2430–2440. https://doi.org/10.1016/j.rser.2009.04.004

Konsolakis, M., Ioakimidis, Z., Kraia, T., & Marnellos, G. E. (2016). Hydrogen Production by Ethanol Steam Reforming (ESR) over CeO_2 Supported Transition Metal (Fe, Co, Ni, Cu) Catalysts: Insight into the Structure-Activity Relationship. Catalysts, 6(3), 39. https://doi.org/10.3390/catal6030039

Kooli, F., Sasaki, T., Mizukami, F., Watanabe, M., Martin, C., & Rives, V. (2001). Characterization and acidic properties of silica pillared titanates. Journal of Materials Chemistry, 11(3), 841–845. https://doi.org/10.1039/b007315f

Kothari, R., Buddhi, D., & Sawhney, R. L. (2008). Comparison of environmental and economic aspects of various hydrogen production methods. Renewable and

Sustainable Energy Reviews, 12(2), 553–563. https://doi.org/10.1016/j.rser.2006.07.012

Krummenacher, J. J., West, K. N., & Schmidt, L. D. (2003). Catalytic Partial Oxidation of Higher Hydrocarbons at Millisecond Contact Times: Decane, Hexadecane, and Diesel Fuel. Journal of Catalysis, 215(2), 332–343. https://doi.org/10.1016/S0021-9517(03)00011-3

Lavina, B., Dera, P., & Downs, R. T. (2014). Modern X-ray Diffraction Methods in Mineralogy and Geosciences. Reviews in Mineralogy and Geochemistry, 78(1), 1–31. https://doi.org/10.2138/rmg.2014.78.1

Lee, C.-S., & Hyun, Y. (2020). Preparation and Characterization of Carbon Nanofibers and its Composites by Chemical Vapor Deposition, Chemical Vapor Deposition - Recent Advances and Applications in Optical, Solar Cells and Solid State Devices, Sudheer Neralla, Intechopen, https://doi.org/10.5772/63755

Liu, X., Zhao, L., Wang, H., Lai, H., Peng, G., Li, J., & Yi, Z., & Chen, K. (2018). Visible-light-driven H_2 production and decomposition of 4-nitrophenol over nickel phosphides. RSC Advances, 8(60), 34259-34265. https://doi.org/10.1039/c8ra06770h

Liu, Z., He, X., Cheng, R., Eisen, M. S., Terano, M., Scott, S. L., & Liu, B. (2014). Chromium catalysts for ethylene polymerization and oligomerization. In Advances in Chemical Engineering (1st ed., Vol. 44, pp. 127–191). https://doi.org/10.1016/B978-0-12-419974-3.00003-8

Llorca, J., Corberán, V. C., Divins, N. J., Fraile, R. O., & Taboada, E. (2013). Hydrogen from Bioethanol. In Renewable Hydrogen Technologies: Production, Purification, Storage, Applications and Safety (pp. 135–169). https://doi.org/10.1016/B978-0-444-56352-1.00007-6

Lopez, T., & Gomez, R. (1998). Evidence for Lewis and Brønsted Acid Sites on MgO Obtained by Sol- Gel. Sol-Gel Science and Technology, 13, 1043–1047. https://doi.org/10.1023/A:1008624718503

Lowell, S., Shields, J.E., Thomas, M.A., Thommes, M. (2006). Characterization of Porous Solids and Powders: Surface Area, Pore Size and Density, Springer, Netherlands.

Manfro, R. L., Ribeiro, N. F. P., & Souza, M. M. V. M. (2013). Production of hydrogen from steam reforming of glycerol using nickel catalysts supported on Al_2O_3, CeO_2 and ZrO_2. Catalysis for Sustainable Energy, 1(2013), 60–70. https://doi.org/10.2478/cse-2013-0001

Marchetti, J. M., Miguel, V. U., & Errazu, A. F. (2007). Possible methods for biodiesel production. Renewable and Sustainable Energy Reviews, 11(6), 1300–1311. https://doi.org/10.1016/j.rser.2005.08.006

Mazloomi, K., & Gomes, C. (2012). Hydrogen as an energy carrier: Prospects and challenges. Renewable and Sustainable Energy Reviews, 16(5), 3024–3033. https://doi.org/10.1016/j.rser.2012.02.028

Meloni, E., Martino, M., & Palma, V. (2020). A Short review on Ni Based Catalysts and Related Engineering Issues for Methane Steam Reforming. Catalysts, 10(3), 352. https://doi.org/10.3390/catal10030352

Meshkani, F., & Rezaei, M. (2014). High temperature water gas shift reaction over promoted iron based catalysts prepared by pyrolysis method. International Journal of Hydrogen Energy, 39(29), 16318–16328. https://doi.org/10.1016/j.ijhydene.2014.07.176

Ming, F., Qingli, X., Wei, Q., Zhikai, Z., Suping, Z., & Yongjie, Y. (2016). Hydrogen production from glycerol steam reforming over Ni/La/Co/Al2O3 catalyst. Energy Sources, Part A: Recovery, Utilization and Environmental Effects, 38(14), 2128–2134. https://doi.org/10.1080/15567036.2015.1052596

Mirza, N. R., Degenkolbe, S., & Witt, W. (2011). Analysis of hydrogen incidents to support risk assessment. International Journal of Hydrogen Energy, 36(18), 12068–12077. https://doi.org/10.1016/j.ijhydene.2011.06.080

Mohamed, W., Atan, R., & Yiap, T. (2009). Current and possible future applications of hydrogen fuel cells in Malaysia. International Conference on Advances in Mechanical Engineering (ICAME), 1–9.

Mohtasham, J. (2015). Review Article-Renewable Energies. Energy Procedia, 74, 1289–1297. https://doi.org/10.1016/j.egypro.2015.07.774

Mondal, P., & Dalai, A.K. (Eds.). (2017). Sustainable Utilization of Natural Resources (1st ed.). CRC Press. https://doi.org/10.1201/9781315153292

Moogi, S., Nakka, L., Potharaju, S. S. P., Ahmed, A., Farooq, A., Jung, S. C., Rhee, G. H. & Park, Y. K. (2020). Copper promoted Co/MgO: A stable and efficient catalyst for glycerol steam reforming. International Journal of Hydrogen Energy, 16(5), 3024–3033. https://doi.org/10.1016/j.ijhydene.2020.08.190

Morlanés, N., Almaksoud, W., Rai, R. K., Ould-chikh, S., Ali, M. M., Vidjayacoumar, B., Al-sabban, B. E., Albahily, K., Basset, J. (2020). Development of catalysts for ammonia synthesis based on metal phthalocyanine materials. Catalysis Science & Technology, 10(3), 844–852. https://doi.org/10.1039/c9cy02326g

Musić, S., Filipović-Vinceković, N., & Sekovanić, L. (2011). Precipitation of amorphous SiO_2 particles and their properties. Brazilian Journal of Chemical Engineering, 28(1), 89–94. https://doi.org/10.1590/S0104-66322011000100011

Nakoua, M. A., & El-Naas, M. H. (2009). GTL Feed by Catalytic Oxidation of Methane in Plate Reactor. In Proceedings of the 1st Annual Gas Processing Symposium (1st ed., pp. 362–369). https://doi.org/10.1016/b978-0-444-53292-3.50044-4

Newborough, M., & Cooley, G. (2020). Developments in the global hydrogen market : The spectrum of hydrogen colours. Fuel Cells Bulletin, 2020(11), 16–22. https://doi.org/10.1016/S1464-2859(20)30546-0

NPTEL. (2014). Lecture 5 Solid catalysts. NPTEL – Chemical Engineering – Catalyst Science and Technology Lecture, 1–254.

Obalı, Z., Sezgi, N. A., & Doğu, T. (2011). The synthesis and characterization of aluminum loaded SBA-type materials as catalyst for polypropylene degradation reaction. Chemical Engineering Journal, 176–177, 202–210. https://doi.org/10.1016/j.cej.2011.04.063

Odenkirk, W., Rheingold, A. L., & Bosnich, B. (1992). Homogeneous Catalysis: A Ruthenium-Based Lewis-Acid Catalyst for the Diels-Alder Reaction. Journal of the American Chemical Society, 114(16), 6392–6398. https://doi.org/10.1021/ja00042a015

Ozkal, E., Cacherat, B., & Morandi, B. (2015). Cobalt(III)-Catalyzed Functionalization of Unstrained Carbon-Carbon Bonds through β-Carbon Cleavage of Alcohols. ACS Catalysis, 5(11), 6458–6462. https://doi.org/10.1021/acscatal.5b01753

Pal, D. B., Chand, R., Upadhyay, S. N., & Mishra, P. K. (2018). Performance of water gas shift reaction catalysts: A review. Renewable and Sustainable Energy Reviews, 93(December 2017), 549–565. https://doi.org/10.1016/j.rser.2018.05.003

Pasman, H. J. (2011). Challenges to improve confidence level of risk assessment of hydrogen technologies. International Journal of Hydrogen Energy, 36(3), 2407–2413. https://doi.org/10.1016/j.ijhydene.2010.05.019

Petre, A. L., Auroux, A., Gélin, P., Caldararu, M., & Ionescu, N. I. (2001). Acid-base properties of supported gallium oxide catalysts. Thermochimica Acta, 379(1–2), 177–185. https://doi.org/10.1016/S0040-6031(01)00615-3

Pinacci, P., Louradour, E., Wimbert, L., Gindrat, M., Jarligo, M. O., Vassen, R., Comite, A., Serra, J.M., Jewulski, J., Mancuso L., Chiesa, P., Prestat, M. & Ivers-Tiffée, E. (2013). Dense membranes for oxygen and hydrogen separation (DEMOYS): Project overview and first results. Energy Procedia, 37, 1030–1038. https://doi.org/10.1016/j.egypro.2013.05.199

Profeti, L. P. R., Ticianelli, E. A., & Assaf, E. M. (2009). Production of hydrogen via steam reforming of biofuels on Ni/CeO_2-Al_2O_3 catalysts promoted by noble metals. International Journal of Hydrogen Energy, 34(12), 5049–5060. https://doi.org/10.1016/j.ijhydene.2009.03.050

Pudukudy, M., & Yaakob, Z. (2015). Methane decomposition over Ni, Co and Fe based monometallic catalysts supported on sol gel derived SiO_2 microflakes. Chemical Engineering Journal, 262, 1009–1021. https://doi.org/10.1016/j.cej.2014.10.077

Ramachandran, R., & Menon, R. K. (1998). An overview of industrial uses of hydrogen. International Journal of Hydrogen Energy, 23(7), 593–598. https://doi.org/10.1016/S0360-3199(97)00112-2

Ran, F., & Tan, Y. (2018). Polyaniline-Based Composites and Nanocomposites. In Polyaniline Blends, Composites, and Nanocomposites (pp. 175–208). https://doi.org/10.1016/b978-0-12-809551-5.00007-2

Reddy, R., Patel, S., Nair, S., & Suvikram, Y. (2011). Preparation of Hydrogen from Glycerol via Steam Reforming Process. Institute of Technology, Nirma University, Ahmedabad – 382 481.

Rhodes, C., Hutchings, G. J., & Ward, A. M. (1995). Water-gas shift reaction: finding the mechanistic boundary. Catalysis Today, 23(1), 43–58. https://doi.org/10.1016/0920-5861(94)00135-O

Rhodes, R. (2011). Explosive Lessons in Hydrogen Safety. Ask Magazine, 41, 46–50. Retrieved from https://www.nasa.gov/pdf/513855main_ASK_41s_explosive.pdf

Roselina, N. R. N., & Azizan, A. (2012). Ni nanoparticles : Study of particles formation and agglomeration. Procedia Engineering, 41, 1620–1626. https://doi.org/10.1016/j.proeng.2012.07.359

Sad, M. E., Duarte, H. A., Vignatti, C., Padró, C. L., & Apesteguía, C. R. (2015). Steam reforming of glycerol: Hydrogen production optimization. International Journal of Hydrogen Energy, 40(18), 6097–6106. https://doi.org/10.1016/j.ijhydene.2015.03.043

Sarıyer, M. (2018). Sorption Enhanced Reforming of Ethanol over Novel Catalysts and Microwave Reactor Application Master of Science. Middle East Technical University, Ankara, Turkey.

Schaaf, T., Grünig, J., Schuster, M. R., Rothenfluh, T., & Orth, A. (2014). Methanation of CO_2 - storage of renewable energy in a gas distribution system.

Energy, Sustainability and Society, 4(1), 1–14. https://doi.org/10.1186/s13705-014-0029-1

Schwengber, C. A., Alves, H. J., Schaffner, R. A., Da Silva, F. A., Sequinel, R., Bach, V. R., & Ferracin, R. J. (2016). Overview of glycerol reforming for hydrogen production. Renewable and Sustainable Energy Reviews, 58, 259–266. https://doi.org/10.1016/j.rser.2015.12.279

Seadira, T., Sadanandam, G., Ntho, T. A., Lu, X., Masuku, C. M., & Scurrell, M. (2017). Hydrogen production from glycerol reforming: conventional and green production. Reviews in Chemical Engineering, 34(5), 695-726. https://doi.org/10.1515/revce-2016-0064

Shen, Y., Jiang, P., Wai, P. T., Gu, Q., & Zhang, W. (2019). Recent Progress in Application of Molybdenum-Based Catalysts for Epoxidation of Alkenes. Catalysts, 9(31), 27. https://doi.org/10.3390/catal9010031

Sherwood, S. C., Dixit, V., & Salomez, C. (2018). The global warming potential of near-surface emitted water vapour. Environmental Research Letters, 13(10). 104006. https://doi.org/10.1088/1748-9326/aae018

Shukla, K. & Srivastava, V.C. (2017) Synthesis of organic carbonates from alcoholysis of urea: A review, Catalysis Reviews, 59(1), 1–43. https://doi.org/10.1080/01614940.2016.1263088

Silva, J. M., Soria, M. A., & Madeira, L. M. (2015). Challenges and strategies for optimization of glycerol steam reforming process. Renewable and Sustainable Energy Reviews, (Vol. 42, pp. 1187–1213). https://doi.org/10.1016/j.rser.2014.10.084

Sivri, S., Dilek, C. & Sezgi, N. (2019). Synthesis and Characterization of Aluminum Containing Silica Aerogel Catalysts for Degradation of PLA. International

Journal of Chemical Reactor Engineering, 17(5), 1-10. 2018-0163. https://doi.org/10.1515/ijcre-2018-0163

Słowik, G., Gawryszuk-Rżysko, A., Greluk, M. et al. (2016). Estimation of Average Crystallites Size of Active Phase in Ceria-Supported Cobalt-Based Catalysts by Hydrogen Chemisorption vs TEM and XRD Methods. Catal Lett 146, 2173–2184. https://doi.org/10.1007/s10562-016-1843-1

Soleimani Dorcheh, A., & Abbasi, M. H. (2008). Silica aerogel; synthesis, properties and characterization. Journal of Materials Processing Technology, 199(1), 10–26. https://doi.org/10.1016/j.jmatprotec.2007.10.060

Song, C. (2002). Fuel processing for low-temperature and high-temperature fuel cells: Challenges, and opportunities for sustainable development in the 21st century. Catalysis Today, 77(1-2), 17-49. https://doi.org/10.1016/S0920-5861(02)00231-6

Spivey, J. J. (2011). Desulfurization for Fuel Cells. In Deactivation of Reforming Catalysts, Elsevier, LA 70803, USA. https://doi.org/10.1016/B978-0-444-53563-4.10011-2

Staffell, I., Scamman, D., Velazquez Abad, A., Balcombe, P., Dodds, P. E., Ekins, P., Shah, N., & Ward, K. R. (2019). The role of hydrogen and fuel cells in the global energy system. Energy and Environmental Science, 12(2), 463–491. https://doi.org/10.1039/c8ee01157e

Stangeland, K., Kalai, D., Li, H., & Yu, Z. (2017). CO_2 Methanation: The Effect of Catalysts and Reaction Conditions. Energy Procedia, 105(1876), 2022–2027. https://doi.org/10.1016/j.egypro.2017.03.577

Sun, B., Khan, F., Süss-Fink, G., & Therrien, B. (2017). Metal Catalysts Intercalated in Smectite Clays. In Encapsulated Catalysts (pp. 387–441). https://doi.org/10.1016/B978-0-12-803836-9.00012-2

Sundari, R., & Vaidya, P. D. (2012). Reaction kinetics of glycerol steam reforming using a Ru/Al_2O_3 catalyst. Energy and Fuels, 26(7), 4195–4204. https://doi.org/10.1021/ef300658n

Surendar, M., Sagar, T. V., Raveendra, G., Ashwani Kumar, M., Lingaiah, N., Rama Rao, K. S., & Sai Prasad, P. S. (2016). Pt doped LaCoO 3 perovskite: A precursor for a highly efficient catalyst for hydrogen production from glycerol. International Journal of Hydrogen Energy, 41(4), 2285–2297. https://doi.org/10.1016/j.ijhydene.2015.12.075

Susi, T., Nasibulin, A. G., Jiang, H., & Kauppinen, E. I. (2008). CVD synthesis of hierarchical 3D MWCNT/carbon-fiber nanostructures. Journal of Nanomaterials, 2008(1), 37–42. https://doi.org/10.1155/2008/425195

Thommes, M. (2010). Physical adsorption characterization of nanoporous materials. Chemie-Ingenieur-Technik, 82(7), 1059–1073. https://doi.org/10.1002/cite.201000064

Thyssen, V. V, Maia, T. A., & Assaf, E. M. (2013). Ni supported on $La_2O_3 – SiO_2$ used to catalyze glycerol steam reforming. Fuel, 105, 358–363. https://doi.org/10.1016/j.fuel.2012.06.105

Torbina, V. V, Vodyankin, A. A., Ten, S., Mamontov, G. V, Salaev, M. A., Sobolev, V. I., & Vodyankina, O. V. (2018). Ag-Based Catalysts in Heterogeneous Selective Oxidation of Alcohols : A Review. Catalysts, 8(10), 447. https://doi.org/10.3390/catal8100447

Vaidya, P. D., & Rodrigues, A. E. (2009). Glycerol Reforming for Hydrogen Production : A Review. Chemical Engineering Technolgy, 32(10), 1463–1469. https://doi.org/10.1002/ceat.200900120

Velthoen, M. E. Z., Nab, S., & Weckhuysen, B. M. (2018). Probing acid sites in solid catalysts with pyridine UV-Vis spectroscopy. Physical Chemistry Chemical Physics, 20(33), 21647–21659. https://doi.org/10.1039/c8cp03991g

Wang, Z., Jiang, X., Pan, M., & Shi, Y. (2020). Nano-Scale Pore Structure and Its Multi-Fractal Characteristics of Tight Sandstone by N_2 Adsorption/Desorption Analyses: A Case Study of Shihezi Formation from the Sulige Gas Filed, Ordos Basin, China. Minerals, 10(4), 377. https://doi.org/10.3390/min10040377

Wilhelm, D. J., Simbeck, D. R., Karp, A. D., & Dickenson, R. L. (2001). Syngas production for gas-to-liquids applications: technologies, issues and outlook. Fuel Processing Technology, 71(1-3), 139–148. https://doi.org/10.1016/S0378-3820 01 00140-0

Wołowiec, M., Pruss, A., Komorowska-Kaufman, M., Lasocka-Gomuła, I., Rzepa, G., & Bajda, T. (2019). The properties of sludge formed as a result of coagulation of backwash water from filters removing iron and manganese from groundwater. SN Applied Sciences, 1(6), 1–10. https://doi.org/10.1007/s42452-019-0653-7

Wu, C., Nahil, M. A., Miskolczi, N., Huang, J., & Williams, P. T. (2016). Production and application of carbon nanotubes, as a co-product of hydrogen from the pyrolysis-catalytic reforming of waste plastic. Process Safety and Environmental Protection, 103, 107–114. https://doi.org/10.1016/j.psep.2016.07.001

Wu, G., Yu, Y., Cheng, X., & Zhang, Y. (2011). Preparation and surface modification mechanism of silica aerogels via ambient pressure drying. Materials Chemistry and Physics, 129(1–2), 308–314. https://doi.org/10.1016/j.matchemphys.2011.04.003

Xu, Z., Chen, Y., Li, W., Li, J., Yu, H., Liu, L., & Luo, L. (2018). RSC Advances carbon fibres and their enhanced antioxidant and. RSC Advances, 8, 17944–17949. https://doi.org/10.1039/C8RA02017E

Yu, F., Yue, B., Wang, X., Geng, S., Lu, X., & Ding, W. (2009). Hydrocracking of tar components from hot coke oven gas over a Ni/Ce-ZrO_2/γ-Al_2O_3 catalyst at atmospheric pressure. Cuihua Xuebao/Chinese Journal of Catalysis, 30(7), 690–696. https://doi.org/10.1016/s1872-2067(08)60119-9

Yusuf N. Y., Masdar M. S., Nordin D., & Husaini T. (2015). Challenges in Biohydrogen Technologies for Fuel Cell Application. American Journal of Chemistry, 5(3A), 40–47. https://doi.org/10.5923/c.chemistry.201501.06

Zamzuri, N. H., Mat, R., Saidina Amin, N. A., & Talebian-Kiakalaieh, A. (2017). Hydrogen production from catalytic steam reforming of glycerol over various supported nickel catalysts. International Journal of Hydrogen Energy, 42(14), 9087–9098. https://doi.org/10.1016/j.ijhydene.2016.05.084

Zhang, N., Xian, G., Li, X., Zhang, P., & Zhang, G. (2018). Iron Based Catalysts Used in Water Treatment Assisted by Ultrasound : A Mini Review. Frontiers in Chemistry, 6(12), 1–6. https://doi.org/10.3389/fchem.2018.00012

Zhang, Y., Yang, B., Yang, Z., & Ye, G. (2019). Ink-bottle Effect and Pore Size Distribution of Cementitious Materials Identified by Pressurization–Depressurization Cycling Mercury Intrusion Porosimetry. Materials 12(9), 1454. https://doi.org/10.3390/ma12091454

Zhao, Y., Li, C., Yao, K., & Liang, J. (2007). Preparation of carbon nanofibers over carbon nanotube-nickel catalyst in propylene decomposition. Journal of Materials Science, 42(12), 4240–4244. https://doi.org/10.1007/s10853-006-0676-5

APPENDICES

A. Calculation of Amount of Metal Loaded on Silica Aerogel

Amounts of metal loaded on silica aerogel were calculated using the Equation A.1.

$$m_{metal\ precursor} = \frac{a\ x\ m_{SA}\ x\ MW_{metal\ precursor}}{MW_{metal}} \qquad A.1$$

where,

a = desired amount of metal content, by weight %

m = amount of metal precursor & silica aerogel, g

MW = molecular weight of metal & metal precursor, g/mole

B. XRD Data of Metals, Metal Oxides and Carbon

XRD data of nickel and nickel oxide were given in Tables B.1 and B.2, respectively.

Table B.1 XRD Data of Nickel

Formula: Ni
PDF Card No: 00-004-0850
Radiation: CuKα1
Wavelength: 1.5405 Å

2θ (°)	**d spacing (Å)**	**Intensity (%)**	**h k l**
44.51	2.034	100.0	1 1 1
51.85	1.762	42.0	2 0 0
76.37	1.246	21.0	2 2 2
92.94	1.062	20.0	3 1 1
98.45	1.017	7.0	2 2 2
121.93	0.881	4.0	4 0 0
144.67	0.808	14.0	3 3 1
155.65	0.788	15.0	4 2 0

Table B.2 XRD Data of Nickel Oxide

Formula: NiO

PDF Card No: 01-089-5881

Radiation: CuKα1

Wavelength: 1.5406 Å

2θ (°)	**d spacing (Å)**	**Intensity (%)**	**h k l**
18.38	4.823	0.1	1 1 1
21.26	4.177	0.1	2 0 0
30.24	2.953	0.1	2 2 2
35.62	2.519	0.1	3 1 1
37.26	2.411	67.2	2 2 2
43.29	2.088	100.0	4 0 0
47.40	1.916	0.1	3 3 1
53.71	1.705	0.1	4 2 2
57.26	1.608	0.1	5 1 1
62.88	1.477	46.6	4 4 0
66.12	1.412	0.1	5 3 1
71.35	1.321	0.1	6 2 0
75.42	1.259	16.2	6 2 2
79.42	1.206	12.0	4 4 4
82.38	1.170	0.1	7 7 1
87.27	1.116	0.1	6 4 2

XRD data of cobalt and cobalt oxide were given in Tables B.3 and B.4, respectively.

Table B.3 XRD Data of Cobalt

Formula: Co **PDF Card No:** 00-015-0806 **Radiation:** CuKα1 **Wavelength:** 1.5406 Å			
2θ (°)	**d spacing (Å)**	**Intensity (%)**	**h k l**
44.23	2.046	100.0	1 1 1
51.53	1.772	42.1	2 0 0
75.87	1.253	16.8	2 2 0

Table B.4 XRD Data of Cobalt Oxide

Formula: CoO_2 **PDF Card No:** 01-089-8399 **Radiation:** CuKα1 **Wavelength:** 1.5406 Å			
2θ (°)	**d spacing (Å)**	**Intensity (%)**	**h k l**
20.93	4.240	100.0	0 0 1
36.76	2.443	20.2	1 0 0
42.68	2.177	52.3	0 0 1
57.51	1.601	24.6	0 1 2
66.21	1.410	10.4	1 1 0
70.28	1.338	9.5	1 1 1
78.04	1.223	7.1	1 0 3
78.19	1.221	4.0	2 0 0
82.03	1.174	5.0	2 0 1

XRD data of chromium and chromium oxide were given in Tables B.5 and B.6, respectively.

Table B.5 XRD Data of Chromium

Formula: Cr
PDF Card No: 00-001-1250
Radiation: MoKα
Wavelength: 0.709 Å

2θ (°)	**d spacing (Å)**	**Intensity (%)**	**h k l**
44.14	2.050	100.0	1 1 0
64.18	1.450	20.0	2 0 0
81.50	1.180	50.0	2 1 1
96.81	1.030	10.0	2 2 0
113.70	0.920	30.0	3 1 0
132.98	0.840	5.0	2 2 2
180.00	0.770	30.0	3 2 1
180.00	0.720	1.0	4 0 0
180.00	0.680	20.0	4 1 1
180.00	0.650	5.0	4 2 0
180.00	0.620	2.0	3 3 2
180.00	0.590	1.0	4 2 2
180.00	0.570	15.0	5 1 0

Table B.6 XRD Data of Chromium Oxide

Formula: Cr_2O_3

PDF Card No: 00-038-1479

Radiation: CuKα1

Wavelength: 1.5406 Å

2θ (°)	d spacing (Å)	Intensity (%)	h k l
24.49	3.631	73.0	0 1 2
33.60	2.665	100.0	1 0 4
36.20	2.480	93.0	1 1 0
39.75	2.266	7.0	0 0 6
41.48	2.175	35.0	1 1 3
44.19	2.048	6.0	2 0 2
50.22	1.815	38.0	0 2 4
54.85	1.672	87.0	1 1 6
57.11	1.611	1.0	2 1 1
58.40	1.579	7.0	1 2 2
63.45	1.465	28.0	2 1 4
65.10	1.432	39.0	3 0 0
72.94	1.296	14.0	1 0 10
73.33	1.290	6.0	1 1 9
76.85	1.239	9.0	2 2 0
79.05	1.210	6.0	3 0 6
80.20	1.196	1.0	2 2 3
82.09	1.173	4.0	3 1 2
84.24	1.149	7.0	0 2 10
85.68	1.133	2.0	0 0 12

XRD data of zirconium and zirconium oxide were given in Tables B.7 and B.8, respectively.

Table B.7 XRD Data of Zirconium

Formula: Zr
PDF Card No: 01-089-4791
Radiation: CuKα1
Wavelength: 1.5406 Å

2θ (°)	**d spacing (Å)**	**Intensity (%)**	**h k l**
31.95	2.799	25.2	1 0 0
34.82	2.574	25.6	0 0 2
36.51	2.459	100.0	1 0 1
47.98	1.895	13.5	1 0 2
56.94	1.616	14.5	1 1 0
63.54	1.463	14.3	1 0 3
66.79	1.399	2.0	2 0 0
68.50	1.369	14.2	1 1 2
69.56	1.350	10.2	2 0 1
73.52	1.287	1.8	0 0 4
77.59	1.229	2.3	2 0 0
82.40	1.169	1.8	1 0 4

Table B.8 XRD Data of Zirconium Oxide

Formula: ZrO_2

PDF Card No: 00-002-0733

Radiation: MoKα

Wavelength: 0.709 Å

2θ (°)	d spacing (Å)	Intensity (%)	h k l
30.48	2.930	100.0	1 0 1
35.60	2.520	40.0	1 1 0
50.37	1.810	60.0	1 1 2
50.98	1.790	100.0	2 0 0
59.60	1.550	50.0	1 0 3
60.46	1.530	100.0	2 1 1
63.20	1.470	60.0	2 0 2
73.33	1.290	40.0	0 0 4
74.68	1.270	60.0	2 2 0
82.35	1.170	40.0	2 1 3
85.95	1.130	40.0	3 1 0
88.90	1.100	60.0	3 1 1
94.38	1.050	40.0	2 0 4
95.57	1.040	70.0	3 1 2
101.74	0.993	40.0	1 0 5
103.93	0.978	70.0	3 2 1

XRD data of molybdenum and molybdenum oxide were given in Tables B.9 and B.10, respectively.

Table B.9 XRD Data of Molybdenum

Formula: Mo **PDF Card No:** 00-042-1120 **Radiation:** CuKα1 **Wavelength:** 1.5406 Å			
2θ (°)	**d spacing (Å)**	**Intensity (%)**	**h k l**
40.52	2.225	100.0	1 1 0
58.61	1.574	16.0	2 0 0
73.68	1.285	31.0	2 1 1
87.60	1.113	9.0	2 2 0
101.41	0.995	14.0	3 1 0
115.96	0.908	3.0	2 2 2
132.64	0.841	24.0	3 2 1

Table B.10 XRD Data of Molybdenum Oxide

Formula: MoO_2 **PDF Card No:** 01-086-0135 **Radiation:** CuKα1 **Wavelength:** 1.5406 Å			
2θ (°)	**d spacing (Å)**	**Intensity (%)**	**h k l**
18.42	4.813	1.5	1 0 0
26.00	3.424	100.0	0 0 1
31.79	2.813	1.8	-1 0 2
36.75	2.444	12.0	-2 0 2

Table B.10 (cont'd) XRD Data of Molybdenum Oxide

2θ (°)	d spacing (Å)	Intensity (%)	h k l
36.90	2.434	8.5	-1 1 2
36.98	2.429	32.7	-2 1 1
37.23	2.413	10.2	0 0 2
37.34	2.406	17.7	2 0 0
41.33	2.183	2.5	-2 1 2
41.49	2.175	1.5	-1 2 1
41.60	2.169	1.1	0 2 1
41.76	2.161	0.8	0 1 2
41.86	2.156	2.2	2 1 0
49.45	1.842	2.0	-3 0 2
49.55	1.838	2.5	-1 2 2
49.90	1.826	0.3	1 2 1
50.20	1.816	0.1	1 0 2
53.04	1.725	9.6	-2 1 3
53.13	1.723	11.4	-2 2 2
53.31	1.717	7.1	-1 1 3
53.48	1.712	18.7	-3 1 1
53.57	1.709	15.5	2 2 0
53.92	1.699	11.7	1 1 2
57.39	1.604	0.4	3 0 0
59.83	1.545	2.3	-3 1 3
60.24	1.535	6.1	0 3 1
60.57	1.527	5.5	0 1 3
60.75	1.523	2.9	3 1 0
63.33	1.467	1.2	-3 2 2

Table B.10 (cont'd) XRD Data of Molybdenum Oxide

2θ (°)	**d spacing (Å)**	**Intensity (%)**	**h k l**
63.47	1.464	0.7	-1 2 3
63.97	1.454	0.1	1 2 2
66.42	1.406	2.1	-2 0 4
66.65	1.402	8.3	-4 0 2
66.88	1.398	4.1	1 3 1
67.58	1.385	3.0	2 0 2
69.28	1.355	0.7	-3 0 4
69.53	1.351	0.4	-3 2 3
69.89	1.345	0.7	-1 0 4
70.10	1.341	0.5	0 2 3
70.26	1.339	0.4	3 2 0
70.66	1.332	0.2	2 1 2
72.46	1.303	1.4	-4 1 3
73.20	1.292	2.1	-4 1 1
73.58	1.286	0.2	1 1 3
73.73	1.284	0.2	3 1 1
78.16	1.222	0.2	-4 0 4
78.53	1.217	2.2	-2 3 3
78.75	1.214	3.5	0 4 0
79.25	1.208	2.2	1 3 2
79.34	1.207	2.0	0 0 4
79.62	1.203	3.1	4 0 0
81.22	1.183	0.9	-3 2 4
81.80	1.176	0.4	-1 2 4
82.06	1.173	0.3	-4 2 1

Table B.10 (cont'd) XRD Data of Molybdenum Oxide

2θ (°)	d spacing (Å)	Intensity (%)	h k l
82.26	1.171	0.1	0 1 4
82.53	1.168	0.1	4 1 0
84.25	1.148	0.6	-3 3 3
84.90	1.141	2.1	0 3 3
87.41	1.115	0.2	-1 4 2
87.69	1.112	0.5	1 4 1
88.84	1.101	0.1	3 0 2
89.78	1.091	1.1	-4 2 4
82.26	1.171	0.1	0 1 4
82.53	1.168	0.1	4 1 0
84.25	1.148	0.6	-3 3 3
84.90	1.141	2.1	0 3 3
87.41	1.115	0.2	-1 4 2
87.69	1.112	0.5	1 4 1
88.84	1.101	0.1	3 0 2
89.78	1.091	1.1	-4 2 4

XRD data of silver and silver oxide were given in Tables B.11 and B.12, respectively.

Table B.11 XRD Data of Silver

Formula: Ag
PDF Card No: 00-004-0783
Radiation: CuKα1
Wavelength: 1.5406 Å

2θ (°)	**d spacing (Å)**	**Intensity (%)**	**h k l**
38.12	2.359	100.0	1 1 1
44.28	2.044	40.0	2 0 0
64.43	1.445	25.0	2 2 0
77.47	1.231	26.0	3 1 1
81.54	1.180	12.0	2 2 2
97.89	1.022	4.0	4 0 0
110.50	0.938	15.0	3 3 1
114.92	0.914	12.0	4 2 0
134.88	0.834	13.0	4 2 2

Table B.12 XRD Data of Silver Oxide

Formula: Ag_2O

PDF Card No: 00-041-1104

Radiation: CuKα1

Wavelength: 1.5418 Å

2θ (°)	**d spacing (Å)**	**Intensity (%)**	**h k l**
26.65	3.342	2.0	1 1 0
32.79	2.729	100.0	1 1 1
38.07	2.362	28.0	2 0 0
47.07	1.929	1.0	2 1 1
54.90	1.671	13.0	2 2 0
65.44	1.425	8.0	3 1 1
68.75	1.364	2.0	2 2 2
81.38	1.182	1.0	4 0 0
90.53	1.084	1.0	3 3 1
93.59	1.057	1.0	4 2 0
105.98	0.965	1.0	4 2 2
115.76	0.909	1.0	5 1 1

XRD data of ruthenium was given in Table B.13.

Table B.13 XRD Data of Ruthenium

Formula: Ru **PDF Card No:** 03-065-1863 **Radiation:** CuKα1 **Wavelength:** 1.5406 Å			
2θ (°)	**d spacing (Å)**	**Intensity (%)**	**h k l**
38.38	3.343	25.8	1 0 0
42.18	2.141	25.7	0 0 2
44.02	2.056	100.0	1 0 1
58.34	1.581	12.4	1 0 2
69.41	1.353	13.0	1 1 0
78.39	1.219	12.9	1 0 3
82.21	1.172	1.8	2 0 0
84.68	1.144	13.3	1 1 2
85.94	1.130	9.5	2 0 1
92.05	1.070	1.8	0 0 4
97.09	1.028	2.3	2 0 2
104.59	0.974	2.0	1 0 4
116.56	0.906	5.2	2 0 3
120.86	0.886	1.7	2 1 0
125.28	0.867	9.9	2 1 1
133.16	0.839	6.5	1 1 4
140.52	0.818	3.2	2 1 2
146.55	0.804	4.8	1 0 5

XRD data of magnesium and magnesium oxide were given in Tables B.14 and B.15, respectively.

Table B.14 XRD Data of Magnesium

Formula: Mg **PDF Card No:** 03-065-7219 **Radiation:** CuKα1 **Wavelength:** 1.5406 Å			
2θ (°)	**d spacing (Å)**	**Intensity (%)**	**h k l**
43.29	2.088	100.0	1 1 0
62.89	1.476	12.5	2 0 0
79.43	1.206	19.3	2 1 1
95.09	1.044	4.8	2 2 0
111.15	0.934	6.1	3 1 0
129.27	0.852	1.6	2 2 2

Table B.15 XRD Data of Magnesium Oxide

Formula: MgO **PDF Card No:** 01-075-1525 **Radiation:** CuKα1 **Wavelength:** 1.5406 Å			
2θ (°)	**d spacing (Å)**	**Intensity (%)**	**h k l**
37.06	2.424	11.6	1 1 1
43.06	2.099	100.0	2 0 0
62.53	1.484	44.9	2 2 0
74.97	1.266	5.0	3 1 1
78.93	1.212	10.9	2 2 2

XRD data of iron oxide was given in Table B.16.

Table B.16 XRD Data of Iron Oxide

Formula: $Fe_{0.925}O$ **PDF Card No:** 01-089-0686 **Radiation:** CuKα1 **Wavelength:** 1.5406 Å			
2θ (°)	**d spacing (Å)**	**Intensity (%)**	**h k l**
36.10	2.486	62.2	1 1 1
41.92	2.153	100.0	2 0 0
60.78	1.523	55.9	2 2 0
72.77	1.298	15.7	3 1 1
76.58	1.243	11.3	2 2 2

XRD data of ferrous manganese oxide - in contact with iron was given in Table B.17.

Table B.17 XRD Data of Ferrous Manganese Oxide

Formula: $(FeO)_{0.899}(MnO)_{0.101}$ **PDF Card No:** 01-077-2356 **Radiation:** CuKα1 **Wavelength:** 1.5406 Å			
2θ (°)	**d spacing (Å)**	**Intensity (%)**	**h k l**
35.91	2.499	67.9	1 1 1
41.70	2.164	100.0	2 0 0
60.45	1.530	46.7	2 2 0
72.35	1.305	16.6	3 1 1
76.13	1.249	11.5	2 2 2

XRD data of carbon was given in Table B.18.

Table B.18 XRD Data of Carbon

Formula: C

PDF Card No: 00-041-1487

Radiation: CuKα1

Wavelength: 1.5406 Å

2θ (°)	**d spacing (Å)**	**Intensity (%)**	**h k l**
26.38	3.376	100.0	0 0 2
42.22	2.139	2.0	1 0 0
44.39	2.039	6.0	1 0 1
50.45	1.807	1.0	1 0 2
54.54	1.681	4.0	0 0 4
59.69	1.548	1.0	1 0 3
77.24	1.234	3.0	1 1 0
83.18	1.160	3.0	1 1 2
86.82	1.121	1.0	0 0 6
93.59	1.057	1.0	2 0 1

XRD data of nickel carbide was given in Table B.19.

Table B.19 XRD Data of Nickel Carbide

Formula: NiC

PDF Card No: 00-014-0020

Radiation: CuKα1

Wavelength: 1.5406 Å

2θ (°)	**d spacing (Å)**	**Intensity (%)**	**h k l**
44.39	2.039	100.0	1 1 1
51.75	1.765	60.0	2 0 0
75.44	1.259	60.0	2 0 -
92.43	1.067	60.0	3 1 1
98.08	1.020	40.0	2 2 2
121.46	0.883	20.0	4 0 0
143.15	0.812	60.0	3 3 1

XRD data of iron nickel was given in Table B.20.

Table B.20 XRD Data of Iron Nickel

Formula: Fe_3Ni_2 **PDF Card No:** 03-065-5131 **Radiation:** CuKα1 **Wavelength:** 1.5406 Å			
2θ (°)	**d spacing (Å)**	**Intensity (%)**	**h k l**
43.53	2.077	100.0	1 1 1
50.70	1.799	42.0	2 0 0
74.53	1.272	17.0	2 2 0
90.48	1.085	15.7	3 1 1
95.74	1.039	4.3	2 2 2
117.82	0.899	1.9	4 0 0
137.87	0.825	6.0	3 3 1
146.44	0.805	5.8	4 2 0

XRD data of magnesium nickel was given in Table B.21.

Table B.21 XRD Data of Magnesium Nickel

Formula: Mg_6Ni **PDF Card No:** 00-051-1179 **Radiation:** CuKα1 **Wavelength:** 1.5406 Å			
2θ (°)	**d spacing (Å)**	**Intensity (%)**	**h k l**
12.45	7.101	9.0	2 2 0
15.26	5.800	10.0	2 2 2
17.63	5.027	17.0	4 0 0

Table B.21 (cont'd) XRD Data of Magnesium Nickel

2θ (°)	**d spacing (Å)**	**Intensity (%)**	**h k l**
21.65	4.102	30.0	4 2 2
37.98	2.367	100.0	8 2 2
42.17	2.141	13.0	6 6 4
44.14	2.050	10.0	8 4 4
48.76	1.866	7.0	8 6 4

XRD data of magnesium nickel was given in Table B.22.

Table B.22 XRD Data of Magnesium Nickel

Formula: $MgNi_2$ **PDF Card No:** 03-065-9715 **Radiation:** CuKα1 **Wavelength:** 1.5406 Å			
2θ (°)	**d spacing (Å)**	**Intensity (%)**	**h k l**
11.21	7.885	0.1	0 0 2
21.33	4.161	18.7	1 0 0
22.07	4.024	63.2	1 0 1
22.53	3.942	35.3	0 0 4
24.16	3.680	22.1	1 0 2
27.31	3.263	0.6	1 0 3
31.23	2.862	0.3	1 0 4
37.40	2.402	10.7	1 1 0
40.56	2.222	36.0	1 0 6
43.85	2.063	17.2	2 0 1
44.11	2.052	100.0	1 1 4

Table B.22 (cont'd) XRD Data of Magnesium Nickel

2θ (°)	d spacing (Å)	Intensity (%)	h k l
45.03	2.012	82.3	2 0 2
45.76	1.981	20.8	1 0 7
46.00	1.971	33.1	0 0 8
46.93	1.935	37.2	2 0 3
49.49	1.840	10.5	2 0 4
52.66	1.737	16.0	2 0 5
56.35	1.631	13.5	2 0 6
58.97	1.565	4.3	2 1 1
59.92	1.542	1.9	2 1 2
62.98	1.475	0.1	1 0 10
65.13	1.431	0.2	2 0 8
67.47	1.387	1.2	3 0 0
69.60	1.350	9.1	2 1 6
72.13	1.308	13.8	3 0 4
73.35	1.290	5.6	2 1 7
75.60	1.257	13.3	2 0 10
79.77	1.201	15.3	2 2 0
97.34	1.026	9.1	2 2 8
121.03	0.885	5.1	4 1 4
132.36	0.842	1.5	4 1 7
145.10	0.807	0.9	2 0 18
149.17	0.799	1.0	2 1 17

XRD data of nickel ruthenium was given in Table B.23.

Table B.23 XRD Data of Nickel Ruthenium

Formula: NiRu **PDF Card No:** 03-065-6490 **Radiation:** CuKα1 **Wavelength:** 1.5406 Å			
2θ (°)	**d spacing (Å)**	**Intensity (%)**	**h k l**
39.90	2.258	0.1	1 0 0
43.07	2.099	100.0	0 0 2
45.59	1.988	0.1	1 0 1
60.15	1.537	0.1	1 0 2
72.45	1.304	10.1	1 1 0
80.74	1.189	0.1	1 0 3
88.16	1.107	9.6	1 1 2
94.47	1.049	5.1	0 0 4
101.58	0.994	0.1	2 0 2
108.10	0.952	0.1	1 0 4
122.51	0.879	0.1	2 0 3
129.02	0.853	0.1	2 1 0
134.18	0.836	0.1	2 1 1
140.92	0.817	3.9	1 1 4

XRD data of nickel ruthenium was given in Table B.24.

Table B.24 XRD Data of Nickel Ruthenium

Formula: $Ni_{0.705}Ru_{0.295}$ **PDF Card No:** 03-065-4309 **Radiation:** CuKα1 **Wavelength:** 1.5406 Å			
2θ (°)	**d spacing (Å)**	**Intensity (%)**	**h k l**
43.20	2.092	100.0	1 1 1
50.31	1.812	42.9	2 0 0
73.91	1.281	18.3	2 2 0
89.65	1.093	17.3	3 1 1
94.83	1.046	4.8	2 2 2
116.47	0.906	2.2	4 0 0
135.79	0.831	7.0	3 3 1
143.81	0.810	6.8	4 2 0

XRD data of molybdenum nickel was given in Table B.25.

Table B.25 XRD Data of Molybdenum Nickel

Formula: $MoNi_4$ **PDF Card No:** 03-065-1533 **Radiation:** CuKα1 **Wavelength:** 1.5406 Å			
2θ (°)	**d spacing (Å)**	**Intensity (%)**	**h k l**
21.96	4.045	5.9	1 1 0
29.51	3.025	5.3	1 0 1
31.25	2.860	2.2	2 0 0

Table B.25 (cont'd) XRD Data of Molybdenum Nickel

2θ (°)	d spacing (Å)	Intensity (%)	h k l
43.51	2.078	100.0	2 1 1
44.78	2.022	0.9	2 2 0
50.41	1.809	29.8	1 3 0
51.22	1.782	13.8	0 0 2
54.54	1.681	0.8	3 0 1
56.37	1.631	0.7	1 1 2
61.23	1.512	0.6	2 0 2
64.21	1.449	1.0	2 3 1
65.18	1.430	0.2	4 0 0
69.69	1.348	0.2	3 3 0
70.36	1.337	0.4	2 2 2
73.14	1.293	0.7	1 4 1
74.06	1.279	6.8	4 2 0
74.72	1.269	13.0	1 3 2
82.94	1.163	0.2	1 0 3
86.73	1.122	0.2	5 1 0
87.36	1115	0.2	4 0 2
90.01	1.074	90.0	3 3 2
91.27	1.077	6.4	2 1 3
91.52	1.075	3.4	3 3 2
95.69	1.039	5.5	4 4 0
98.35	1.018	0.4	5 2 1
99.24	1.011	0.1	4 4 0
103.48	0.981	0.2	3 0 3
107.80	0.953	0.1	6 0 0

Table B.25 (cont'd) XRD Data of Molybdenum Nickel

2θ (°)	d spacing (Å)	Intensity (%)	h k l
108.46	0.949	0.3	5 1 2
115.81	0.909	0.3	6 1 1
116.79	0.904	1.8	2 6 0
117.22	0.902	1.2	1 4 3
138.38	0.824	6.0	5 0 3
149.03	0.799	3.0	1 3 4

C. Calculation of Crystallite Size of Metal

The crystallite sizes of the metals were calculated according to the XRD data using Scherrer equation given in Equation C.1.

$$t_{crystallite\ size} = \frac{C\ x\ \lambda}{B\ x\ cos(\frac{2\theta}{2})} \qquad C.1$$

where,

C: crystal shape factor (0.89)

λ: X-Ray Wavelength (0.154 nm for copper)

B: Full width at half max.

2θ: Peak angle

B (Full width at half max.) value was calculated by using Equation C.2.

$$B\ (radians) = FWHM_{Ni}\ x\ \frac{3.14}{180} \qquad C.2$$

D. EDX Analysis of 10Ni/SA & 10Ni/SA-wet Catalysts

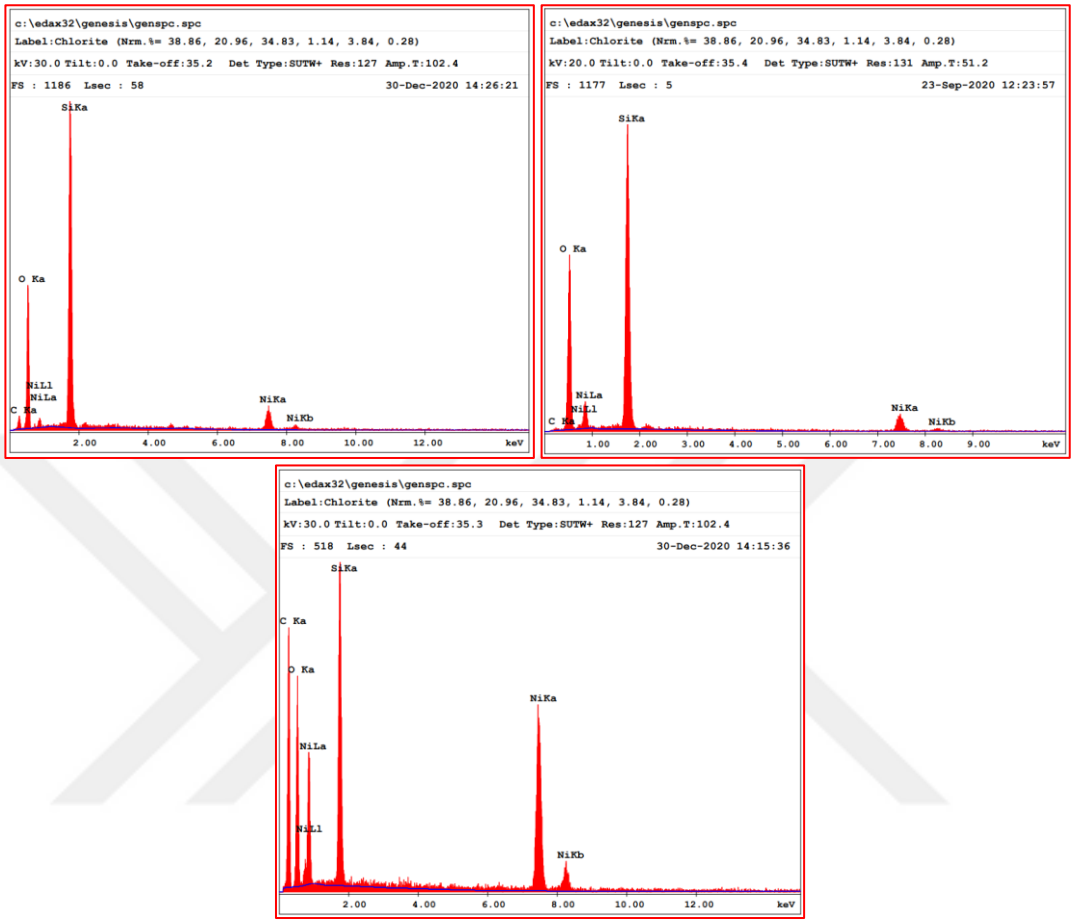

Figure D.1 EDX Analysis of 10Ni/SA of Different Regions

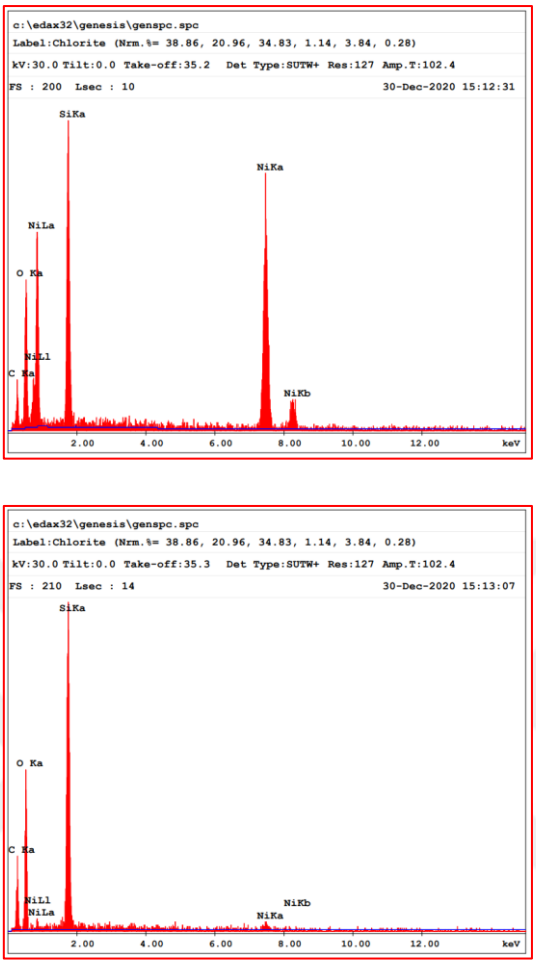

Figure D.2 EDX Analysis of 10Ni/SA-wet of Different Regions

E. Gas and Liquid Calibration Factor Calculations

Gas calibration factor was calculated to determine the retention time and calibration (β) factors of gases in the standard gas mixture containing 1 v % H_2, 1 v % CO_2, 1 v % CO, 1 v % CH_4, 1 v % C_2H_4, and 95 v % Ar.

The calibration factor of each gas compound was calculated using Equation. E.1. by feeding the standard gas mixture online to the GC.

$$\frac{N_i}{N_{CO_2}} = \frac{A_i \beta_i}{A_{CO_2} \beta_{CO_2}} \qquad E.1$$

where,

β_{CO_2} = 1

N_i = number of moles of species i

A_i = mean peak area of species i

The mole fraction of each compound with their retention time, mean peak area and calculated beta factor values in the standard gas mixture were tabulated in Table E.1.

Table E.1 Calibration Factor Values of Gas Compounds

Compound	***Mole Fraction***	***Retention Time (min.)***	***Mean Peak Area***	***β Factor***
H_2	0.0092	2.35	2536128	0.0096
CO	0.0097	5.72	172722	0.1484
CH_4	0.0099	10.41	97069	0.2694
CO_2	0.0100	13.78	26418	1.0000
C_2H_4	0.0084	17.98	52317	0.4242

Liquid calibration factor was calculated by following the similar route with gas calibration factor calculations. The glycerol water liquid mixture was prepared by using the water-glycerol mixture with the molar ratio of 20. The prepared liquid mixture was manually injected into the GC until the mean peak area consistency was achieved, the moles of glycerol and water were calculated using Equation E.2.

$$N_i = \frac{V_i \rho_i}{MW_i} \qquad E.2$$

where,

N_i = number of moles of species i

V_i = volume of species i

ρ_{H_2O}= 1 g/cm^3

$\rho_{C_3H_8O_3}$= 1.26 g/cm^3

MW_{H_2O} = 18.02 g/mole

$MW_{C_3H_8O_3}$= 92.09 g/mole

Then, calibration (β) factor of water was calculated using Equation E.3.

$$\frac{N_{H_2O}}{N_{C_3H_8O_3}} = \frac{A_{H_2O}\beta_{H_2O}}{A_{C_3H_8O_3}\beta_{C_3H_8O_3}} \qquad E.3$$

where,

$\beta_{C_3H_8O_3}$ = 1

The mole fraction of each compound with their retention time, mean peak area and calculated beta factor values in the liquid mixture were tabulated in Table E.2.

Table E.2 Calibration Factor Values of Liquid Compounds

Compound	*Mole Fraction*	*Retention Time (min.)*	*Mean Peak Area*	*β Factor*
H_2O	0.9881	7.88	4126045	1.0952
$C_3H_8O_3$	0.0119	20.88	54536	1.0000

F. Calculation of the Product Mole Fractions, Hydrogen Yield and Glycerol Conversion

Product Mole Fraction Calculation

The areas of each gas compound were obtained from GC and multiplied by the calibration factors. The product mole fractions, glycerol conversion and hydrogen yield were then calculated.

The moles of each species in the gas mixture and total moles of gas were calculated using Equations F.1 and F.2, respectively.

$$N_i = Area_i x\, \beta_i \qquad F.1$$

$$N_{Total} = N_{H_2} + N_{CO} + N_{CH_4} + N_{CO_2} \qquad F.2$$

The mole fractions of each compound in gas stream were then calculated using Equation F.3.

$$y_i(\%) = \frac{N_i}{N_{Total}} x\, 100 \qquad F.3$$

Glycerol Conversion and Hydrogen Yield Calculations

The volumetric flow rate of the product gas stream was measured with the aid of a soap bubble flow meter. The average volumetric product flow rate was determined from measurements including a constant argon flow rate of 30 ml/min throughout the experiments.

The total flow rate of the gaseous products was calculated from Equation F.4.

$$Q_{Gas\ Products} = Q_{Total} - Q_{Argon} \qquad F.4$$

The volumetric flow rate was then calculated for each gas species using Equation F.5.

$$Q_i = Q_{Gas\ Products}\ x\ y_i \qquad F.5$$

Density values for each compound were calculated using Equation F.6.

$$\rho_i = \frac{P\ x\ MW_i}{R\ x\ T_{room}} \qquad F.6$$

where,

$P = 1\ atm$

$T_{room} = 293\ K$

$R = 82.05\ \frac{ml.atm}{mole.K}$

$MW_{H_2} = 2\ g/mole$

$MW_{CO} = 28\ g/mole$

$MW_{CO_2} = 44\ g/mole$

$MW_{CH_4} = 16\ g/mole$

Molar flow rate of each compound was calculated using Equation F.7.

$$F_i = \frac{Q_i\ x\ \rho_i}{MW_i} \qquad F.7$$

Molar flow rate of unreacted glycerol was calculated using Equation F.8.

$$F_{C_3H_8O_3,liquid} = \frac{m_{liquid}\ *\ x_{C_3H_8O_3}}{MW_{C_3H_8O_3}\ *\ x_{C_3H_8O_3} + MW_{H_2O}\ *\ x_{H_2O}} \qquad F.8$$

where,

m_{liquid}: total mass flow rate of collected liquid products from the condenser, g/min

$x_{C_3H_8O_3}$: mole fraction of glycerol in collected liquid products from the condenser

x_{H_2O}: mole fraction of water in collected liquid products from the condenser

$MW_{C_3H_8O_3}$: 92 g/mole

MW_{H_2O}: 18 g/mole

The molar flow rate of the fed glycerol was calculated from the carbon balance using Equation F.9.

$$F^o_{C_3H_8O_3} = \frac{F_{CO}}{3} + \frac{F_{CH_4}}{3} + \frac{F_{CO_2}}{3} + F_{C_3H_8O_3,liquid} \qquad F.9$$

Glycerol conversion and hydrogen yield were then calculated using the Equation F.10 and F.11, respectively.

$$X_{C_3H_8O_3} = \frac{F^o_{C_3H_8O_3} - F_{C_3H_8O_3,liquid}}{F^o_{C_3H_8O_3}} \qquad F.10$$

$$Y_{H_2} = \frac{F_{H_2}}{F^o_{C_3H_8O_3}} \qquad F.11$$

The percentage of hydrogen yield was calculated using Equation F.12.

$$Y_{H_2}(\%) = \frac{Y_{H_2}}{7} x\ 100 \qquad F.12$$

G. Experimental Results

In this chapter, experimental results performed at various reaction conditions in the presence of various catalysts were stated. According to experiments, gas compounds were produced steadily after 60 or 90 minutes with approximately complete glycerol conversion (99%). In each experiment, the product gas stream contains four compounds, H_2, CO_2, CO, & CH_4. The product distribution of the compounds ranged from 4-66, 5-33, 1-77, and 0-4 mole %, respectively. The large variation between the values is attributed to the diverse reaction conditions and tested catalysts such as water-glycerol feed flow rate, reaction temperature, water-to-glycerol molar ratio, catalyst synthesis method, loaded metal amount, mono metal type and bi & trimetal type. Generally, in experiments performed in the presence of Ni loaded SA, the product distributions were quite close to each other regardless of the experimental conditions, and the H_2 yield obtained is high. The highest H_2 formation and hence the highest H_2 yield was achieved not only in the presence of monometallic Ni, but also in the bimetallic form of Ni with Ru. However, H_2 yield obtained in the presence of other bi or trimetallic forms of Ni or different monometallic catalysts are low.

The product distribution and H_2 yield of each experiment with respect to time were depicted in Figures G.1-G.64. In addition, average product composition of all experiments was given in Table G.1.

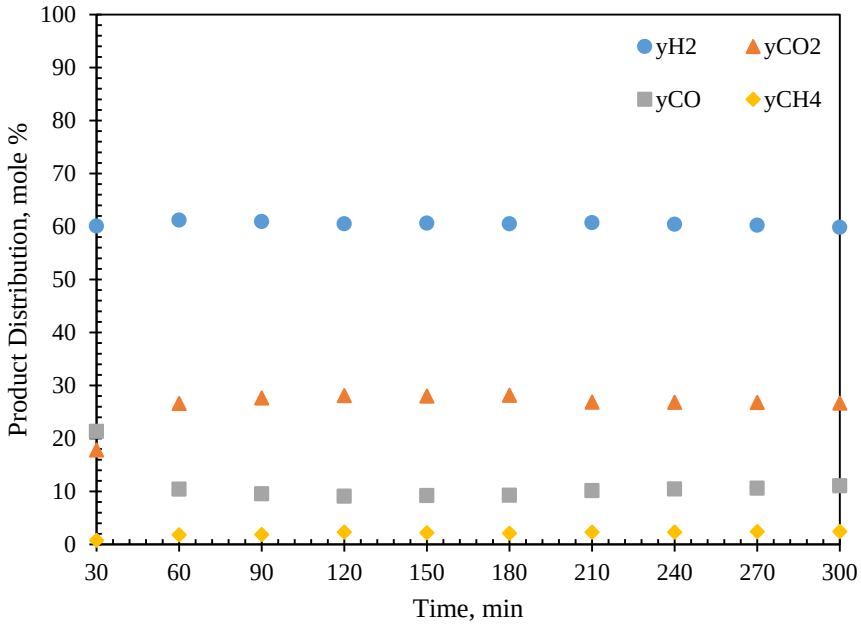

Figure G.1 Product Distribution of the GSR Reaction

(Catalyst:10Ni/SA(1035)(1035), T_{rxn}:965ºC, FFR:0.8ml/h, WGMR:3)

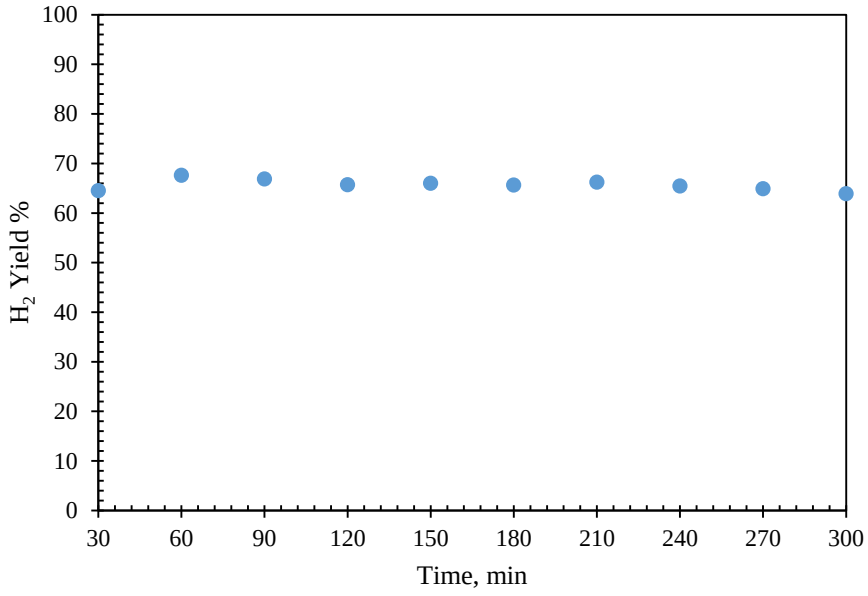

Figure G.2 H_2 Yield of the GSR Reaction

(Catalyst:10Ni/SA(1035)(1035), T_{rxn}:965ºC, FFR:0.8ml/h, WGMR:3)

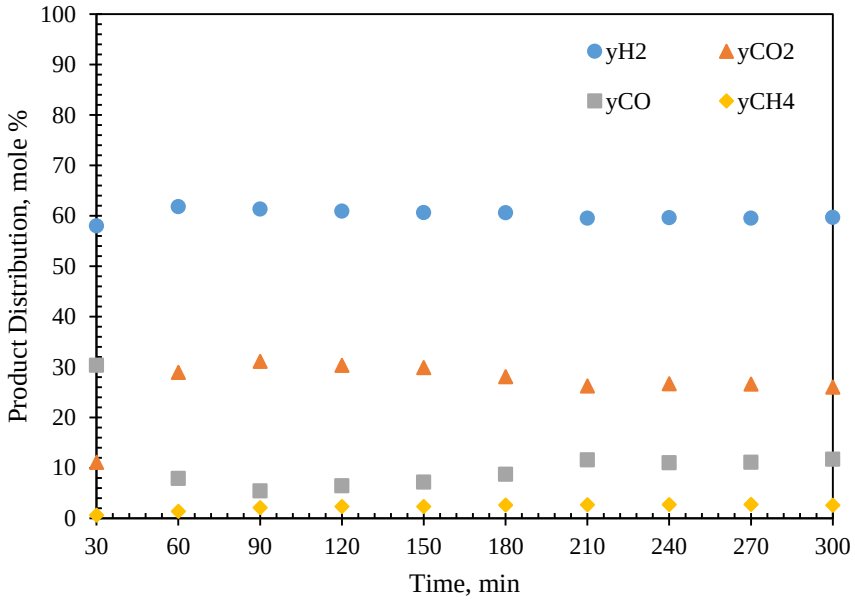

Figure G.3 Product Distribution of the GSR Reaction

(Catalyst:10Ni/SA(1035)(1035), T_{rxn}:965°C, FFR:1.0ml/h, WGMR:3)

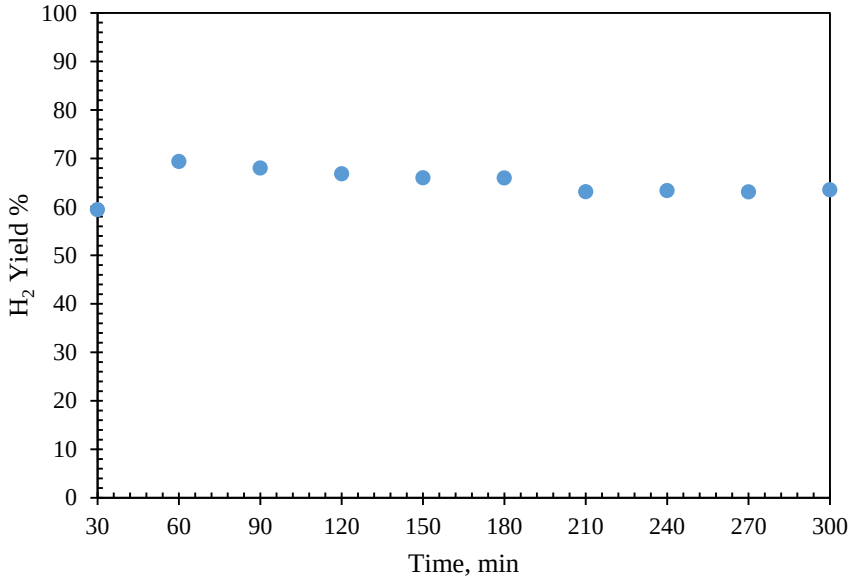

Figure G.4 H_2 Yield of the GSR Reaction

(Catalyst:10Ni/SA(1035)(1035), T_{rxn}:965°C, FFR:1.0ml/h, WGMR:3)

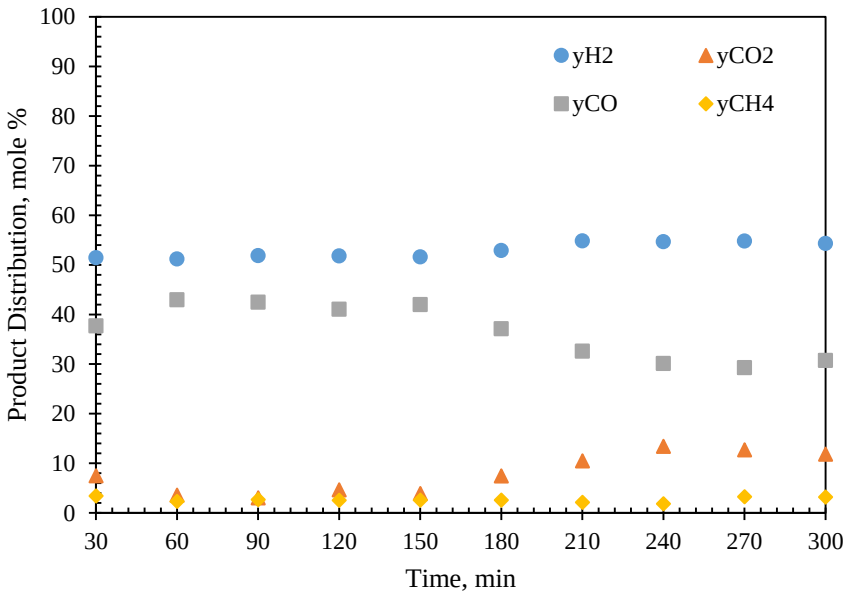

Figure G.5 Product Distribution of the GSR Reaction
(Catalyst:10Ni/SA(700)(1035), T_{rxn}:470°C, FFR:0.9ml/h, WGMR:3)

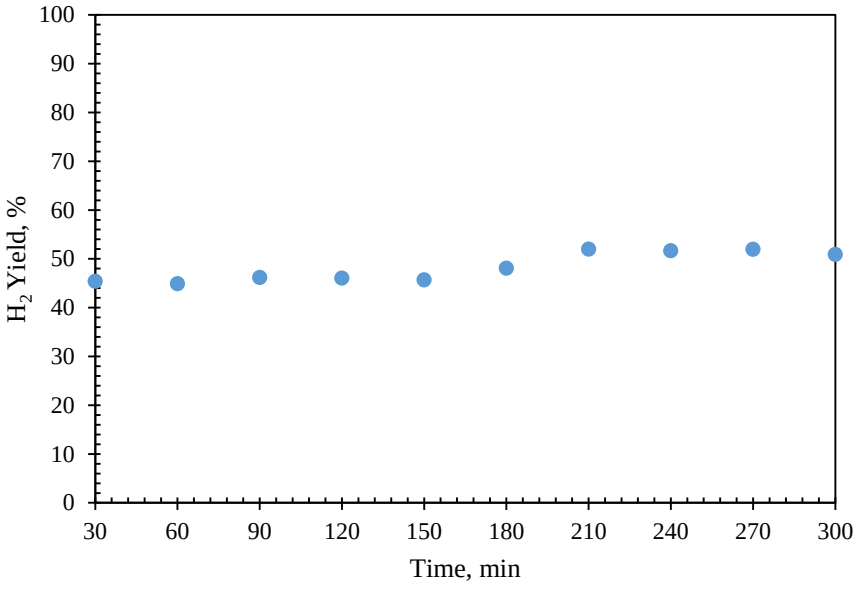

Figure G.6 H_2 Yield of the GSR Reaction
(Catalyst:10Ni/SA(700)(1035), T_{rxn}:470°C, FFR:0.9ml/h, WGMR:3)

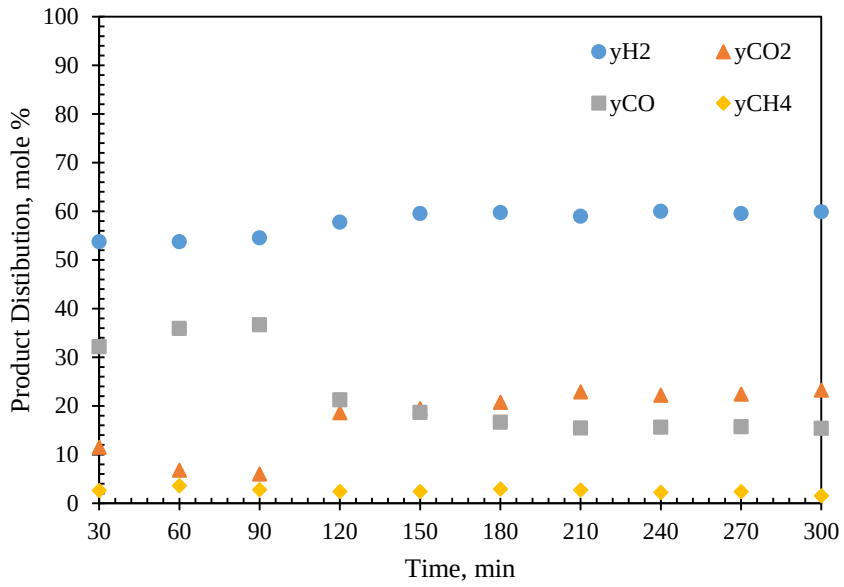

Figure G.7 Product Distribution of the GSR Reaction

(Catalyst:10Ni/SA(700)(1035), T_{rxn}:500°C, FFR:0.9ml/h, WGMR:3)

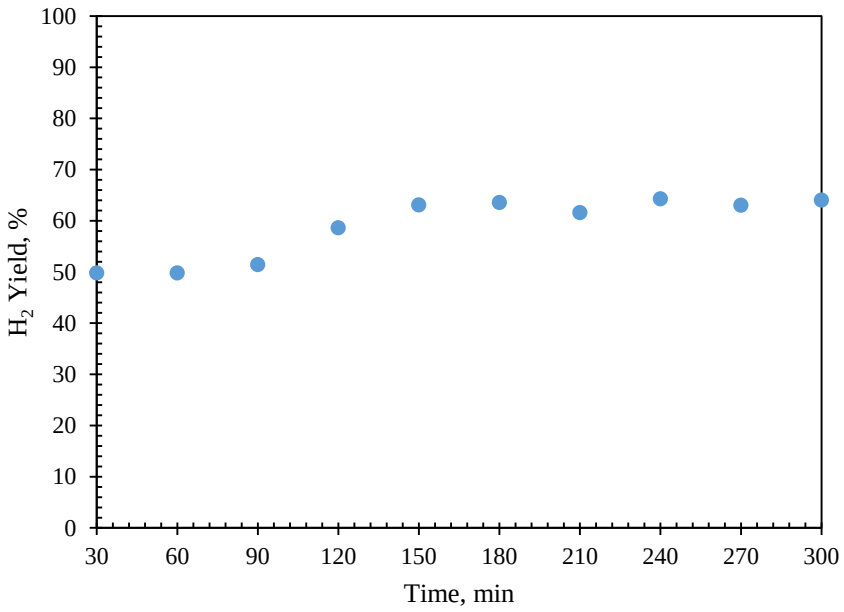

Figure G.8 H_2 Yield of the GSR Reaction

(Catalyst:10Ni/SA(700)(1035), T_{rxn}:500°C, FFR:0.9ml/h, WGMR:3)

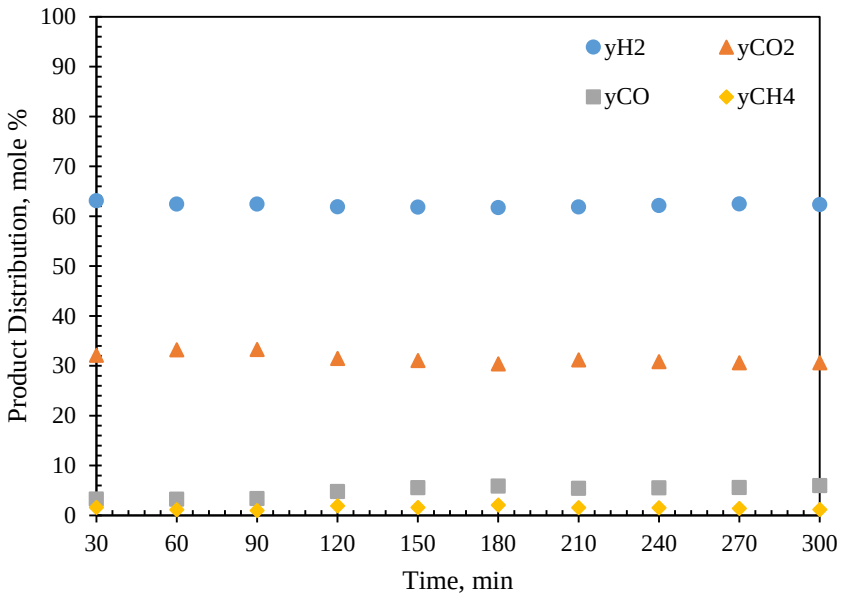

Figure G.9 Product Distribution of the GSR Reaction
(Catalyst:10Ni/SA(700)(1035), T_{rxn}:540°C, FFR:0.9ml/h, WGMR:3)

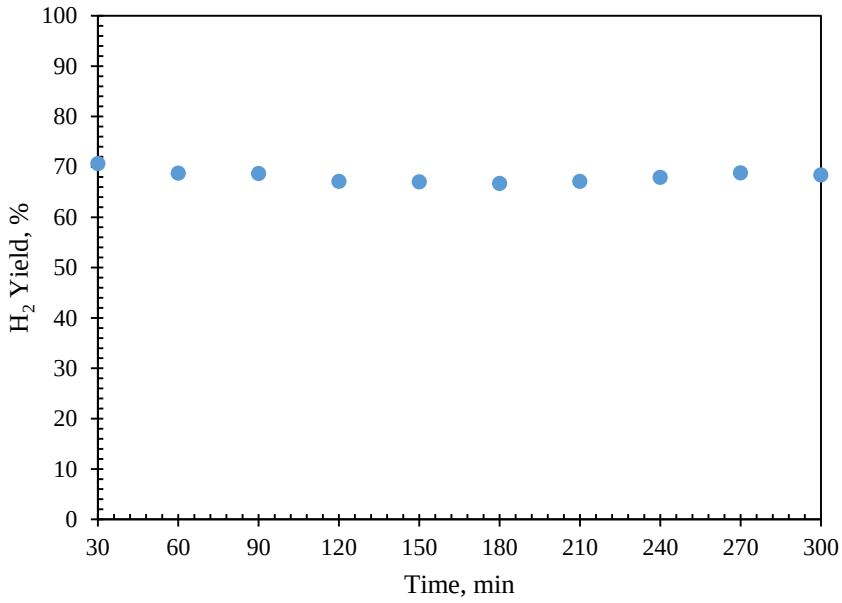

Figure G.10 H_2 Yield of the GSR Reaction
(Catalyst:10Ni/SA(700)(1035), T_{rxn}:540°C, FFR:0.9ml/h, WGMR:3)

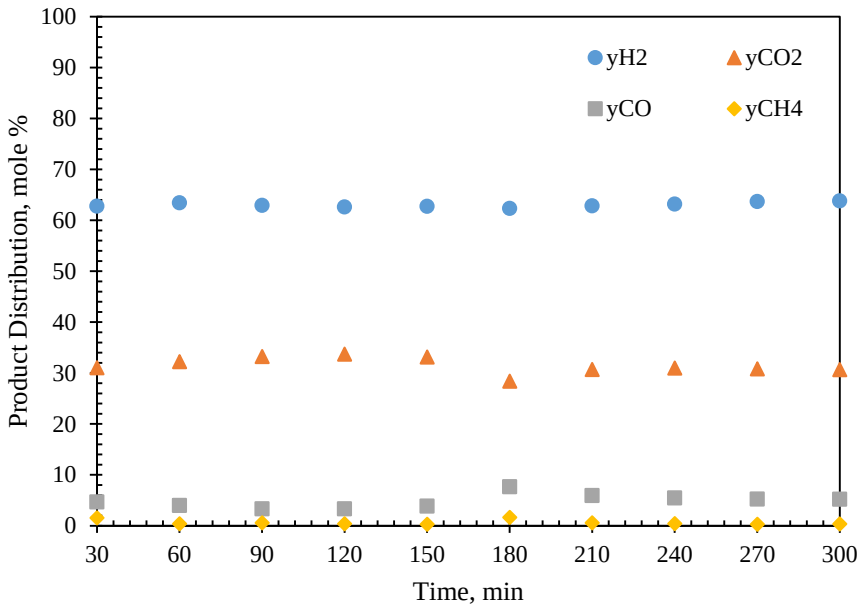

Figure G.11 Product Distribution of the GSR Reaction

(Catalyst:10Ni/SA(700)(1035), T_{rxn}:610°C, FFR:0.9ml/h, WGMR:3)

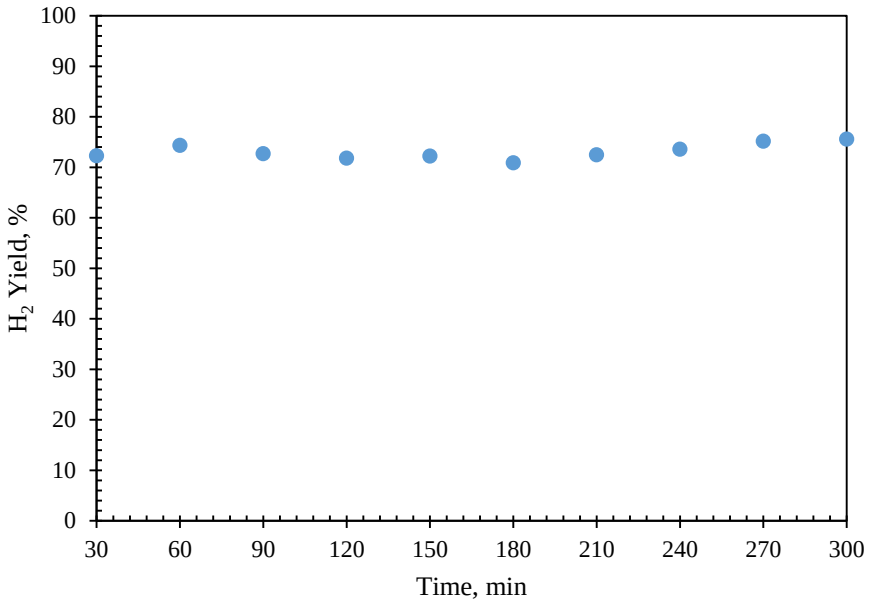

Figure G.12 H_2 Yield of the GSR Reaction

(Catalyst:10Ni/SA(700)(1035), T_{rxn}:610°C, FFR:0.9ml/h, WGMR:3)

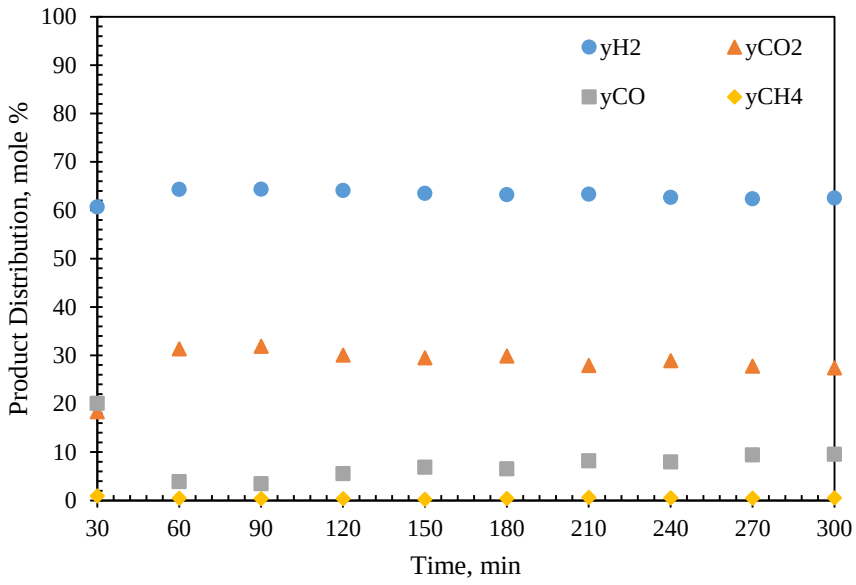

Figure G.13 Product Distribution of the GSR Reaction
(Catalyst:10Ni/SA(700)(1035), T_{rxn}:755°C, FFR:0.9ml/h, WGMR:3)

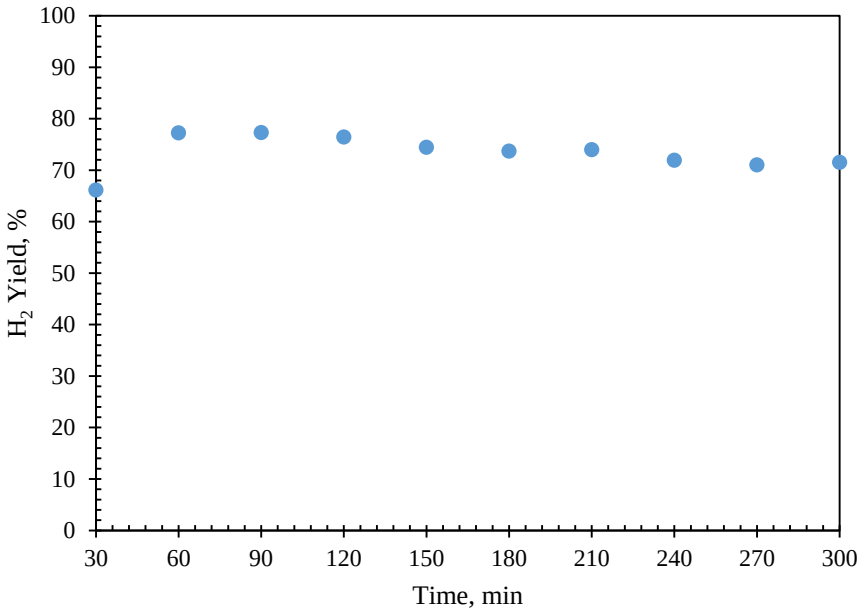

Figure G.14 H_2 Yield of the GSR Reaction
(Catalyst:10Ni/SA(700)(1035), T_{rxn}:755°C, FFR:0.9ml/h, WGMR:3)

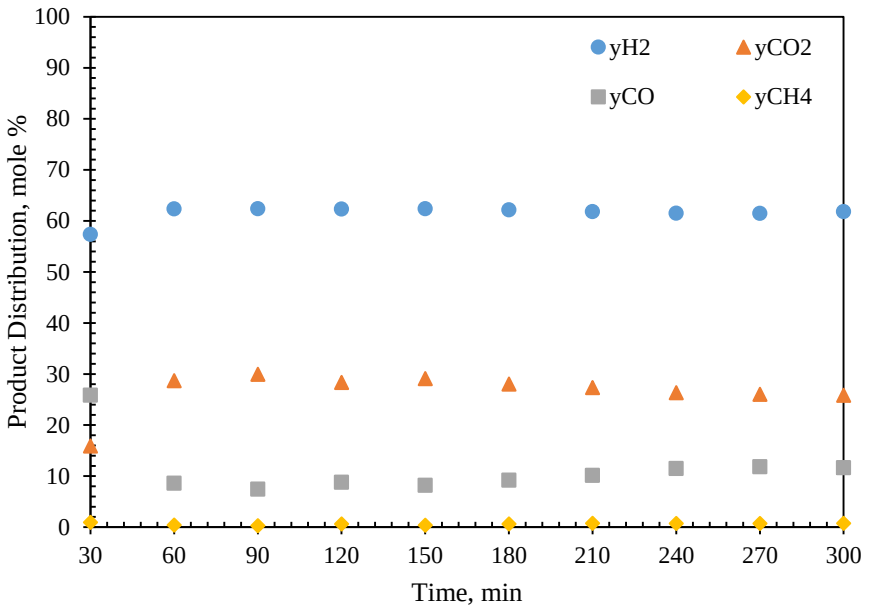

Figure G.15 Product Distribution of the GSR Reaction

(Catalyst:10Ni/SA(700)(1035), T_{rxn}:825°C, FFR:0.9ml/h, WGMR:3)

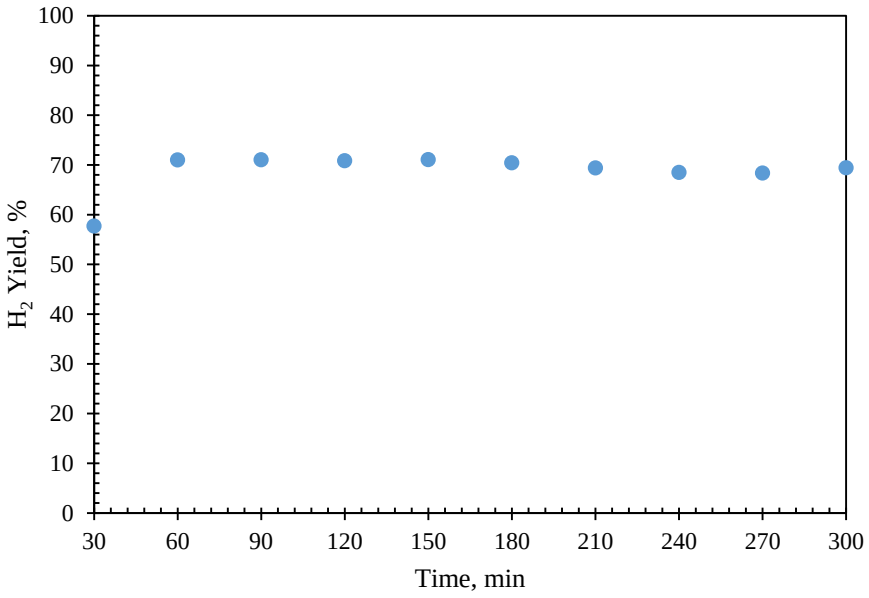

Figure G.16 H_2 Yield of the GSR Reaction

(Catalyst:10Ni/SA(700)(1035), T_{rxn}:825°C, FFR:0.9ml/h, WGMR:3)

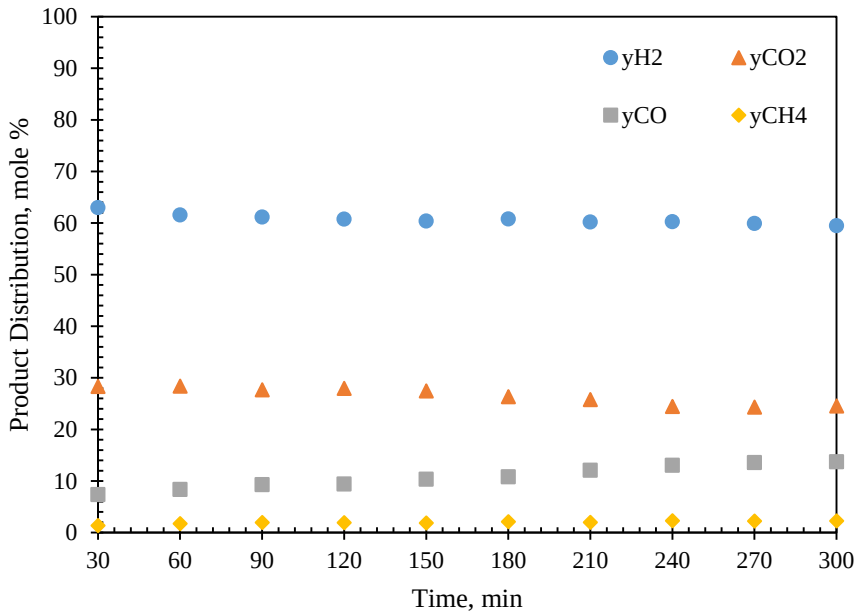

Figure G.17 Product Distribution of the GSR Reaction

(Catalyst:10Ni/SA(700)(1035), T_{rxn}:895°C, FFR:0.9ml/h, WGMR:3)

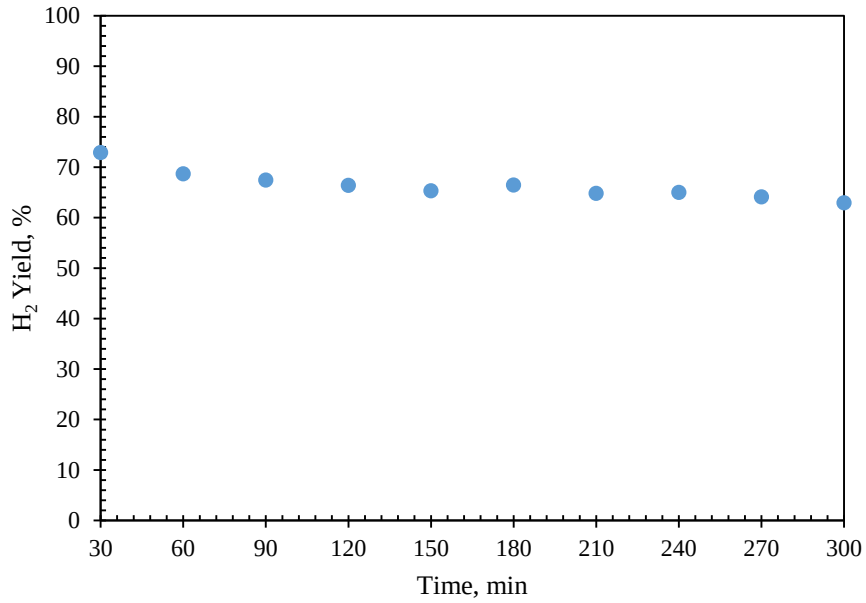

Figure G.18 H_2 Yield of the GSR Reaction

(Catalyst:10Ni/SA(700)(1035), T_{rxn}:895°C, FFR:0.9ml/h, WGMR:3)

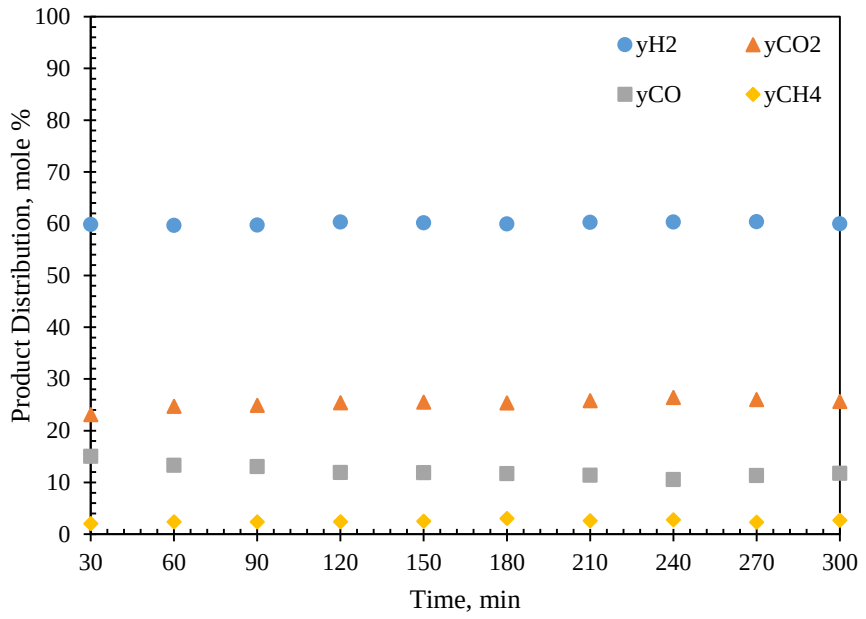

Figure G.19 Product Distribution of the GSR Reaction

(Catalyst:10Ni/SA(700)(1035), T_{rxn}:965°C, FFR:0.9ml/h, WGMR:3)

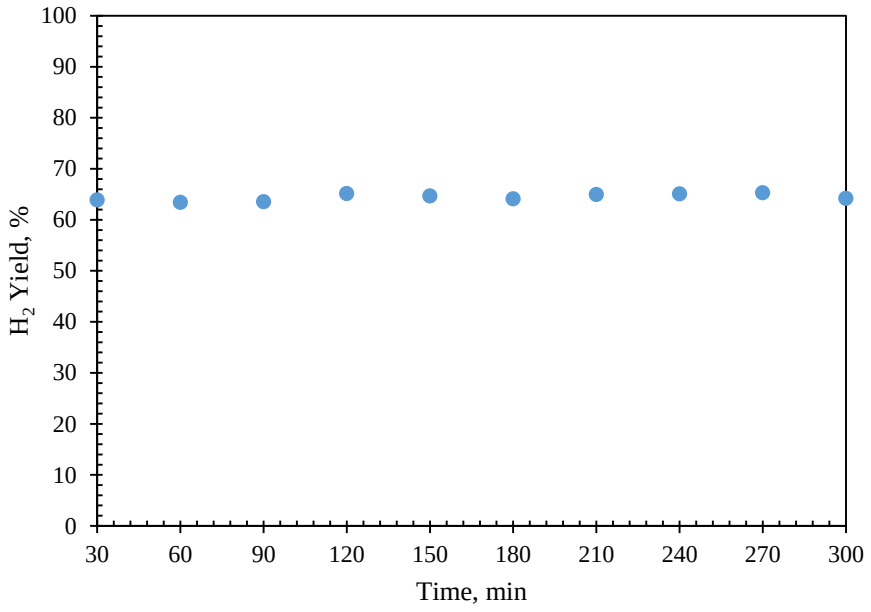

Figure G.20 H_2 Yield of the GSR Reaction

(Catalyst:10Ni/SA(700)(1035), T_{rxn}:965°C, FFR:0.9ml/h, WGMR:3)

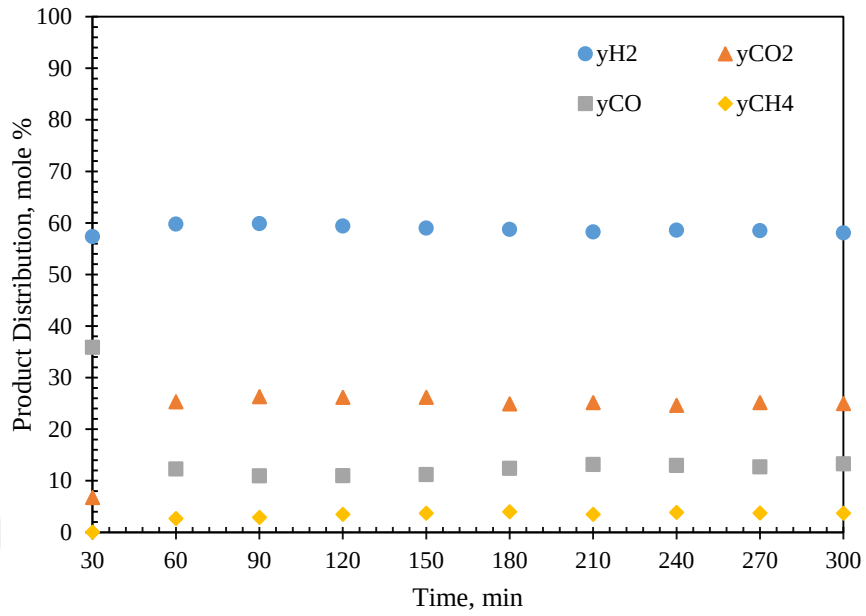

Figure G.21 Product Distribution of the GSR Reaction

(Catalyst:10Ni/SA(700)(1035), T_{rxn}:1035°C, FFR:0.9ml/h, WGMR:3)

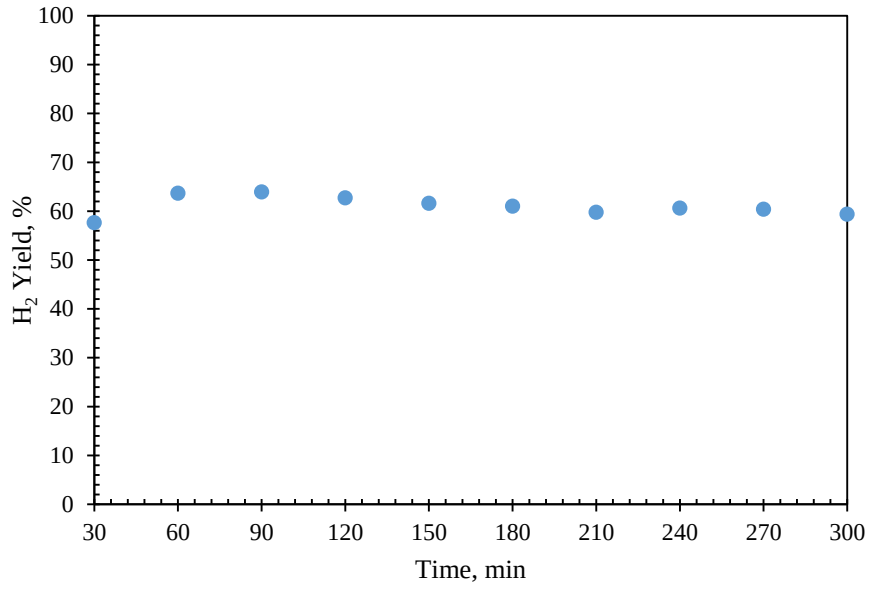

Figure G.22 H_2 Yield of the GSR Reaction

(Catalyst:10Ni/SA(700)(1035), T_{rxn}:1035°C, FFR:0.9ml/h, WGMR:3)

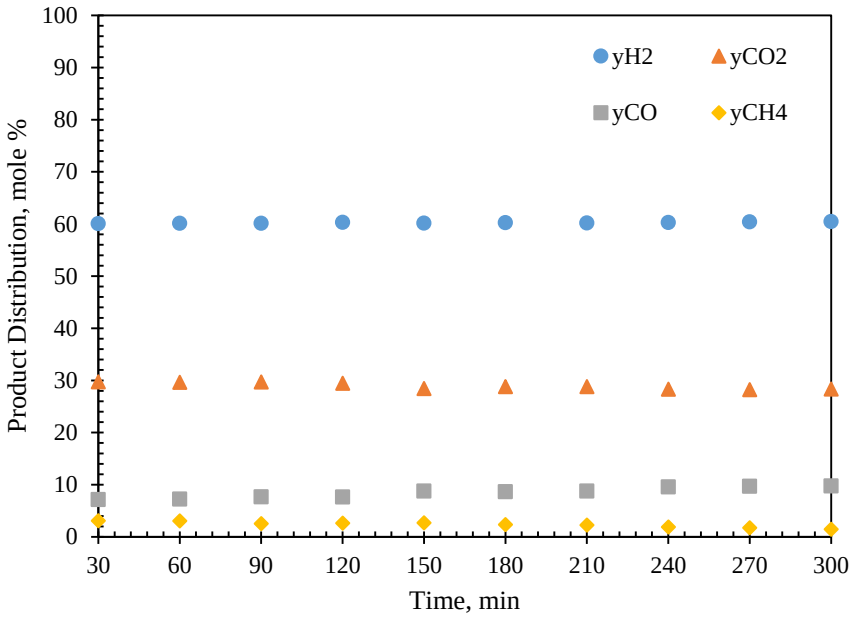

Figure G.23 Product Distribution of the GSR Reaction

(Catalyst:10Ni/SA(700)(1035), T_{rxn}:680°C, FFR:0.9ml/h, WGMR:1)

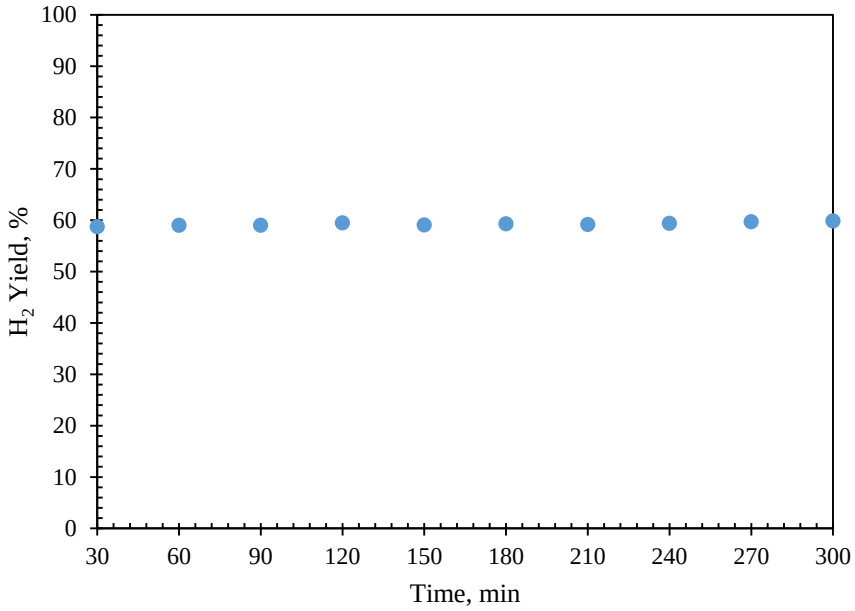

Figure G.24 H_2 Yield of the GSR Reaction

(Catalyst:10Ni/SA(700)(1035), T_{rxn}:680°C, FFR:0.9ml/h, WGMR:1)

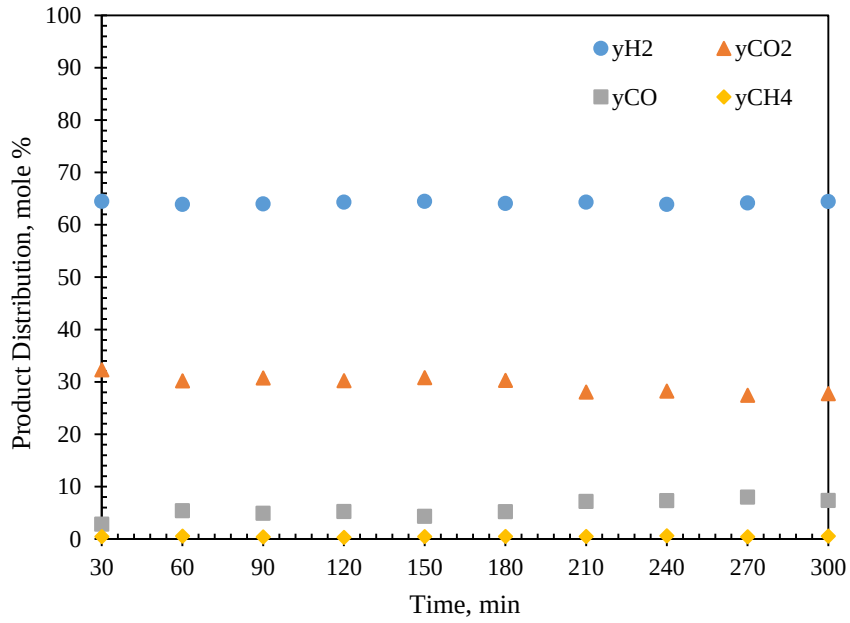

Figure G.25 Product Distribution of the GSR Reaction

(Catalyst:10Ni/SA(700)(1035), T_{rxn}:680°C, FFR:0.9ml/h, WGMR:6)

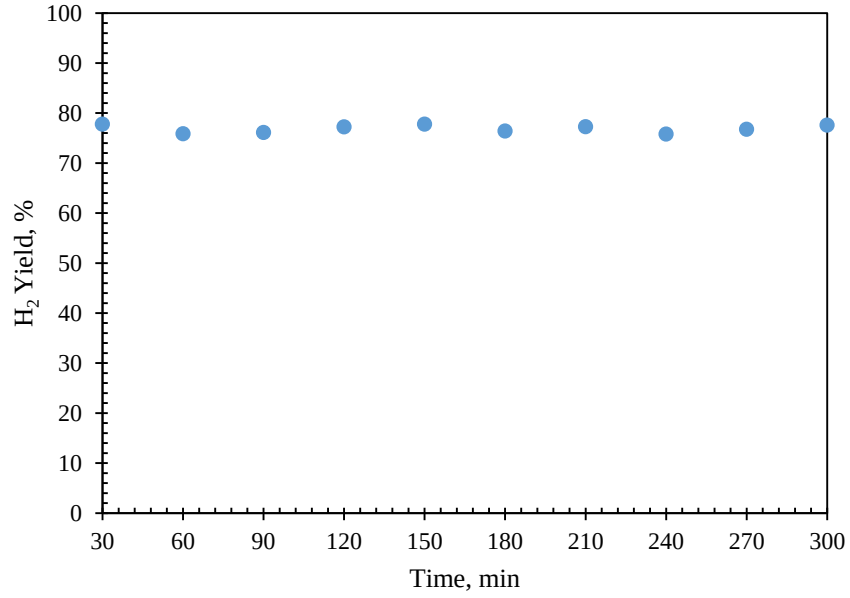

Figure G.26 H_2 Yield of the GSR Reaction

(Catalyst:10Ni/SA(700)(1035), T_{rxn}:680°C, FFR:0.9ml/h, WGMR:6)

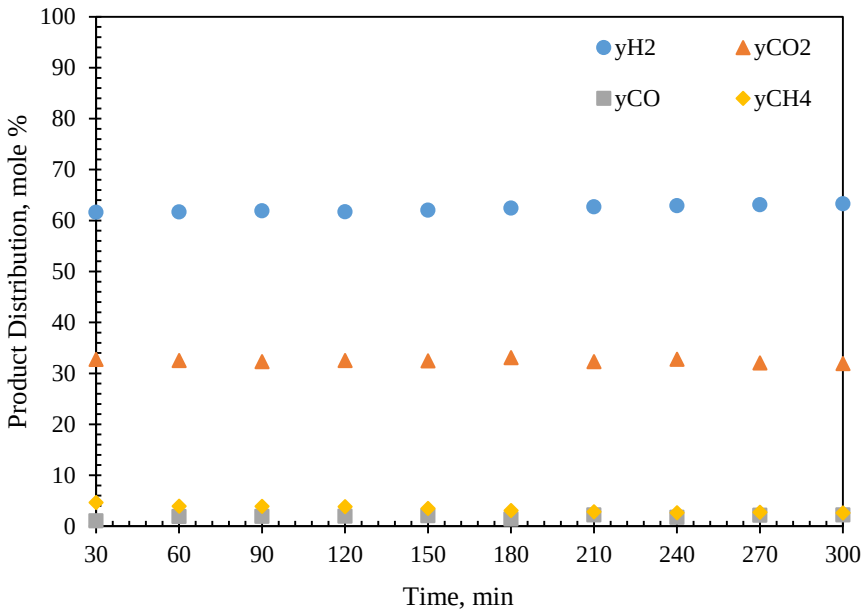

Figure G.27 Product Distribution of the GSR Reaction

(Catalyst:10Ni/SA(700)(1035), T_{rxn}:470°C, FFR:0.9ml/h, WGMR:9)

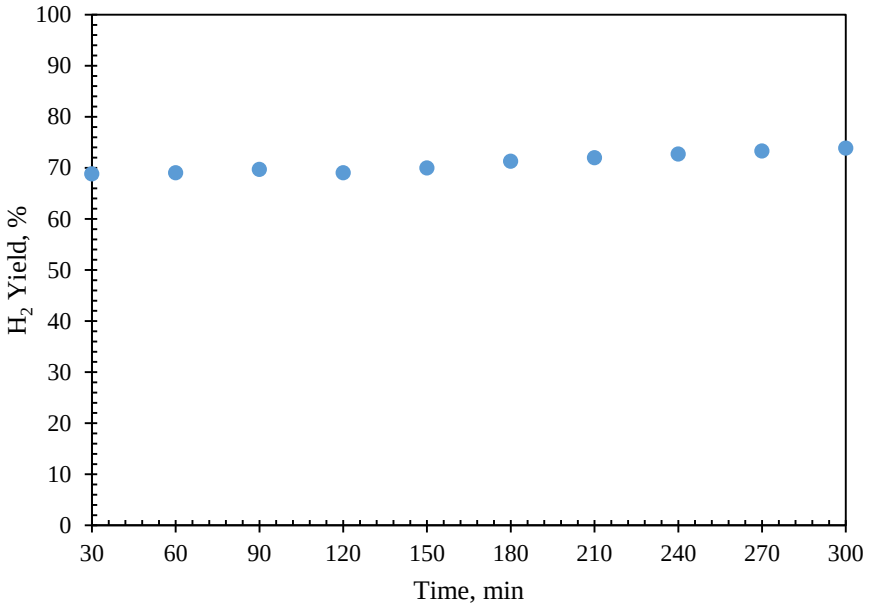

Figure G.28 H_2 Yield of the GSR Reaction

(Catalyst:10Ni/SA(700)(1035), T_{rxn}:470°C, FFR:0.9ml/h, WGMR:9)

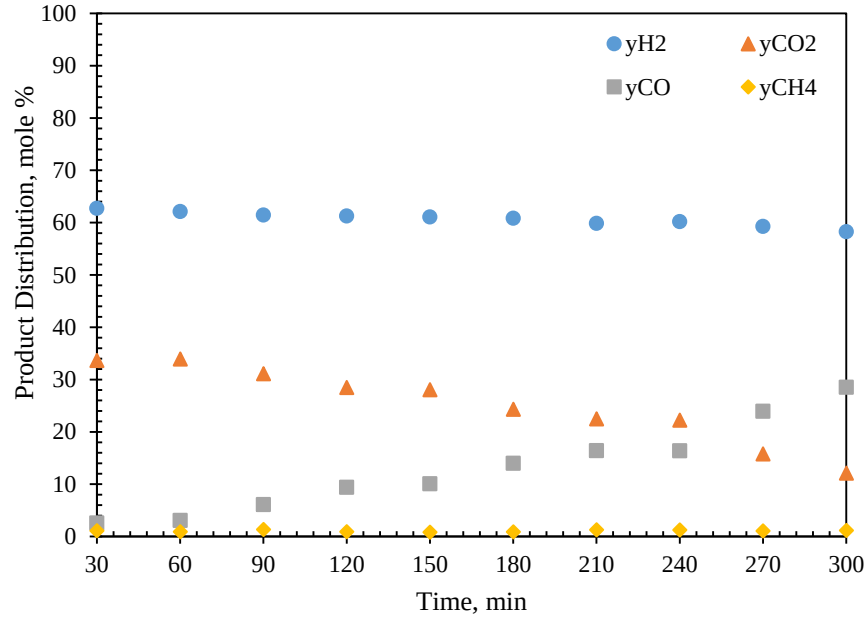

Figure G.29 Product Distribution of the GSR Reaction

(Catalyst:10Ni/SA(700)(1035)-wet, T_{rxn}:470°C, FFR:0.9ml/h, WGMR:9)

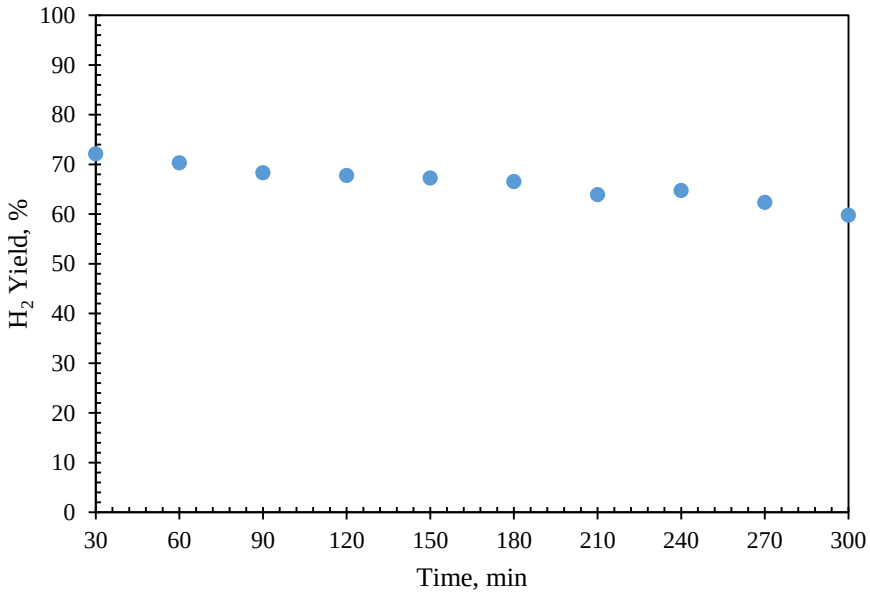

Figure G.30 H_2 Yield of the GSR Reaction

(Catalyst:10Ni/SA(700)(1035)-wet, T_{rxn}:470°C, FFR:0.9ml/h, WGMR:9)

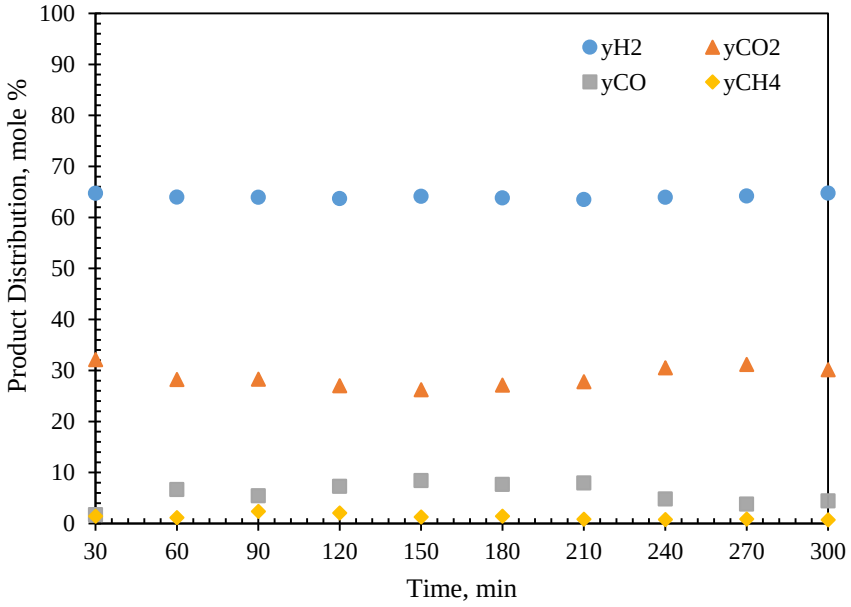

Figure G.31 Product Distribution of the GSR Reaction
(Catalyst:10Ni/SA(700)(1035)-wet, T_{rxn}:550°C, FFR:0.9ml/h, WGMR:9)

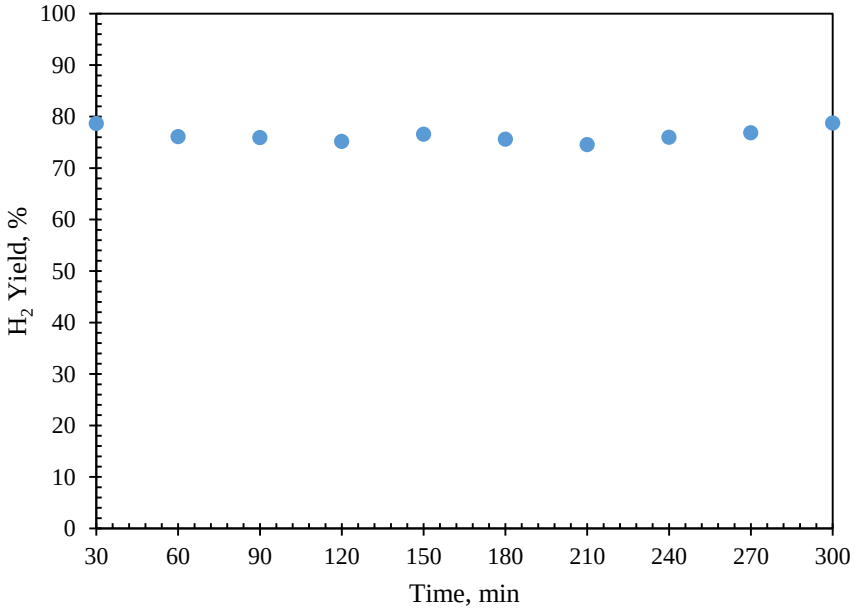

Figure G.32 H_2 Yield of the GSR Reaction
(Catalyst:10Ni/SA(700)(1035)-wet, T_{rxn}:550°C, FFR:0.9ml/h, WGMR:9)

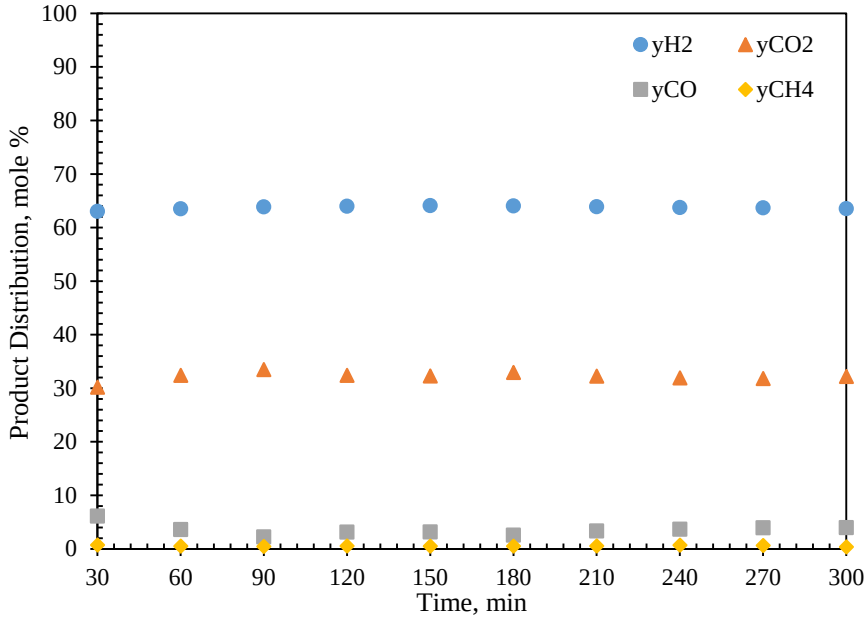

Figure G.33 Product Distribution of the GSR Reaction

(Catalyst:10Ni/SA(700)(1035)-wet, T_{rxn}:680°C, FFR:0.9ml/h, WGMR:9)

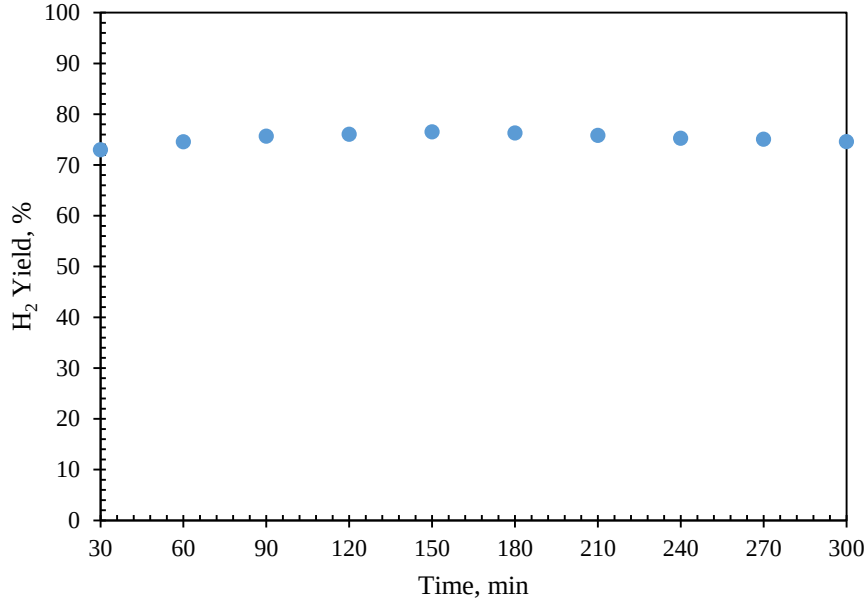

Figure G.34 H_2 Yield of the GSR Reaction

(Catalyst:10Ni/SA(700)(1035)-wet, T_{rxn}:680°C, FFR:0.9ml/h, WGMR:9)

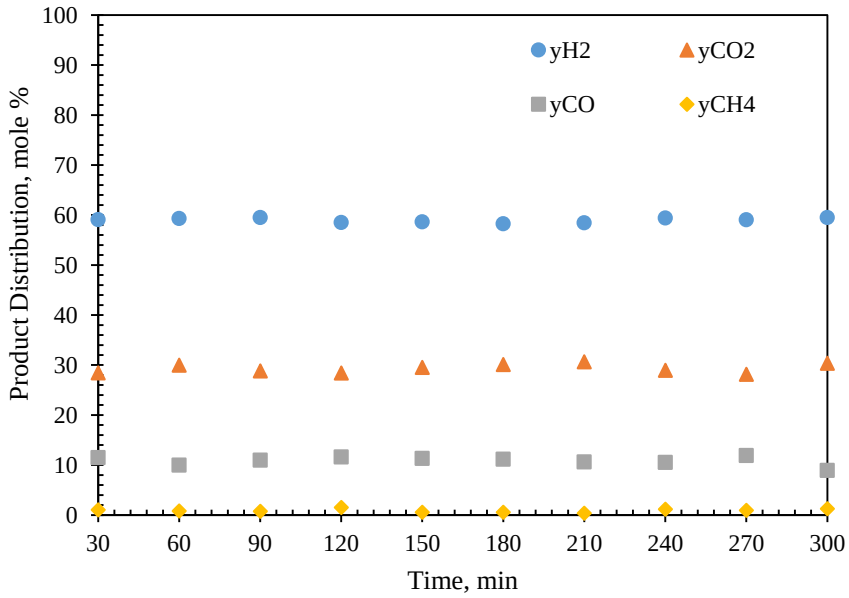

Figure G.35 Product Distribution of the GSR Reaction

(Catalyst:2.5Ni/SA(700)(1035), T_{rxn}:550°C, FFR:0.9ml/h, WGMR:9)

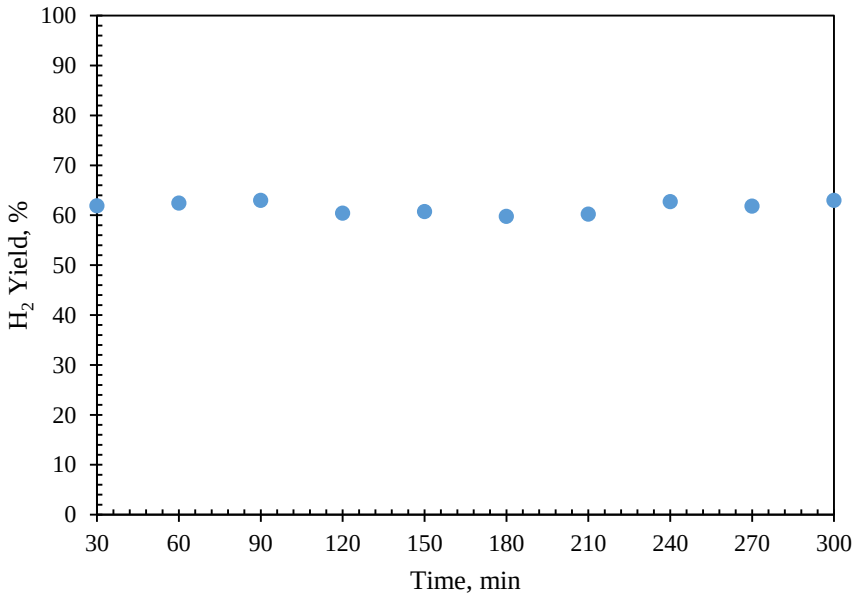

Figure G.36 H_2 Yield of the GSR Reaction

(Catalyst:2.5Ni/SA(700)(1035), T_{rxn}:550°C, FFR:0.9ml/h, WGMR:9)

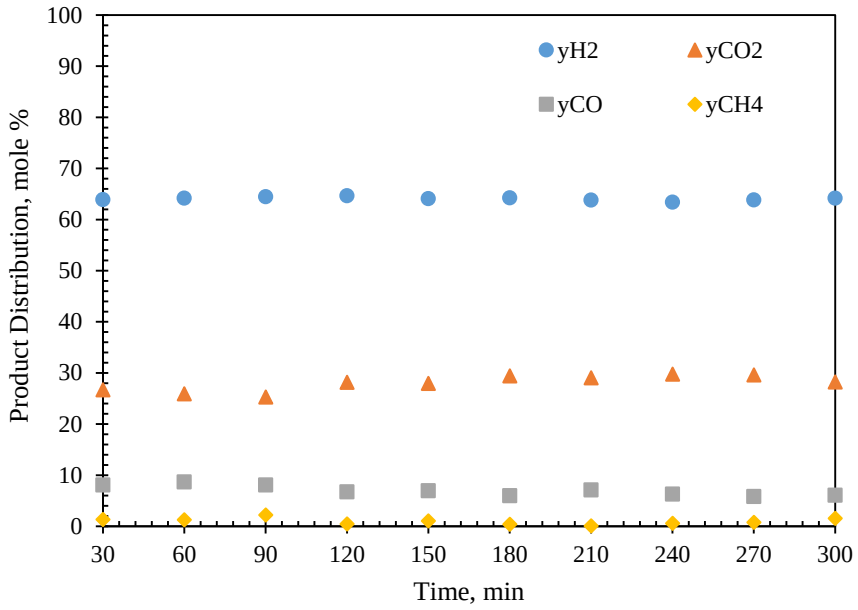

Figure G.37 Product Distribution of the GSR Reaction
(Catalyst:5Ni/SA(700)(1035), T_{rxn}:550°C, FFR:0.9ml/h, WGMR:9)

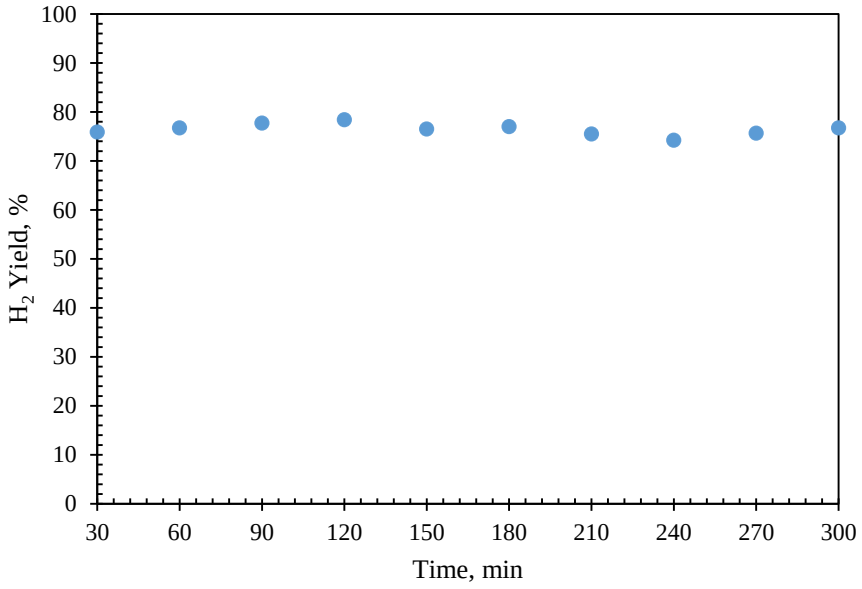

Figure G.38 H_2 Yield of the GSR Reaction
(Catalyst:5Ni/SA(700)(1035), T_{rxn}:550°C, FFR:0.9ml/h, WGMR:9)

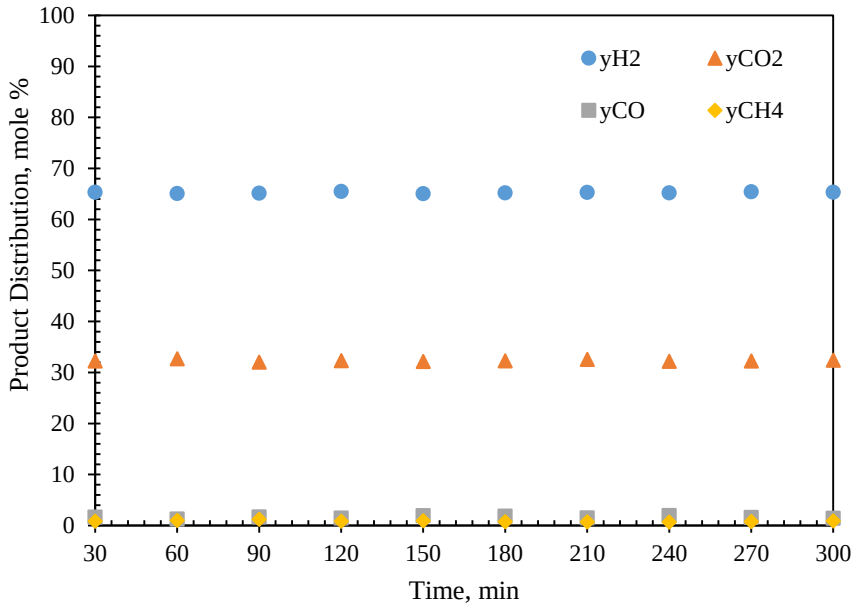

Figure G.39 Product Distribution of the GSR Reaction

(Catalyst:8Ni/SA(700)(1035), T_{rxn}:550°C, FFR:0.9ml/h, WGMR:9)

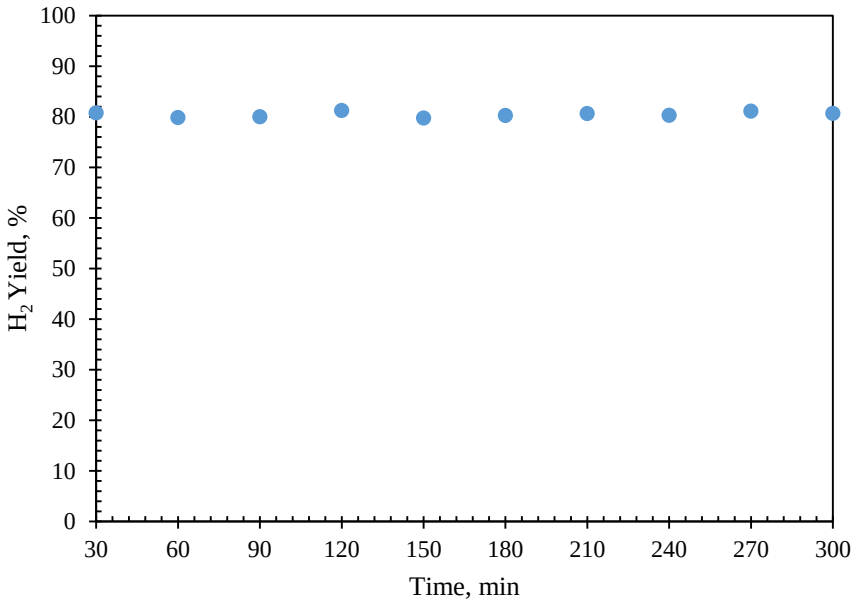

Figure G.40 H_2 Yield of the GSR Reaction

(Catalyst:8Ni/SA(700)(1035), T_{rxn}:550°C, FFR:0.9ml/h, WGMR:9)

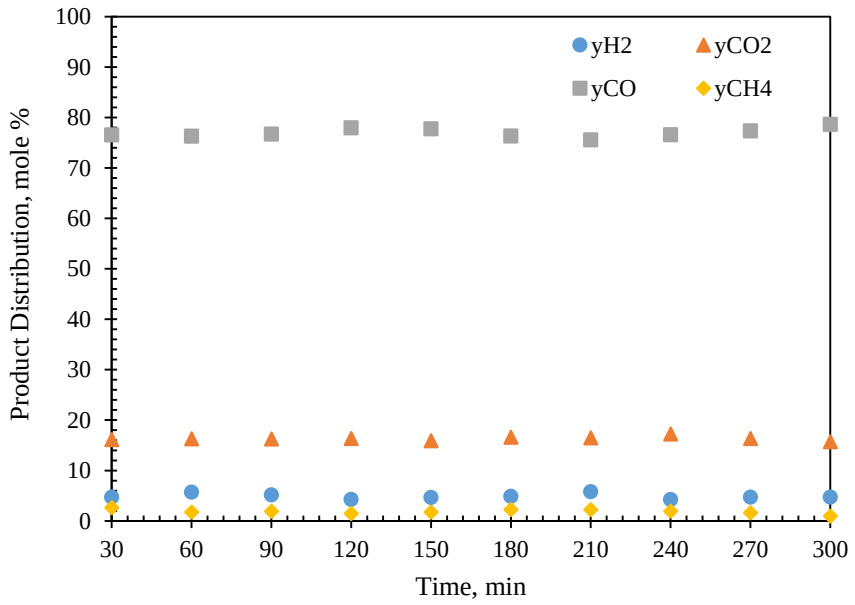

Figure G.41 Product Distribution of the GSR Reaction
(Catalyst:10Zr/SA(700)(1035), T_{rxn}:550°C, FFR:0.9ml/h, WGMR:9)

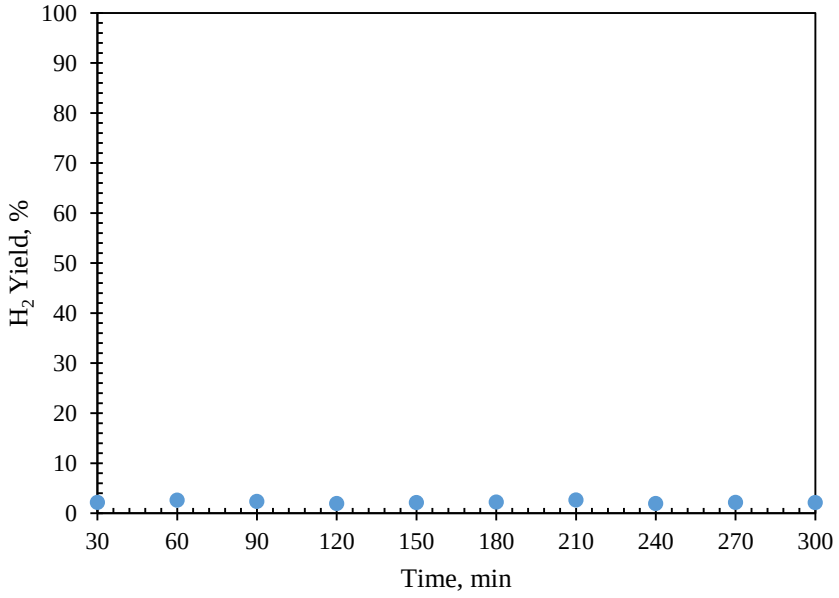

Figure G.42 H_2 Yield of the GSR Reaction
(Catalyst:10Zr/SA(700)(1035), T_{rxn}:550°C, FFR:0.9ml/h, WGMR:9

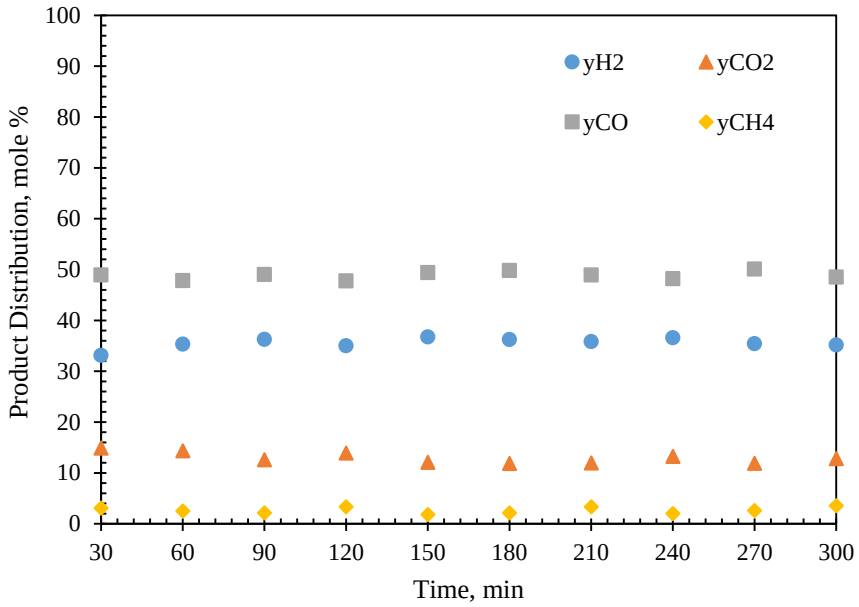

Figure G.43 Product Distribution of the GSR Reaction

(Catalyst:10Co/SA(700)(1035), T_{rxn}:550°C, FFR:0.9ml/h, WGMR:9)

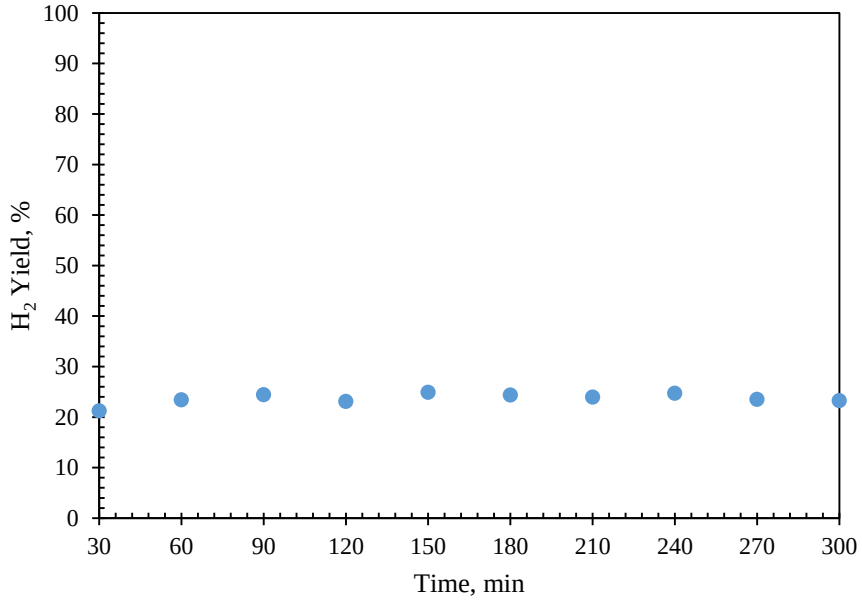

Figure G.44 H_2 Yield of the GSR Reaction

(Catalyst:10Co/SA(700)(1035), T_{rxn}:550°C, FFR:0.9ml/h, WGMR:9

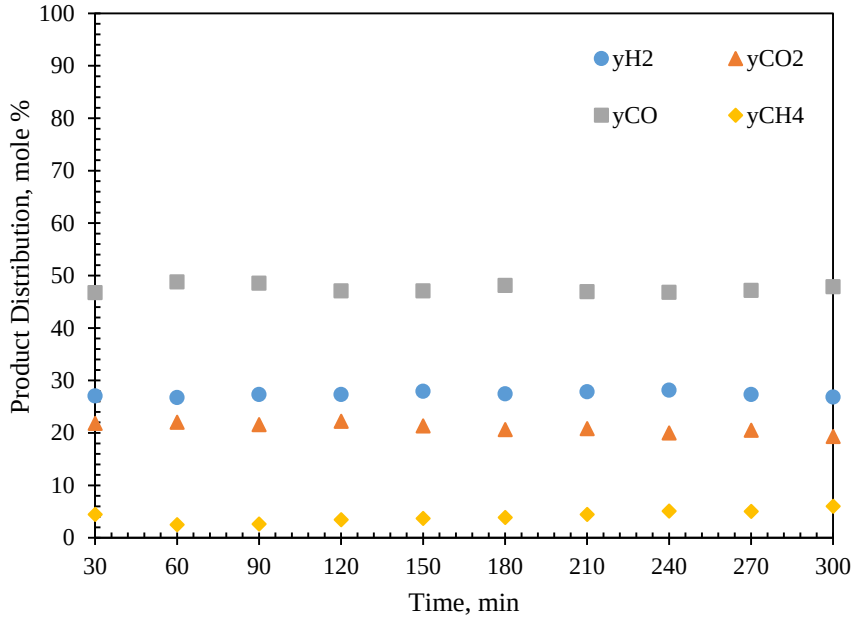

Figure G.45 Product Distribution of the GSR Reaction

(Catalyst:10Cr/SA(700)(1035), T_{rxn}:550°C, FFR:0.9ml/h, WGMR:9)

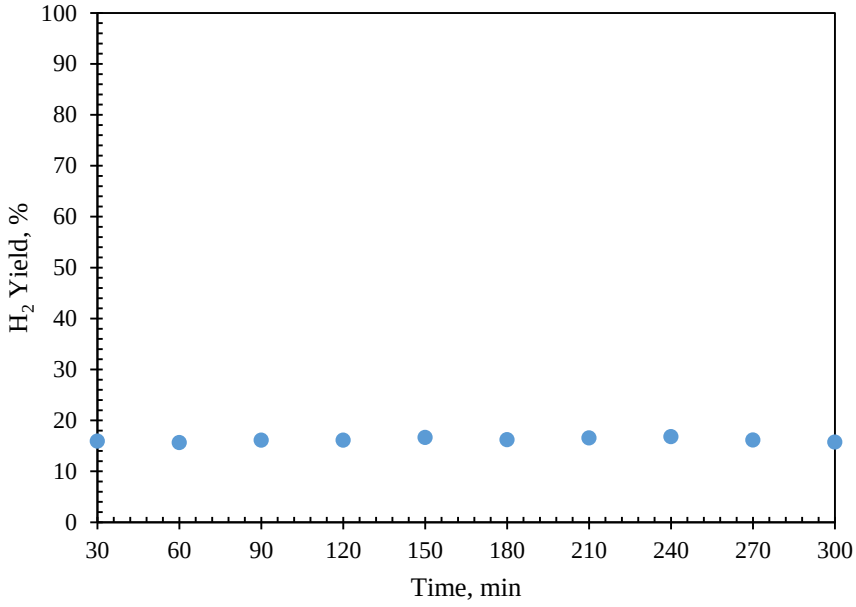

Figure G.46 H_2 Yield of the GSR Reaction

(Catalyst:10Cr/SA(700)(1035), T_{rxn}:550°C, FFR:0.9ml/h, WGMR:9

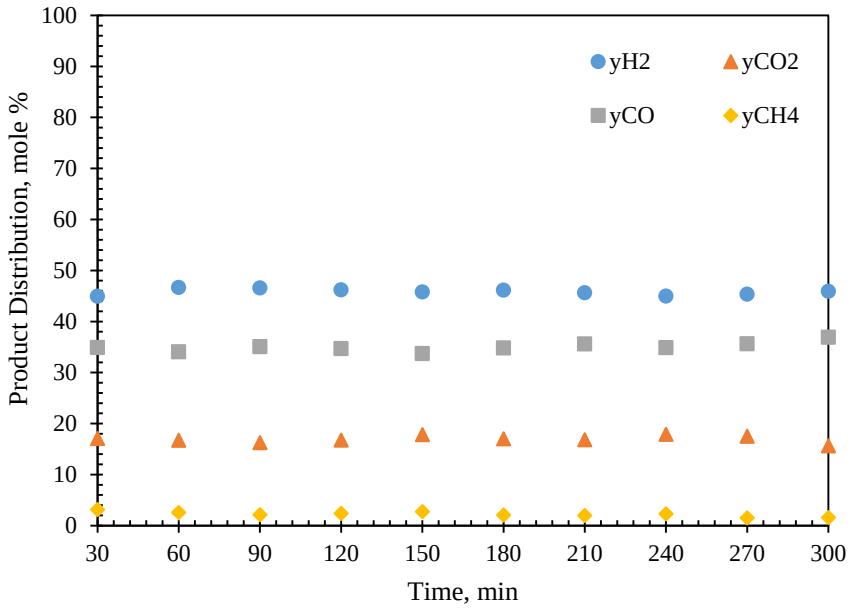

Figure G.47 Product Distribution of the GSR Reaction

(Catalyst:10Ag/SA(700)(1035), T_{rxn}:550°C, FFR:0.9ml/h, WGMR:9)

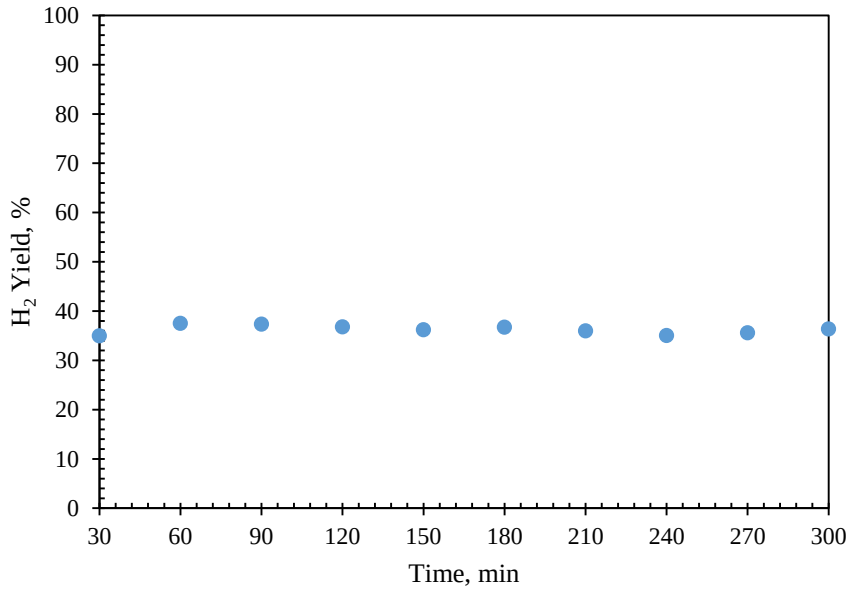

Figure G.48 H_2 Yield of the GSR Reaction

(Catalyst:10Ag/SA(700)(1035), T_{rxn}:550°C, FFR:0.9ml/h, WGMR:9

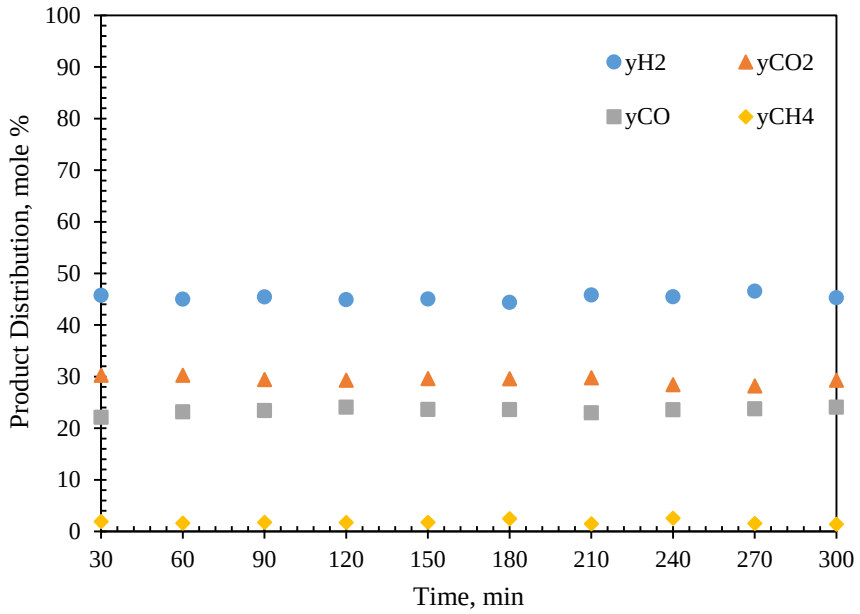

Figure G.49 Product Distribution of the GSR Reaction
(Catalyst:10Mo/SA(700)(1035), T_{rxn}:550°C, FFR:0.9ml/h, WGMR:9)

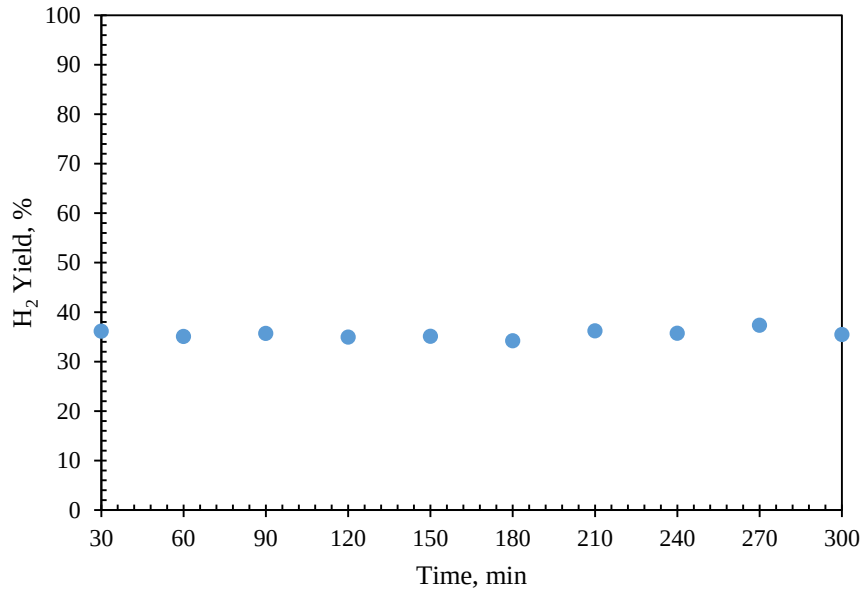

Figure G.50 H_2 Yield of the GSR Reaction
(Catalyst:10Mo/SA(700)(1035), T_{rxn}:550°C, FFR:0.9ml/h, WGMR:9

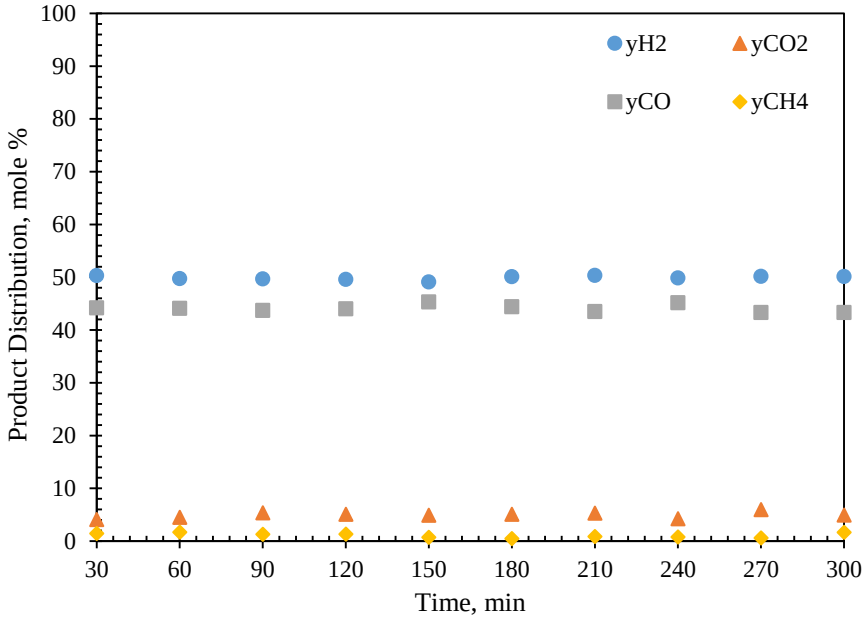

Figure G.51 Product Distribution of the GSR Reaction

(Catalyst:8Ni-2Mo(I)/SA(700)(1035), T_{rxn}:550°C, FFR:0.9ml/h, WGMR:9)

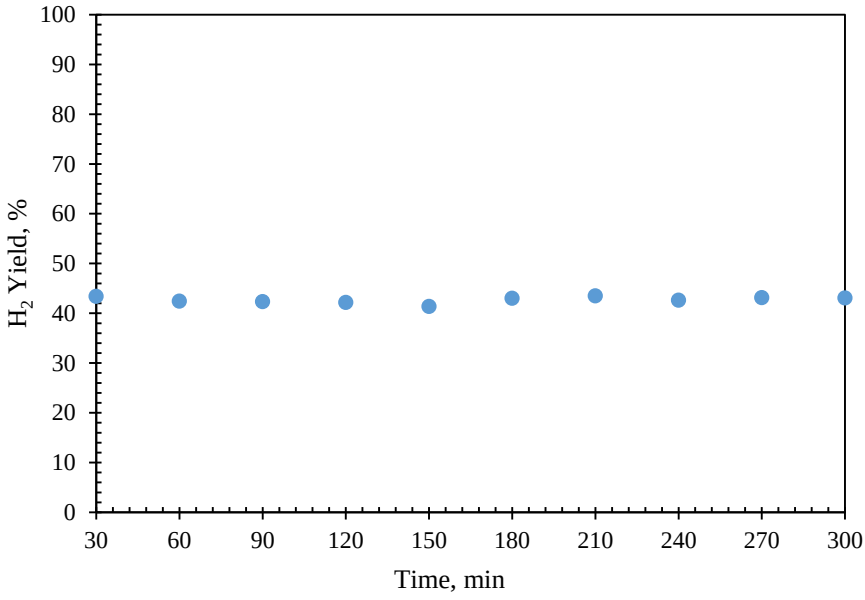

Figure G.52 H_2 Yield of the GSR Reaction

(Catalyst:8Ni-2Mo(I)/SA(700)(1035), T_{rxn}:550°C, FFR:0.9ml/h, WGMR:9)

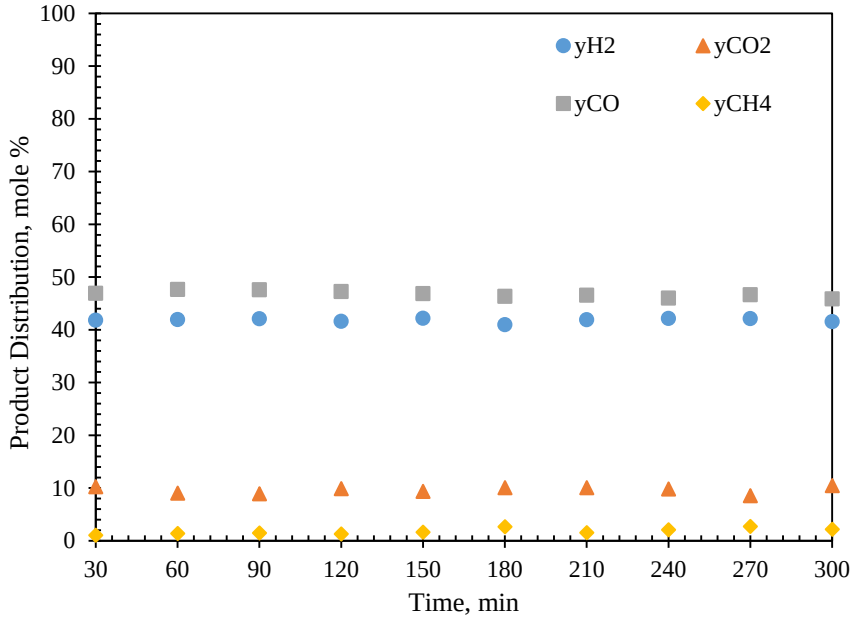

Figure G.53 Product Distribution of the GSR Reaction

(Catalyst:8Ni-2Mo(II)/SA(700)(1035), T_{rxn}:550°C, FFR:0.9ml/h, WGMR:9)

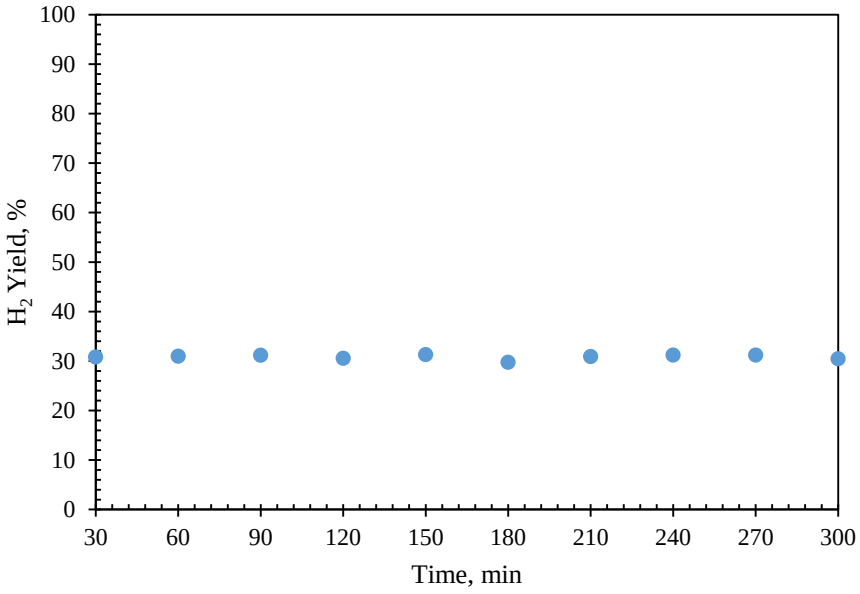

Figure G.54 H_2 Yield of the GSR Reaction

(Catalyst:8Ni-2Mo(II)/SA(700)(1035), T_{rxn}:550°C, FFR:0.9ml/h, WGMR:9)

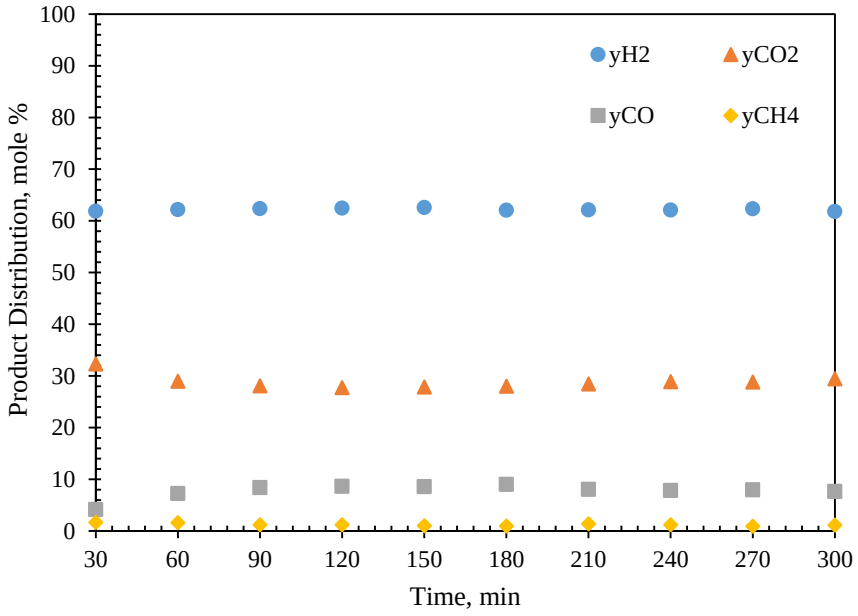

Figure G.55 Product Distribution of the GSR Reaction (Catalyst:10Ni-3Mg/SA(700)(700), T_{rxn}:550°C, FFR:0.9ml/h, WGMR:9)

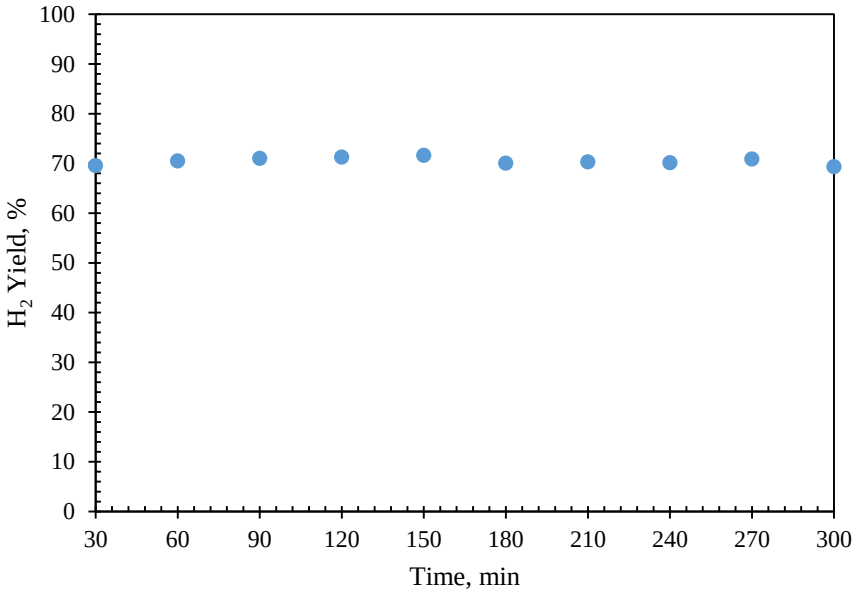

Figure G.56 H_2 Yield of the GSR Reaction (Catalyst:10Ni-3Mg(700)(700), T_{rxn}:550°C, FFR:0.9ml/h, WGMR:9)

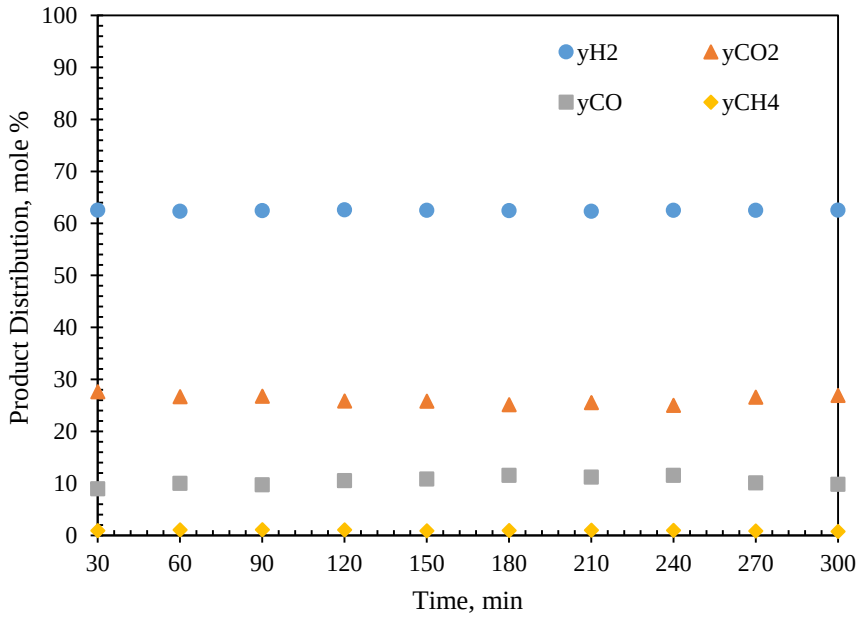

Figure G.57 Product Distribution of the GSR Reaction

(Catalyst:10Ni-3Fe/SA(700)(550), T_{rxn}:550°C, FFR:0.9ml/h, WGMR:9)

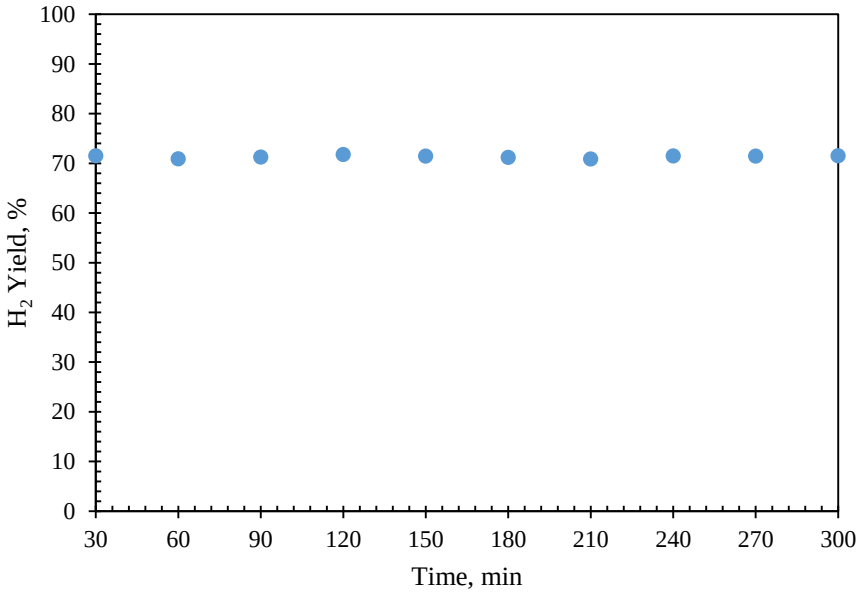

Figure G.58 H_2 Yield of the GSR Reaction

(Catalyst:10Ni-3Fe/SA(700)(550), T_{rxn}:550°C, FFR:0.9ml/h, WGMR:9)

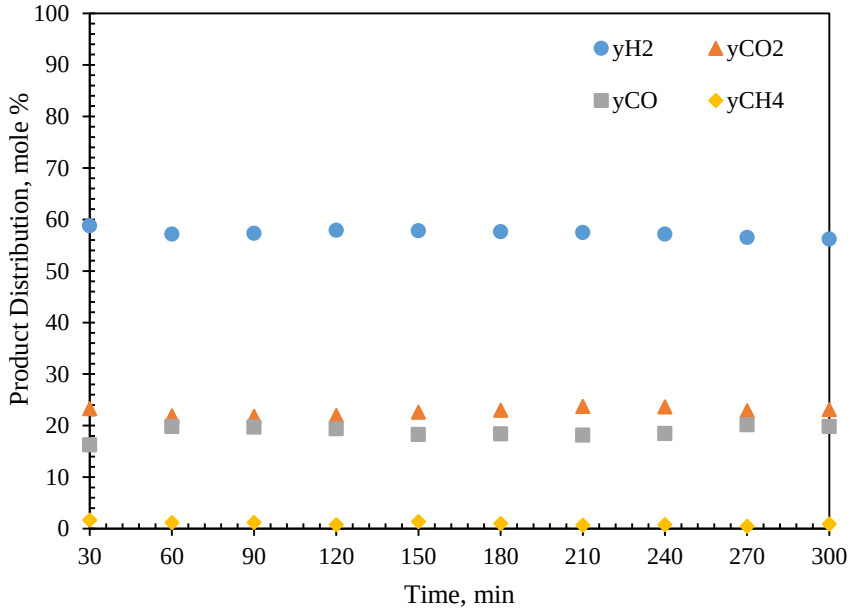

Figure G.59 Product Distribution of the GSR Reaction (Catalyst:10Ni-3Fe-0.3Mn/SA(700)(550), T_{rxn}:550°C, FFR:0.9ml/h, WGMR:9)

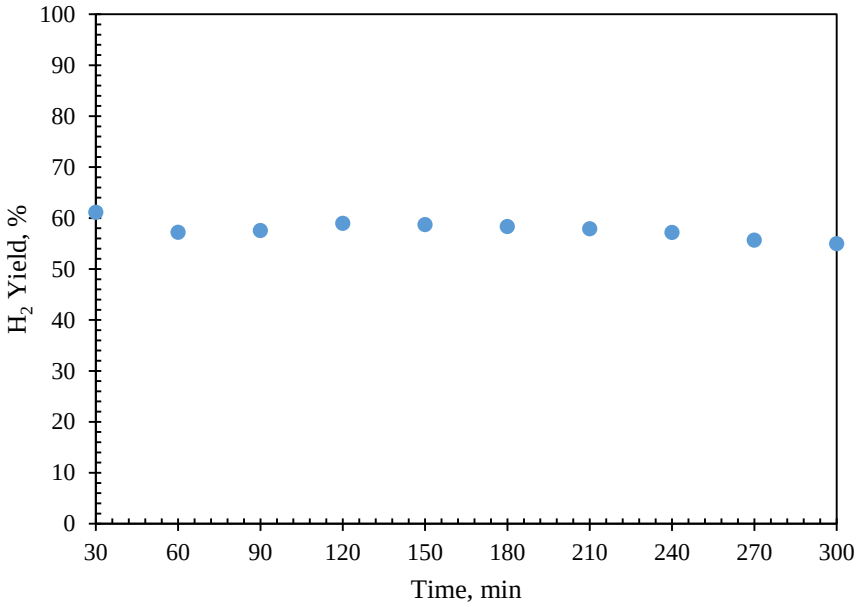

Figure G.60 H_2 Yield of the GSR Reaction (Catalyst:10Ni-3Fe-0.3Mn(700)(550), T_{rxn}:550°C, FFR:0.9ml/h, WGMR:9)

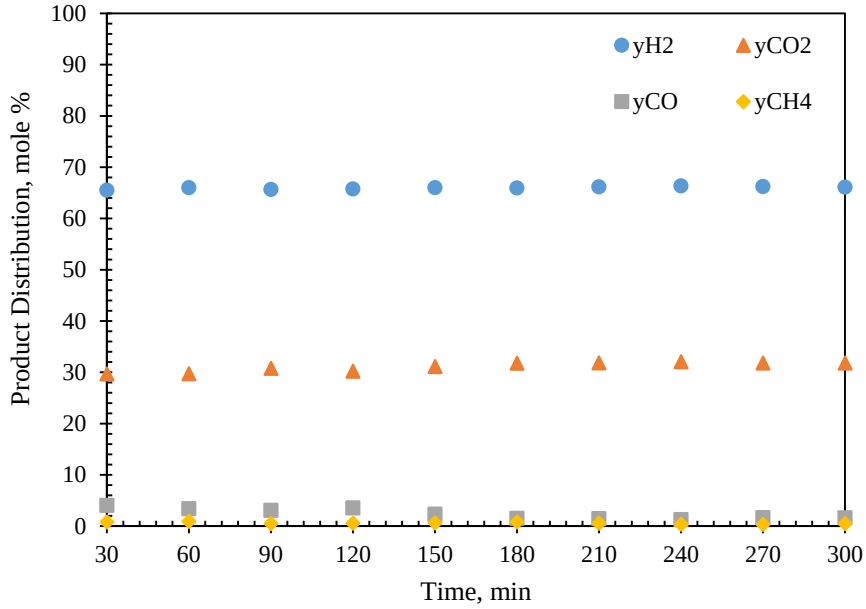

Figure G.61 Product Distribution of the GSR Reaction
(Catalyst:10Ni-1Ru/SA(700)(700), T_{rxn}:550°C, FFR:0.9ml/h, WGMR:9)

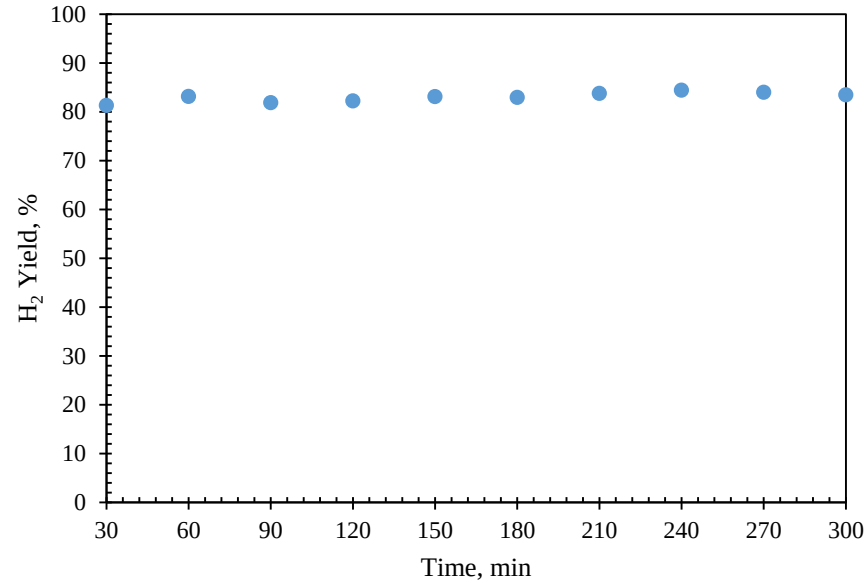

Figure G.62 H_2 Yield of the GSR Reaction
(Catalyst:10Ni-1Ru/SA(700)(700), T_{rxn}:550°C, FFR:0.9ml/h, WGMR:9)

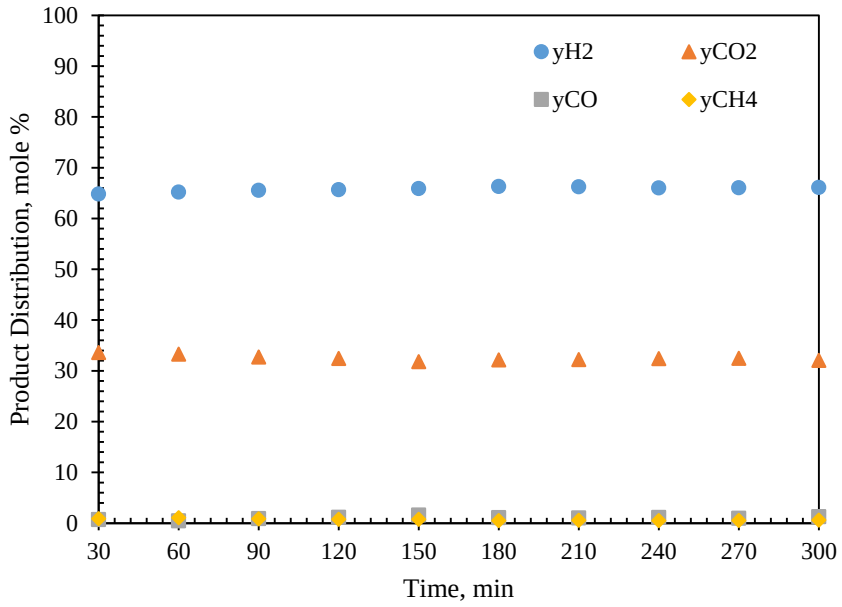

Figure G.63 Product Distribution of the GSR Reaction

(Catalyst:10Ni-3Ru/SA(700)(700), T_{rxn}:550°C, FFR:0.9ml/h, WGMR:9)

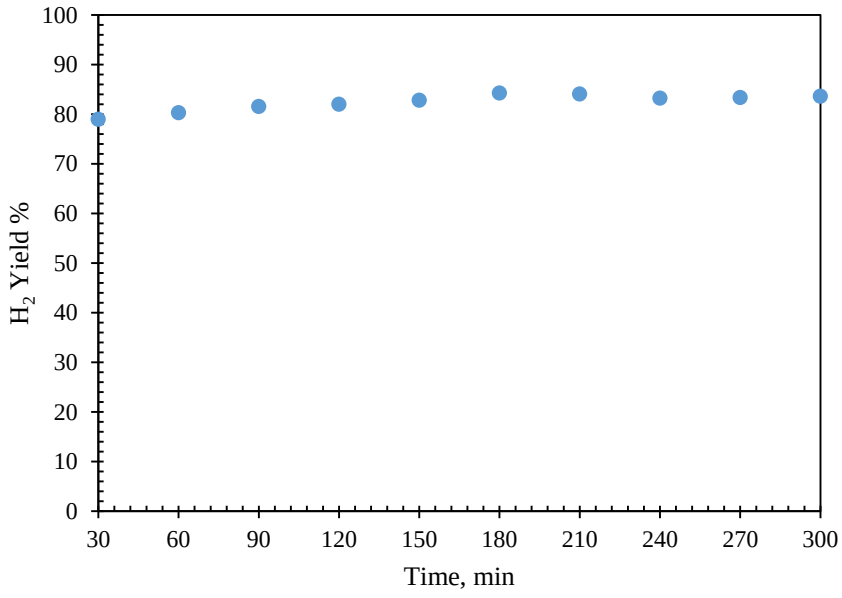

Figure G.64 H_2 Yield of the GSR Reaction

(Catalyst:10Ni-3Ru/SA(700)(700), T_{rxn}:550°C, FFR:0.9ml/h, WGMR:9)

Table G.1 Experimental Results

T_{rxn} (°C)	FFR (ml/h)	WGMR	Catalyst	Average Product Composition (mole %)				Average H_2 Yield %
				H_2	CO_2	CO	CH_4	
965	0.8	3	10Ni/SA(1035)(1035)	60.6±0.5	26.2±1.4	11.2±0.9	2.0±0.1	65.7±1.2
	0.9			60.7±0.5	27.5±1.4	9.8±0.9	2.0±0.1	66.4±1.2
	1.0			60.2±0.5	26.4±1.4	11.3±0.9	2.2±0.1	64.8±1.2
470	0.9	3	10Ni/SA(700)(1035)	52.9±0.1	7.9±1.8	36.6±2.1	2.7±0.2	48.3±0.2
500				57.7±0.1	17.4±1.8	22.3±2.1	2.6±0.2	58.9±0.2
540				62.2±0.1	31.5±1.8	4.8±2.1	1.5±0.2	68.1±0.2
610				62.8±0.1	31.7±1.8	4.8±2.1	0.7±0.2	72.8±0.2
680				63.4±0.1	29.7±1.8	6.3±2.1	0.6±0.2	74.2±0.2

Table G.1 (cont'd) Experimental Results

T_{rxn} (°C)	FFR (ml/h)	WGMR	Catalyst	Average Product Composition (mole %)				Average H_2 Yield %
				H_2	CO_2	CO	CH_4	
755	0.9	3	10Ni/SA(700)(1035)	63.1±0.1	28.3±1.8	8.1±2.1	0.5±0.2	73.3±0.2
825				61.5±0.1	26.6±1.8	11.3±2.1	0.6±0.2	68.8±0.2
895				60.7±0.1	26.5±1.8	10.8±2.1	2.0±0.2	66.4±0.2
965				60.0±0.1	25.3±1.8	12.2±2.1	2.5±0.2	64.4±0.2
1035				58.7±0.1	23.5±1.8	14.6±2.1	3.2±0.2	61.1±0.2
680		1		60.2±0.3	29.9±0.7	8.5±0.5	2.4±0.4	59.1±1.0
		6		64.1±0.3	29.6±0.7	5.9±0.5	0.5±0.4	76.6±1.0
		9		64.9±0.3	29.5±0.7	5.0±0.5	0.6±0.4	79.3±1.0

Table G.1 (cont'd) Experimental Results

T_{rxn} (°C)	FFR (ml/h)	WGMR	Catalyst	Average Product Composition (mole %)				Average H_2 Yield %
				H_2	CO_2	CO	CH_4	
470	0.9	9	10Ni/SA(700)(1035)	62.3±0.3	32.5±0.7	1.8±0.5	3.4±0.4	70.9±1.0
550				65.7±0.3	29.9±0.7	3.6±0.5	0.8±0.4	82.1±1.0
470			10Ni/SA(700)(1035)-wet	61.2	28.0	9.7	1.1	66.3
550				64.1	28.9	6.0	1.3	76.4
680				63.7	32.2	3.5	0.6	75.3
550			2.5Ni/SA(700)(1035)	59.0±0.2	29.3±2.8	10.8±2.6	0.9±0.2	61.6±0.8
			5Ni/SA(700)(1035)	64.1±0.2	28.0±2.8	7.0±2.6	1.0±0.2	76.4±0.8
			8Ni/SA(700)(1035)	65.2±0.2	32.3±2.8	1.6±2.6	0.9±0.2	80.4±0.8

Table G.1 (cont'd) Experimental Results

T_{rxn} (^oC)	FFR (ml/h)	WGMR	Catalyst	Average Product Composition (mole %)				Average H_2 Yield %
				H_2	CO_2	CO	CH_4	
550	0.9	9	10Co/SA(700)(1035)	35.6±0.2	12.1±2.8	48.8±2.6	2.6±0.2	23.7±0.8
			10Cr/SA(700)(1035)	27.4±0.2	21.0±2.8	47.5±2.6	4.1±0.2	16.2±0.8
			10Zr/SA(700)(1035)	4.9±0.2	16.3±2.8	77.0±2.6	1.8±0.2	2.2±0.8
			10Ag/SA(700)(1035)	45.8±0.2	16.9±2.8	35.0±2.6	2.2±0.2	36.3±0.8
			10Mo/SA(700)(1035)	45.3±0.2	29.4±2.8	23.4±2.6	1.8±0.2	35.6±0.8
			8Ni-2Mo/SA(700)(1035)(I)	49.9±0.1	4.9±0.1	44.1±0.2	1.1±0.1	42.7±0.2
			8Ni-2Mo/SA(700)(1035)(II)	41.8±0.1	9.6±0.1	46.8±0.2	1.8±0.1	30.8±0.2
			10Ni-3Mg/SA(700)(700)	62.2±0.1	28.9±0.1	7.7±0.2	1.2±0.1	70.5±0.2

Table G.1 (cont'd) Experimental Results

T_{rxn} (°C)	FFR (ml/h)	WGMR	Catalyst	Average Product Composition (mole %)				Average H_2 Yield %
				H_2	CO_2	CO	CH_4	
550	0.9	9	10Ni-3Fe/SA(550)(550)	62.5±0.1	26.2±0.1	10.4±0.2	1.0±0.1	71.3±0.2
			10Ni-3Fe-0.3Mn/SA(550)(550)	57.4±0.1	22.8±0.1	18.8±0.2	1.0±0.1	57.7±0.2
			10Ni-1Ru/SA(700)(700)	66.0±0.1	31.1±0.1	2.4±0.2	0.6±0.1	83.0±0.2
			10Ni-2Ru/SA(700)(700)	66.3±0.1	30.0±0.1	3.2±0.2	0.5±0.1	84.5±0.2
			10Ni-3Ru/SA(700)(700)	65.8±0.1	32.5±0.1	1.0±0.2	0.7±0.1	82.4±0.2

H. Calculation of Carbon Deposition Amount in Catalysts

Amount of carbon deposited in the catalysts was obtained by considering the weight loss in the catalysts according to the TGA results. Equation H.1 was used to determine the amount of carbon deposited in the catalysts during the reaction period.

$$carbon\ deposition\ amount = \frac{weight\ loss\ percent * weight\ of\ catalyst\ used\ in\ the\ reaction}{reaction\ period} \qquad H.1$$

where,

Carbon deposition [=] $g_C/g_{Cat}h^{-1}$

Weight loss percent [=] %

Weight of catalyst used in the reaction = 0.15 g

Reaction period = 5 h